Contents

List of Tables

List of Figures

Chapter 1

Introduction

The assimilation system described in this document is a frozen version of the Goddard Earth Observing System Data Assimilation System (GEOS DAS), significant features of which include: the finite-volume dynamics of the finite-volume Community Climate Model (fvCCM); version 3 of the Community Climate Model Physics, with the addition of version two of the Community Land Model (CLM2); the Physical-space Statistical Analysis System (PSAS); and an interactive retrieval system (IRET) for assimilating TOVS radiance data.

The primary performance drivers for the production of GEOS DAS assimilation fields are the radiation budget needs of the CERES instrument team, and the transport needs of the Stratospheric chemistry community. Other significant concerns for GEOS DAS (throughout its existence) have involved the provision of near real-time mission support for a number of chemistry mission field campaigns as well as off-line support for other EOS instrument teams, notably MODIS, AIRS and TRMM.

The validation process seeks to assess both the overall scientific behavior of a candidate upgrade to GEOS DAS, as well as its capability to address specific issues (usually issues that were drivers for changing/upgrading the DAS). This assessment activity requires contributions from science efforts across the entire GMAO organization. The specific validation objectives, as well as the organization of this validation exercise are covered in Chapter 4.

This validation documentation is organized as follows:

- An overview of the development of GEOS-4 (the latest version of GEOS DAS), and its context in the development of atmospheric assimilation systems at NASA/GSFC is given in Chapter 2.

- The main characteristics of the climate model and the assimilation system are described in Chapeter 3.

- The analysis and model changes that are the drivers for this particular validation effort, as well as the approach for performing the validation are summarized in Chapter 4.

- The results of the several validation evaluation efforts are detailed in Chapter 5.

- The final summary and recommendation is given in Chapeter 6.

Chapter 2

Background

GEOS DAS has evolved over a number of years, with the primary milestones driven by major launches of the EOS series of satellites. It is reasonable to set the start of the current GEOS DAS development process to GEOS-1, which combined a version of the Phoenix 4th order GCM with a mini-volume version of Optimum Interpolation (OI) analysis, and used an Incremental Analysis Updating (IAU) framework (Schubert et al. 1993). That system (model and analysis) had a horizontal resolution of 2 degrees latitude by 2.5 degrees longitude, and it was used to produce one of the first multi-year reanalyses. More than 100 papers and presentations came from the GEOS-1 reanalysis effort. A workshop on the GEOS-1 products was held in 1995, and improvements to the Phoenix model were made as a consequence of results presented at that workshop. The modified GEOS-1 system, with changes made both to GCM and analysis, was used to support many NASA-sponsored aircraft missions to study stratospheric chemistry, as well as some tropospheric chemistry missions.

With the advent of subsequent reanalyses by the National Centers for Environmental Prediction (NCEP) and the European Center for Medium-range Weather Forecasts (ECMWF) that were significant improvements beyond the GEOS-1 reanalysis, an effort to re-do the FGGE year (1979) with a modified version of GEOS-1 (based largely on the changes made after the GEOS-1 reanalysis workshop) was planned. This modified version of GEOS became instead GEOS-2, a testing platform for a new analysis: Physical-Space Statistical Analysis System (PSAS). The main driver for GEOS-2 therefore became the preparation for the upcoming launch of the EOS-AM (now TERRA) platform. Along with the inevitable teething pains of implementing a new analysis in a full assimilation system, there were also a number of significant changes to other parts of the assimilation process that complicated greatly the development process for GEOS-2. A brief list of the these issues would include:

- Moist Boundary Layer (Schubert et al. 1993);

- Mosaic Land Surface Model;

- On-line Quality Control (see section 3.3);

- Moisture Bias Adjustment (Dee and Todling 2000);

- Total Precipitable Water (TPW) Assimilation (Hou et al. 2000a).

Ultimately a version of GEOS-2, which had a 1x1 degree GCM and 2x2.5 degree analysis, was used in a "pre-ops" form in support of the CERES-TRMM mission in 1999.

As 2000, and the launch of TERRA approached, the CERES-TRMM version of GEOS was subjected to an extensive overhaul to prepare it for operations; little of the scientific behavior was affected by that work. This EOS-launch version, which produced 1x1 degree output, became version 3.0 of GEOS DAS. Subsequent modifications that were incorporated in the GEOS-3.x series were:

- Interactive Retrievals (iRET), for assimilating TOVS radiance data;

- Modified Vertical Interpolation, for better coupling model and analysis;

- Precipitation Assimilation, (Hou et al. 2000b, 2001).

The final operational version of GEOS-3.x was 3.3.9, and the final research version with precipitation assimilation was 3.4.1. Even though the GEOS-3.x system had met basic validation requirements, there remained significant issues that needed to be addressed. The system was slow, making reanalysis efforts with it an extremely cumbersome and expensive affair. The DAS fields had excessively noisy structures in the Stratosphere, creating significant problems when using GEOS-3 fields as forcing for transport modeling (especially ozone). There was also a skin temperature bias that created problems for radiation budget investigations (*e.g.* CERES).

In order to address these issues, a major effort to change the assimilation GCM was undertaken in 1999. The model combined the finite-volume dynamics developed at the DAO (Lin and Rood 1996, 1998) with the physics developed for the NCAR Community Climate Model (CCM, see Kiehl et al. 1985, 1998). The DAS formed by combining the fvGCM with the PSAS analysis became the "fvDAS" system, and this system then evolved into the operational system referred to as GEOS-4. This approach marked a substantial break with the previous 10 years of GEOS development; a whole new hydrodynamics as well as physics was implemented, along with a substantially modified analysis-model interface, and IAU was abandoned. A surface skin temperature assimilation was introduced to control a significant skin temperature bias. The resolution was changed to 1x1.25 degree (lat-lon) resolution for fvGCM efficiency considerations; there were 55 vertical layers (in a hybrid sigma-pressure coordinate system) with the model top at 0.01 hPa.

The version of GEOS-4 that is the subject of this validation document has several modifications beyond the original fvDAS system; these issues will be discussed in chapter 3 which describes GEOS-4 in some detail.

Chapter 3

GEOS-4 Data Assimilation System

In this Chapter, the salient features of the GEOS-4 Data Assimilation System (GEOS-4 DAS) will be described. For the purposes of this exposition, the DAS will be described in four main sections:

- General Circulation Model (GCM)

- Analysis (PSAS in this case)

- Quality Control (of observations)

- Model–Analysis Interface.

Each of these items will be covered in some detail in the sections that follow in this Chapter. The validation effort that is the subject of this document was concerned with the third (and final) operational version of GEOS-4 DAS; this system was designated as 4.0.3, or "C403." It was also version 1.4r2 on the fvDAS development tree (which explains the occasional appearance of this label in some of the results presented in Chapter 5).

3.1 GEOS-4 GCM

3.1.1 Hydrodynamics

The General Circulation Model used for the GEOS-4 DAS is the model jointly developed by the Data Assimilation Office (DAO) and the Climate and Global Dynamics Division (CGDD) at NCAR. The finite-volume dynamical core of this model was developed at the DAO, and it has an extensive documentation in the open literature (cf. Lin and Rood 1996; Lin 1997; Lin and Rood 1997, 1998).

3.1.2 Physics

The operational version of fvGCM adopted the physics from the NCAR CCM3 (Community Climate Model version 3) and WACCM (Whole Atmosphere Community Climate Model)

with several important modifications to make it more suitable for high-resolution weather prediction applications and for coupling to a data assimilation system.

3.1.2.1 CCM3 Parameterizations

The NCAR CCM3 parameterizations are a well-balanced set of processes with a long history of development and documentation (Kiehl et al. 1985, 1998). The package includes four major groups of physical processes: precipitation processes, clouds and radiation, turbulent mixing, and surface processes. Each of these in turn is subdivided into various components. The precipitation processes are comprised of deep convection, shallow/middle moist convection, and large-scale stable condensation. The clouds and radiation include cloud parameterization, longwave radiation, and shortwave radiation. The turbulent mixing consists of the vertical diffusion, planetary boundary layer parameterization, and gravity wave drag. The surface processes provide surface fluxes obtained from land, ocean and sea ice models.

3.1.2.1.1 CCM3 precipitation processes The process of moist penetrative convection is treated with a scheme developed by Zhang and McFarlane (1995). The scheme is based on a plume ensemble approach where it is assumed that an ensemble of convective updrafts and the associated downdrafts may exist whenever the atmosphere is conditionally unstable in the lower troposphere. The cumulus plumes act to consume convective available potential energy (CAPE) at an exponential rate using a specified adjustment time scale. The treatment of shallow and middle-level convection processes is based on Hack (1994). The cloud microphysics in fvGCM followed the simple diagnosed condensate parameterization in the standard CCM3. Stratiform condensation takes place when a grid box is completely saturated. The diagnosis of cloud fraction is a generalization of the scheme introduced by Slingo (1987), with modifications described in Kiehl et al. (1998). Cloud fraction depends on relative humidity, vertical velocity, atmospheric stability and convective mass fluxes. Three types of cloud are diagnosed by the scheme: low-level marine stratus, convective cloud, and layered cloud. Clouds are allowed to form in any model layer, except the layer nearest the surface.

3.1.2.1.2 CCM3 clouds and radiation The vertical distribution of in-cloud condensate used in the radiative transfer calculation is prescribed as a function of the vertical integrated water vapor (Hack 1998). Clouds are assumed to be plane parallel and randomly overlapped between layers. The parameterization of cloud droplet size and other cloud optical properties is described in Kiehl et al. (1998). For the radiation package, the longwave radiative transfer is based on an absorptivity-emissivity formulation (Ramanathan and Downey 1986) and the shortwave radiative parameterization used the δ-Eddington method (Briegleb 1992) with 18 spectral bands. The model accounts for the radiative effects of water vapor, O2, CO2, O3, and trace gases: CH4, N2O, CFC11, and CFC12. The distribution of the trace gases is specified in terms of zonal-mean mixing ratios for each species (Kiehl et al. 1985). A uniform background boundary layer aerosol is included in the shortwave radiative parameterization. The aerosol is assumed well mixed in the bottom three layers of the model.

3.1.2.1.3 CCM3 turbulent mixing The free atmospheric turbulent diffusivities are based on the gradient Richardson number. The atmospheric boundary-layer turbulence parameterization utilizes the "nonlocal" formulation (Holtslag and Boville 1993). The eddy diffusivity and the nonlocal terms are dependent on the PBL height that is estimated from a bulk Richardson number with surface friction. The fvGCM incorporates the gravity wave drag parameterization from the NCAR Whole Atmosphere Community Climate Model (WACCM). The scheme includes orographic gravity wave drag based on McFarlane (1987) and a parameterization of a spectrum of traveling gravity waves.

3.1.2.1.4 CCM3 surface processes The surface exchange of heat, moisture and momentum between the atmosphere and land, ocean or sea ice surfaces are treated with a bulk exchange formulation based on Monin-Obukhov similarity theory. In fvGCM, the NCAR Land Surface Model (LSM; Bonan 1998) in CCM3 was replaced by the Community Land Model CLM2 (Bonan et al. 2002). A brief description of the land model will be provided later. The fvGCM employs a specified distribution of sea surface temperatures and sea ice, either from an observed weekly/monthly mean time series or annually repeating climatological mean. Sea ice is calculated via a multi-layer thermodynamic model.

3.1.2.2 fvGCM Modifications

Many important modifications to the CCM3 physics have been incorporated into the fvGCM to make it more suitable for coupling to a data assimilation system as well as for high-resolution weather prediction and climate simulation. When compared to CCM3, the changes to the model physics fall into four major categories: modifications to initial and boundary data; improvements and tunings of the existing schemes; addition and tuning of a new land surface model, CLM2; and the addition of other optional physical packages.

3.1.2.2.1 Modifications to initial and boundary data In its standard configuration the fvGCM employs a horizontal $1° \times 1.25°$ resolution with 55 vertical levels from surface to 1 Pascal. The initial and boundary data need to match the model resolution and vertical domain. The new zonal mean climatological ozone dataset used in fvGCM is a combination of AMIP (Atmospheric Model Intercomparison Project) ozone data, the Free University Berlin (FUB) data, and the Upper Atmosphere Research Satellite (UARS) ozone data. The surface orography and its sub- grid scale standard deviation were derived from the 30-second US Geological Survey Global Topographic Data (GTOPO30). An area-preserving algorithm was used to map the high-resolution GTOPO30 dataset to model resolutions. The sea surface temperature and sea ice concentrations in fvGCM are derived from the weekly $1° \times 1°$ Reynolds' optimum interpolation sea surface temperature (OISST) version 2 (Reynolds et al. 2002). They are updated every time step using linear interpolation in time. The fvGCM also employs an option to nudge the stratospheric water vapor to the zonal mean climatological HALOE (Halogen Occultation Experiment) and MLS (Microwave Limb Sounder) water vapor data (Randel et al. 1998).

3.1.2.2.2 Changes to moist physics Changes to the moist physics include the incorporation of a convective rain re-evaporation scheme, the introduction of ice-phase latent

heating associated with freezing and melting in the calculation of large-scale stable condensation, and a revision to the diagnosed in-cloud water condensate. The fvGCM employs a Sundqvist (1988) style evaporation of the convective precipitation as it makes its way to the surface. In climate simulations, this evaporation scheme produces a very small moistening in the lower troposphere and reduction in the convective precipitation. The cloud parameterization of the standard CCM3 assumes clouds in the near-surface layers always have about the same water content ($0.21\ gm^{-3}$) everywhere. This assumption produces an abundance of very bright, low cloud with very strong cloud top longwave radiation cooling in the low troposphere, especially over the polar region. In the fvGCM, the in-cloud water content in the near-surface layers is limited to 5 percent of the saturated water vapor mixing ratio. This change reduced the systematic polar cold bias in the lower troposphere and prevented the extreme supersaturation over the Antarctic region in data assimilation analyses.

The original physics package of the NCAR CCM3 has been tuned for T42 resolution. With the use of substantially higher horizontal resolutions in the GEOS systems, along with modifications to model algorithms and the use of new initial and boundary data, a significant re-tuning of the fvGCM physics was required. The WACCM gravity wave drag scheme was heavily tuned to produce reasonable climate due to the introduction of GTOPO30 high-resolution topography data and higher model horizontal resolution. Cloud and radiation components were re-tuned to restore energy balance at the surface and top-of-atmosphere. Parameters that have been adjusted include: the relative humidity thresholds for low and high clouds, the differential threshold at which clouds form over land verse ocean, the effective radius of the cloud droplets and ice crystals, and the background aerosol formulation. As a result, the global mean absolute errors at the surface and top-of-atmosphere are less than $1\ Wm^{-2}$, while maintaining very good agreement with global observational estimates of cloud forcing.

3.1.2.2.3 CLM2 land model The fvGCM incorporates version 2 of the Community Land model (CLM2) that provides for the comprehensive treatment of land surface processes. It was developed collaboratively by an open interagency/university group of scientists. CLM2 is a one-dimensional land surface model that includes comprehensive biogeophysics, hydrological and biogeochemical processes, and vegetation dynamics components. Sub-grid scale tiles are used to represent the surface horizontal heterogeneity. It has one vegetation layer with a realistic photosynthesis-conductance model based on Bonan (1996) to realistically depict evapotranspiration. There are 10 unevenly spaced vertical layers for soil with soil temperature, soil liquid water, and ice lens mass as model state variables in each layer. The CLM2 features up to five snow layers depending on the snow depth with water flow, refreezing, compaction and aging allowed. In addition, the CLM2 utilizes two-stream canopy radiative transfer, the Bonan lake model (1996), topographic enhanced streamflow based on TOPMODEL (Beven and Kirkby 1979), and turbulence is considered above, within, and below the canopy. Additional model details are provided in Zeng et al. (2002), Bonan et al. (2002), and Dai et al. (2003).

A number of significant changes to the model formulations of CLM2 have been made at NASA/GSFC. The drag coefficient under the canopy was newly formulated as a function of the Leaf Area Index (LAI). This change had substantial impact on the reduction in model warm and dry bias. The energy balance equation at the leaf surface was revised to include

the effect of leaf heat capacity. This modification improved the simulation of the diurnal cycle with only marginal impact on the overall skin temperature error. A new efficient implicit scheme was used to solve the water and energy balance of the vegetation canopy. The incorporation of precipitation sub-grid scale variability into the canopy interception scheme caused a decrease of interception loss and increase in canopy infiltration (Dickinson et al. 2003). The positive impacts were an increase in the soil moisture and improved water partitioning. With the modified interception scheme, the sub-surface runoff scheme was turned off. This change corrected some overestimation of lateral sub-surface runoff, and reduced warming caused by the revised interception. The thickness of the vertical layers in the lake model was modified to prevent the Great Lakes from being perpetually frozen. The interpolation scheme of the land boundary data was revised to avoid the faulty assignment of lake points to wetlands in high-resolution applications. To compare with the observed surface skin temperature from satellites, the calculation of model skin temperature was modified to be based on the surface outgoing longwave radiation and the emissivities of sub-grid tiles. Collectively these modifications substantially reduce systematic biases in the CLM2. As a result, the CLM2 was found to be superior to the NCAR LSM in climate simulation, numerical weather prediction and data assimilation.

3.1.2.2.4 Optional physics packages The incorporation of other optional physical packages in fvGCM included NASA/GSFC moist level 2.5, second-order turbulence closure schemes (Helfand and Labraga 1988); NASA/GSFC longwave and shortwave radiation scheme (Chou et al. 1999, 2003); McRAS (Microphysics of Clouds with Relaxed Arakawa-Schubert Scheme) cloud scheme (Sud and Walker 1999); and the NOAA/NCEP deep convective scheme (Hong and Pan 1998). These options allow model developers and users to study the impacts of different parameterizations on climate simulation, numerical weather prediction and data assimilation.

3.1.3   AMIP (Climatology) Results

Periodically, Atmospheric Model Intercomparison Project (AMIP) runs are performed at the GMAO to provide benchmarks with existing models as a first step in the process of developing or implementing new atmospheric GCMs for a new DAS effort.

The fvGCM (the model in the GEOS-4 DAS) was examined in such an AMIP context; this effort consisted of a base version of fvGCM, some versions of fvGCM having variations in physics, the model used in the GEOS-3 DAS, and the models used and being developed by the NASA Seasonal-to-Interannual Prediction Project (NSIPP). The following is a list of the GCMs evaluated:

Model #1) GEOS-3 (2x2.5 x 48 Levels, Aries Dynamical Core, Goddard Physics)

Model #2) fvGCM (1x1.25 x 55 Levels, Finite Volume Core, NCAR Physics)

Model #3) fvGCM w/McRAS Moist Physics

Model #4) fvCSU (fvGCM w/CSU Moist Physics)

Model #5) NSIPP-1 (1x1.25 x 34 Levels, Aries Dynamical Core, NSIPP-1 Physics)

Model #6) NSIPP-2 (2x2.5 x 40 Levels, Aries Dynamical Core, NSIPP-2 Physics)

The models were run from January 1982 through December 1998 using the Hadley Centre SST and Sea-Ice datasets. Detailed results from the intercomparison are available from the GMAO Web home page:

http://gmao.gsfc.nasa.gov/research/modeling/models/private/amip/index.php

Of particular interest in this validation context is the precipitation climatology of the GEOS-4 GCM. Analysis of the seasonal mean precipitation fields show that the operational GEOS-4 GCM (Model #2 described above) produced simulations that were comparable to the other models and quite realistic when compared to GPCP data for the same time period. Figures 3.1 and 3.2 display the mean seasonal DJF and JJA, respectively) precipitation fields from the six runs and a GPCP verification. Figures 3.3 and 3.4 show the pattern of differences of the six precipitation patterns with the verification.

It can be seen that while specific subtle differences exist between models, the dominant seasonal mean errors are quite similar when compared to the GPCP data. This result is significant in light of the DAS results presented in Chapter 5, where the DAS-forced precipitation differs strongly from climatology.

A sense of the differences in variability (anomalies with respect to the above means) can be seen through the use of Taylor diagrams. A point on a Taylor diagram represents a polar-coordinate point: the radius is a model's anomaly standard deviation divided by the verification anomaly standard deviation; the angle from the x-axis is the arc-cosine of the correlation between a model and the verification anomalies. Thus a "perfect" agreement between a model's anomaly pattern and a verification anomaly pattern would be represented by a circle at "1.00" on the x-axis. The anomaly pattern correlation and ratio of anomaly standard deviations in Figure 3.5 indicate that the GEOS-4 GCM produces results comparable to the other model runs.
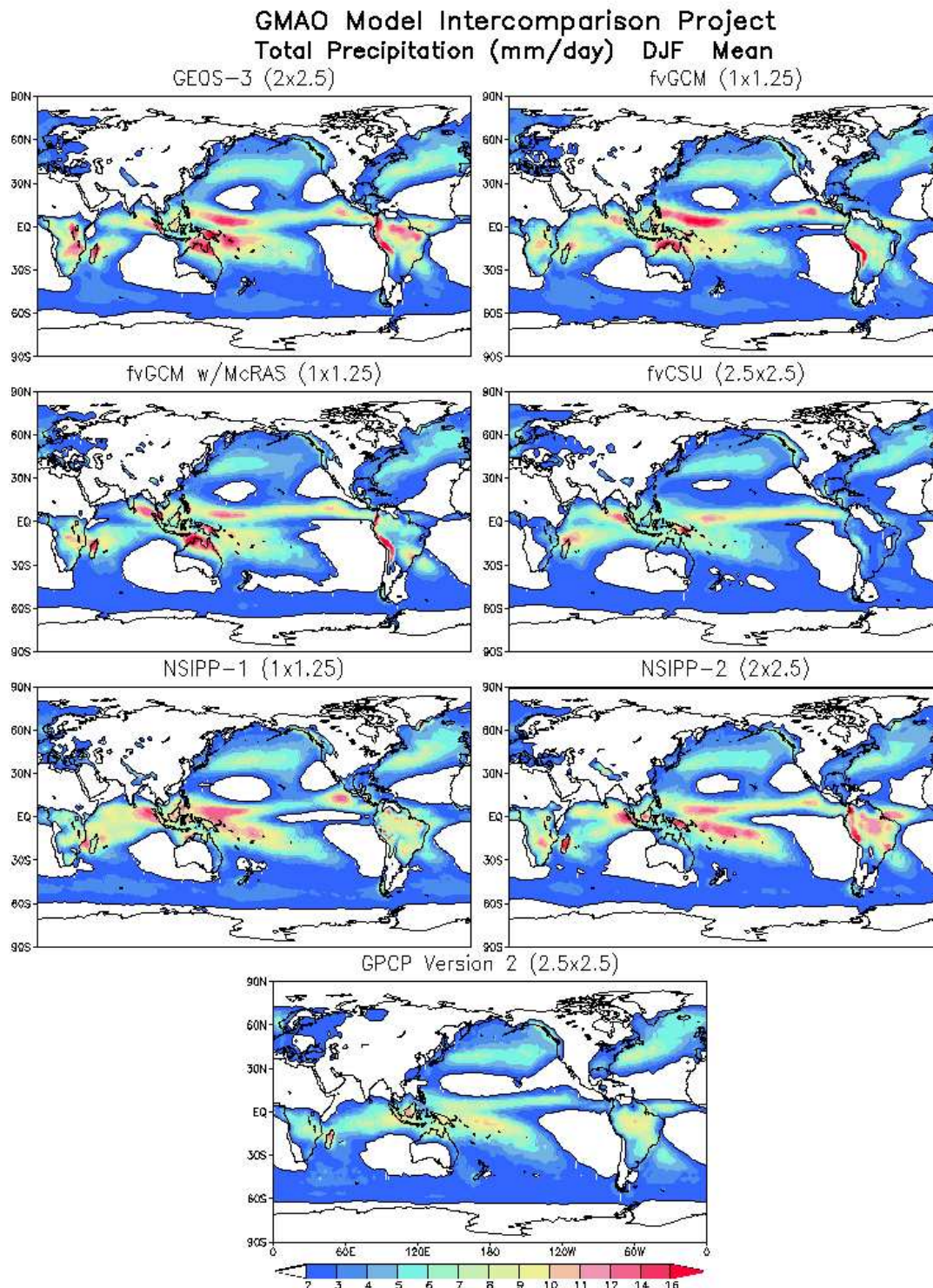
Figure 3.1: December, January, February (DJF) mean total precipitation in mm/day for the six intercompared models. GPCP verification climatology for this period is shown at the bottom.
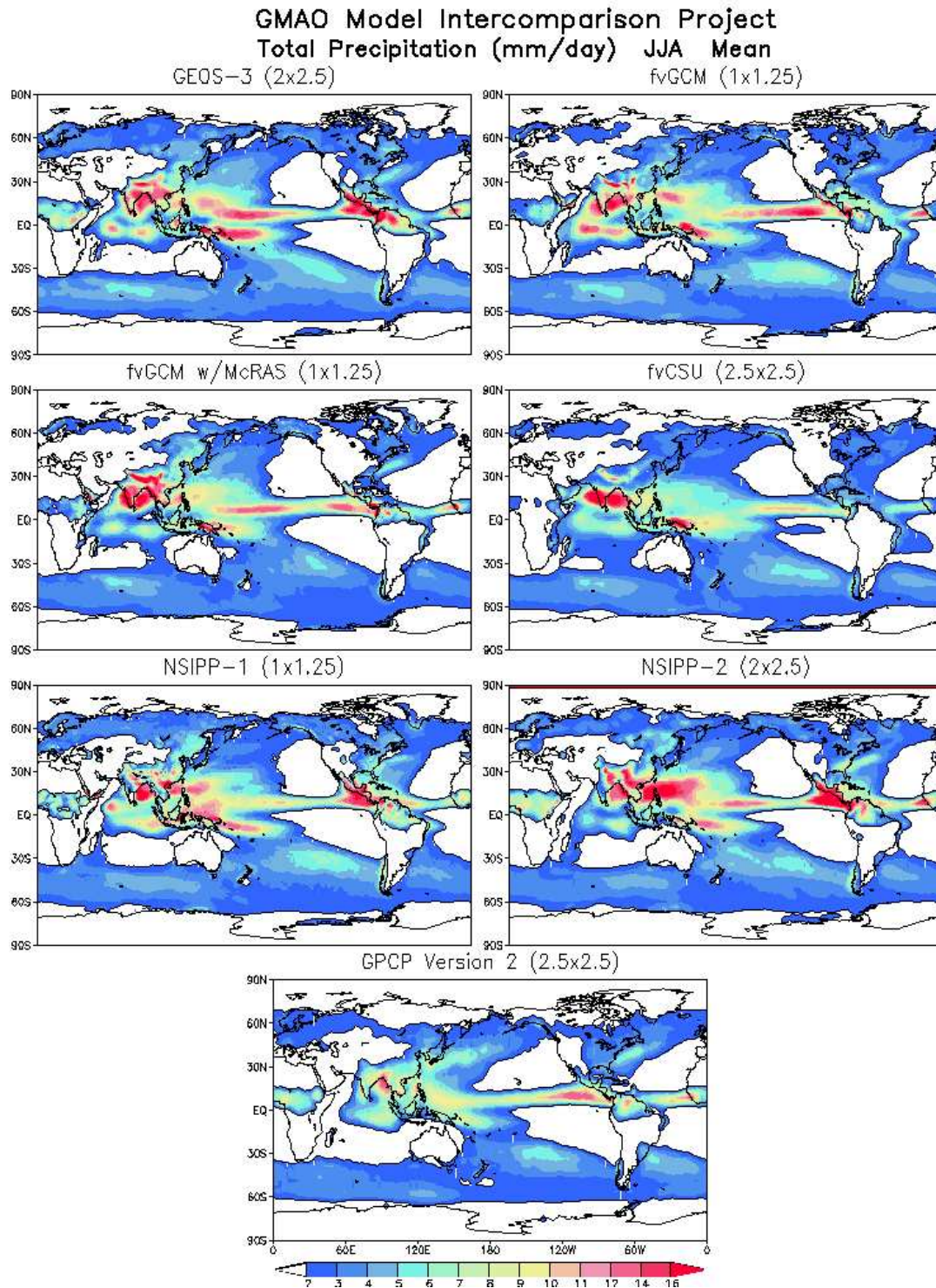
Figure 3.2: Same as 3.1, except the period is June, July, August (JJA)
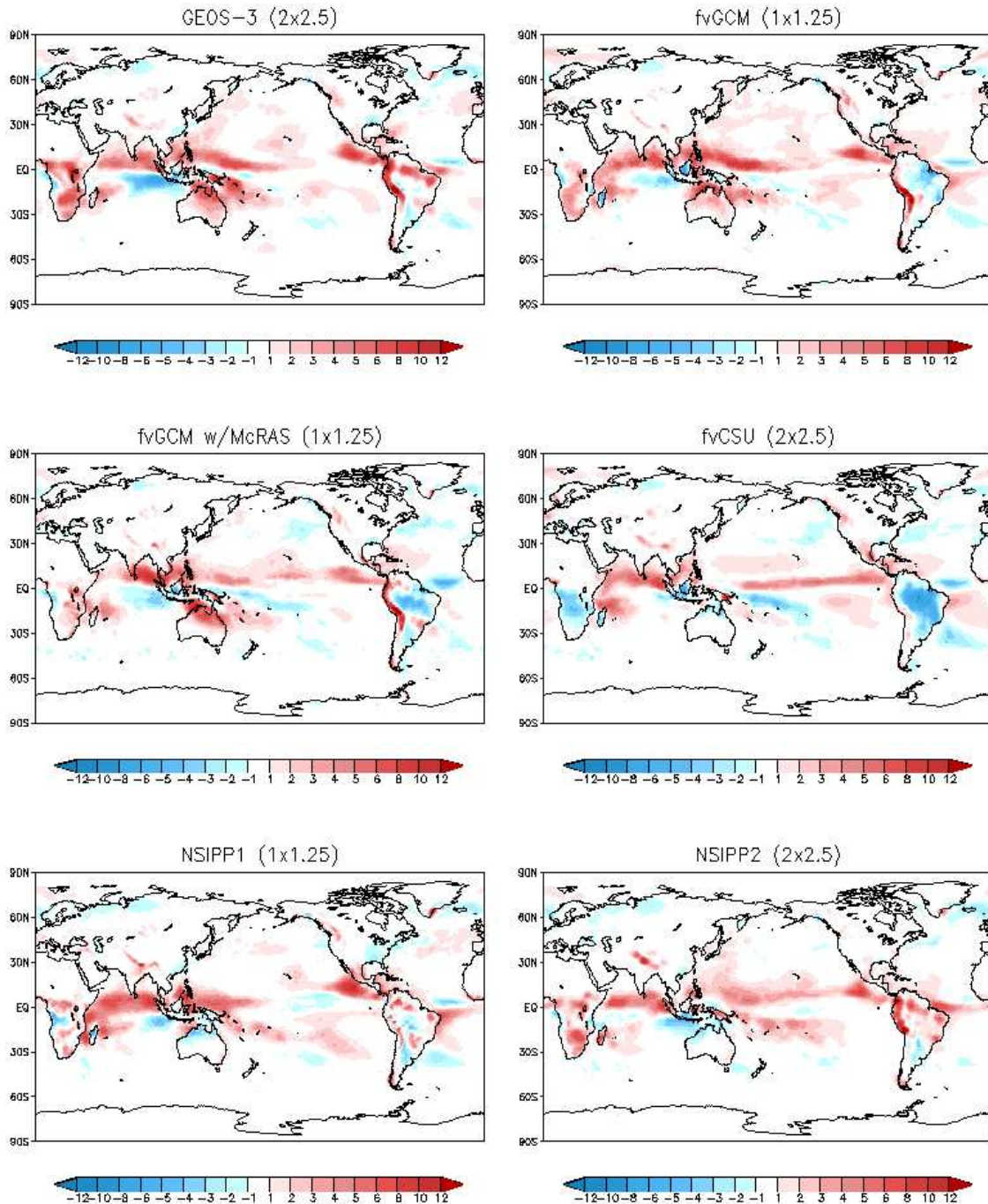
Figure 3.3: December, January, February (DJF) precipitation differences in mm/day for each of the six models compared with the GPCP verification.
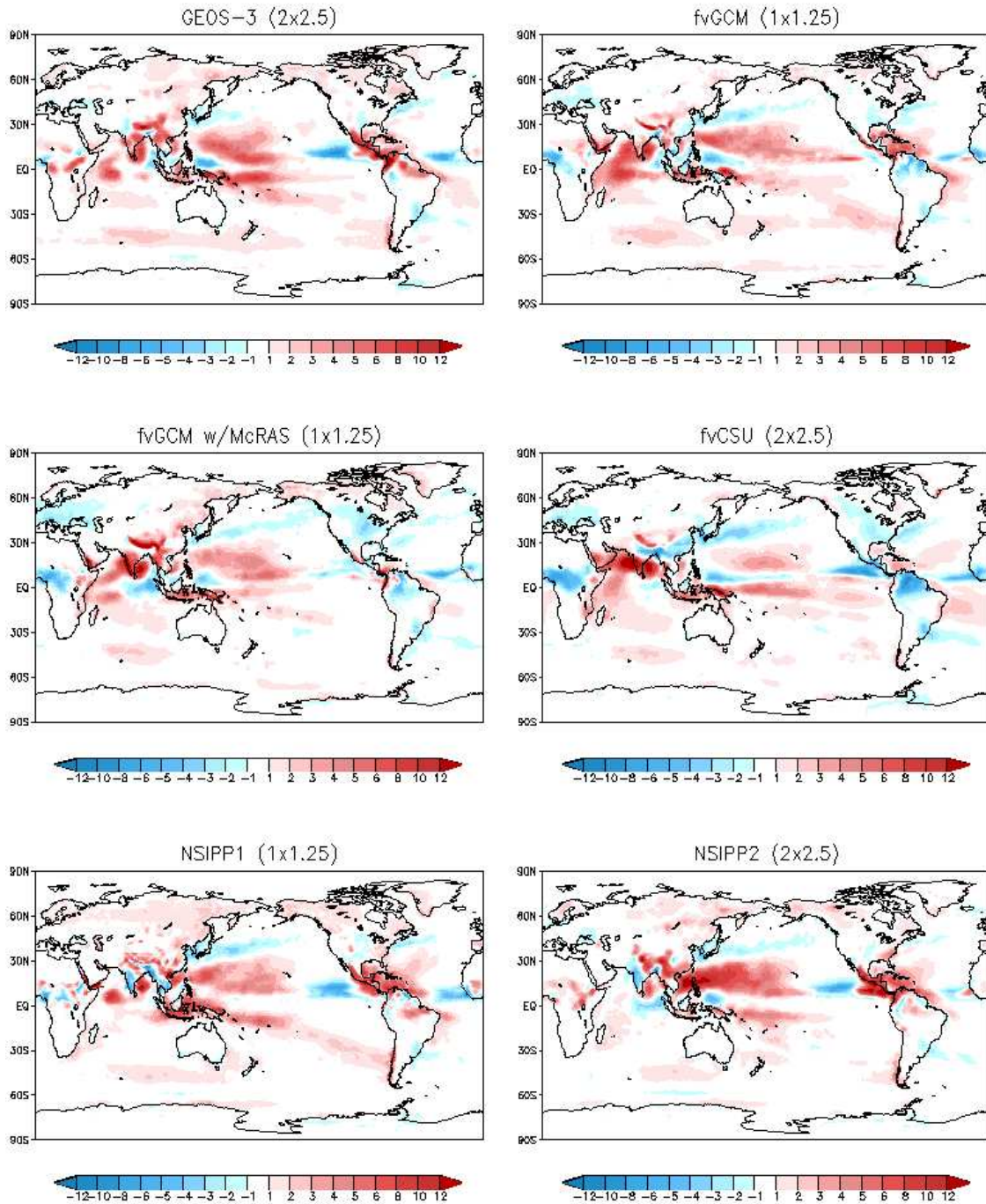
Figure 3.4: Same as 3.3, except the period is June, July, August (JJA)
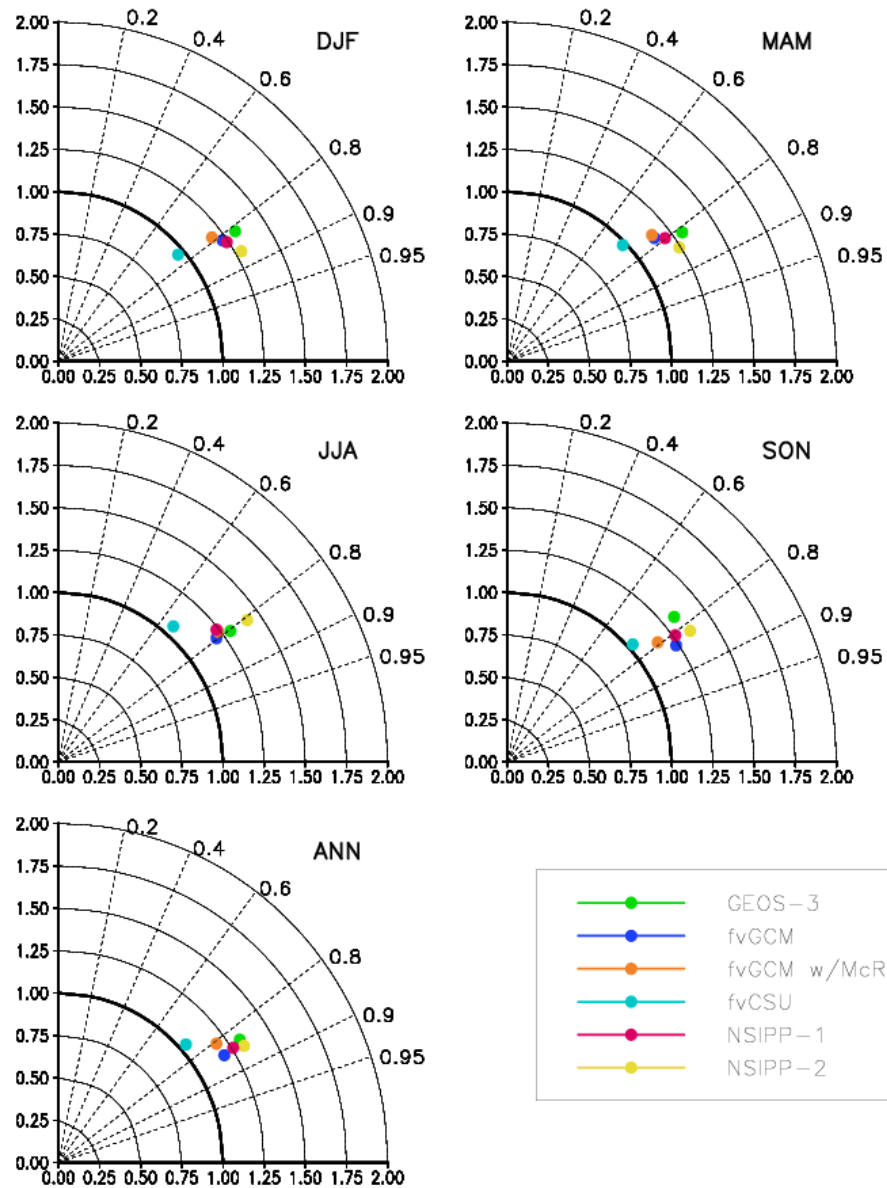
Figure 3.5: Taylor plots of model precipitation anomaly behavior (see text for Taylor plot description): DJF: Dec-Feb, MAM: Mar-May, JJA: Jun-Aug, SON: Sep-Nov, ANN: Annual.

3.1.4 Specific Implementation for C403

The GCM used in GEOS-4.0.3 has a 1° latitude by 1.25° longitude horizontal resolution, with the prognostic variables discretized on a staggered D-grid (Figure 3.6). The system is run with an effective time step of 30 minutes.
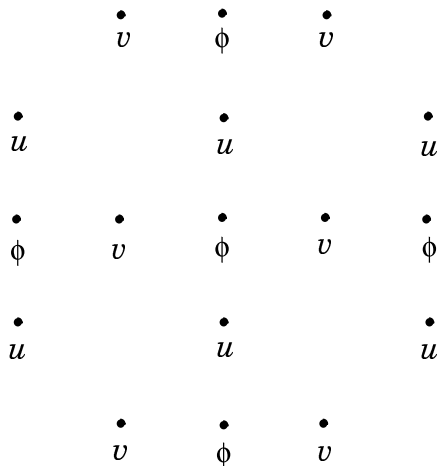
Figure 3.6: D-grid layout in GEOS-4 GCM; "ϕ"-points denote mass locations.

The GEOS-4.0.3 model employs a generalized hybrid sigma-pressure vertical coordinate system, where the pressures of the *edges* of the vertical layers are determined from the surface pressure (p_s) and two sets of coefficients, A_k and B_k, with "k" a vertical index running from 1 to the number of model layers + 1. Table 3.1 shows the coefficients used to generate the vertical grid for GEOS-4. Note that the pressures of the mid-points of the 55 layers in the GEOS-4 model are obtained by simply taking the average of the layer edge pressures, and that the bounding edge pressures are surface pressure (bottom) and 0.01 hPa (top). In addition, the hybrid nature of the vertical coordinate can be seen where the B_k coefficients are all zero for values of k less than 43; for these values of k, the GEOS-4 model is using a pure pressure-coordinate (mainly above 200 hPa). A sense of how the vertical layers are distributed can be seen by plotting A_k and B_k, as shown in Figure 3.7.

Figure 3.8 is a schematic depiction of the state variables in the GEOS-4 model, and how they are arranged in the vertical. The primary variables are: wind components (u,v); scaled virtual potential temperature ($\theta = T_v/p^\kappa$); pressure thickness (of the Lagrangian control volume, δp); and specific humidity (q). Although the pressure thickness is a prognostic variable which is evolved by the finite-volume dynamical core, there is a mapping process after each model time-step which maps all fields from this Lagrangian control-volume vertical coordinate back to the fixed Eulerian reference coordinates given in Table 3.1.
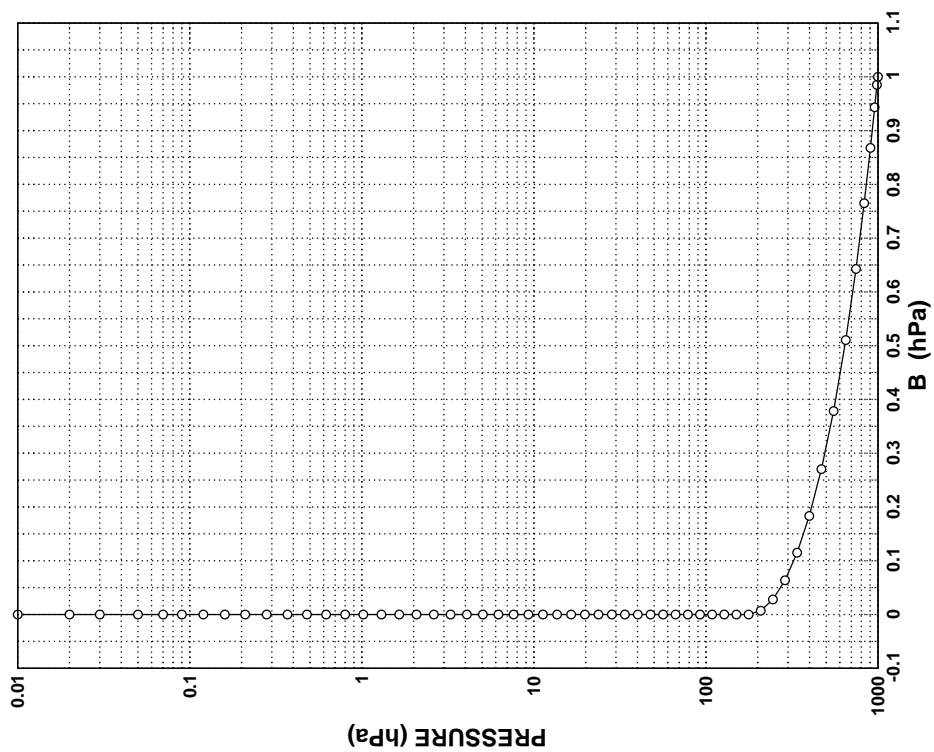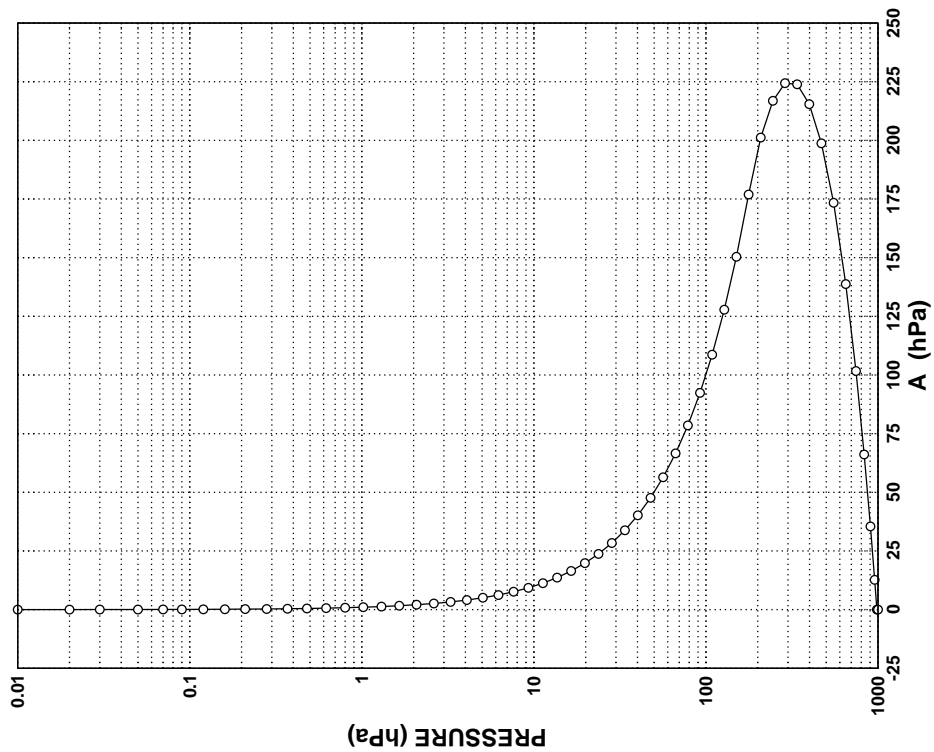
Figure 3.7: Vertical distribution of GEOS-4 model layers for the case of $p_s = 1000 \ hPa$, values of A and B from Table 3.1.
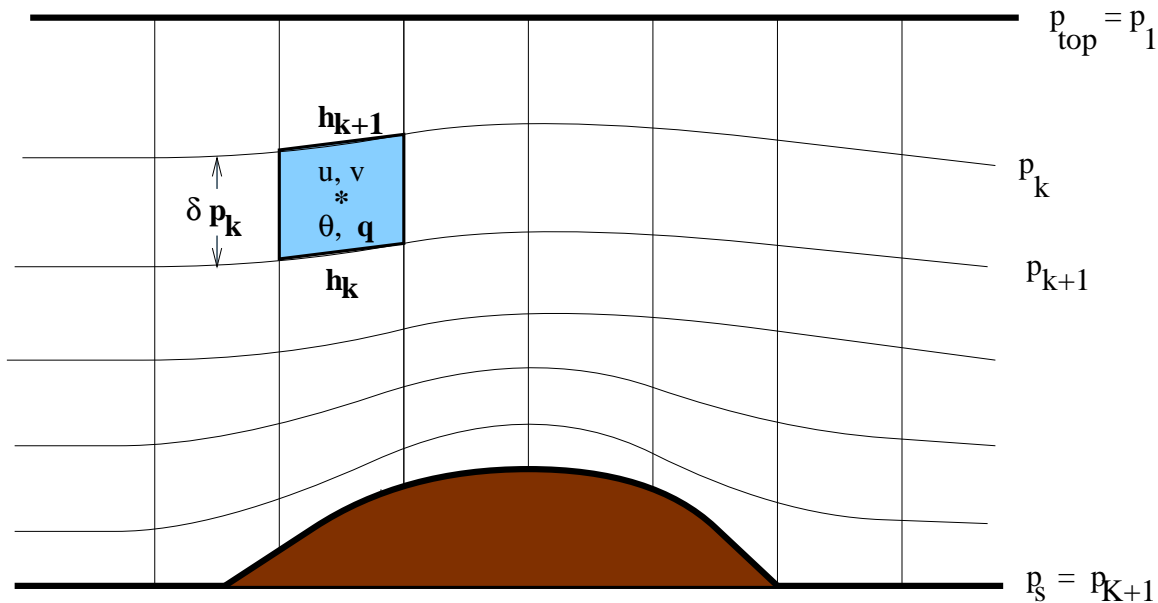
Figure 3.8: Finite Lagrangian control-volume and state variables for GEOS-4 GCM.

Vertical Layer Distribution

k	p_k	A_k	B_k	k	p_k	A_k	B_k	k	p_k	A_k	B_k
1	0.01	0.01	0.00000	20	3.28	3.28	0.00000	39	108.66	108.66	0.00000
2	0.02	0.02	0.00000	21	4.08	4.08	0.00000	40	127.84	127.84	0.00000
3	0.03	0.03	0.00000	22	5.05	5.05	0.00000	41	150.39	150.39	0.00000
4	0.05	0.05	0.00000	23	6.22	6.22	0.00000	42	176.93	176.93	0.00000
5	0.07	0.07	0.00000	24	7.62	7.62	0.00000	43	208.15	201.19	0.00696
6	0.09	0.09	0.00000	25	9.29	9.29	0.00000	44	244.87	216.86	0.02801
7	0.12	0.12	0.00000	26	11.28	11.28	0.00000	45	288.08	224.36	0.06372
8	0.16	0.16	0.00000	27	13.64	13.64	0.00000	46	338.91	223.88	0.11503
9	0.21	0.21	0.00000	28	16.46	16.46	0.00000	47	398.72	215.42	0.18330
10	0.28	0.28	0.00000	29	19.79	19.79	0.00000	48	469.07	198.74	0.27033
11	0.37	0.37	0.00000	30	23.73	23.736	0.00000	49	551.84	173.40	0.37844
12	0.48	0.48	0.00000	31	28.37	28.374	0.00000	50	649.20	138.74	0.51046
13	0.62	0.62	0.00000	32	33.81	33.819	0.00000	51	744.38	101.67	0.64271
14	0.80	0.80	0.00000	33	40.18	40.183	0.00000	52	831.02	66.10	0.76492
15	1.02	1.02	0.00000	34	47.64	47.649	0.00000	53	903.30	35.47	0.86783
16	1.30	1.30	0.00000	35	56.39	56.396	0.00000	54	955.99	12.70	0.94329
17	1.65	1.65	0.00000	36	66.60	66.606	0.00000	55	985.11	0.00	0.98511
18	2.08	2.08	0.00000	37	78.51	78.518	0.00000	56	1000.00	0.00	1.00000
19	2.62	2.62	0.00000	38	92.37	92.372	0.00000				

Table 3.1: Layer edge pressures and the associated coefficients used to generate them. $p_k = A_k + B_k p_s$ for k=1,56. The values of p_k here are generated using a representative value of $p_s = 1000$ hPa.

3.2 GEOS-4 Analysis

An atmospheric analysis performed within a data assimilation context seeks to combine in some "optimal" fashion the information from irregularly distributed atmospheric observations with a model state obtained from a forecast initialized from a previous analysis. The analyzed variables are geopotential height, zonal and meridional wind components, and pseudo-relative humidity (observation mixing ratio scaled by the background saturated mixing ratio, Dee and da Silva 2003). A number of details concerning the GEOS-4 analysis algorithm follow in section 3.2.1.

The types of observations that are used ("observing system") in the GEOS-4 analysis are discussed in section 3.2.3. Information pertaining to the implementation of the analysis for version 4.0.3 of GEOS-4 is given in section 3.2.5.

3.2.1 PSAS Algorithm

The PSAS algorithm solves the analysis equations (3.1) and (3.2):

$$
\begin{aligned}
w_k^f &= a_{k-1}\left(w_{k-1}^a\right) \\
y_k &= \left[F_k \mathcal{I}_k P_k^f \mathcal{I}_k^T F_k^T + R_k\right]^{-1}\left(w_k^o - f(w_k^f)\right) \\
&= \left[H_k P_k^f H_k^T + R_k\right]^{-1}\left(w_k^o - f(w_k^f)\right) \tag{3.1} \\
w_k^a &= w_k^f + P_k^f \mathcal{I}_k^T F_k^T y_k \\
&= w_k^f + P_k^f H_k^T y_k, \tag{3.2}
\end{aligned}
$$

with

n	number of gridpoints $\times$ variables	$n \sim 10^6$
p	number of observations	$p \sim 10^5$
w^a	gridded analysis state vector	$\in \mathbb{R}^n$
w^f	gridded forecast state vector	$\in \mathbb{R}^n$
w^o	observation vector	$\in \mathbb{R}^p$
$\mathcal{I}$	interpolation operator	$\mathcal{I} : \mathbb{R}^n \to \mathbb{R}^p$
	(interpolates from model grid to observation locations)	
f	non-linear observation operator	$f : \mathbb{R}^p \to \mathbb{R}^p$
F	tangent linear version of f, $F = \partial f/\partial w$	$F : \mathbb{R}^p \to \mathbb{R}^p$
H	tangent linear version of h, $H = F\mathcal{I}$,	$H : \mathbb{R}^p \to \mathbb{R}^n$
a	non-linear forecast model	$a : \mathbb{R}^n \to \mathbb{R}^n$
A	tangent linear version of a	$A : \mathbb{R}^n \to \mathbb{R}^n$
P^f	forecast error covariance	$P^f : \mathbb{R}^n \to \mathbb{R}^n$
R	observation error covariance	$R : \mathbb{R}^p \to \mathbb{R}^p.$

The *innovation covariance matrix*,

$$
M \equiv H P^f H^T + R, \tag{3.3}
$$

appearing in (3.1) is symmetric positive definite, making a standard pre-conditioned conjugate gradient (CG) algorithm (Golub and van Loan 1989) the method of choice for solving the large linear system (3.1). For the current observing system, setting up and solving the linear system (3.1) represents about half the computational effort of PSAS, and involves computation in observation space: $M \in I\!\!R^{p \times p}$ and $y \in I\!\!R^p$. The other half of the computational expense is taken by step (3.2) which transfers the solution y to the state space: $P^f H^T y \in I\!\!R^n$. Additional technical details on the implementation of the PSAS solver are given in da Silva and Guo (1996), Guo and da Silva (1997), Guo et al. (1998), Larson et al. (1998).

3.2.2 Specification of Error Statistics

A crucial part of the implementation of the PSAS analysis is the specification of the background error covariance P^f and the observation error covariance R needed to solve Equations 3.1 and 3.2. As the dimensionality of these multivariate covariances is extremely large (essentially the number of variables times the number of gridpoints for the rank of the background covariance), it is necessary to parameterize them with covariance models having a limited number of parameters.

The main characteristics of the covariance models used in GEOS-4 are:

- Compactly supported spline functions are used for modeling all single-level univariate correlations. The modeled horizontal correlations are exactly zero beyond a certain finite distance (6000 km for GEOS-4). These univariate correlations are horizontally isotropic. Three-dimensional covariances are constructed in terms of single-level isotropic covariances.

- Geopotential height and mixing ratio errors are uncorrelated.

- Wind-mass covariances are modeled according to a linear friction balance which ensures the geostrophic balance of the analysis increments in the extra-tropics, and cross-isobar flow near the surface and in the tropics.

- Wind errors possess a unbalanced component which results in height-decoupled wind analysis increments in the tropics.

- Error covariance parameters are obtained from a maximum-likelihood procedure (Dee and da Silva 1999).

The background and observation correlation models used in GEOS-4 are expressed as isotropic functions of the separation distance between two points on a sphere: $\|\mathbf{r_i} - \mathbf{r_j}\|$. A chord-length approximation is used for this distance: $s_{ij} \approx 2a \, sin(\frac{\theta}{2})$, where θ is the angular separation between points i and j, and "a" is the Earth's radius (6371 km). The following subsections describe the design of the covariance models used in GEOS-4, with the specifics of how the models have been implemented given in section 3.2.5.

3.2.2.1   Background Error Covariance

The GEOS-4 analysis is performed in two independent steps: a univariate moisture analysis and a multivariate height-wind analysis. The foundation of the height-wind covariance is the univariate background height error covariance, the remaining wind and wind-height covariances are developed upon this foundation.

3.2.2.1.1   Moisture and Height   The basic 3-dimensional univariate covariance model between horizontal locations (i,j) and vertical levels (m,n) in GEOS-4 can be expressed as:

$$P_{ij}^f(x; m, n) = \sigma_i^f(x; m) \, \sigma_j^f(x; n) \, \nu_x^f(m, n) \, B_{ij}^f(x; m, n) \, C_{ij}^f(x), \tag{3.4}$$

where "x" is a label denoting either moisture (x=q) or height (x=h). The function B is a power-law correlation function:

$$
\begin{aligned}
B_{ij}^f(m, n) &= \frac{\sqrt{L_m L_n}}{L_{mn}} \frac{1}{1 + \frac{1}{2}\left(\frac{s_{ij}}{L_{mn}}\right)^2} \,, \\
L_{mn} &= \frac{L_m + L_n}{2},
\end{aligned}
\tag{3.5}
$$

where L_m is a level-dependent length scale parameter. Note that this formulation of the correlation function is *non-separable*, since the length scale of the horizontal correlation varies with height; a *separable* form could be recovered by having all the length parameters L_m set to one constant.

The function C is a compactly supported window correlation function (see Gaspari and Cohn 1999, for details). This function serves the purpose of causing the overall correlation to vanish beyond a set separation distance, but doing so in a manner that retains positive-definiteness, a crucial property for global analysis schemes. If the cutoff distance is $2c = 6000\,km$, and a non-dimensional distance variable is defined, $Z = \frac{s_{ij}}{c}$, then C takes the form:

$$
C_{ij}^f =
\begin{cases}
-\frac{1}{4}Z^5 + \frac{1}{2}Z^4 + \frac{5}{8}Z^3 - \frac{5}{3}Z^2 \qquad\quad + 1 & 0 \le Z \le 1 \\[6pt]
\frac{1}{12}Z^5 - \frac{1}{2}Z^4 + \frac{5}{8}Z^3 + \frac{5}{3}Z^2 - 5Z + 4 - \frac{2}{3}Z^{-1} & 1 \le Z \le 2 \\[6pt]
0 & 2 \le Z \,.
\end{cases}
\tag{3.6}
$$

The remaining terms in equation 3.4, the standard deviations of background moisture and geopotential height errors as well as the vertical correlation structures for moisture and height, are shown as tables in section 3.2.5.

3.2.2.1.2   Wind   The upper-air analysis in GEOS-4 is multivariate in geopotential height and wind components. This leads to an immediate complication in equation 3.4, as now covariances among all the interrelated background variables need to be specified. In principle

one could simply recast equation 3.4 for the multivariate case as a 3×3 matrix,

$$
\begin{bmatrix}
P_{HH}^{f} & P_{HU}^{f} & P_{HV}^{f} \\
P_{UH}^{f} & P_{UU}^{f} & P_{UV}^{f} \\
P_{VH}^{f} & P_{VU}^{f} & P_{VV}^{f}
\end{bmatrix},
\tag{3.7}
$$

with each of its elements having the form of equation 3.4. In practice, however, there is insufficient independent data to obtain all the required parameters for such an approach.

In order to reduce the number of independent parameters needed for the multivariate statistics, some constraints are imposed on the nature of the wind errors. First, the wind component errors are decomposed into two parts:

$$
\begin{bmatrix} u \\ v \end{bmatrix} = \begin{bmatrix} u_h \\ v_h \end{bmatrix} + \begin{bmatrix} u_d \\ v_d \end{bmatrix},
\tag{3.8}
$$

where the subscripts "h" and "d" indicate wind component errors that are derived from height errors and wind component errors that are independent from height errors respectively. The coupled wind errors are then assumed to have the following dependence on the height errors:

$$
\begin{bmatrix} u_h \\ v_h \end{bmatrix} = \frac{g}{2\Omega} \begin{bmatrix} a_{11}(\varphi,p) & a_{12}(\varphi,p) \\ a_{21}(\varphi,p) & a_{22}(\varphi,p) \end{bmatrix} \begin{bmatrix} \partial_\lambda h \\ \partial_\varphi h \end{bmatrix},
\tag{3.9}
$$

where g is Earth's gravitational acceleration, 2Ω is the Earth's rotation rate, ϕ is latitude, λ is longitude, $\partial_\varphi = \frac{\partial}{a\partial\varphi}$, and $\partial_\lambda = \frac{1}{a\,cos(\varphi)}\frac{\partial}{\partial\lambda}$. The decoupled wind component errors are expressed in terms of streamfunction (ψ) and velocity potential (χ) errors:

$$
\begin{bmatrix} u_d \\ v_d \end{bmatrix} = \begin{bmatrix} -\partial_\varphi \psi + \partial_\lambda \chi \\ \partial_\lambda \psi + \partial_\varphi \chi \end{bmatrix}.
\tag{3.10}
$$

The statistics for ψ and χ have the same univariate form as equation 3.4 (*i.e.* now "x" ranges over q, h, ψ and χ). Using the shorthand notation $\langle UU \rangle = P_{UU}^{f}$, and assuming that $\langle \psi\chi \rangle = \langle h\chi \rangle = \langle h\psi \rangle = 0$, it follows from equations 3.8 - 3.10 that the height-wind and wind-wind terms in equation 3.7 are various combinations of the h, ψ and χ covariances and their $\varphi-$ and $\lambda-$ derivatives. For example, the height-u component (P_{HU}^{f}) element of 3.7 is expressed as:

$$
\begin{aligned}
\langle HU \rangle &= \frac{g}{2\Omega} \left\langle \left(a_{11}(j)h_i\partial_{\lambda_j}h + a_{12}(j)h_i\partial_{\varphi_j}h \right) \right\rangle \\
&= \frac{g}{2\Omega} \left(a_{11}(j)\partial_{\lambda_j} \langle HH \rangle_{ij} + a_{12}(j)\partial_{\varphi_j} \langle HH \rangle_{ij} \right).
\end{aligned}
$$

The wind-wind covariance elements, while straightforward to derive, are cumbersome in detail and will not be shown here. See Guo et al. (1998) or Pfaendtner et al. (1995) for more details.

There are some additional approximations employed in the modeling of the background error covariance statistics:

- A "homogeneity" approximation for the background height error standard deviations is used. Although there is a latitudinal variation in these standard deviations (cf. figures 3.9 and 3.10 in section 3.2.5), the derivatives of these quantities are ignored in the height-wind and wind-wind covariance modeling.

- The height-wind coupling constants are modeled as follows:

$$a_{11} = a_{22} = A(p) + B(p) \exp\left[-\left(\varphi/L(p)\right)^2\right] \tag{3.11}$$

$$-a_{12} = a_{21} = b(p)\left(1 - \exp\left[-\left(\varphi/K(p)\right)^2\right]\right)/\sin\varphi. \tag{3.12}$$

The values of $A(p), B(p), b(p), K(p)$, and $L(p)$ are given in Table 3.3 in section 3.2.5.

- The error standard deviations of velocity potential and streamfunction also follow the homogeneity approximation, and they have a latitudinal structure:

$$\sigma_\psi = \sigma_s \exp\left[-\left(\varphi/J(p)\right)^2\right] \tag{3.13}$$

$$\sigma_\chi = \sigma_v \exp\left[-\left(\varphi/J(p)\right)^2\right]. \tag{3.14}$$

The values of σ_s, σ_v, and $J(p)$ are given in Table 3.3 in section 3.2.5.

3.2.2.2 Observation Error Covariance

The observation error covariances are all univariate for the observing system used in GEOS-4. Although in principle the covariance model described by equation 3.4 applies to observations, in practice the situation is much simpler. For all observations except heights and moisture from rawinsondes and heights from iRET, the correlation terms in equation 3.4 are unity, leaving only the standard deviations. Global constants (usually varying by level) for the observation error standard deviations used in GEOS-4 are given in section 3.2.5.

3.2.2.2.1 Rawinsonde Rawinsonde moisture and height observations are assumed to have no horizontally correlated errors. Rawinsonde height observations are assumed to have a vertically correlated error structure within the same profile. The table for $\nu_h^{obs}(m,n)$ used in GEOS-4.0.3 is given in section 3.2.5.

3.2.2.2.2 TOVS The observation height error covariance for TOVS retrievals contains two parts, one having a horizontally correlated errors and one with the errors having no horizontal correlation (here $\delta_{i,j}$ is equal to 1 if $i = j$, and 0 otherwise):

$$\begin{aligned} P_{ij}^{sat}(h;m,n) = \ & \sigma_i^{oc}(m)\,\sigma_j^{oc}(n)\,\nu^{oc}(m,n)\,B_{ij}^o(m,n)\,C_{ij}^o(sat) \\ & + \ \sigma_i^{ou}(m)\,\sigma_j^{ou}(n)\,\nu^{ou}(m,n)\,\delta_{i,j}\,. \end{aligned} \tag{3.15}$$

Tables of the parameters in 3.15 are given in section 3.2.5. The moisture observations from TOVS retrievals are currently assumed have no spatially correlated errors.

3.2.3   Observing System

GEOS-4 assimilates observations from a diverse, heterogeneous observing system:

- Land Surface

- Ocean Surface

- Upper-air "conventional" (or *in situ*)

- Upper-air "satellite" (or *remotely sensed*).

3.2.3.1   Land Surface Observations

Two sources of land surface information are used in GEOS-4. One is surface pressure (reduced to sea level pressure) from the hourly observations taken at land stations. There is a diverse array of land station observations. GEOS-4 treats two broad categories somewhat differently. The "standard" land surface observations are limited to a 3-hour window centered on the analysis time; automated or METAR data are limited to a 1-hour window. These observations are then "recast" as 1000 hPa geopotential heights using the hydrostatic relation in concert with assumptions involving synthetic ("underground") lapse rates for grid points above sea level and estimates of the near-surface temperatures taken from the GCM 6 hour forecast.

A second source of of land information is an estimate of T_{skin} obtained in 1-hour windows every 3 hours. Although these data are not assimilated, off-line analyses incorporating these data do influence output diagnostic fields which are of considerable importance to customers of GMAO products (*e.g.* CERES). T_{skin} "observations" are obtained as a byproduct of the iRET process (see section 3.4).

3.2.3.2   Ocean Surface Observations

GEOS-4 is capable of assimilating sea level pressure and winds from ships, buoys, and sea platforms. Sea level pressure observations are transformed to 1000 hPa (or 925 hPa, depending on the initial background sea level pressure) heights for assimilation in the upper air analysis.

In addition to the above sources of conventional sea surface observations, there is a significant additional source of sea-level wind vectors which are inferred from the backscatter return from space-borne radars: ERS-2 and QuikScat. Just as GEOS-4 infers an upper-air mass variable (geopotential height) from surface mass information (sea level pressure) for assimilation in the upper-air analysis, a similar process is followed for the assimilation of ocean surface wind information. The sea surface wind observations are homogenized to a standard (model) level, just above the surface layer, using similarity theory.

3.2.3.3 Conventional Upper-Air

The predominant source of conventional upper-air data in GEOS-4 is rawinsondes, which supply height, temperature, wind and moisture information at mandatory levels. Rawinsondes also report "significant" level information, but these data are not assimilated in GEOS-4. The PSAS analysis in GEOS-4 assimilates heights (not temperatures) and wind components; the moisture information is assimilated in a separate univariate analysis.

While rawinsonde data are quite valuable, providing profiles of mass and wind information, they are very anisotropically distributed, favoring land over ocean and the Northern Hemisphere over the Southern Hemisphere. The rawinsonde network is augmented to a limited degree by dropwinsondes (from aircraft) and pilot balloons (which provide low-level wind profiles of lesser accuracy).

Another significant source of conventional upper-air wind data is aircraft winds. These data are also highly anisotropic, and they have the additional characteristic of being single-level data. As these data are extremely dense over North America and Europe, they are thinned, before use in the analysis, using an equal-area grid with resolution of approximately 1.4° latitude by 1.75° longitude (at the Equator).

3.2.3.4 Satellite Upper-Air

Remotely sensed information from satellites typically offer much greater and more isotropic coverage than those from conventional *in situ* sources. GEOS-4 utilizes three major types of satellite data: height and moisture profiles obtained from layer mean retrievals using TOVS radiance data; single level cloud motion vector winds obtained from geostationary satellite images; and column Total Precipitable Water (TPW) obtained from the SSM/I instrument on board the DMSP series of satellites.

3.2.3.4.1 TOVS TOVS consists of three separate sounding instruments:

- Highresolution Infrared Radiation Sounder 2 (HIRS2), later HIRS3;

- Microwave Sounding Unit (MSU), later the Advanced Microwave Sounding Unit (AMSU);

- Stratospheric Sounding Unit (SSU).

TOVS has flown on the TIROS-N satellite and on National Oceanic and Atmospheric Administration (NOAA) operational polar-orbiting environmental satellites (POES) 6-12 and 14. NOAA 10 and 12 did not have an SSU instrument. The Advanced TOVS instrument (ATOVS), consisting of HIRS3 and AMSU has been launched on the latest series of NOAA satellites; NOAA-15, 16 and 17.

The TOVS instruments measure the radiance from Earth passively in spectral elements or channels. The measured radiance includes thermal emission in the microwave and infrared channels and reflected solar radiation in the visible and shorter-wavelength infrared

channels. Radiance is commonly expressed in terms of equivalent blackbody temperature (brightness temperature), as brightness temperature behaves more linearly with atmospheric temperature and other parameters than does the radiance. HIRS2 has 19 infrared channels with center frequencies ranging from approximately 670 to 2660 cm^{-1} along with a single visible channel. MSU has 4 channels centered near the 57 GHz oxygen cluster. SSU employs the pressure modulation technique to measure stratospheric emission in 3 channels of the 15 μm CO$_2$ band.

GEOS-4 employs an interactive retrieval process (iRET, see section 3.4) that produces layer mean temperatures and moisture, as well as an estimate of the skin temperature (T_{skin} that is used in the off-line surface analysis (mentioned in section 3.2.3.1). The GEOS-4 analysis requires that temperature observation profiles need to be converted to geopotential height profiles (using the hydrostatic relation, and "anchoring" the profile with either the background surface pressure, or the background 250 hPa height for microwave-only retrieved profiles above the cloud-clearing cut-off level).

3.2.3.4.2 AMV Atmospheric motion vectors (AMVs, also known as cloud-track winds or cloud-drift winds) are observations derived from sequences of images observed by satellites. The winds are calculated by an objective procedure that selects targets, assigns pressure altitude, and calculates atmospheric motion from the motion of the selected targets in successive images.

Currently the GEOS-4 assimilation system uses cloud-track winds from geostationary satellites produced by NESDIS, JMA, and EUMETSAT; data from these sources provides near global coverage of AMV winds, equatorward of 60 degrees. The geostationary satellite winds from two layers (surface-700 hPa and above 400 hPa) are used, and are thinned using an equal-area grid with resolution of approximately 1.4° latitude by 1.75° longitude (at the Equator).

The GEOS-4 system has enabled the use of winds from the Terra (and eventually Aqua) MODIS instrument. MODIS winds from all levels are used, except for the winds within 2 degrees of the poles, and they should provide coverage that complements that provided by the geostationary satellite winds. These winds are also thinned to the 1.4° by 1.75° resolution. The specific impact of the MODIS winds is not a major issue in this validation, and it will be addressed in future testing (beyond the scope of the current validation effort).

3.2.3.4.3 TPW The GEOS-4 assimilation system uses total precipitable water (TPW) data from the SSM/I (Special Sensor Microwave / Imager) series of satellites. The 22.235 GHz channel on the SSM/I satellites is sensitive to atmospheric water vapor and can be used along with the other channels on the instrument to derive the water vapor in the column between the sea surface and the satellite.

The SSM/I TPW data used in GEOS-4 comes from two sources. The first-look assimilation uses TPW data obtained from NCEP. The NCEP TPW observations are derived using the Neural Net 3 algorithm (Krasnopolsky et al. 2000). The SSM/I TPW retrievals are superobbed by NCEP to a 1 x 1 degree resolution. A website with information about the Neural Net 3 algorithm is

```
http://polar.ncep.noaa.gov/winds/NNs/OMBNN3.html .
```

The late-look assimilation uses SSM/I TPW data produced by Remote Sensing Systems using the Wentz algorithm (Wentz 1997). The SSM/I retrievals are currently produced using Version 5 of the algorithm. For the late-look assimilation we use the interim product files (file name with "rt") that are produced in near real time. Other assimilations (such as the CERES reanalysis) use the SSM/I final product (file name with "v5"). Information about the Remote Sensing Systems Wentz SSM/I products can be found at their website:

`http://www.ssmi.com/ssmi/ssmi_description.html` .

The TPW retrievals are thinned on input to fvDAS to an equal-area grid with resolution of approximately 1.4° latitude by 1.75° degrees longitude (at the Equator). These data are ingested into the GEOS-4 moisture analysis as 850 hPa mixing ratio observations, using the assumption that the preponderance of column moisture in the atmosphere occurs at the lowest levels. The analysis spreads the information in the vertical to a limited degree, a consequence of the use of narrow vertical correlation functions for moisture (shown by table 3.6 in section 3.2.5).

3.2.4 Skin Temperature Analysis

T_{skin} plays a very important role in radiation budget calculations. It has been determined over the course of the development from fvDAS to GEOS-4 that the upper-air data are insufficient to constrain biases in T_{skin} which arise from inaccuracies in the surface parameterizations. A two-pronged approach has been taken to address this issue for the final version of GEOS-4: an improved land surface model (see 3.1.2.2.3); and an off-line T_{skin} analysis utilizing the data described in (3.2.3.1).

This is an off-line analysis, *i.e.* it only generates a *diagnostic* output field that does not feed back onto the assimilation state.

3.2.5 Analysis Details for C403

There are a large number of parameters that govern the behavior of the GEOS-4.0.3 analysis. The tables of error standard deviations, correlation coefficients and other tuning parameters largely reflect the estimation processes used their construction, values needed at other levels (*e.g.* 925 hPa) are obtained by interpolating the relevant table entries.

3.2.5.1 GEOS-4.0.3 analysis grid

The cost of the "matrix-multiply" step of the analysis (equation 3.2) is roughly comparable to the "matrix-solve" step (equation 3.1). Since the cost of this step scales as the number of model grid-points, and that the scales of the analysis increments are fairly broad (as can be seen by looking at the values of L in Table 3.3), it therefore follows that the analysis can be performed on a horizontal grid having a resolution of $2° \times 2\frac{1}{2}°$, thereby improving the overall cost of the analysis without a large penalty in accuracy. The analysis is interpolated to $1° \times 1\frac{1}{4}°$ for use by the GCM.

Table 3.2.5.1 shows the vertical analysis grid for GEOS-4.0.3 as well as the one from the previous GEOS-4.0.2 version. The current version of GEOS performs the step in equation 3.2 to all of the model levels below roughly 30 hPa. Quantities at all of the other levels are obtained via vertical interpolation.

GEOS-4.0.3			GEOS-4.0.2			GEOS-4.0.3			GEOS-4.0.2	
	LAYER ID	MEAN PRESS [hPa]		LAYER ID	MEAN PRESS [hPa]		LAYER ID	MEAN PRESS [hPa]		LAYER ID	MEAN PRESS [hPa]
	1	0.015		1	0.015		29	22.		29	22.
x	2	0.026	x	2	0.026	x	30	26.	x	30	26.
x	3	0.040	x	3	0.040		31	31.		31	31.
x	4	0.057	x	4	0.057		32	37.	x	32	37.
x	5	0.078	x	5	0.078		33	44.	x	33	44.
	6	0.10		6	0.10		34	52.		34	52.
x	7	0.14	x	7	0.14		35	61.	x	35	61.
x	8	0.19	x	8	0.19		36	73.		36	73.
x	9	0.25	x	9	0.25		37	85.	x	37	85.
x	10	0.32	x	10	0.32		38	100.		38	100.
	11	0.42		11	0.42		39	118.	x	39	118.
x	12	0.55	x	12	0.55		40	139.		40	139.
x	13	0.71	x	13	0.71		41	163.	x	41	163.
	14	0.91		14	0.91		42	192.		42	192.
x	15	1.2	x	15	1.2		43	225.	x	43	225.
x	16	1.5	x	16	1.5		44	265.		44	265.
	17	1.9		17	1.9		45	310.		45	310.
x	18	2.4	x	18	2.4		46	365.	x	46	365.
	19	2.9	x	19	2.9		47	429.		47	429.
	20	3.7		20	3.7		48	504.		48	504.
x	21	4.6	x	21	4.6		49	592.	x	49	592.
	22	5.6		22	5.6		50	687.		50	687.
	23	6.9	x	23	6.9		51	776.	x	51	776.
x	24	8.5	x	24	8.5		52	854.		52	854.
	25	10.		25	10.		53	914.		53	914.
x	26	12.	x	26	12.		54	955.		54	955.
	27	15.		27	15.		55	977.		55	977.
x	28	18.	x	28	18.						

Table 3.2: Comparison of the vertical analysis levels, GEOS-4.0.3 and GEOS-4.0.2. An "x" denotes an omitted level, quantities on these levels are obtained by interpolation from the other levels.

3.2.5.2   Background Error Covariance Model Parameters

Table 3.3 contains the length scale, standard deviation and coupling coefficients required for the background error covariance models. Note, the values of σ_h in this table are only *representative* of the background height error standard deviations; Figures 3.9 and 3.10 show the background error standard deviation structure, $\sigma_h^f(\varphi)$ used in GEOS-4.0.3. In the Troposphere (Figure 3.9) the largest values occur at the extra-Tropical jetstream levels, with a pronounced minimum in Tropics. In the upper levels of the model (Figure 3.10), the largest values occur in the Equatorial region.

	mass-coupled parms			standard deviations				length scales [km]			
p [hPa]	$A(p)$	$B(p)$	$b(p)$	σ_h	σ_s	σ_v	σ_q	L_h	L_ψ	L_χ	L_q
0.01	0.	0.	0.30	77.208	40.	10.	0.147	7026.5	1100.	1000.	287.
0.2	0.	0.	0.30	62.109	40.	10.	0.147	7026.5	1100.	1000.	287.
0.4	0.	0.	0.30	50.544	40.	10.	0.147	7026.5	1100.	1000.	287.
0.5	0.	0.	0.30	47.907	40.	10.	0.147	5267.9	1100.	1000.	287.
0.7	0.	0.	0.30	42.228	40.	10.	0.147	4025.7	1100.	1000.	287.
1.	0.	0.	0.30	38.455	40.	10.	0.147	3303.1	1100.	1000.	287.
2.	0.	0.	0.30	37.368	40.	10.	0.147	2503.7	1100.	1000.	287.
3.	0.	0.	0.30	34.783	40.	10.	0.147	2201.1	1100.	1000.	287.
5.	0.	0.	0.30	33.538	40.	10.	0.147	1907.3	1100.	1000.	287.
7.	0.	0.	0.30	32.973	40.	10.	0.147	1749.1	1100.	1000.	287.
10.	0.	0.	0.30	27.872	35.1	11.7	0.147	1603.1	1100.	1000.	287.
20.	0.	0.	0.30	25.498	28.3	11.9	0.147	1365.1	1000.	1000.	287.
30.	0.	0.	0.30	23.964	21.3	10.6	0.147	1246.3	920.	1000.	287.
50.	0.	0.	0.40	22.902	19.1	12.5	0.147	1112.4	860.	1000.	287.
70.	0.	0.	0.50	21.204	18.3	14.9	0.147	1031.9	800.	1000.	287.
100.	0.	0.	0.60	20.315	19.3	19.3	0.147	952.0	750.	1000.	287.
150.	0.	0.	0.70	21.306	23.8	23.8	0.147	866.9	690.	1000.	287.
200.	0.	0.	0.80	23.274	24.4	24.4	0.147	809.6	640.	1000.	287.
250.	0.	0.1	0.80	24.088	20.4	20.4	0.147	766.8	610.	1000.	287.
300.	0.	0.25	0.80	23.241	16.9	16.9	0.147	732.8	600.	1000.	287.
400.	0.	0.4	0.80	19.088	16.6	16.6	0.147	680.6	610.	1000.	287.
500.	0.	0.45	0.80	15.758	15.8	15.8	0.147	641.3	620.	1000.	287.
700.	0.	0.5	0.80	10.168	15.2	15.2	0.135	583.8	640.	1000.	287.
850.	0.07	0.6	0.80	7.510	13.9	15.4	0.122	551.5	660.	1000.	287.
925.	0.12	0.7	0.66	7.183	12.6	15.5	0.110	537.6	680.	1000.	287.
1000.	0.20	0.8	0.45	7.494	12.	14.7	0.110	524.9	700.	1000.	287.
1040.	n.a	n.a	n.a	7.878	n.a	n.a	0.073	n.a	n.a	n.a	n.a

Table 3.3: GEOS-4.0.3 background error covariance model parameters, described in section 3.2.2.1. The length scales are used by the Power Law function, equation 3.6. The moisture pseudo-relative humidity analysis uses a smaller "window" in equation 3.6, *i.e.* $2c = 3000\,km$ for moisture. The mass-coupled parameters are used in equations 3.11- 3.12. Note that the $J(p), K(p)$, and $L(p)$ terms in equations 3.11, 3.12, 3.13, and 3.14 are constant for all levels: $K(p) = L(p) = 0.4$ radians, and $J(p) = 4$ radians.

Tables 3.4 - 3.6 contain the vertical correlations used in the background error covariances. Note that the vertical correlation structure for the decoupled wind components and moisture have a scale of roughly 1 km in the vertical; heights (and thus the coupled wind components) have a considerably broader vertical correlation structure. The covariance parameters for levels not specified in the tables are obtained through interpolation.
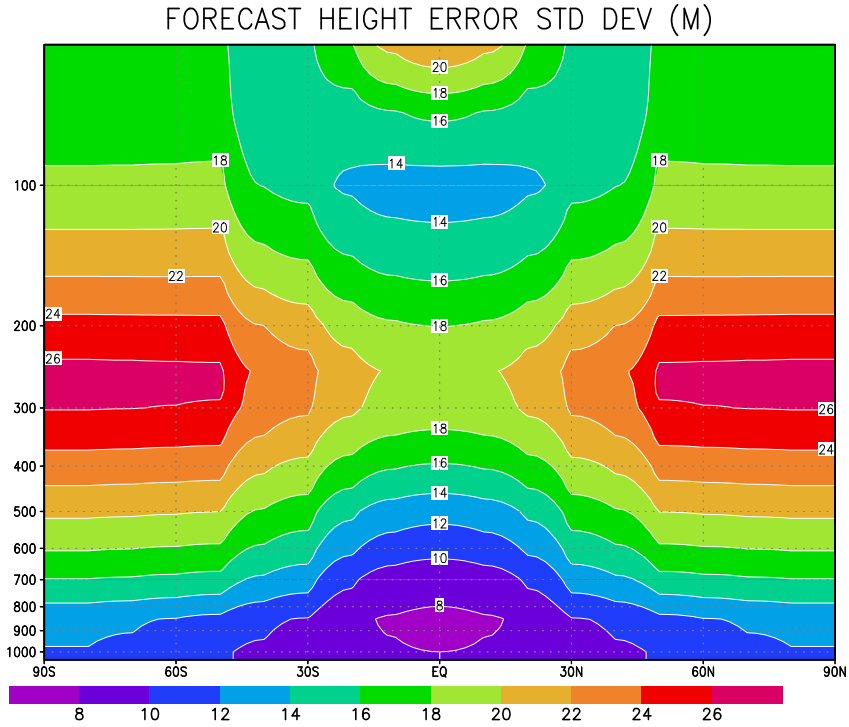
Figure 3.9: Background height error standard deviation, $\sigma_h^o(\varphi)$, with a focus primarily on the Troposphere.
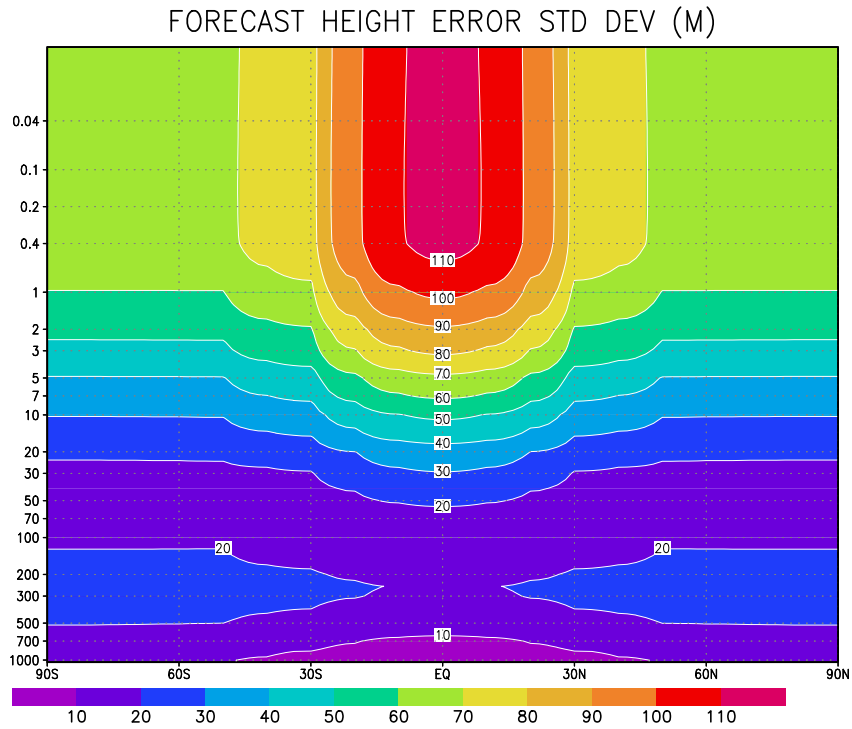
Figure 3.10: As in figure 3.9, only now showing the whole model domain.

Page 3.27, GEOS-4 Data Assimilation System, GMAO ValDoc v 0.2, December 03, 2004

	1040	1000	925	850	700	500	400	300	250	200	150	100	70	50
1040	1.000													
1000	0.990	1.000												
925	0.911	0.952	1.000											
850	0.764	0.819	0.944	1.000										
700	0.452	0.495	0.662	0.835	1.000									
500	0.270	0.265	0.369	0.527	0.797	1.000								
400	0.222	0.200	0.280	0.424	0.681	0.947	1.000							
300	0.182	0.152	0.221	0.355	0.583	0.834	0.940	1.000						
250	0.176	0.146	0.216	0.348	0.562	0.786	0.887	0.975	1.000					
200	0.182	0.158	0.229	0.356	0.558	0.751	0.828	0.908	0.962	1.000				
150	0.199	0.186	0.254	0.366	0.547	0.707	0.748	0.793	0.849	0.932	1.000			
100	0.209	0.211	0.264	0.338	0.466	0.573	0.571	0.577	0.617	0.701	0.840	1.000		
70	0.200	0.212	0.251	0.293	0.371	0.430	0.403	0.396	0.436	0.521	0.656	0.875	1.000	
50	0.185	0.203	0.232	0.253	0.297	0.321	0.278	0.262	0.304	0.397	0.539	0.740	0.903	1.000
40	0.177	0.198	0.222	0.234	0.262	0.270	0.219	0.198	0.240	0.336	0.487	0.690	0.834	0.962
30	0.166	0.189	0.208	0.211	0.226	0.219	0.162	0.135	0.175	0.271	0.428	0.643	0.770	0.875
20	0.152	0.176	0.190	0.185	0.186	0.167	0.106	0.076	0.112	0.204	0.357	0.581	0.713	0.790
10	0.128	0.152	0.160	0.148	0.137	0.108	0.048	0.018	0.050	0.131	0.269	0.475	0.607	0.691
7	0.126	0.150	0.158	0.143	0.127	0.095	0.033	0.001	0.032	0.114	0.254	0.462	0.595	0.681
5	0.122	0.146	0.152	0.135	0.117	0.082	0.020	-0.012	0.018	0.098	0.236	0.442	0.574	0.658
3	0.113	0.136	0.141	0.123	0.102	0.066	0.005	-0.026	0.002	0.078	0.209	0.407	0.535	0.615
2	0.110	0.133	0.137	0.118	0.095	0.056	-0.004	-0.036	-0.008	0.066	0.196	0.393	0.520	0.600
1	0.100	0.122	0.125	0.105	0.080	0.041	-0.017	-0.047	-0.022	0.048	0.169	0.354	0.473	0.549
0.400	0.088	0.109	0.110	0.090	0.064	0.026	-0.028	-0.057	-0.034	0.029	0.139	0.308	0.417	0.487
0.200	0.084	0.104	0.104	0.083	0.056	0.017	-0.036	-0.064	-0.043	0.018	0.124	0.289	0.396	0.463
0.050	0.068	0.085	0.085	0.065	0.039	0.002	-0.043	-0.068	-0.050	0.000	0.090	0.230	0.322	0.380
0.010	0.055	0.069	0.068	0.050	0.025	-0.008	-0.048	-0.069	-0.055	-0.013	0.063	0.181	0.259	0.308

	40	30	20	10	7	5	3	2	1	0.400	0.200	0.050	0.010
40	1.000												
30	0.944	1.000											
20	0.833	0.905	1.000										
10	0.725	0.754	0.797	1.000									
7	0.719	0.753	0.790	0.951	1.000								
5	0.695	0.731	0.773	0.904	0.959	1.000							
3	0.650	0.684	0.725	0.857	0.882	0.918	1.000						
2	0.635	0.668	0.708	0.839	0.865	0.886	0.951	1.000					
1	0.582	0.613	0.650	0.767	0.795	0.820	0.861	0.881	1.000				
0.400	0.517	0.545	0.579	0.683	0.706	0.727	0.768	0.791	0.839	1.000			
0.200	0.492	0.520	0.553	0.651	0.674	0.694	0.732	0.753	0.806	0.919	1.000		
0.050	0.405	0.428	0.456	0.536	0.555	0.571	0.603	0.620	0.661	0.761	0.787	1.000	
0.010	0.329	0.349	0.372	0.437	0.453	0.466	0.491	0.505	0.537	0.618	0.637	0.824	1.000

Table 3.4: Vertical height background error correlations, $\nu_h^f(m,n)$ in equation 3.4.

	1000	925	850	700	500	400	300	250	200	150	100	70	50	40	30
1000	1.00														
925	0.91	1.00													
850	0.66	0.89	1.00												
700	0.13	0.29	0.55	1.00											
500	0.00	0.00	0.01	0.16	1.00										
400	0.00	0.00	0.00	0.01	0.45	1.00									
300	0.00	0.00	0.00	0.00	0.02	0.27	1.00								
250	0.00	0.00	0.00	0.00	0.00	0.03	0.59	1.00							
200	0.00	0.00	0.00	0.00	0.00	0.00	0.07	0.45	1.00						
150	0.00	0.00	0.00	0.00	0.00	0.00	0.00	0.02	0.27	1.00					
100	0.00	0.00	0.00	0.00	0.00	0.00	0.00	0.00	0.00	0.07	1.00				
70	0.00	0.00	0.00	0.00	0.00	0.00	0.00	0.00	0.00	0.00	0.13	1.00			
50	0.00	0.00	0.00	0.00	0.00	0.00	0.00	0.00	0.00	0.00	0.00	0.16	1.00		
40	0.00	0.00	0.00	0.00	0.00	0.00	0.00	0.00	0.00	0.00	0.00	0.01	0.45	1.00	
30	0.00	0.00	0.00	0.00	0.00	0.00	0.00	0.00	0.00	0.00	0.00	0.00	0.02	0.27	1.00
20	0.00	0.00	0.00	0.00	0.00	0.00	0.00	0.00	0.00	0.00	0.00	0.00	0.00	0.00	0.07
15	0.00	0.00	0.00	0.00	0.00	0.00	0.00	0.00	0.00	0.00	0.00	0.00	0.00	0.00	0.00
10	0.00	0.00	0.00	0.00	0.00	0.00	0.00	0.00	0.00	0.00	0.00	0.00	0.00	0.00	0.00
7	0.00	0.00	0.00	0.00	0.00	0.00	0.00	0.00	0.00	0.00	0.00	0.00	0.00	0.00	0.00
5	0.00	0.00	0.00	0.00	0.00	0.00	0.00	0.00	0.00	0.00	0.00	0.00	0.00	0.00	0.00
3	0.00	0.00	0.00	0.00	0.00	0.00	0.00	0.00	0.00	0.00	0.00	0.00	0.00	0.00	0.00
2	0.00	0.00	0.00	0.00	0.00	0.00	0.00	0.00	0.00	0.00	0.00	0.00	0.00	0.00	0.00
1	0.00	0.00	0.00	0.00	0.00	0.00	0.00	0.00	0.00	0.00	0.00	0.00	0.00	0.00	0.00
0.700	0.00	0.00	0.00	0.00	0.00	0.00	0.00	0.00	0.00	0.00	0.00	0.00	0.00	0.00	0.00
0.500	0.00	0.00	0.00	0.00	0.00	0.00	0.00	0.00	0.00	0.00	0.00	0.00	0.00	0.00	0.00
0.400	0.00	0.00	0.00	0.00	0.00	0.00	0.00	0.00	0.00	0.00	0.00	0.00	0.00	0.00	0.00
0.200	0.00	0.00	0.00	0.00	0.00	0.00	0.00	0.00	0.00	0.00	0.00	0.00	0.00	0.00	0.00
0.050	0.00	0.00	0.00	0.00	0.00	0.00	0.00	0.00	0.00	0.00	0.00	0.00	0.00	0.00	0.00
0.010	0.00	0.00	0.00	0.00	0.00	0.00	0.00	0.00	0.00	0.00	0.00	0.00	0.00	0.00	0.00

	20	15	10	7	5	3	2	1	0.700	0.500	0.400	0.200	0.050	0.010
20	1.00													
15	0.27	1.00												
10	0.00	0.07	1.00											
7	0.00	0.00	0.13	1.00										
5	0.00	0.00	0.00	0.16	1.00									
3	0.00	0.00	0.00	0.00	0.02	1.00								
2	0.00	0.00	0.00	0.00	0.00	0.07	1.00							
1	0.00	0.00	0.00	0.00	0.00	0.00	0.00	1.00						
0.700	0.00	0.00	0.00	0.00	0.00	0.00	0.00	0.13	1.00					
0.500	0.00	0.00	0.00	0.00	0.00	0.00	0.00	0.00	0.16	1.00				
0.400	0.00	0.00	0.00	0.00	0.00	0.00	0.00	0.00	0.01	0.45	1.00			
0.200	0.00	0.00	0.00	0.00	0.00	0.00	0.00	0.00	0.00	0.00	0.00	1.00		
0.050	0.00	0.00	0.00	0.00	0.00	0.00	0.00	0.00	0.00	0.00	0.00	0.00	1.00	
0.010	0.00	0.00	0.00	0.00	0.00	0.00	0.00	0.00	0.00	0.00	0.00	0.00	0.00	1.00

Table 3.5: Background decoupled wind error (both χ and ψ): vertical correlations, $\nu^f_{\chi,\psi}(m,n)$ in equation 3.4.

	1000	925	850	700	500	400	300	250	200	150	100	70	50	40	30
1000	1.00														
925	0.23	1.00													
850	0.00	0.37	1.00												
700	0.00	0.16	0.32	1.00											
500	0.00	0.00	0.00	0.28	1.00										
400	0.00	0.00	0.00	0.00	0.42	1.00									
300	0.00	0.00	0.00	0.00	0.14	0.44	1.00								
250	0.00	0.00	0.00	0.00	0.00	0.22	0.37	1.00							
200	0.00	0.00	0.00	0.00	0.00	0.00	0.00	0.00	1.00						
150	0.00	0.00	0.00	0.00	0.00	0.00	0.00	0.00	0.00	1.00					
100	0.00	0.00	0.00	0.00	0.00	0.00	0.00	0.00	0.00	0.00	1.00				
70	0.00	0.00	0.00	0.00	0.00	0.00	0.00	0.00	0.00	0.00	0.00	1.00			
50	0.00	0.00	0.00	0.00	0.00	0.00	0.00	0.00	0.00	0.00	0.00	0.00	1.00		
40	0.00	0.00	0.00	0.00	0.00	0.00	0.00	0.00	0.00	0.00	0.00	0.00	0.00	1.00	
30	0.00	0.00	0.00	0.00	0.00	0.00	0.00	0.00	0.00	0.00	0.00	0.00	0.00	0.00	1.00
20	0.00	0.00	0.00	0.00	0.00	0.00	0.00	0.00	0.00	0.00	0.00	0.00	0.00	0.00	0.00
15	0.00	0.00	0.00	0.00	0.00	0.00	0.00	0.00	0.00	0.00	0.00	0.00	0.00	0.00	0.00
10	0.00	0.00	0.00	0.00	0.00	0.00	0.00	0.00	0.00	0.00	0.00	0.00	0.00	0.00	0.00
7	0.00	0.00	0.00	0.00	0.00	0.00	0.00	0.00	0.00	0.00	0.00	0.00	0.00	0.00	0.00
5	0.00	0.00	0.00	0.00	0.00	0.00	0.00	0.00	0.00	0.00	0.00	0.00	0.00	0.00	0.00
3	0.00	0.00	0.00	0.00	0.00	0.00	0.00	0.00	0.00	0.00	0.00	0.00	0.00	0.00	0.00
2	0.00	0.00	0.00	0.00	0.00	0.00	0.00	0.00	0.00	0.00	0.00	0.00	0.00	0.00	0.00
1	0.00	0.00	0.00	0.00	0.00	0.00	0.00	0.00	0.00	0.00	0.00	0.00	0.00	0.00	0.00
0.700	0.00	0.00	0.00	0.00	0.00	0.00	0.00	0.00	0.00	0.00	0.00	0.00	0.00	0.00	0.00
0.500	0.00	0.00	0.00	0.00	0.00	0.00	0.00	0.00	0.00	0.00	0.00	0.00	0.00	0.00	0.00
0.400	0.00	0.00	0.00	0.00	0.00	0.00	0.00	0.00	0.00	0.00	0.00	0.00	0.00	0.00	0.00
0.200	0.00	0.00	0.00	0.00	0.00	0.00	0.00	0.00	0.00	0.00	0.00	0.00	0.00	0.00	0.00
0.050	0.00	0.00	0.00	0.00	0.00	0.00	0.00	0.00	0.00	0.00	0.00	0.00	0.00	0.00	0.00
0.010	0.00	0.00	0.00	0.00	0.00	0.00	0.00	0.00	0.00	0.00	0.00	0.00	0.00	0.00	0.00

	20	15	10	7	5	3	2	1	0.700	0.500	0.400	0.200	0.050	0.010
20	1.00													
15	0.00	1.00												
10	0.00	0.00	1.00											
7	0.00	0.00	0.00	1.00										
5	0.00	0.00	0.00	0.00	1.00									
3	0.00	0.00	0.00	0.00	0.00	1.00								
2	0.00	0.00	0.00	0.00	0.00	0.00	1.00							
1	0.00	0.00	0.00	0.00	0.00	0.00	0.00	1.00						
0.700	0.00	0.00	0.00	0.00	0.00	0.00	0.00	0.00	1.00					
0.500	0.00	0.00	0.00	0.00	0.00	0.00	0.00	0.00	0.00	1.00				
0.400	0.00	0.00	0.00	0.00	0.00	0.00	0.00	0.00	0.01	0.00	1.00			
0.200	0.00	0.00	0.00	0.00	0.00	0.00	0.00	0.00	0.00	0.00	0.00	1.00		
0.050	0.00	0.00	0.00	0.00	0.00	0.00	0.00	0.00	0.00	0.00	0.00	0.00	1.00	
0.010	0.00	0.00	0.00	0.00	0.00	0.00	0.00	0.00	0.00	0.00	0.00	0.00	0.00	1.00

Table 3.6: Background moisture error vertical correlations, $\nu_q^f(m,n)$ in equation 3.4.

3.2.5.3   Observation Error Covariance Model Parameters

The observation error standard deviations used in GEOS-4.0.3 are grouped into three tables: upper-air profile data from TOVS and rawinsondes in Table 3.7; observations from surface locations (ships, QuikScat, land stations) in Table 3.8; and single-level upper-air wind observations from cloud tracked winds and various aircraft reports in Table 3.9. One additional item, not in the tables, is the observation error standard deviation assigned to the 850 hPa moisture observation obtained from the SSM/I TPW: $\sigma_q^{TPW} = 0.06$.

Tables 3.10, 3.11 and 3.12 contain the vertical error correlations for the profile observations. Note that the (horizontally) uncorrelated TOVS errors have a slightly different vertical correlation than do the correlated TOVS errors (3.11 vs 3.12).

p [hPa]	TOVS			Rawinsonde		
	σ_q^o	$\sigma_h^o(u,c)$	$\sigma_h^o(tot)$	σ_h^o	σ_u^o	σ_q^o
0.4	.	43.3	(61.2)	.	.	.
1.	.	25.8	(36.5)	.	.	.
2.	.	22.8	(32.2)	100.0	2.7	.
5.	.	20.6	(29.1)	60.0	2.7	.
10.	.	15.5	(21.9)	35.8	2.7	.
30.	.	12.3	(17.4)	27.7	2.7	.
50.	.	10.0	(14.1)	23.5	2.7	.
70.	.	10.2	(14.4)	21.9	2.7	.
100.	0.12	10.5	(14.8)	19.3	2.7	0.19
150.	0.12	10.9	(15.4)	16.3	2.7	0.18
200.	0.12	10.3	(14.6)	14.5	3.3	0.17
250.	0.12	9.5	(13.4)	13.5	3.4	0.16
300.	0.12	9.1	(12.9)	12.8	3.4	0.15
400.	0.11	7.6	(10.8)	10.8	3.2	0.14
500.	0.10	6.1	(8.6)	8.6	2.7	0.13
700.	0.09	4.4	(6.2)	6.2	2.3	0.12
850.	0.09	4.0	(5.7)	5.6	2.2	0.11
1000.	0.06	3.8	(5.4)	5.4	2.0	0.10
1040.	0.06	3.7	(5.2)	5.2	2.0	0.10

Table 3.7: Observation error standard deviations for the two sources of vertical profile data used in GEOS-4. units are m for h and $m\,s^{-1}$ for wind (u and v components the same). Also, the correlated and uncorrelated TOVS height error standard deviations are the same; $\sigma_h^o(tot)$ is simply $\sqrt{2}$ times $\sigma_h^o(u,c)$, and is included for comparison with the rawinsonde entries for σ_h.

p [hPa]	σ_h^o	σ_u^o	σ_v^o	σ_q^o
400	.	3.2	3.4	.
500	8.6	2.7	3.2	0.10
700	6.2	2.3	2.7	0.09
850	5.6	2.2	2.3	0.09
1000	5.4	2.0	2.2	0.06
1040	5.2	2.0	2.2	0.06

Table 3.8: Observation error standard deviations for data from surface sources: ships, buoys, QuikScat winds, and land stations. units: m for heights, $m\,s^{-1}$ for wind.

p [hPa]	Pibal	ASDAR	Airep	ACARS	CTW
10	3.0	2.3	4.0	2.3	2.70
30	3.0	2.3	4.0	2.3	2.70
50	3.0	2.3	4.0	2.3	2.70
70	3.0	2.3	4.0	2.3	2.70
100	3.0	2.3	4.0	2.3	2.70
150	2.9	2.3	4.0	2.3	2.70
200	2.8	2.3	4.0	2.3	2.70
250	2.7	2.3	4.0	2.3	2.45
300	2.6	2.3	4.0	2.3	2.20
400	2.6	2.4	4.0	2.4	1.90
500	2.6	2.5	3.9	2.5	1.70
700	2.6	2.5	3.8	2.5	1.60
850	2.6	2.5	3.6	2.5	1.50
1000	2.6	2.5	3.5	2.5	1.50
1040	2.6	2.5	3.5	2.5	1.50

Table 3.9: Single-level upper-air wind observation error standard deviations, u and v components the same, units $m\,s^{-1}$.

	1040	1000	925	850	700	500	400	300	250	200	150	100	70	50	40	30	20	10
1040	1.00																	
1000	0.77	1.00																
925	0.54	0.77	1.00															
850	0.38	0.54	0.77	1.00														
700	0.34	0.38	0.53	0.67	1.00													
500	0.29	0.34	0.37	0.39	0.57	1.00												
400	0.20	0.29	0.30	0.31	0.43	0.76	1.00											
300	0.15	0.20	0.21	0.22	0.31	0.58	0.82	1.00										
250	0.11	0.15	0.16	0.17	0.25	0.48	0.69	0.88	1.00									
200	0.06	0.11	0.12	0.12	0.19	0.39	0.56	0.76	0.87	1.00								
150	0.00	0.06	0.07	0.08	0.13	0.30	0.44	0.59	0.67	0.83	1.00							
100	0.00	0.00	0.00	0.03	0.07	0.18	0.31	0.42	0.47	0.61	0.80	1.00						
70	0.00	0.00	0.00	0.00	0.04	0.12	0.21	0.31	0.35	0.47	0.68	0.76	1.00					
50	0.00	0.00	0.00	0.00	0.00	0.07	0.15	0.22	0.25	0.38	0.52	0.61	0.79	1.00				
40	0.00	0.00	0.00	0.00	0.00	0.05	0.12	0.17	0.20	0.31	0.44	0.48	0.65	0.85	1.00			
30	0.00	0.00	0.00	0.00	0.00	0.00	0.09	0.13	0.14	0.23	0.36	0.36	0.52	0.69	0.89	1.00		
20	0.00	0.00	0.00	0.00	0.00	0.00	0.05	0.08	0.09	0.15	0.24	0.24	0.39	0.54	0.72	0.82	1.00	
10	0.00	0.00	0.00	0.00	0.00	0.00	0.00	0.05	0.08	0.09	0.15	0.24	0.24	0.39	0.54	0.72	0.82	1.00

Table 3.10: Rawinsonde height error vertical correlations, $\nu_h^o(m,n)$ in equation 3.4.

	1000	925	850	700	500	400	300	250	200	150	100	70	50	40
1000	1.00													
925	0.85	1.00												
850	0.71	0.85	1.00											
700	0.54	0.68	0.82	1.00										
500	0.37	0.47	0.58	0.83	1.00									
400	0.29	0.37	0.45	0.68	0.86	1.00								
300	0.20	0.26	0.32	0.52	0.63	0.81	1.00							
250	0.16	0.21	0.26	0.42	0.52	0.71	0.83	1.00						
200	0.12	0.16	0.20	0.32	0.41	0.57	0.66	0.80	1.00					
150	0.08	0.11	0.14	0.22	0.29	0.42	0.49	0.59	0.75	1.00				
100	0.03	0.04	0.07	0.12	0.18	0.27	0.32	0.39	0.49	0.66	1.00			
70	0.00	0.00	0.03	0.06	0.11	0.18	0.22	0.26	0.34	0.46	0.70	1.00		
50	0.00	0.00	0.00	0.02	0.06	0.12	0.15	0.18	0.24	0.32	0.50	0.72	1.00	
40	0.00	0.00	0.00	0.00	0.03	0.09	0.11	0.14	0.19	0.25	0.39	0.57	0.80	1.00
30	0.00	0.00	0.00	0.00	0.00	0.06	0.08	0.10	0.14	0.19	0.29	0.43	0.60	0.80
20	0.00	0.00	0.00	0.00	0.00	0.00	0.04	0.05	0.09	0.12	0.19	0.29	0.40	0.53
15	0.00	0.00	0.00	0.00	0.00	0.00	0.03	0.03	0.05	0.08	0.14	0.22	0.30	0.40
10	0.00	0.00	0.00	0.00	0.00	0.00	0.00	0.00	0.00	0.04	0.09	0.15	0.20	0.26
7	0.00	0.00	0.00	0.00	0.00	0.00	0.00	0.00	0.00	0.00	0.05	0.10	0.14	0.19
5	0.00	0.00	0.00	0.00	0.00	0.00	0.00	0.00	0.00	0.00	0.03	0.08	0.10	0.13
3	0.00	0.00	0.00	0.00	0.00	0.00	0.00	0.00	0.00	0.00	0.00	0.05	0.05	0.08
2	0.00	0.00	0.00	0.00	0.00	0.00	0.00	0.00	0.00	0.00	0.00	0.00	0.00	0.05
1	0.00	0.00	0.00	0.00	0.00	0.00	0.00	0.00	0.00	0.00	0.00	0.00	0.00	0.03
0.70	0.00	0.00	0.00	0.00	0.00	0.00	0.00	0.00	0.00	0.00	0.00	0.00	0.00	0.00
0.50	0.00	0.00	0.00	0.00	0.00	0.00	0.00	0.00	0.00	0.00	0.00	0.00	0.00	0.00
0.40	0.00	0.00	0.00	0.00	0.00	0.00	0.00	0.00	0.00	0.00	0.00	0.00	0.00	0.00

	30	20	15	10	7	5	3	2	1	0.70	0.50	0.40
30	1.00											
20	0.66	1.00										
15	0.50	0.75	1.00									
10	0.33	0.50	0.67	1.00								
7	0.23	0.35	0.47	0.70	1.00							
5	0.16	0.25	0.33	0.50	0.71	1.00						
3	0.09	0.15	0.20	0.31	0.43	0.63	1.00					
2	0.06	0.10	0.13	0.21	0.29	0.44	0.70	1.00				
1	0.00	0.03	0.07	0.11	0.15	0.25	0.41	0.57	1.00			
0.70	0.00	0.00	0.05	0.08	0.10	0.20	0.32	0.44	0.76	1.00		
0.50	0.00	0.00	0.03	0.06	0.08	0.16	0.26	0.36	0.60	0.78	1.00	
0.40	0.00	0.00	0.03	0.05	0.06	0.14	0.23	0.32	0.52	0.66	0.85	1.00

Table 3.11: TOVS uncorrelated height error vertical correlations, $\nu_h^o(m,n)$ in equation 3.4.

1000	1.00													
925	0.84	1.00												
850	0.68	0.84	1.00											
700	0.53	0.67	0.81	1.00										
500	0.35	0.46	0.56	0.81	1.00									
400	0.27	0.35	0.44	0.64	0.79	1.00								
300	0.18	0.25	0.32	0.46	0.58	0.75	1.00							
250	0.13	0.19	0.25	0.38	0.48	0.62	0.83	1.00						
200	0.09	0.14	0.19	0.29	0.38	0.49	0.66	0.80	1.00					
150	0.06	0.09	0.13	0.20	0.28	0.36	0.49	0.59	0.75	1.00				
100	0.00	0.03	0.06	0.10	0.17	0.23	0.32	0.39	0.50	0.75	1.00			
70	0.00	0.00	0.03	0.04	0.11	0.16	0.22	0.27	0.34	0.52	0.79	1.00		
50	0.00	0.00	0.00	0.00	0.07	0.11	0.15	0.19	0.24	0.37	0.56	0.71	1.00	
40	0.00	0.00	0.00	0.00	0.05	0.08	0.11	0.15	0.19	0.29	0.44	0.57	0.80	1.00
30	0.00	0.00	0.00	0.00	0.03	0.05	0.08	0.11	0.14	0.22	0.33	0.43	0.60	0.80
20	0.00	0.00	0.00	0.00	0.00	0.00	0.04	0.07	0.09	0.14	0.22	0.28	0.40	0.53
15	0.00	0.00	0.00	0.00	0.00	0.00	0.00	0.04	0.07	0.10	0.16	0.21	0.30	0.40
10	0.00	0.00	0.00	0.00	0.00	0.00	0.00	0.00	0.03	0.07	0.10	0.14	0.20	0.27
7	0.00	0.00	0.00	0.00	0.00	0.00	0.00	0.00	0.00	0.04	0.06	0.10	0.14	0.19
5	0.00	0.00	0.00	0.00	0.00	0.00	0.00	0.00	0.00	0.03	0.03	0.07	0.10	0.13
3	0.00	0.00	0.00	0.00	0.00	0.00	0.00	0.00	0.00	0.00	0.00	0.04	0.05	0.08
2	0.00	0.00	0.00	0.00	0.00	0.00	0.00	0.00	0.00	0.00	0.00	0.03	0.03	0.05
1	0.00	0.00	0.00	0.00	0.00	0.00	0.00	0.00	0.00	0.00	0.00	0.00	0.00	0.03
0.70	0.00	0.00	0.00	0.00	0.00	0.00	0.00	0.00	0.00	0.00	0.00	0.00	0.00	0.00
0.50	0.00	0.00	0.00	0.00	0.00	0.00	0.00	0.00	0.00	0.00	0.00	0.00	0.00	0.00
0.40	0.00	0.00	0.00	0.00	0.00	0.00	0.00	0.00	0.00	0.00	0.00	0.00	0.00	0.00

30	1.00											
20	0.67	1.00										
15	0.50	0.75	1.00									
10	0.34	0.50	0.67	1.00								
7	0.24	0.35	0.47	0.70	1.00							
5	0.17	0.25	0.34	0.50	0.72	1.00						
3	0.10	0.15	0.20	0.31	0.44	0.62	1.00					
2	0.07	0.10	0.14	0.21	0.30	0.43	0.69	1.00				
1	0.00	0.04	0.07	0.11	0.16	0.23	0.39	0.55	1.00			
0.70	0.00	0.00	0.05	0.08	0.12	0.18	0.29	0.42	0.74	1.00		
0.50	0.00	0.00	0.04	0.06	0.09	0.14	0.23	0.33	0.57	0.78	1.00	
0.40	0.00	0.00	0.03	0.05	0.08	0.12	0.20	0.28	0.48	0.67	0.86	1.00

Table 3.12: TOVS correlated height error vertical correlations, $\nu_h^o(m,n)$ in equation 3.4.

3.3 Quality Control

The PSAS algorithm (as do other analyses based on Estimation Theory constructs) makes strong assumptions about the statistical nature of the errors in both the forecast fields and in the observations. Observations that clearly violate these statistical assumptions (*i.e.* "outliers") must be identified and removed from the analysis process; this is done through a Quality Control (QC) process.

GEOS-4 employs an on-line Statistical Quality Control (SQC) system (Dee et al. 2001) that seeks to identify observations that are likely to be contaminated by gross errors. Its algorithms involve statistical tests of the actual data against assumptions about their expected errors and about GCM forecast errors. Essentially, a local statistical analysis is performed for each outlier observation, i.e., for each observation that differs significantly from the short-term forecast produced by the GCM. If this analysis indicates that the observation is inconsistent with surrounding data, then that observation is marked for rejection.

The SQC encompasses a *background check*, a *buddy check*, a *wind check*, and a *profile check*, each of which is described below. All checks are formulated in terms of the observed-minus-forecast residuals (O-F) rather than the observations themselves. All checks potentially modify the quality control marks associated with the observations, but leave all other data attributes unchanged. The background check and buddy check involve the forecast and observation error variances for the quantities being tested, which are prescribed in the global analysis system.

3.3.1 Statistical Aspects

The SQC algorithms operate on the vector of observed-minus-forecast residuals, v, defined by

$$v = w^o - f(\mathcal{I} w^f), \tag{3.16}$$

where w^o, w^f, f, and $\mathcal{I}$ are defined in 3.2.1. The observation operator, f, maps model variables to observables. For remotely sensed radiances, for example, the function f represents a radiative transfer model. It is simply the identity for conventional, *in situ* observations of model variables.

The SQC attempts to identify corrupt data based on statistical expectations. This requires knowledge of the covariance S of the observed-minus-forecast residuals, defined by

$$S_{ij} = \langle v_i v_j \rangle, \tag{3.17}$$

with i, j indicating location. In general these covariances are poorly known, but a rough estimate is available from the global analysis system. It follows from (3.16) that

$$S \approx F \mathcal{I} P^f \mathcal{I}^T F^T + R, \tag{3.18}$$

where F is the linearized observation operator,

$$F = \left. \frac{\partial f}{\partial w} \right|_{w=w^f}, \tag{3.19}$$

and P^f, R are the covariances of forecast and observation errors, respectively. Equation (3.18) would be exact if forecast and observation errors were entirely independent (they are not, since both types of errors depend on the true state) and if all observation operators were linear.

If the prescribed error statistics in the global analysis system are reasonably accurate, then the right-hand side of (3.18) can be presumed to provide some useful information about the residual error covariances. Accordingly, prescribed error statistics are used to define tolerances for the background check, whose main purpose is to mark outlier observations for subsequent reexamination in the buddy check. However, since actual errors depend on many unknown model defects and other intangibles, covariance specifications in operational data assimilation systems cannot be relied upon to accurately describe error characteristics in all situations at all times. In particular, during extreme events—when quality control decisions become especially important—the covariances as prescribed by the global analysis system are almost certainly inadequate. Thus, a key aspect of the SQC is the attempt to adjust the prescribed error statistics based on actual data. This adjustment takes place during the buddy check, before a final accept/reject decision is reached for an outlier observation.

3.3.2 The Background Check

The background check tests each single observation against a background estimate, which is simply the 6-hour model forecast interpolated to the time and location of the observation. If the discrepancy is extremely large then the observation is rejected outright. If the discrepancy is large, but within some specified rejection tolerance, then the observation is marked as "suspect" or a potential outlier, to be reexamined in the buddy check. The tolerances for the background check are defined in terms of standard deviations obtained from the error statistics as prescribed by the global analysis system.

The algorithm is as follows:

For each observation w_i^o:

$$\text{mark } w_i^o \text{ as \textbf{outlier} if} \quad |v_i| > \tau_o \sigma_i \ ,$$
$$\text{mark } w_i^o \text{ as \textbf{excluded} if} \quad |v_i| > \tau_x \sigma_i \ .$$

Here $\sigma_i = \sqrt{S_{ii}}$, and τ_s, τ_x are prescribed non-dimensional tolerance parameters. Typically we take $\tau_o = 2, \tau_x = 10$.

The rate at which the background check produces suspect marks presents a useful check on the accuracy of the prescribed error statistics. If the forecast and observation error variances are correctly tuned, and if the errors are roughly normally distributed, then the suspect rate can be predicted. For example, when $\tau_o = 2$, the rate should be about 4.5%. If the actual suspect rate is larger (smaller), then the prescribed error variance is too small (large). This is illustrated in Fig. 3.11. Monitoring the background check failure rates for specific instruments has, in a number of cases, led to adjustments of observation error statistics in GEOS DAS.
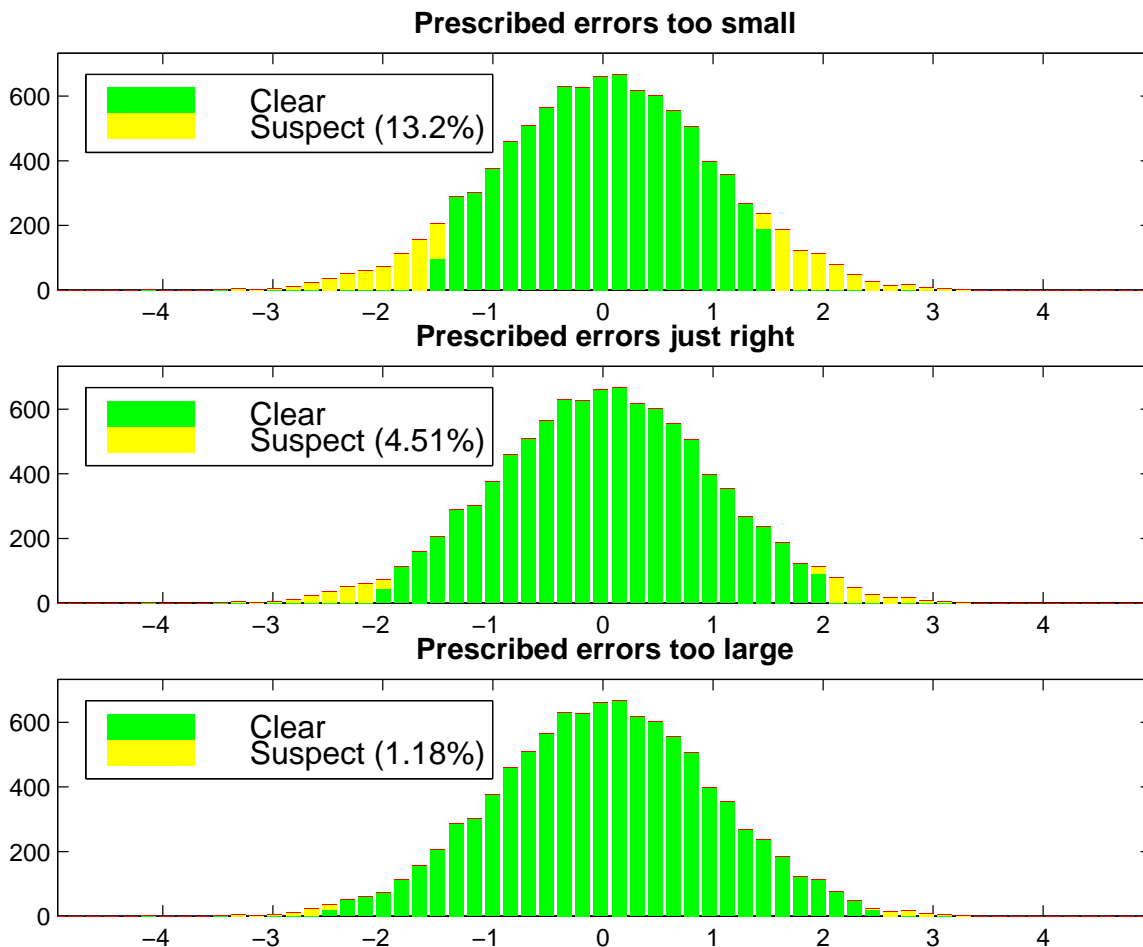
Figure 3.11: Illustration of the relationship between the rate at which the background check marks observations as outliers and the prescribed error statistics, for normally distributed errors. The yellow tails of the histograms correspond to observations marked as outliers.

3.3.3 The Buddy Check

The buddy check is applied to a subset of observations which are considered suspect, either because they were identified as outliers by the background check, or because they were marked as suspect during the preprocessing stage. The buddy check attempts to predict the value of a suspect observation from nearby non-suspect observations (the *buddies*.) If the predicted value is in reasonable agreement (defined below) with the observation, then the observation is no longer considered suspect. If a sufficient number of buddies is available, then the tolerance for the buddy check is adjusted based on a local estimate of O-F standard deviations. Once all suspect observations have been tested, the entire process is repeated for all observations that are still considered suspect. The process stops when the set of suspects no longer changes: all remaining suspects are then rejected.

The buddy check initially labels observations as suspect based on their quality control history. A single iteration of the algorithm proceeds as follows:

For each suspect observation w_j^o:

1. Define the set of buddies:

   Nearby non-suspect observations of the same data type as w_j^o are ranked according to the scalar weight that each would receive in an optimal univariate statistical analysis at the location of w_j^o. The buddies are simply the n highest ranking of these, where n is a configuration parameter. Typically $n = 50$.

2. Predict the value of the suspect observation based on its buddies:

   Using the weights determined in the previous step, the weighted average $v_j^\star$ of the v_i associated with the buddies provides the optimal univariate analysis of the buddies at the location of w_j^o.

3. Adjust the prescribed estimate of the local O-F standard deviation:

   If $\widehat{\sigma}_j^2$ is the sample variance of the v_i associated with the buddies, the prescribed variance σ_j^2 is adjusted according to

   $$(\sigma_j^\star)^2 = (n^\star \sigma_j^2 + n\widehat{\sigma}_j^2)/(n^\star + n) \tag{3.20}$$

   where $n^\star$ is a configuration parameter. Typically we take $n^\star = 25$.

4. Re-evaluate the status of w_j^o:

   Change the status of w_j^o to non-suspect if

   $$|v_j - v_j^\star| < \tau_b \sigma_j^\star \tag{3.21}$$

   where τ_b is a prescribed non-dimensional tolerance parameter. Typically $\tau_b = 3$.

These steps are repeated until no further observations change status. At that point, any remaining suspect observations are marked for rejection.

The adaptive nature of the buddy check has two important consequences. First, the final quality control decisions are not very sensitive to the prescribed error statistics in the global analysis system. This has been verified experimentally by varying the tolerance parameter, τ_o, of the background check. It was found that the final accept/reject status of observations is not very sensitive to the background check failure rate, as long as this rate is roughly between 1% and 10%. This insensitivity to the prescribed statistics is a major practical advantage, since (1) these statistics are not very reliable and (2) the SQC algorithms do not require retuning each time the prescribed statistics in the global analysis change.

The second consequence of adjusting rejection limits on the fly based on the local variability of surrounding data is that the buddy check becomes increasingly tolerant in synoptically active situations (and, conversely, more stringent when the flow is smooth). This is best illustrated by an example, in which we contrast the results of a nonadaptive buddy check against those of the adaptive buddy check. Figure 3.12 shows two maps with quality control marks for zonal wind observations (obtained from aircraft and rawinsonde reports) over North America at or near 200hPa, on January 14 1998. The top panel shows rejections (indicated by red marks) by a non-adaptive buddy check, based on tolerances derived from prescribed statistics. Yellow marks indicate data that were marked as outliers by the

background check, but which passed the buddy check. The lower panel shows rejections by the adaptive buddy check. Tolerances are increased due to greater variability than implied by the prescribed statistics, resulting in the acceptance of several additional outlier observations. The effect on the wind analysis (not shown) is to increase wind speeds by about $3m/s$ in some places.

3.3.4   The Wind Check

This check is applied to all u-wind and v-wind data to make sure that wind components pass the quality control in pairs. The algorithm determines whether two wind components are paired (i.e., whether they originate from the same report) by matching their location attributes, instrument type, and sounding index.

3.3.5   The Profile Check

This check eliminates an entire vertical sounding in case any of the data from that sounding are marked for exclusion. It is applied to selected data types only. Currently the profile check is used for TOVS height retrievals only. For example, if the buddy check rejects a TOVS height observation at 10hPa, then the entire sounding is marked for rejection.

3.3.6   Special Treatment of Moisture Observations

The analyses moisture field in GEOS DAS is water vapor mixing ratio, which is highly variable in space and time. This causes difficulties for the buddy check, which presumes that the field is spatially coherent on the scales resolved by the observing network. Experience has shown that a buddy check applied to water vapor mixing ratio observations (or, equivalently, specific humidity) tends to reject too many of them, unless the tolerances are relaxed to a point where the quality control becomes almost completely inactive. This is obviously not acceptable, unless preprocessing quality control is completely reliable.

To remedy this situation, the statistical tests (background check and buddy check) in the SQC are applied to relative humidity residuals. These residuals are computed in two ways: first, using observed mixing ratios and observed temperatures, and second, using observed mixing ratios and model-predicted temperatures. This prevents the situation in which a relative humidity looks good even though both mixing ratio and temperature are corrupt. The tests are applied in sequence to both types of residuals, and an observation passes QC only if none of the tests fails.
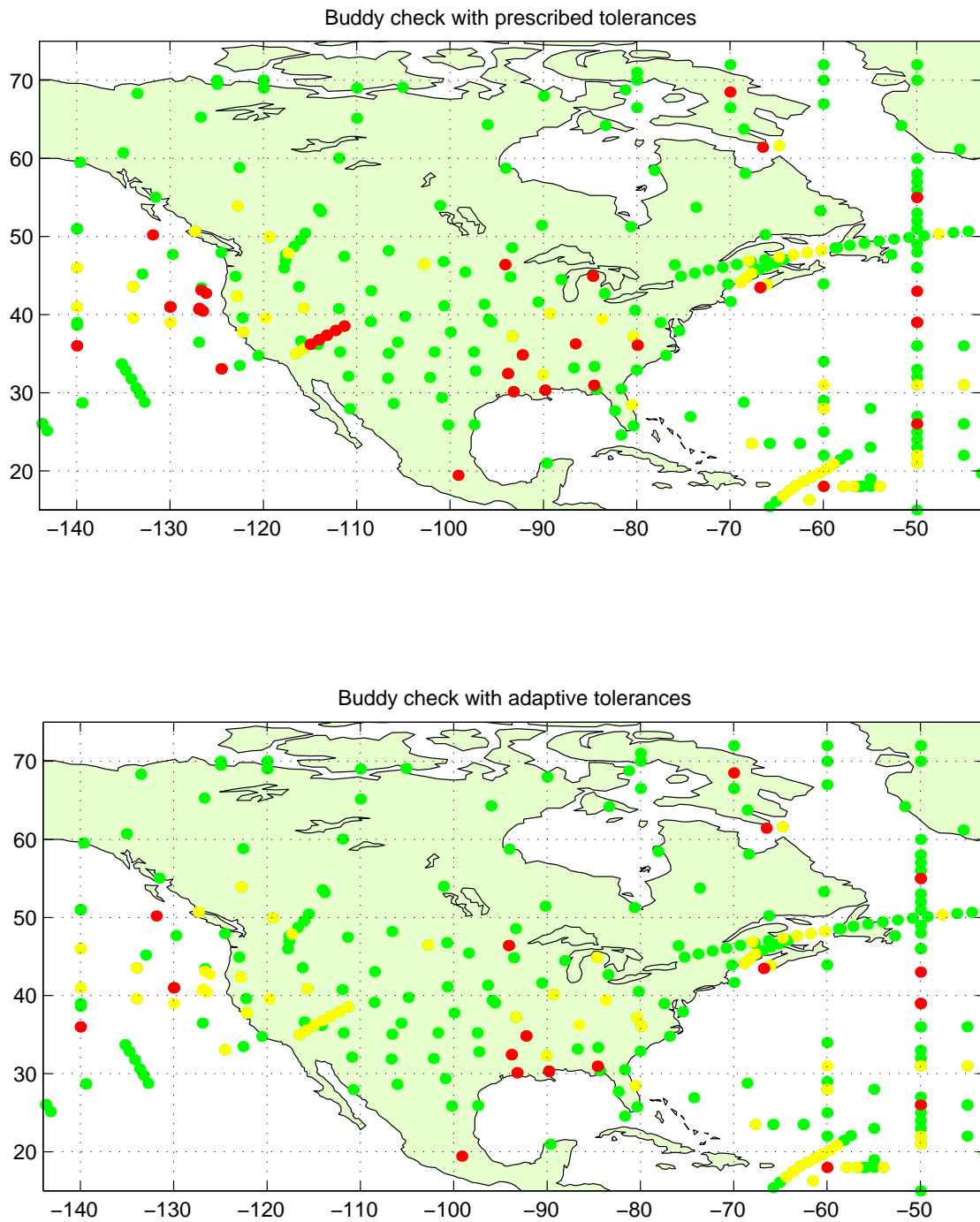
Figure 3.12: Quality control decisions for zonal wind observations at 200hPa on January 14 1998, using a non-adaptive buddy check (top) and adaptive buddy check (bottom). Green dots indicate observations that passed the background check, yellow dots indicate suspect observations that were accepted by the buddy check, red dots indicate rejected observations.

3.4 Interactive Retrievals – iRET

The interactive retrieval process in GEOS-4 uses a variational approach (1DVAR) to extract layer mean temperature, moisture and surface properties from observed remotely sensed radiances in a number of channels. What makes iRET "interactive" is that the 1DVAR process uses GEOS-4 background fields in the retrieval process, and the retrieved information is in turn assimilated into the GEOS-4 system. The salient features of the iRET 1DVAR system are:

- Use of raw data (level 1b radiances);

- Variational cloud clearing (Joiner and Rokke 2000);

- Physically-based systematic error correction (tuning);

- GLATOVS forward model (Susskind et al. 1997; Sienkiewicz 1996);

- Runs in assimilation, future retrievals affected by information from prior retrievals;

- Use of both cloud and land affected data;

- Rawinsonde shadowing, TOVS data in vicinity of rawinsondes not assimilated;

- Tuning using collocated rawinsondes (*not* the background), updated daily.

Joiner and Rokke (2000) provides considerable additional detail on a number of the above topics, especially on the issues of cloud-clearing and tuning, although the system described in that paper was non-interactive. One key aspect of the tuning process in iRET is the identification of cloud-contaminated channels, and the generation (and assimilation) retrieved information for vertical levels above any levels influenced by clouds. In practice iRET identifies cloudy regions, and only generates retrieval profiles above some pre-set "cut-off" level. In GEOS-4.0.3, this level was set to 250 hPa (as can be seen in figure 5.58).

3.5 Model – Analysis Interface

A number of steps are required to move between the "world" (defined by the state variables and their spatial discretization) of the GEOS-4 GCM and the GEOS-4 analysis. Some are relatively minor, such as interpolating wind components back and forth from the GCM D-grid (Figure 3.8) to the analysis A-grid (essentially the "ϕ" points in Figure 3.8).

A significant amount of care needs to be taken with communicating the mass variable information between model and analysis. The principal issue is that while the model state variable is (scaled, potential) temperature, the analysis works with geopotential height. The hydrostatic relation is the mechanism for the interchange:

$$\theta_k = -\frac{g}{C_p} \cdot \frac{h_k - h_{k+1}}{p_k^\kappa - p_{k+1}^\kappa}, \qquad \kappa = R/C_p. \tag{3.22}$$

Given a set of θs and pressures, one can generate a consistent set of heights to serve as background fields for the analysis. The reverse process requires some extra consideration,

since the analysis changes both the geopotential heights and the surface pressure (and thus the definition of all the vertical levels).

A specific approximation in the GEOS-4 system is to localize the effects of the analysis change to the surface pressure to the lowest model control volume. The first step in this approach is the estimation of the analyzed surface pressure (p_s^a) from the upper-air analyzed heights. Figure 3.13 shows the arrangement of variables in this process. For the lowest atmospheric layer, the analyzed height is:

$$\hat{h}_{K+1}^a = h_s + \delta\hat{h}_{K+1}^a \tag{3.23}$$

where h_s is the topographic height; it then follows that adjustments must be made to p_s and θ_* to have the after-analysis bottom edge height correspond to the surface height (h_s). A straightforward rearrangement of 3.22 for the bottom layers (using the variables shown in Figure 3.13) yields the following estimate for p_s^a:

$$p_s^a = p_s^f \cdot \left[1 + \frac{g\delta\hat{h}_{K+1}^a}{C_p\theta_*(p_s^f)^\kappa}\right]^{1/\kappa}. \tag{3.24}$$

Notice that θ_* enters this equation in the denominator, and therefore the final value of p_s^a is not very sensitive to the precise value of θ_*. For typical values, $p_s^f \sim 1000$ hPa, $\delta\hat{h}_{K+1}^a \sim 100$ m, $T_* = (p_s^f)^\kappa\theta_* \sim 300$ K, one can estimate that an error of 5 K in T_* corresponds to less than 0.2 hPa error in p_s^a. For the calculation in (3.24), θ_* is approximated as a layer-mean virtual temperature at the lowest control-volume associated with p_s^f:

$$\theta_* \approx -\frac{g}{C_p} \cdot \frac{\hat{h}_{K+1}^a - \hat{h}_K^a}{(p_{K+1}^f)^\kappa - (p_K^f)^\kappa}. \tag{3.25}$$

Once an estimate of the after-analysis surface pressure has been obtained, the question then arises of what should be used for the after-analysis pressure-thickness δp^a for each finite control-volume. There is nothing in the analysis process that dictates how the upper-air height increments should be partitioned into δp^a and temperature increments. In order to close the problem in GEOS-4, mass from the lowest layers is added or removed. When $p_s^a > p_s^f$, mass is added to the lowest model layer by setting

$$\delta p_K^a = \delta p_K^f + \left(p_s^a - p_s^f\right) \tag{3.26}$$

keeping $\delta p_k^a = \delta p_k^f$, for $k = 1, ..., K - 1$. The volume-mean values of all quantities are not altered by this expansion of the lowest control volume.

However, when $p_s^a < p_s^f$, (3.26) can lead to very small or even negative values of δp_K^a, requiring some special handling. In some cases, it is necessary to remove one or more of the model lowest layers in order to accommodate the new value of the surface pressure p_s^a. (In practice, model layers are removed by assigning an extremely small mass to them.)

The main advantage of this *shaving method* is that no mapping or interpolation is necessary except for those one or two lowest model layers affected. However, the resulting Lagrangian control volume could be very different from the fixed Eulerian reference coordinate (3.1). For this reason, this method has output deferred until the completion of the Finite-volume dynamical core and physics modules, during which a remapping to the fixed Eulerian reference coordinate system is performed, along with any necessary physical adjustments.
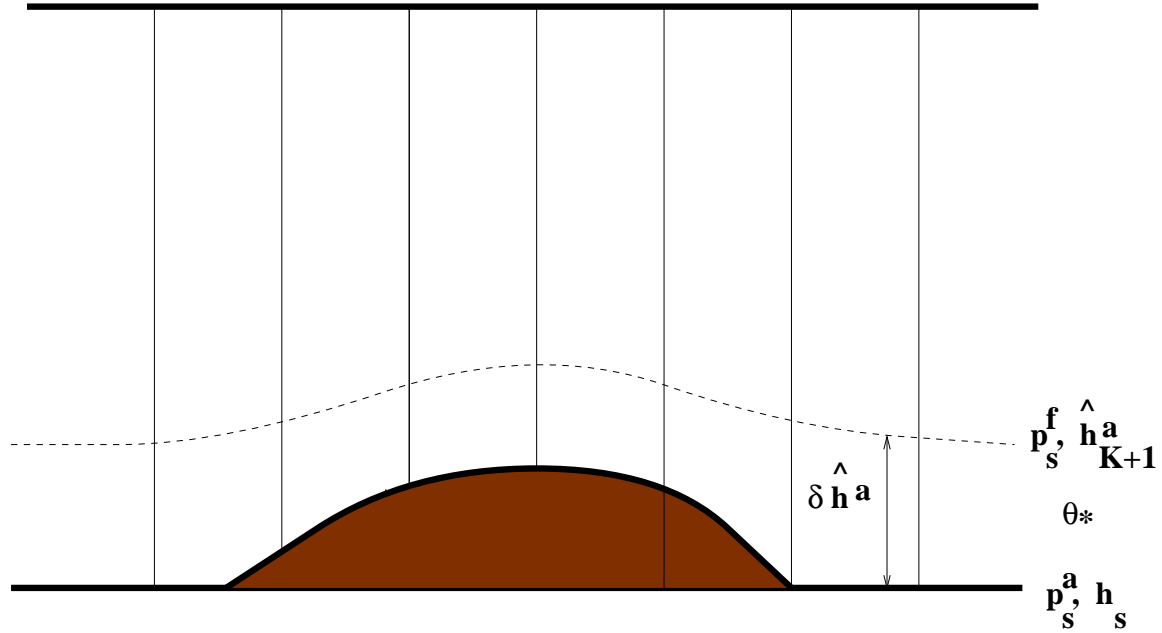
Figure 3.13: After-analysis height and surface pressure.

3.6   GEOS-4 Development History

The antecedents to the current GEOS-4 system were described in Chapter 2. This validation effort is concerned with the evaluation of the third version of GEOS-4, labeled "4.0.3." The prior two operational GEOS-4 versions were:

GEOS-4.0.1 *First operational version of fvDAS*

- validation: December 2001
- entered operations: 1 October 2002

GEOS-4.0.2 *Used for MODIS reprocessing run*

- needed to address T_{skin} feedback problem
- entered operations: 16 April 2003
- also used for MODIS reprocessing period

Issues involving the changes for GEOS-4.0.3 are discussed in Chapter 4. The validation process addresses the entire GEOS-4.0.3 system, not just the changes from GEOS-4.0.2 to GEOS-4.0.3.

Chapter 4

Validation Issues

The GMAO (and formerly the DAO), has always worked from the premise that short to medium range forecast skill is not the absolute measure of the quality of the assimilation state. In fact, it is possible to improve forecast skill at the expense of analysis accuracy. This situation arises because there may be compensating errors in the model-analysis-data combination during the assimilation process. Furthermore, many of the problems of interest to customers of the GMAO are not well represented by the forecast skill metrics (*e.g.* forecasts of 500 hPa geopotential heights, or sea level pressure). Therefore, more general methods of validation are required to ensure that the needs of customers of the GEOS-4 products are met.

If the assimilation system is focused at generalized applications, the number of possible problems requiring metrics to measure improvement becomes very large. Often conflicts develop because efforts to improve performance in one area result in degraded performance in another area. The temptation to fix a problem with an *ad hoc* specification of a system parameter is high. Inevitably such fixes haunt future development because typically they are "shortcuts" for a more involved nonlinear tuning process. As a result, engineering fixes tend to short-circuit feedback loops that are overlooked, unanticipated or poorly understood. In this regard, the validation process acts as a "safety net" for the development process. However it is greatly to be preferred that such tuning problems be caught by aggressive system testing; problems that result in a candidate system failing validation really should lead to changes in the testing process as well as modifications to the system that failed to meet minimum validation criteria.

The effort described in this document is a *System Validation*, a process by which a "candidate" data assimilation system, which has significant modifications beyond a currently running system, is evaluated and judged to be scientifically suitable to be put into operations for the production of products for GMAO customers. System Validation efforts tend to be demanding of resources across the organization, as they must bring to bear the results of the relevant scientific investigations, new verification data, and the diagnostic tools which are best suited for evaluating the system modifications at hand.

The following section describes the changes that went into the candidate system for GEOS-4.0.3. The final section in this chapter outlines how this System Validation effort was organized. Results from this effort will follow in the next chapter.

4.1 GEOS-4.0.3

The validation effort for GEOS-4.0.3 was unusual in that it proceeded in two stages, with a preliminary evaluation effort in October 2003, followed by a final evaluation effort (which is the subject of this document) in December 2003. For the sake of clarity, the two stages in the development of GEOS-4.0.3 will be referred to by their *development tags*: 1.4_r1 and 1.4_r2. While the evaluation of 1.4_r1 yielded satisfactory results, it became clear during the following months that there remained some customer-driven issues that had to be addressed before the candidate system could be considered ready for operations. The changes implemented to address these problems (described in 4.1.2) resulted in the 1.4_r2 system, which in turn was evaluated. A significant constraint on the evaluation of 1.4_r2 was that this system had to retain the positive validated behavior obtained for 1.4_r1.

The following two sections give an overview of the changes implemented for the two stages of GEOS-4.0.3 development. This material, with considerable additional details, resides on the following Monitoring web page:

> http://gmao.gsfc.nasa.gov/science/dolms/validation/

4.1.1 1.4_r1

The following list summarizes the major changes in the 1.4_r1 system:

- Modified mass-wind balance

- QC changes

- CTW selection

- Increased iRET coverage over ice

- 25 → 36 levels in analysis

- MPI PSAS (efficiency increase)

The first three items will be discussed in more detail below. The increased coverage of interactive retrievals (see 3.4) over ice was an attempt to address a serious lack of data coverage in GEOS over the Southern Oceans. The enhanced vertical resolution of the analysis output grid helped to reduce the impact of interpolation from the analysis to model grids. The implementation of message-passing interface code (MPI) in the PSAS greatly improves the computational efficiency of the analysis; while this should not directly influence the scientific behavior of the system, this is still a greatly desirable change as it allows for many more tuning and testing runs with limited resources.

4.1.1.1 Modified Mass-Wind Balance

Of the three analysis changes made in GEOS 4.0.3, the most profound was the modification made to the analysis mass-wind balance by means of an extensive retuning of the mass-wind coupling statistics statistics (see the description in section 3.2.2.1; the specific tuning

parameters used in GEOS-4.0.3 are shown in section 3.2.5.2. This change actually addresses problems that have existed in the PSAS analysis going back as far as the GEOS-2 system.

4.1.1.2 Modified QC Gross-Check

It was noted in the weekly monitoring meetings that the Quality Control in previous GEOS-4 versions appeared on occasion to be overly "generous" in its treatment of grossly bad data. Eventually the problem was traced to a mistakenly set parameter ($\tau_x = 1000$ in section 3.3.2) within the Quality Control algorithm that basically had the result of outright outlier observations never being flagged for rejection. For this version of GEOS-4, this parameter was reset to a more reasonable value ($\tau_x = 10$). Some of the previous bad cases were rerun with this value, with far more satisfactory results.

The objective of validation here is to examine the overall QC statistics, as well as to examine some case studies, to insure that the new settings are behaving properly.

4.1.1.3 CTW selection

Problems with mid-level (*i.e.* 700-400 hPa) cloud motion vector wind data (or "CTW" for short) have been evident in monitoring throughout the entire operational life of GEOS, with the worst behavior in the Tropics. As these data typically occur in isolation from other wind data, they pose a stiff challenge to the Quality Control implemented in GEOS (see 3.3 and subsections therein). An alternative approach (followed at NCEP) is to restrict the usage of these problematic data; so this version of GEOS summarily eliminates the participation of mid-level CTW data.

4.1.2 1.4_r2

The following list summarizes the major changes in the 1.4_r2 system:

- CLM2 land surface model

- Modified T_{skin} analysis

- RH fix over high topography

It should be noted that there are other changes in the GEOS-4.0.3 system (listed on the monitoring web page) that are not playing a role in the current validation process: the use of NOAA-17 retrievals; the use of MODIS cloud-track wind data; and the output file structures added for the study of transports in the Stratosphere. These changes were largely implemented and examined after the validation exercise described in this document.

4.1.2.1 CLM2

In order to address significant problems with skin temperature biases in the earlier versions of GEOS-4, a completely revamped land surface model (CLM2) was incorporated into the

system. A brief overview of this module is given in section 3.1.2.2.3. This change has the greater significance for validation as it directly affects all the model surface fluxes which in turn can participate in a number of feedback loops in the system.

4.1.2.2 Modified Skin Temperature Analysis

It was found that the rapid changes in T_{skin} at certain times of day put strong constraints on the time-windowing allowed for using observational estimates of T_{skin} in an analysis. To address this issue, the off-line analysis was modified to run every 3 hours (instead of 6 hours), with the data windowed in 1 hour intervals (instead of 6 hour intervals). With the narrowed time windowing, and the use of the new CLM2 land model, it was also determined that a T_{skin} bias estimation/correction process could also be dropped in the new version.

The objective of validation in this case is to check that T_{skin} and associated radiation diagnostics (*e.g.* , Outgoing Longwave Radiation) retain their desired behavior in the full assimilation system.

4.1.2.3 Near-ground Moisture Modification

A problem in the GCM low-level moisture near high topography in polar regions was noticed during the course of the weekly monitoring activity. The modification described in the first paragraph of section 3.1.2.2.2 was introduced to address this issue. As this problem was of a highly localized and intermittent nature, its modification is less of an issue for the overall system behavior. Validation's role here is to check that the process of removing this problem did not lead to other unintended consequences.

4.2 System Validation: Methodology and Resources

There are intersecting broad themes in this validation effort:

- Does the modified system meet customer requirements?

- Do the system changes retain their intended benefits?

  - T_{skin} and radiation (from both analysis and model)
  - Antarctic moisture anomaly correction
  - Mass-wind issues
  - Gross-check parameter modification

- Overall scientific behavior of modified system?

This validation effort has been accomplished by the distribution of the evaluation effort among several investigators, each focusing on specific areas/metrics that, taken as a whole, encompass all of the above validation themes. Table 4.1 displays the investigators and their topics.

Validation Topics

Theme	Topic	Investigator	Metrics
CUS, CHG	clear sky OLR, tskin	M.-L. Wu	Comparisons with ECMWF and CERES
CUS, CHG	surface fields (esp tskin)	M. Bosilovich J. Radakovich	ISSCP Comparisons Station Data
CUS, SYS	Stratosphere	S. Pawson W. Tan	Residual Circulation
CUS	ozone	I. Stajner L.-P. Chang K. Wargan	Comparisons with NOAA-16 SBUV, TOMS Rawinsondes
SYS	precipitation surface stress	S. Schubert D. VanPelt	ERA-40, GPCP, SSM/I comparisons Monthly Means, Taylor Plots
SYS	precipitation variability on MJO time scale	M.-L. Wu	TRMM comparisons
SYS	data impact	M. Sienkiewicz	Data Withholding, Forecast Skills
CHG, SYS	monitoring	A. Conaty S. Bloom	O-F, O-A, QC Stats; Case Studies
CHG: verify system change CUS: customer requirement SYS: diagnose system behavior			

Table 4.1: Organization of the GEOS 4.0.3 Validation effort.

The other major consideration for System Validation, given the themes to be examined, is the choice of assimilation runs of the candidate system to serve as the "raw material" for the evaluation process. Ideally, long multi-seasonal runs with sampling from different years would be used for the evaluations. However, there are very real constraints on resources, both for executing the assimilation runs as well as for having a diverse group of investigators budget their time for completing their validation commitments.

For this validation effort, output from two separate runs were used:

- *CERES RUN*

  - May 2000 - December 2001
  - long run, providing monthly means from different seasons

- *PARALLEL RUN*

  - 2003
  - behavior with current observing system

In addition to the wide array of diagnostic quantities to be examined, there are also other off-line processing steps for this work: radiation calculations for CERES; transport calculations using GEOS-4 winds for Ozone.

Chapter 5

Validation Results

This chapter presents the results of the several validation evaluation efforts listed in table 4.1. Each entry in the table has its own section in this chapter. The results given here were presented in the GMAO System Validation meeting held on 12 December 2003; a number of the presentations can also be found at:

    http://gmao.gsfc.nasa.gov/science/dolms/validation/fv14r2.html .

5.1 CERES Radiation Comparisons

The CERES Instrument Team has been a significant customer of GEOS products. Their radiation calculations place tight tolerances on the temperature and moisture profiles, as well as on T_{skin}, that are produced by GEOS. The results in this section are organized as follows:

- CERES concerns with previous GEOS-4 T_{skin} products

- Improvements in T_{skin} with candidate system

- Cloud-clearing issues

- OLR comparisons

5.1.1 CERES Concerns

The first figure (Figure 5.1) shows a clear sky OLR computation using a prior version of GEOS-4 (GEOS-4.0.2) for May 2001. Comparisons with OLR from ECMWF fields and the corresponding CERES satellite results show the GEOS4 OLR bias against CERES to be in general larger than the ECMWF bias. The GEOS-4 biases over land are mainly due to T_{skin} biases which are presented in Figure 5.2.

Figure 5.2 contains scatter-plots of T_{skin} for five regions: Australia, North Africa, Saudi Arabia, Eastern and Western US. In all cases, the CERES retrieved T_{skin} is on the horizontal
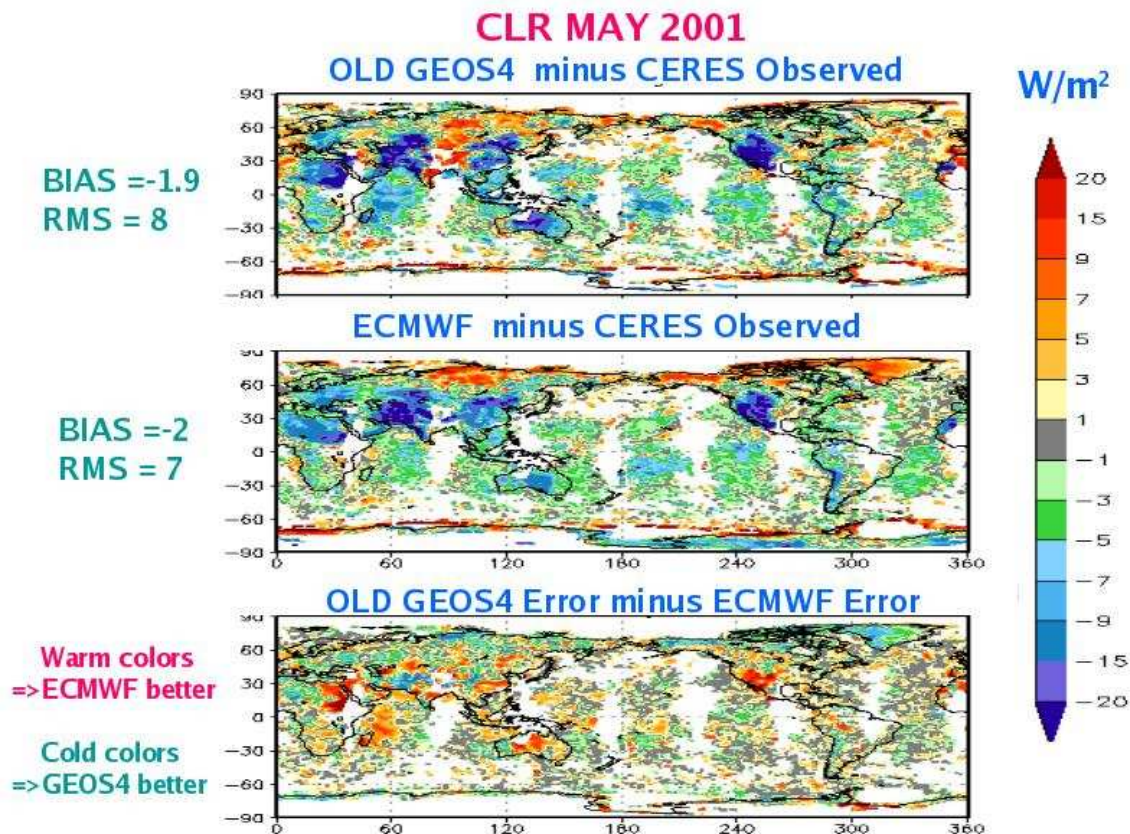
Figure 5.1: Comparisons of GEOS-4.0.2 ("OLD GEOS") and ECMWR clear sky OLR with CERES OLR. The bottom panel is the difference of the absolute value of the fields in the first two panels.

axis, and GEOS-4.0.2 T_{skin} is on the vertical axis. Perfect correspondence between the two sets of temperatures would align the points along the dashed line; in all these cases, the actual alignment shows the GEOS-4.0.2 T_{skin} to be too warm during the nighttime and too too cold during the daytime. Two likely sources of these biases are: deficiencies in the land-surface model used GEOS-4.0.2; and the use of 6-hourly analyses of T_{skin}, although the temperatures (and thus the CERES estimates) can be rapidly varying over that time interval.

5.1.2 T_{skin} Improvements

Figure 5.3 (a-d) shows the impact of the changes described in section 4.1.2 . The four parts of this figure show groups of scatter-plots of T_{skin} for four months (January, April, July and October) in 2001. Each grouping is arranged as follows:

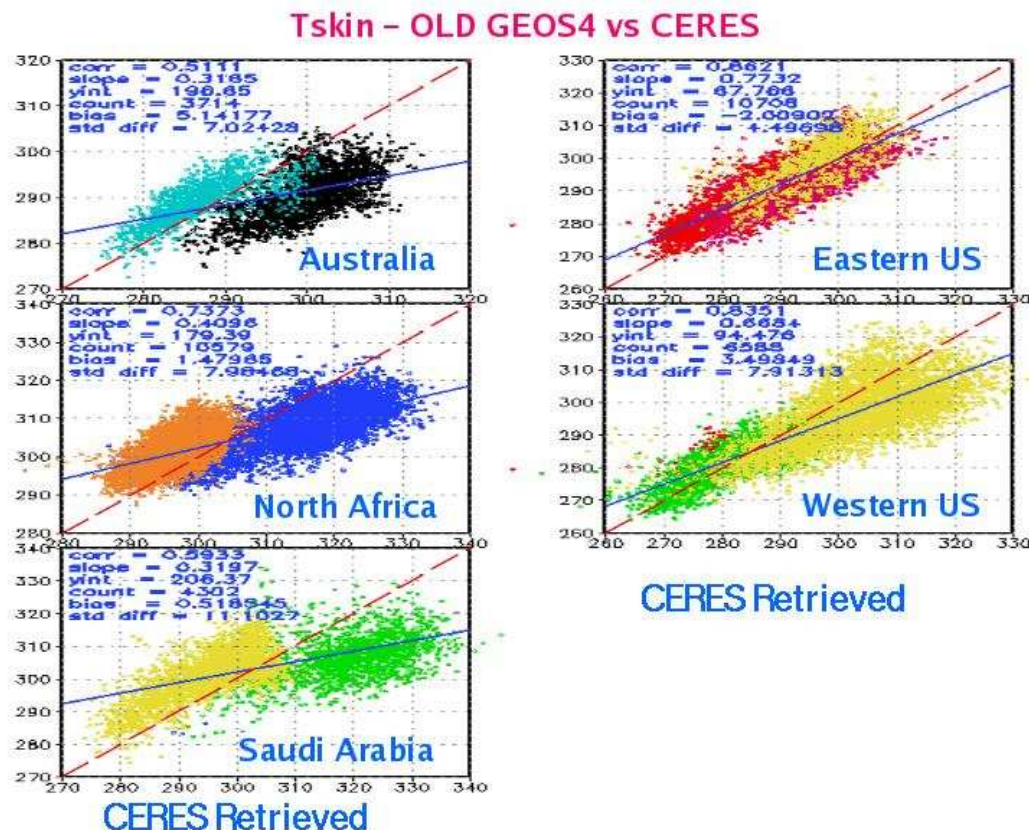| ECMWF | vs | CERES | | | |
| C403 | vs | CERES | C402 | vs | CERES |
| C403 | vs | ECMWF | C402 | vs | ECMWF |

Figure 5.2: Scatter-plots of CERES retrieved T_{skin} (horizontal axis) versus GEOS-4.0.2 T_{skin} (vertical axis) for the five regions on the panels. See text for details.

where "C403" and "C402" are shorthand labels for GEOS-4.0.3 and GEOS-4.0.2 (the previous version of GEOS) respectively. The different colors represent nighttime (orange) and daytime (blue) T_{skin} estimates. Comparing the the top left and middle left plots with the top right plots in Figure 5.3 (a-d), it is apparent that GEOS-4.0.3 has superior agreement to the CERES data than does the prior version of GEOS, and that this agreement is comparable with the ECMWF agreement with CERES. The bottom plots reinforce this point by showing how GEOS-4.0.3 is in much better agreement with ECMWF than was GEOS-4.0.2. Scatter plots for other regions (not shown) show similar behavior to those in Figure 5.3.

Global intercomparisons of monthly means of T_{skin} are shown in Figure 5.4 (a-d), for the same time periods as in Figure 5.3 (a-d). In this figure, each of the panels consists of three plots: GEOS-4.0.3 minus CERES (top); ECMWF minus CERES (middle); and $|(GEOS\_4.0.3 - CERES)| - |(ECMWF - CERES)|$ (bottom). The plots with the difference of absolute values allow one a ready view of which of the GEOS or ECMWF T_{skin}s agree better with the CERES retrieved T_{skin} values. In the absolute difference plots "warm" colors (reds, yellows) indicate better ECMWF agreement with CERES, while "cool" colors (blue, green) indicate better GEOS agreement with CERES. Inspection of the bottom plots in Figures 5.3 (a-d) shows a general preponderance of the "cool" colors over land, indicating that for these time periods GEOS-4.0.3 had less T_{skin} bias than ECMWF when compared to CERES. This conclusion is borne out quantitatively by the bias and RMS numbers included
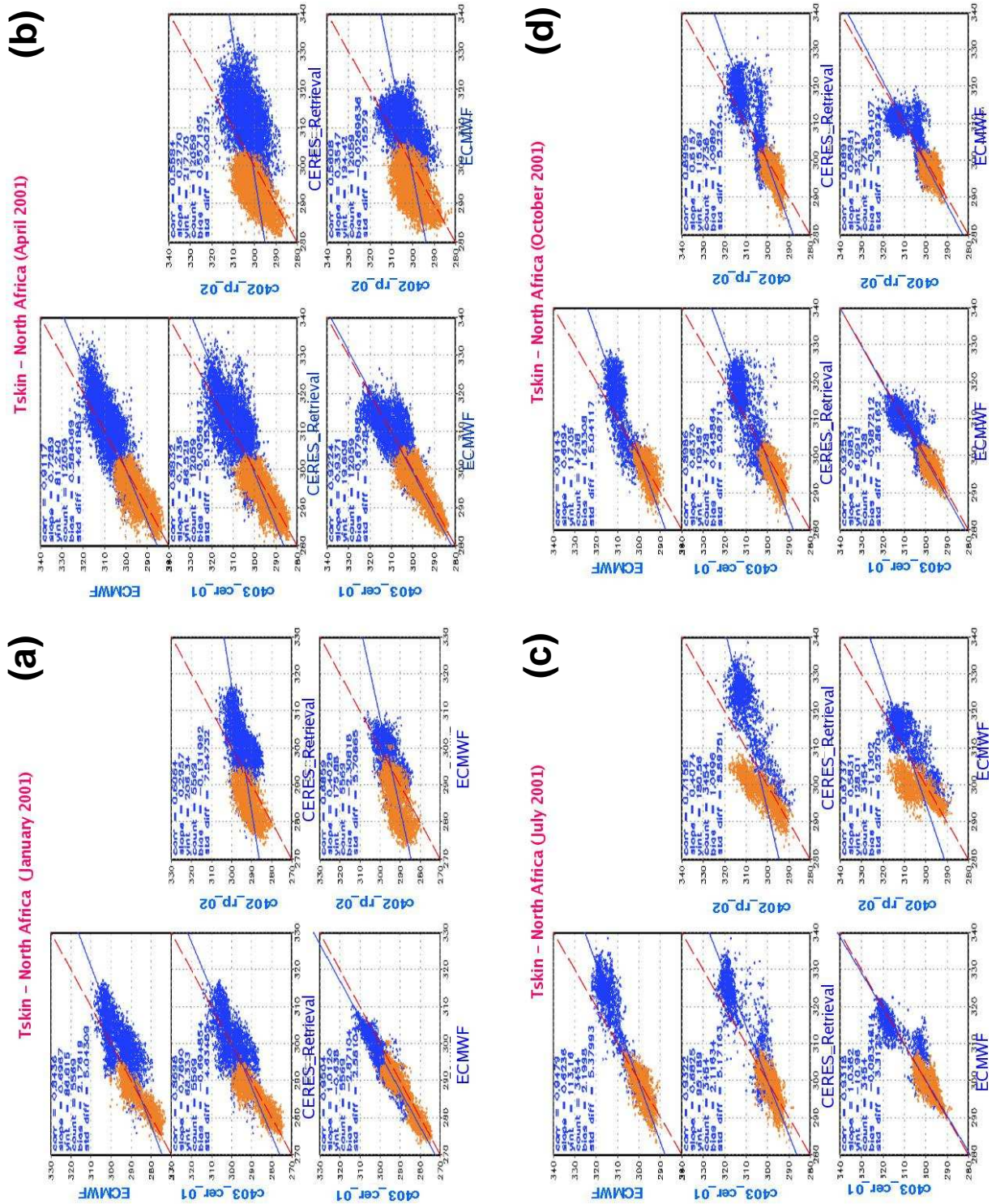
Figure 5.3: Scatter plots of T_{skin}, intercomparing CERES data with model estimates from GEOS-4.0.3 (C403), GEOS-4.0.2 (C402) and ECMWF for four months during 2001: (a) January, (b) April, (c) July, and (d) October. See text for discussion.
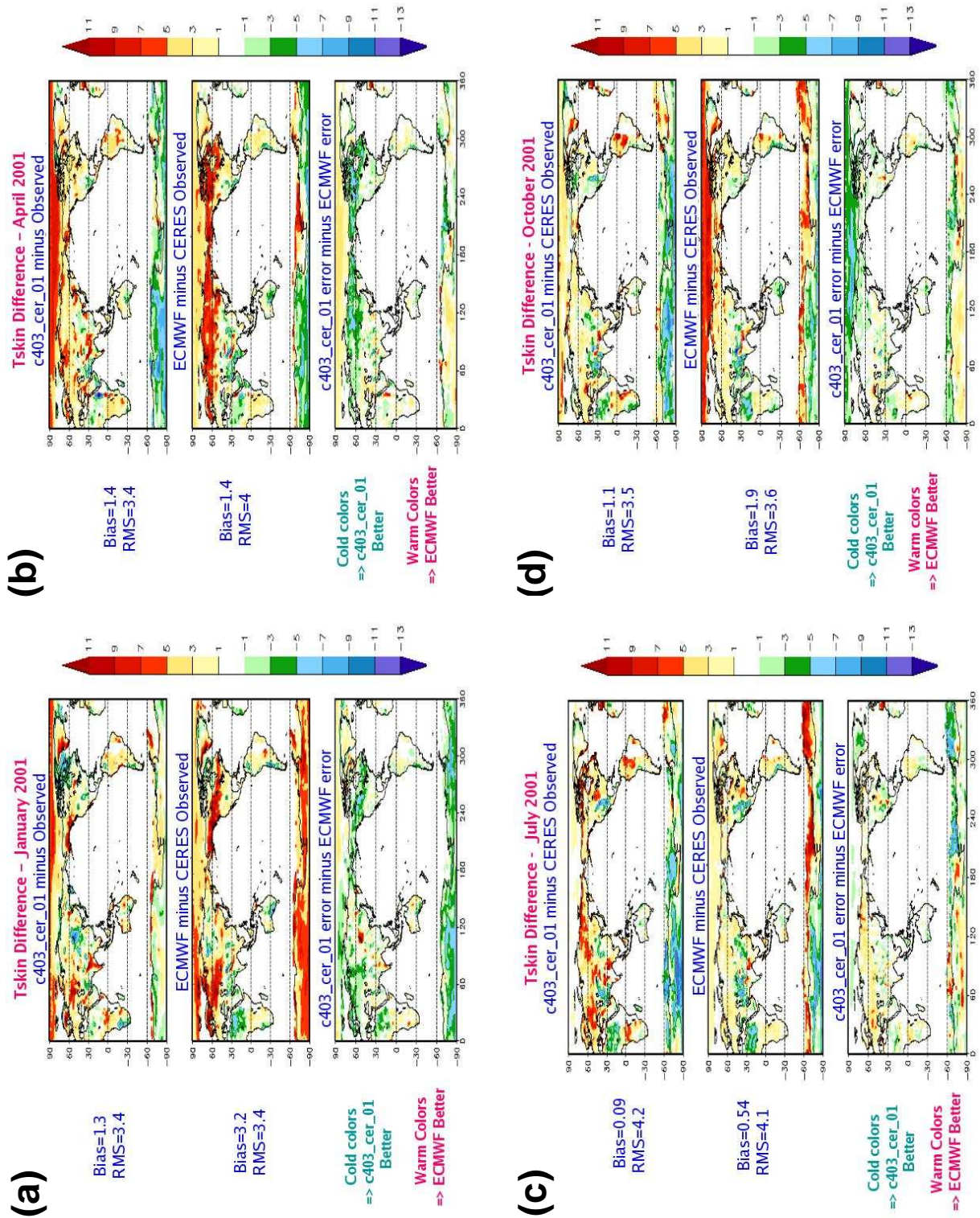
Figure 5.4: Global monthly mean T_{skin} intercomparisons, GEOS-4.0.3 and ECMWF vs CERES, for four months during 2001: (a) January, (b) April, (c) July, and (d) October.

on the plots in Figure 5.3.

5.1.3 Cloud-Clearing Issues

As retrievals of T_{skin} from CERES are being used as a verification standard, it is important to be aware of any potential problems with the use of these data for this purpose. Figure 5.5 shows an example of a potential problem. The left two panels show ECMWF and GEOS4 having similar biases vs CERES retrieved T_{skin} for January 2001. The right two panels show that an independent estimate of cloud cover (ISCCP) has a large amount of cold clouds in the Northern high latitudes, where the ECMWF and GEOS4 biases are the largest. The problem here is that a failure to recognize the presence of cold clouds in a scene could lead to an anomalously low retrieved value of T_{skin}. Figures 5.6 and 5.7 provide more detailed examples of possible cloud issues with the CERES estimates of T_{skin}, for a period in early January 2001. Figure 5.6 focuses on an area over the Weddell Sea off the coast of Antarctica, while Figure 5.7 examines an area north of the Black and Caspian Seas in Central Eurasia.

Figure 5.6 (a) compares the GEOS4 T_{skin} estimate to that from CERES (lower left and upper left plots, respectively) and also shows the corresponding ISCCP cloud coverage and cloud top temperatures (lower and upper right plots) for January 5, 2001. While the GEOS4 T_{skin} field is relatively featureless over the Weddell Sea, there is a pronounced (less than 260 K) minimum in the CERES field, which does not appear to be a reasonable estimate for an ocean or ocean-ice region. The CERES feature does correlate well with an area having an extensive coverage of clouds with cold cloud tops. It should be noted that these plots represent nighttime conditions (03Z for the T_{skin} estimates, 06Z for the ISCCP data). The implication here is that the nighttime cold clouds are not identified as such, and thus end up making an inappropriate contribution to the CERES T_{skin} estimate. Figure 5.6 (b) tends to confirm this hypothesis, by examining the behavior of area-averages of T_{skin} (for ECMWF, GEOS4 and CERES) as well as ISCCP cloud top temperatures over the course of a week in January 2001. The nighttime data points are encircled for clarity. The striking feature of this figure is how the ECMWF, GEOS4 and the *daytime* CERES values tend to cluster together, while the *nighttime* CERES estimates tend toward the ISCCP cloud top temperatures.

Figure 5.7 examines the behavior of the T_{skin} estimates over Eurasia. While the results in this figure are not as dramatic as those in the previous figure, the strong disagreement between GOES4 and CERES north of the Caspian Sea again has a strong CERES minimum correlating with a maximum in ISCCP cold cloud top coverage. In addition, the clustering behavior of areal averages of T_{skin} is repeated for this region, with the nighttime CERES estimates tending to follow the ISCCP cloud top temperatures.
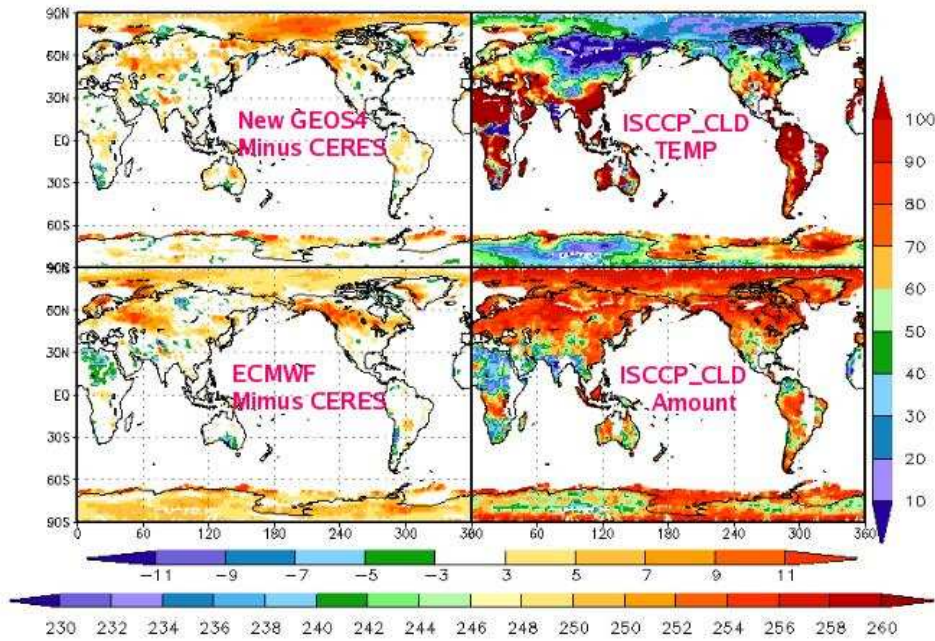
Figure 5.5: T_{skin} biases (differences between GEOS4 and CERES retrieved T_{skin}) and cloud parameters from ISCCP: Cold biases occur over areas having high cloud amount with cold cloud top temperatures.

5.1.4   OLR Comparisons

Figures 5.8 and 5.9 show that the positive T_{skin} results shown above are reflected in the Outgoing Longwave Radiation (OLR) computations. Monthly bias results against CERES (for January, April, July and October 2001) shown in Figure 5.8 show the GEOS-4.0.3 Clear Sky OLR biases against CERES to be very comparable to those from ECMWF, with the global bias and standard deviation figures somewhat better for GEOS-4.0.3. Figure 5.9 shows Clear Sky OLR RMS comparisons of GEOS4 and ECMWF against CERES over three types of surface: Ocean, Desert and Crop-land. OLR comparisons over desert should have T_{skin} as the dominant signal; OLR differences over oceans should be dominated by upper-air moisture and temperature profiles; the crop-land signal should behave somewhat between the desert and ocean signals. The desert and crop-land RMS results indicate that there is very little difference between GEOS4 and ECMWF. There is a consistently larger RMS for GEOS4 over oceans, which is a consequence of a significant bias in upper Tropospheric moisture in GEOS4.
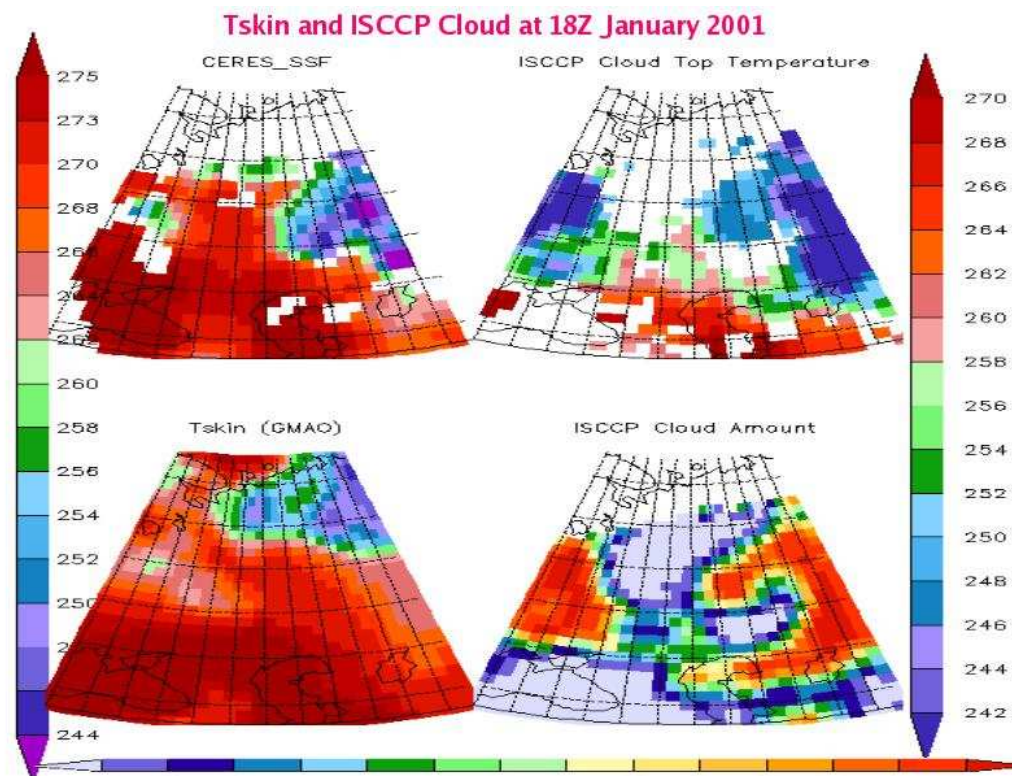
(a)
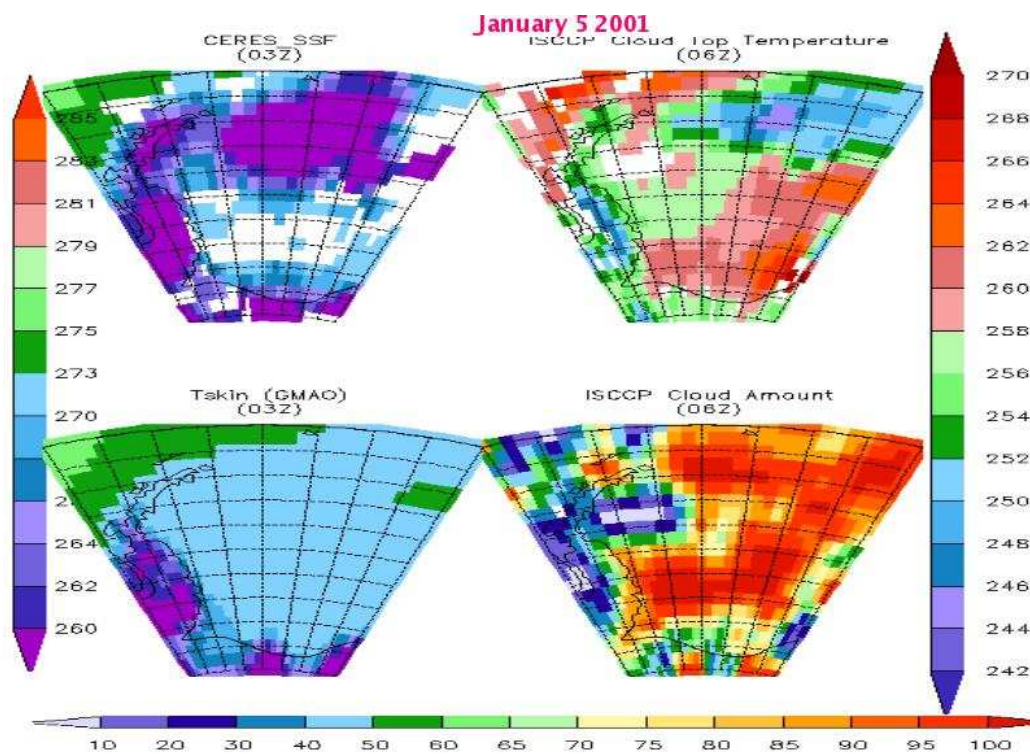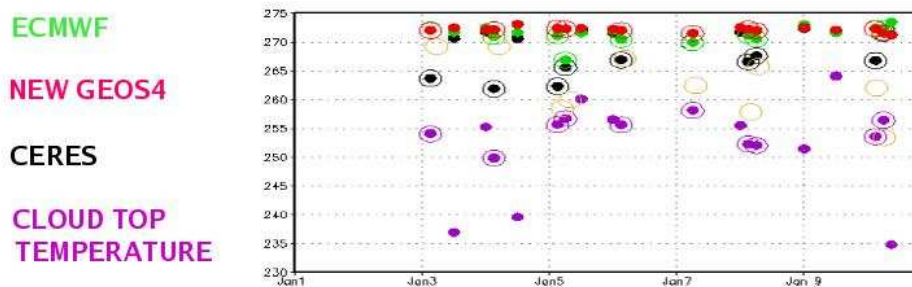
(b)

Figure 5.6: Cloud contamination example: Antarctica.

(a)
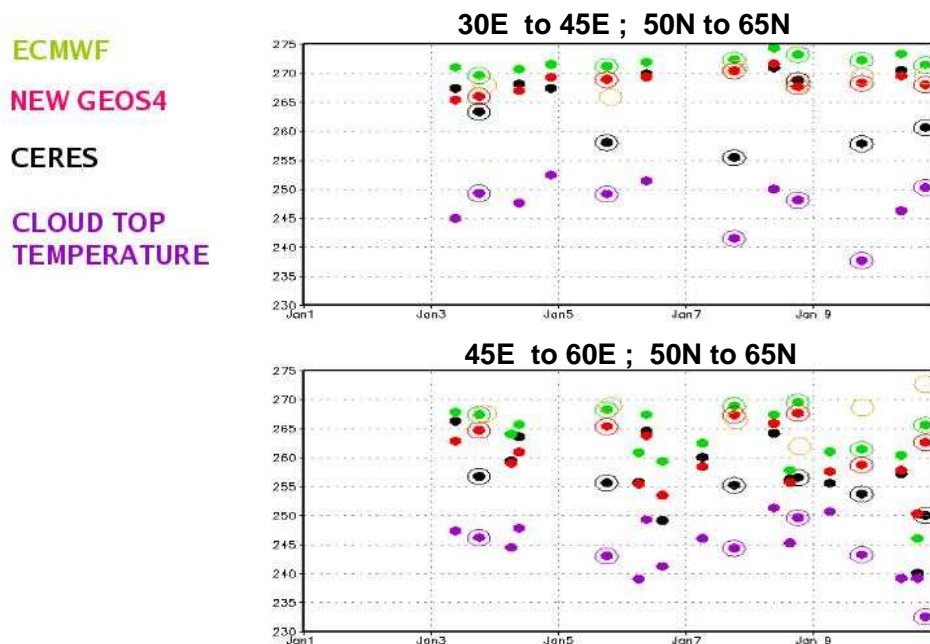
(b)

Figure 5.7: Cloud contamination example: Eurasia.

5.1.5 Summary

- Previous version of GEOS4 (4.0.2) had significant T_{skin} problems

- Current version of GEOS4 (4.0.3) now comparable to ECMWF

  - new LSM, improved surface albedos
  - T_{skin} analysis at 3 hr intervals
  - 1 hour data window

- Clear-sky OLR comparisons

  - over land, statistics (bias, RMS) GEOS4 and ECMWF are comparable
  - over ocean, GEOS4 upper-Troposphere moisture bias results in poorer performance compared to ECMWF

- Common biases (ECMWF, GEOS4) indicate possible cloud clearing problems in CERES retrievals.
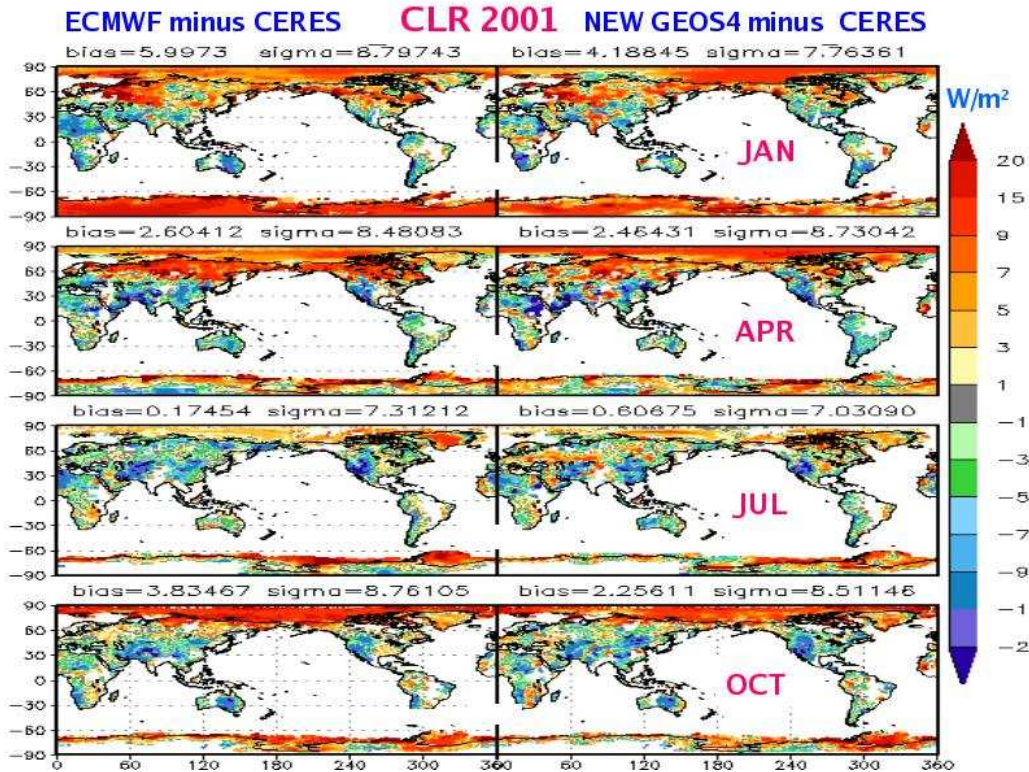
Figure 5.8: Clear sky OLR comparisons. Statistics show that the GEOS4 based clear sky OLR is comparable to that from ECMWF.
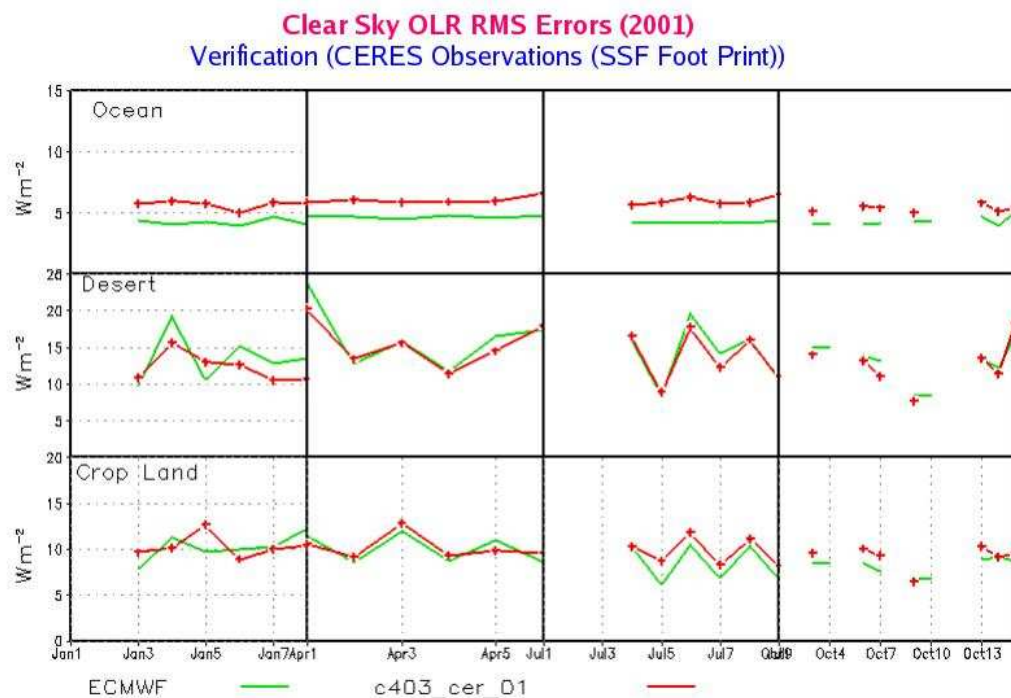

Figure 5.9: Clear sky OLR rms errors. It shows that the GEOS4 based clear sky OLR is comparable to that from ECMWF.

5.2 ISCCP and Station Observation Comparisons

ISCCP DX data provides 30km 3-hourly surface temperature fields for clear sky conditions. Figure 5.10 shows the day time and night time differences of surface temperature averaged for July 2001. In day and night, GEOS4.0.3 analysis skin temperature is generally warmer than the ISCCP data. Some regions do exhibit diurnal variations in the mean bias, but it is difficult to discern a systematic diurnal bias. The difference between ISCCP surface temperatures and the TOVS retrievals that are being analyzed is also provided (Figure 5.10, bottom). Since the TOVS data is itself warm compared to ISCCP, any further improvements to the TOVS analysis will not make this difference much smaller. It has not been ruled out that ISCCP may be biased cold, but this needs further study.

Several *in situ* stations, available from many different providers through the Coordinated Enhanced Observing Period (CEOP), include surface skin and air temperature as well as the radiation components and turbulent fluxes of heat. There are many issues involved in comparing surface site observations to grid point data, such as the heterogeneity of the real world is not adequately represented, but systematic problems may be identified. The sites used in this analysis are shown in Table 5.1:

CEOP Stations

CSE	Name	station	lat	lon
BALTEX	Cabauw	Cabauw	51.97	4.93
BALTEX	Lindenberg	Lindenberg	52.17	14.12
CAMP	Mongolia	330	46.13	106.37
GAPP	Bondville	Bondville	40.01	-88.29
GAPP	Ft_Peck	Ft_Peck	48.31	-105.10
GAPP	SGP	E13_Lamont_CF1	36.60	-97.49
LBA	Manaus	Manaus	-2.61	-60.21
LBA	Rondonia	Rondonia	-10.08	-61.93
MAGS	BERMS	Old_Black_Spruc	53.99	-105.12
NSA	ARM	C2_Atqasuk	70.47	-157.41
NSA	ARM	C1_Barrow	71.32	-156.61

Table 5.1: CEOP observing stations for *in situ* comparisons.

Note that in the ISCCP comparison (Figure 5.10) shows a significant daytime cold bias extending from Texas through the Northern Plains states. This feature can be seen as well in two of panels of Figure 5.11 ("Ft_Peck" and "Lamont"); the panels in this figure depict monthly mean surface temperature and near-surface air temperature for July 2001 (the black and red bars denote the fraction of available observations, shown as dots). In contrast to the Fort Peck and Lamont (ARM SGP) sites, there is a marked warm bias in the daytime temperatures at the Bondville (Illinois) site. The remaining panels of Figure 5.11 show a better agreement between model and observations. The North Slope of Alaska (NSA), Atqasuk mean diurnal cycle is reasonably represented. The amplitude of the diurnal cycle for Barrow conforms well to the observations; the bias of the model results at this location may be related to a difference of altitude between the model grid point and station elevation (the model point would be at a lower altitude). Rondonia, near complicated

JUL 2001 TSKIN Differences

Monthly Mean c403 ANA − ISCCP (Daytime)
Bias = 1.5487; SD = 3.107
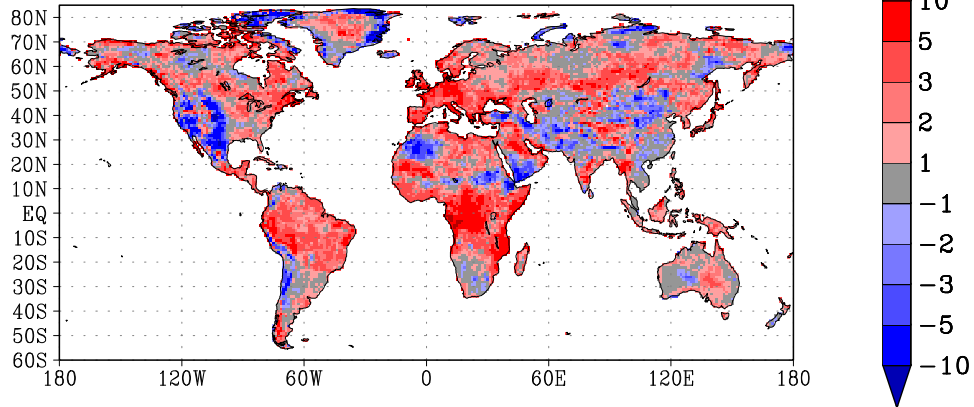
Monthly Mean c403 ANA − ISCCP (Nighttime)
Bias = 1.7450; SD = 2.414
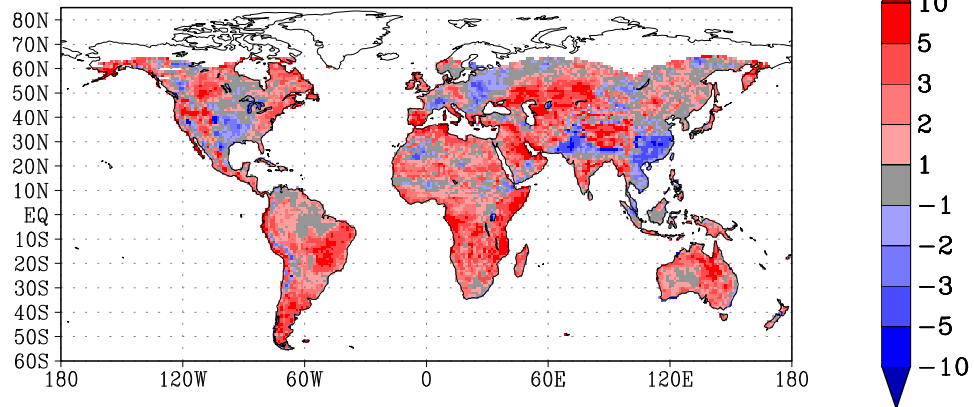
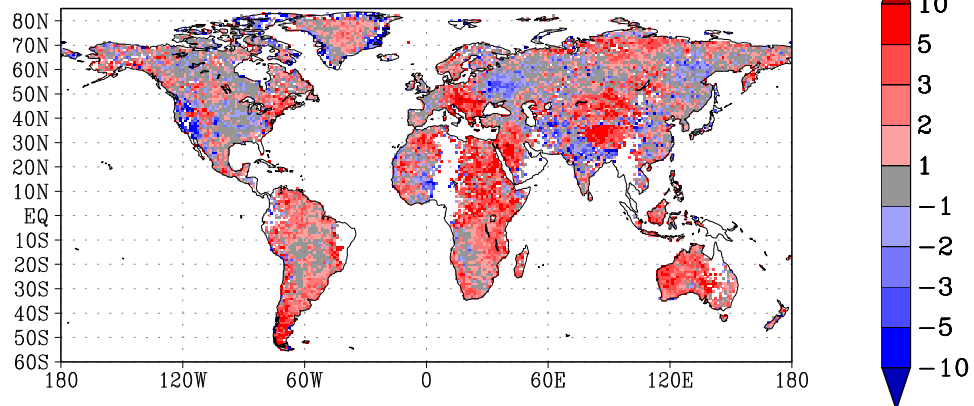### Monthly Mean c403 TOVS − ISCCP
Bias = 1.3032; SD = 2.880

Figure 5.10: Monthly mean differences between c403 and ISCCP clear sky skin temperature observations for July 2001 (top-daytime, middle night time). The bottom panel shows the differences between the TOVS retrieved T_{skin} and the ISCCP observations, averaged only when both coexist in the time series. (Units Kelvin).

rainforest terrain, exhibits some differences between the simulated and observed surface temperatures. The mean diurnal cycle of the Mongolia site is reasonably represented, though when evaluating the time series, the analysis system does have difficulty regularly reaching the observed daytime maximum.

Figure 5.12 shows the monthly mean diurnal cycle of radiation at several reference sites. In a general sense, the incoming shortwave radiation (black curves) is somewhat overestimated (at some stations, a day-time average difference can be as much as $+100Wm^{-2}$). The upward shortwave (red curves) is also generally larger than the observations, but it and the longwave radiation components do not appear to balance the discrepancy in incoming shortwave radiation. Figure 5.13 shows the net radiation, ground and turbulent energy fluxes (at the corresponding stations for the radiation data). The availability of the turbulent and ground heat flux observations is not as regular as the radiation observations. In many of the regions the net radiation exceeds observations, following the downwelling shortwave radiation bias. In some, but not all stations, this can lead to excessive turbulent heat transport. Not all the stations have reliable ground heat to attempt to close the budget, however, there are biases in the diurnal cycle of ground heat that are typical of most land parameterizations (*e.g.* Bondville and Fort Peck). Care must be taken when evaluating the surface fluxes against station observations. For example the high latent heat that occurs in Lamont, is a result of an overactive precipitation event produced by the analysis system, that was observed as mostly clouds with little precipitation. The high latent heat flux followed this erroneous precipitation forcing.
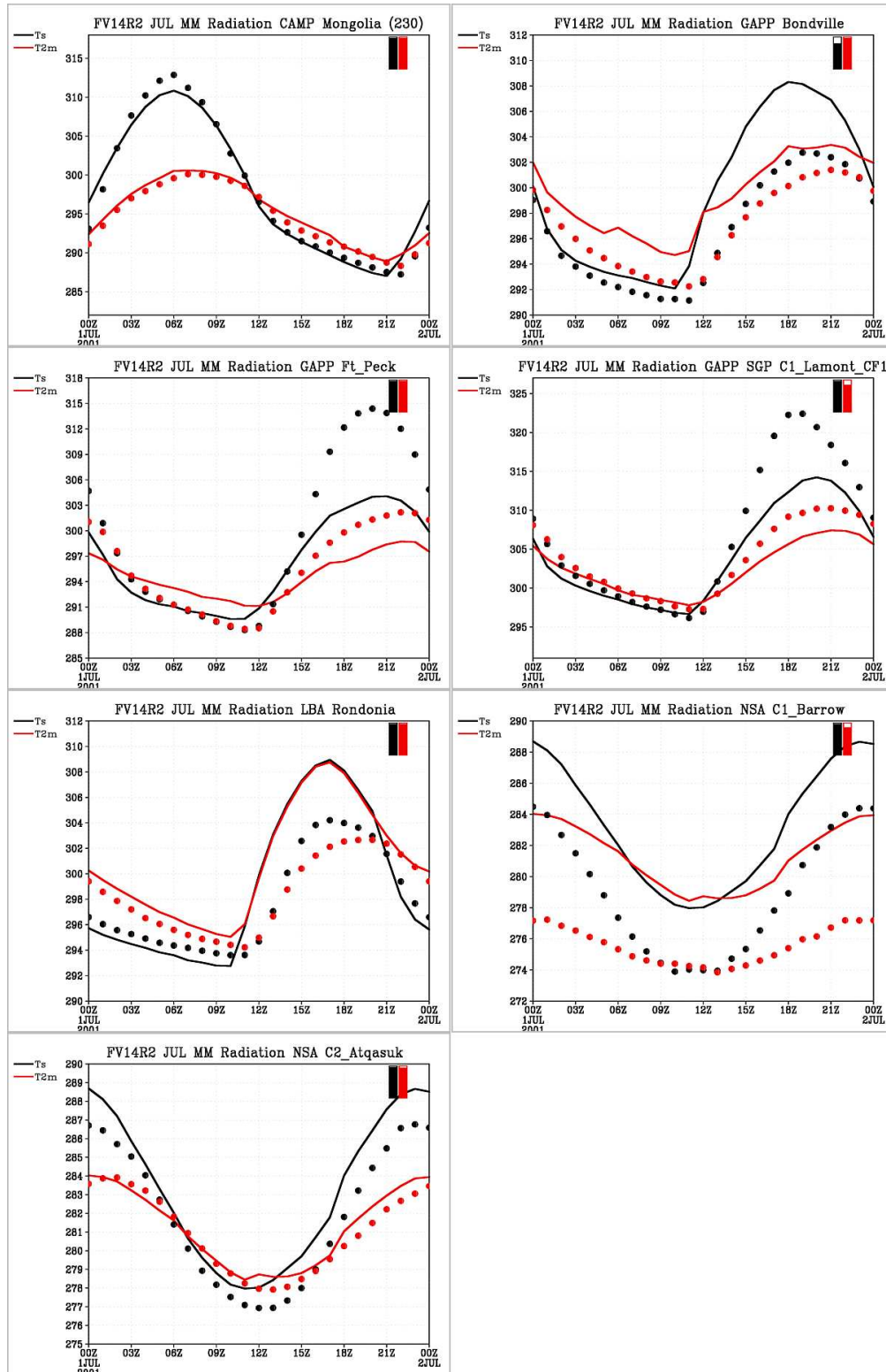
Figure 5.11: Mean diurnal cycle of several in situ reference site stations (data shown as dots) and corresponding C403 grid point surface temperature and near surface air temperature for July 2001. The red and black bars denote the fraction of available observations. (Units Kelvin)
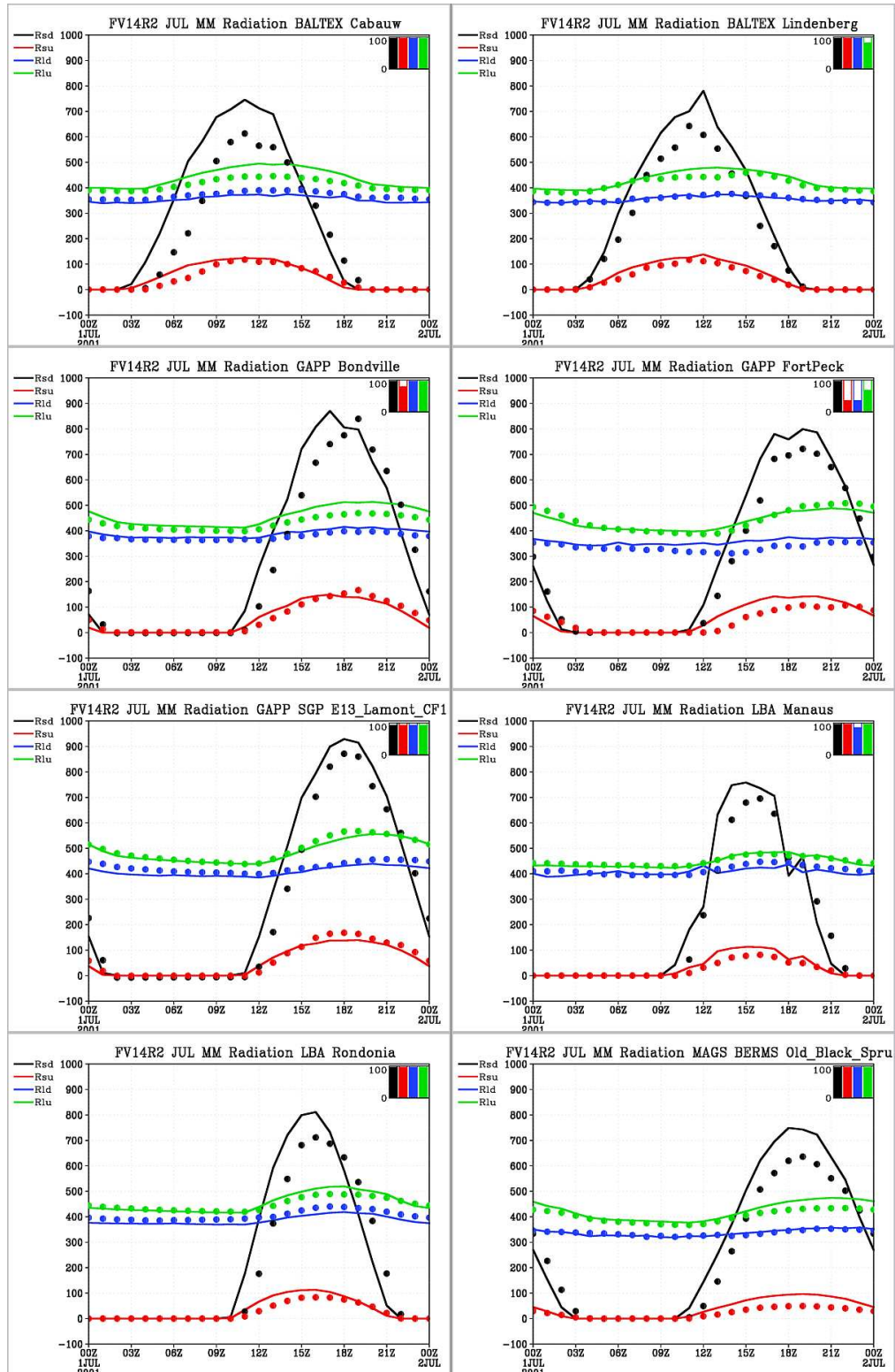
Figure 5.12: Mean diurnal cycle of radiation components at the surface from in situ references sites and the nearest model grid point: downward shortwave (black); upward shortwave (red); downward longwave (blue); and upward longwave (green). Color bars indicate the percentage of available observations during the month. (Units Wm^{-2})
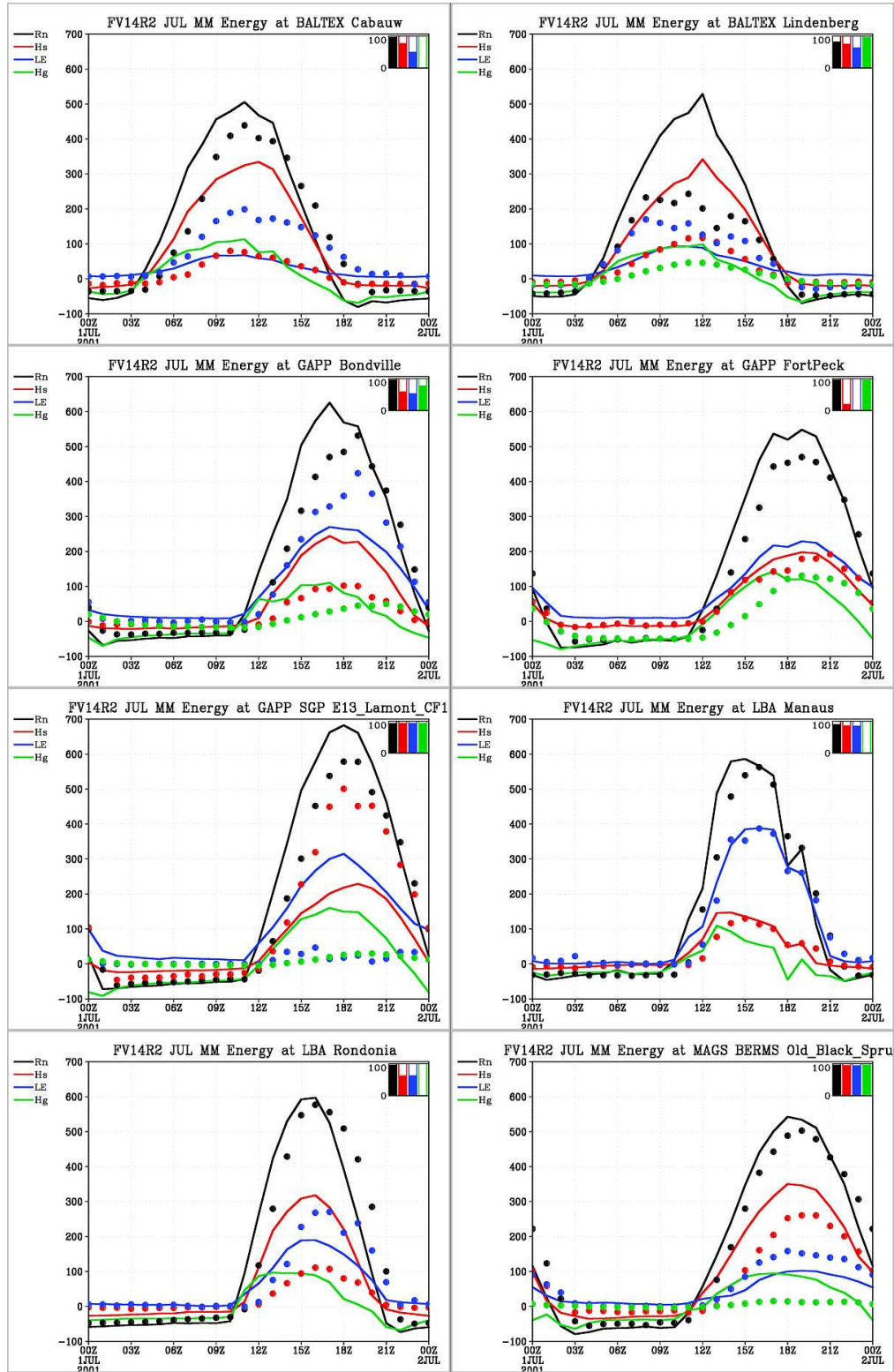
Figure 5.13: As in Figure 5.12, except for the surface energy flux components: net radiation (black); turbulent heat flux (red); turbulent flux of latent heat (blue); and heat flux from ground (red).

5.3 Stratospheric Circulation

The Stratospheric circulations of GEOS-4.0.2 and GEOS-4.0.3 were compared, with an emphasis on those derived variables that are important indicators for realistic transport. The following discussion examines:

- latitude-height cross sections of zonal-mean temperatures

- latitude-height cross sections of zonal-mean zonal wind

- the relation between the meridional gradient of vorticity and zonal wind

- equivalent length

- rates of isentropic transport

- the residual circulation

- the difference between 6-hourly instantaneous background winds and 6-hrly averaged diagnostic winds.

Since most of the variables examined are indicators of global-scale processes that are not observed directly, there are no independent observations available for the validation process. In this situation the validation process then becomes an exercise in the subjective evaluation of features and behaviors in analysis fields.

5.3.1 Temperature and Zonal Wind

Figure 5.14 shows the monthly averages of zonal mean temperature and zonal wind between 1000 hPa and 0.2 hPa for 2001 (Figure 5.14a) and 2003 (Figure 5.14b). The shaded areas in this figure identify regions of temperatures lower than 210 K, negative values in the zonal wind and negative differences. The global structures of temperature and wind are very similar in the two systems. In January 2001, apart from the equatorial lower Stratosphere near 50 hPa, and the summer polar region near 100 hPa, the temperature differences are small below 10 hPa. Above 10 hPa, the differences in temperature generally increase with height, with the largest values occurring in the winter extratropics. At the top of the domain, the temperature differences show a pronounced meridional pattern with alternating colder and warmer regions. The zonal wind differences behave similarly to the temperature differences in that they are relatively small below 10 hPa. Between 10 hPa and 1 hPa, the tropical winds in GEOS-4.0.3 are much more easterly compared to those in GEOS-4.0.2, with a difference of 20 $m\ s^{-1}$ at the equator. Large differences between the wind fields can also be found above 1 hPa. Since there are no wind observations above 10 hPa, these differences could likely due to changes in the wind-mass relationship introduced into GEOS-4.0.3.

In August 2003, both the temperature and zonal wind exhibit large differences above 2 hPa. In contrast to January 2001, the GEOS-4.0.3 temperatures above 2 hPa are warmer than those in GEOS-4.0.2 for all latitudes, with the exception of the polar area near 0.3 hPa. The meridional pattern of the August 2003 differences in zonal wind is similar to
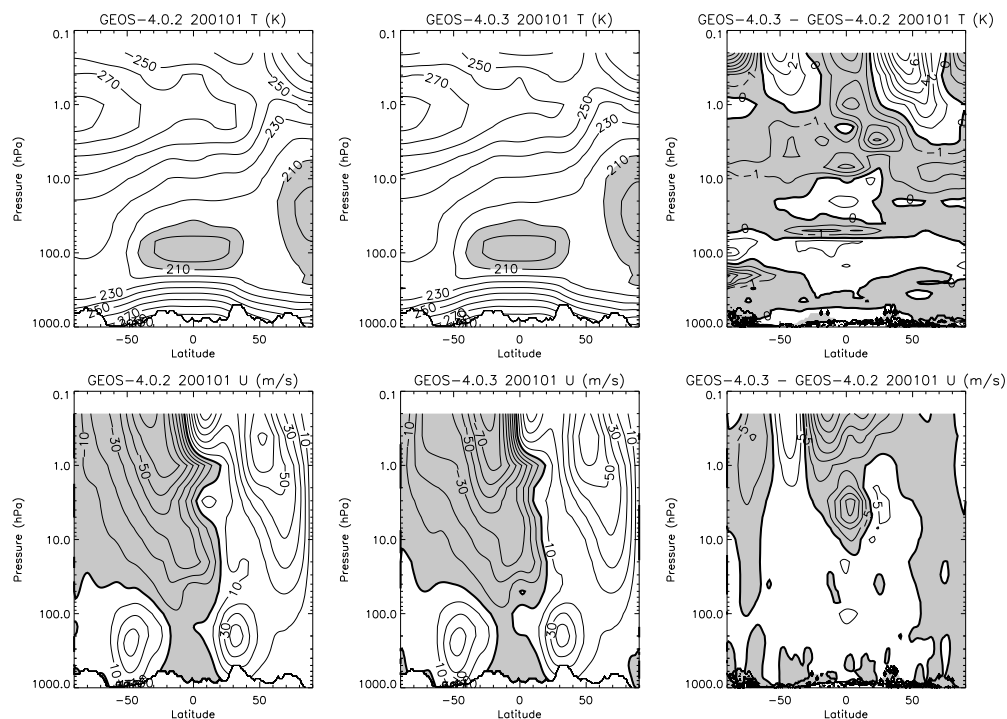
Figure 5.14: (a) Monthly average of zonal mean temperature and zonal wind for January 2001. The last panel in each row shows the difference between GEOS-4.0.2 and GEOS-4.0.3.
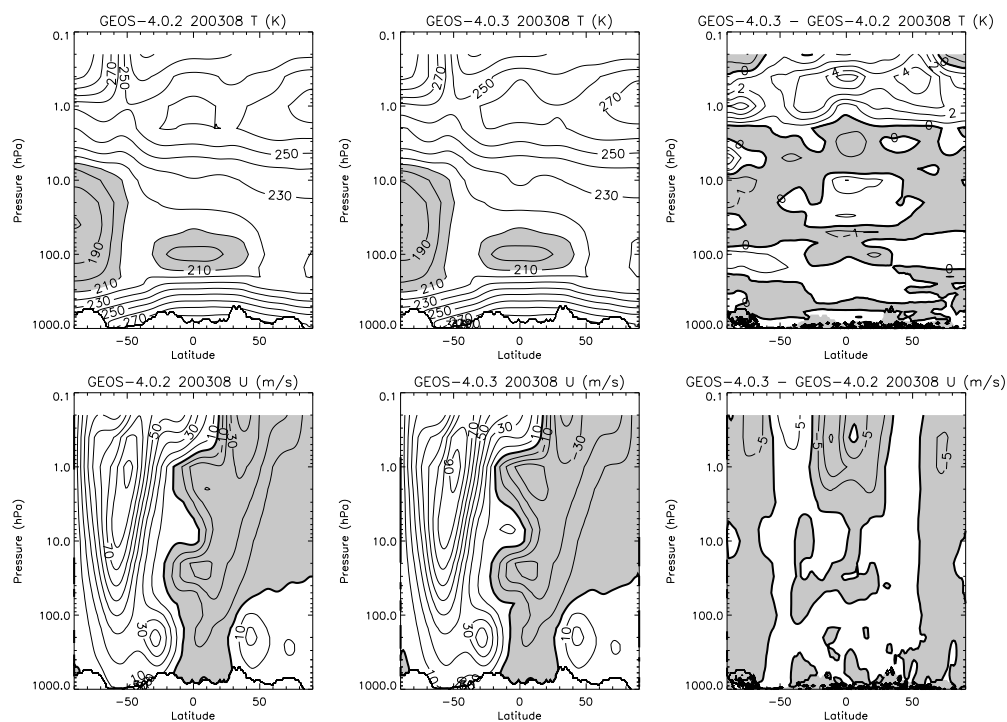

Figure 5.14: (b) Monthly average of zonal mean temperature and zonal wind for August 2003.
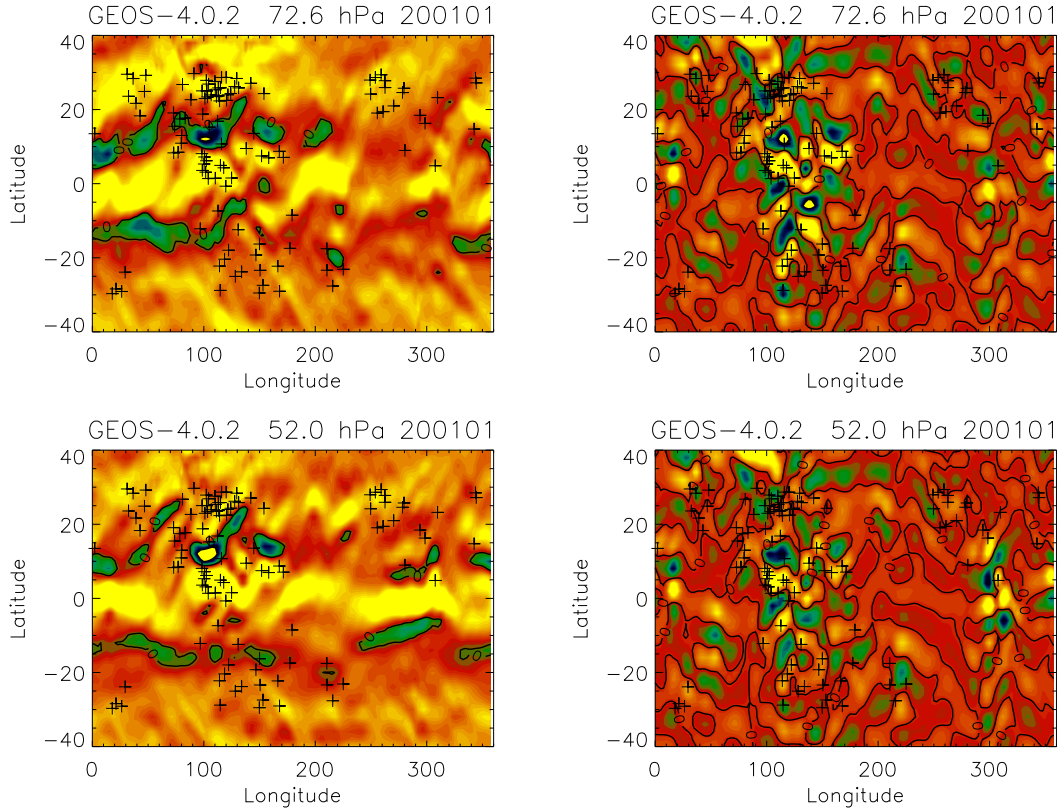
Figure 5.15: (a) GEOS-4.0.2 meridional gradients of vorticity (left panels) and vorticity increments calculated from the analysis increments of the wind fields (right panel) at 72hPa and 52hPa. Negative values are depicted in shades of green and blue bounded by the zero contours. Crosses indicate the locations of the sonde stations.

January 2001, apart from the top of the domain in the northern high latitudes. However, the magnitude of the August 2003 differences is smaller than that in January 2001.

Since the top analysis level is at 0.4 hPa, it is not surprising that the largest differences are found above 1 hPa. With no constraint from observations, two runs could drift apart significantly at the top levels of the model.

5.3.2 Vorticity and Winds

Previous studies have found that in certain cases, analysis increments in the wind fields could generate regions with a negative vorticity gradient in the subtropics. These unstable regions lead to excessive subtropical transport and mixing in comparison to results obtained from running the GCM in simulation mode (Tan *et al.*, 2004). Figure 5.15 shows the meridional gradients of vorticity (left panels) and vorticity increments calculated from the analysis increments of the wind fields (right panels). The plots of meridional gradient of vorticity are at 72 hPa and 52 hPa, and depict negative values in shades of green and blue bounded by the zero contours. The corresponding panels for the meridional gradient of vorticity increments use the same color scheme; crosses indicate the locations of the sonde stations.
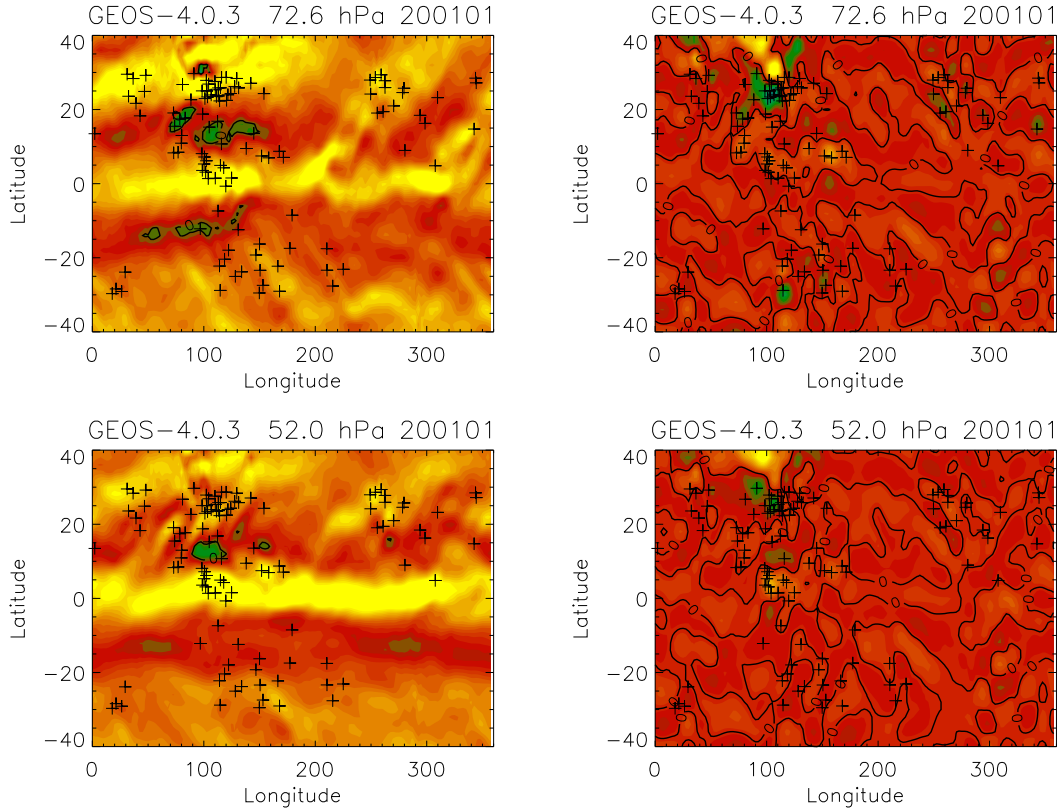
Figure 5.15: (b) Same as (a) but for GEOS-4.0.3.

Note that the subtropics in GEOS-4.0.2 are replete with patches of negative vorticity gradients. Close examination shows that some of these regions directly mirror similar structures in the meridional gradient of the vorticity analysis increments. In GEOS-4.0.3, the magnitudes of the analysis increments are greatly reduced compared to those in GEOS-4.0.2, and there is a corresponding reduction in regions with negative vorticity gradient. As a result of the reduction in these unstable regions, subtropical transport and mixing are less excessive in GEOS-4.0.3, as shown in a following subsection.

5.3.3   Equivalent Length

Equivalent length and effective diffusivity are measures of isentropic transport and mixing (*e.g.* Nakamura, 1995). In regions where transport and mixing are inhibited, the isopleths of potential vorticity (PV) or a long-lived constituent field are relatively undisturbed or stretched. On the other hand, in regions where transport is strong, the isopleths will be stretched and folded into complex shapes, with abundant filamentary structures. A suitably defined metric based on the gradient and geometry of these isopleths can be used to compare isentropic transport and mixing between two systems. Equivalent length calculated using PV on theta surfaces is one such metric. Figure 5.16 shows the equivalent length for January 2001 and August 2003. The ordinate is potential temperature and the abscissa is equivalent latitude. The calculations were performed on the 450 K, 550 K, 700 K, 850 K, and 1000 K theta surfaces. This selection encompasses pressure levels from 70 hPa to
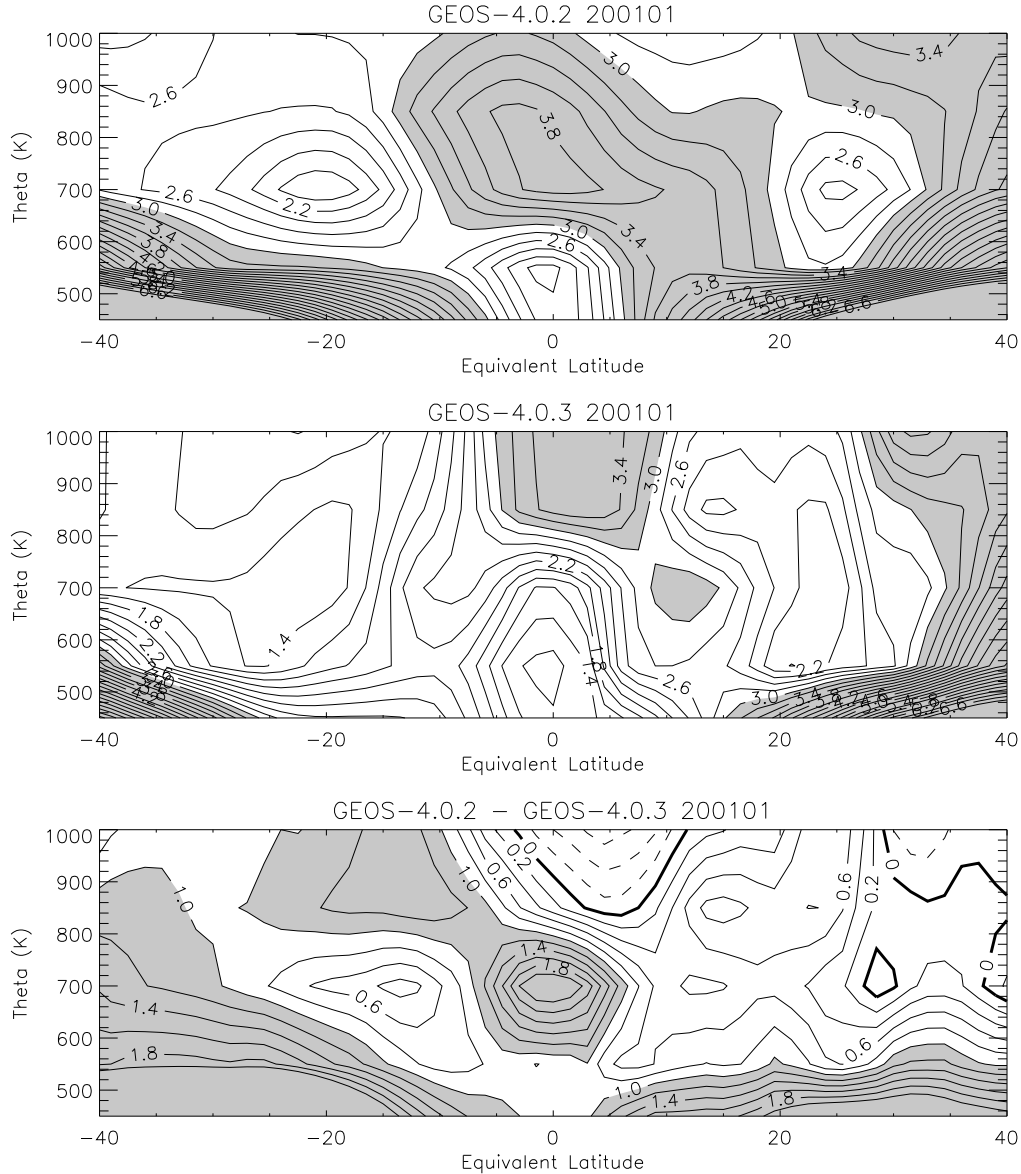
Figure 5.16: (a) Equivalent length for January 2001. In the top two panels, values larger than 3 are shaded. Bottom panel shows the difference between GEOS-4.0.2 and GEOS-4.0.3, with values larger than 1 shaded and negative values depicted with dashed contours.

7 hPa in the Tropics. A value of one indicates that an isopleth is completely undisturbed, with effective length equals to the length of the equivalent latitude circle. In the top two panels, contours with values larger than 3 shaded. The bottom panel shows the difference between GEOS-4.0.2 and GEOS-4.0.3, with values greater than 1 shaded and negative values depicted with dashed contours.

For January 2001, the two data sets exhibit similar structures. Around the Equator, a minimum extends from the bottom of the domain to around 700 K while a maximum can be found in the top half of the domain. In the subtropics of both hemispheres, there is a minimum near 20°, extending from 550 K to the top of the domain. In comparison to
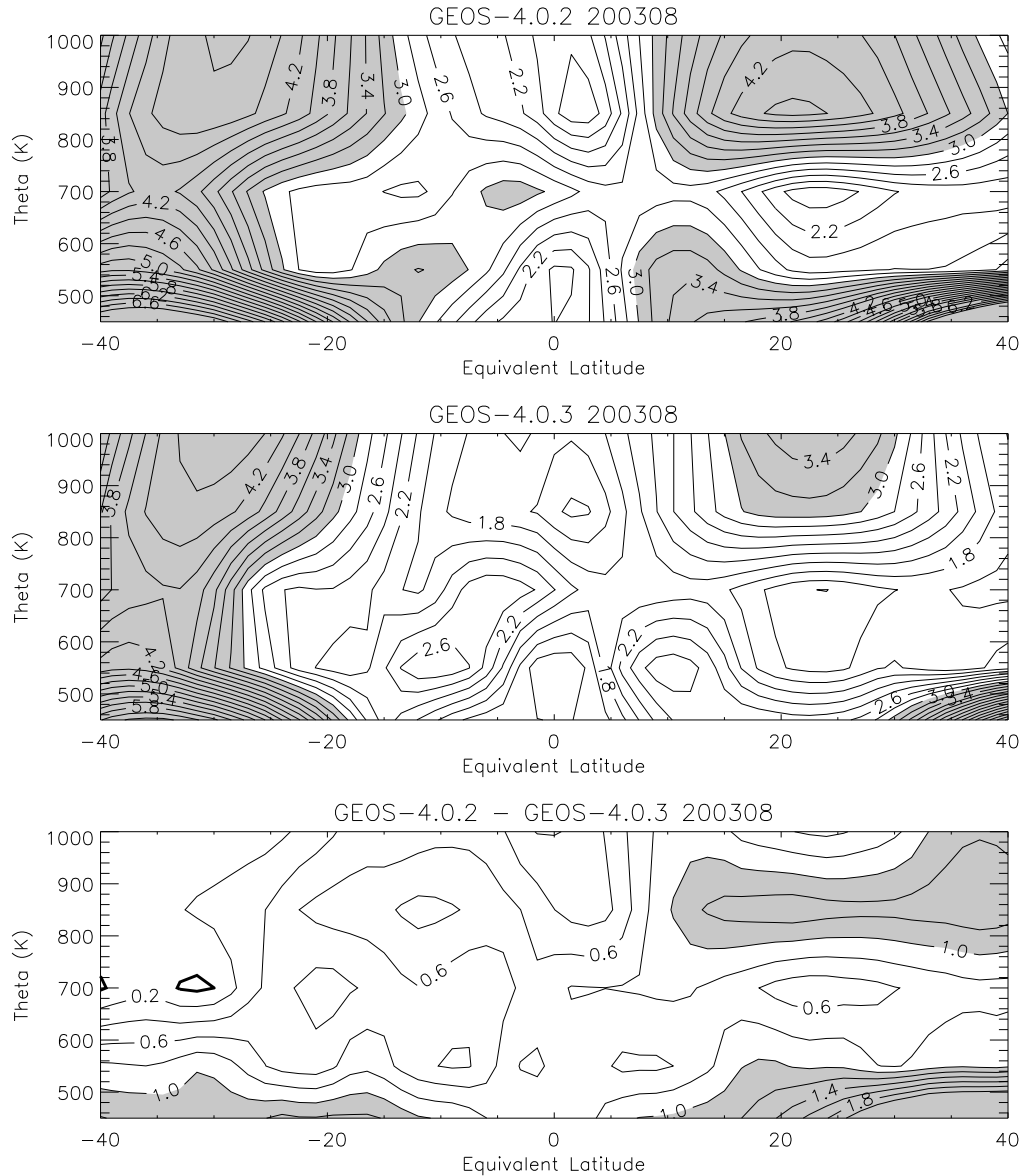
Figure 5.16: (b) Same as (a) but for August 2003.

GEOS-4.0.2, the minima in GEOS-4.0.3 are more elongated in the vertical direction. While the basic features are similar, the amplitudes are generally much larger in GEOS- 4.0.2, except above 800 K in the northern Tropics and midlatitudes.

For August 2003, a minimum extends from the bottom to the top of the domain at the equator. There is a minimum at around 20°N, below 700 K. In the Southern Hemisphere, there is a minimum near 20°S at 550 K. It tilts toward the equator and extends upward to 700 K. The overall features in the two systems are similar, again with the amplitudes being larger in GEOS-4.0.2 nearly everywhere.

For both time periods, these results show that isentropic stirring is more vigorous in the Subtropics of GEOS-4.0.2. This is in general agreement with the result of unstable regions

shown in the previous section and the calculations of the rates of isentropic transport described in the following subsection.

5.3.4   Rates of Isentropic Transport

The rates of isentropic transport were examined using the trajectory method. On the 11th, 21st, and 31st day of the month, a group of parcels were initialized on a $0.5° \times 0.5°$ grid between 30°S and 30°N, on the 450 K, 550 K, 700 K, 850 K, and 1000 K isentropes. These parcels were advected backward for 10 days using horizontal winds interpolated to the isentropes. The ratio of parcels within a latitude band around the equator that came from higher latitudes 10 days before the initialization was defined as the entrainment rate. In our calculations, the equatorial band was defined between 10°S and 10°N. Parcels that came from locations 10°S poleward of each boundary were counted as entrained into the band from higher latitudes. Note that a more rigorous calculation should define the subtropical transport barrier or a proxy of the subtropical transport barrier, and use that as the reference latitude to set the band boundaries. However, a simple definition as described above is adequate to provide a means to compare isentropic transport and mixing in the subtropics.

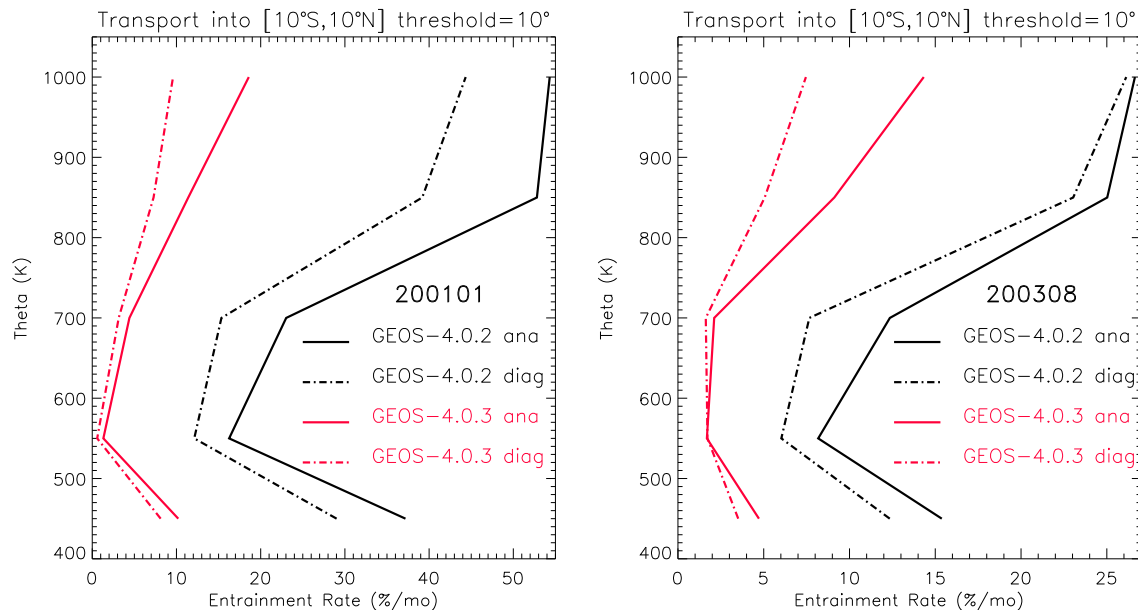Figure 5.17 shows the monthly rates of isentropic transport obtained by summing the

Figure 5.17: Monthly rates of isentropic transport. Black solid curve depicts GEOS- 4.0.2 entrainment rates calculated using 6-hrly instantaneous analyzed winds and black dash-dotted curve depicts GEOS-4.0.2 entrainment rates calculated using 6-hrly averaged diagnostic winds. Corresponding red curves show the entrainment rates for GEOS-4.0.3. Left panel January 2001; Right panel August 2003.

results of three 10-day calculations. Black solid curve depicts GEOS-4.0.2 entrainment rates calculated using 6-hourly instantaneous analyzed winds and black dash-dotted curve depicts GEOS-4.0.2 entrainment rates calculated using 6-hourly averaged diagnostic winds. The corresponding red curves show the entrainment rates for GEOS-4.0.3. In both January 2001 and August 2003, the rates in GEOS-4.0.2 are much larger than those in GEOS-4.0.3. In all cases, the minima of the rates are located at 550 K. When a threshold value of $20°$ was used, the entrainment rates reduced vastly in all cases, showing that a large percentage of the entrained parcels came from within the subtropics. In other words, mixing occurred mainly within the same dynamical zone. Nevertheless, the rates in GEOS-4.0.2 remain significantly larger than those in GEOS-4.0.3 even when larger thresholds are used.

A comparison of the solid and dash-dotted curves in Figure 5.17 shows that the use of 6-hourly averaged diagnostic winds reduces the entrainment rate by up to 40% over that obtained by using the 6-hourly instantaneous analyzed winds. These results are consistent with the equivalent length results presented above. The vast reduction in entrainment rates in GEOS-4.0.3 is related to the reduction in the unstable regions with negative meridional gradient of vorticity.

5.3.5   The Residual Circulation

The known climatology of the vertical residual velocity of the middle atmosphere in the solstices exhibits a simple structure, with upwelling in the tropics and most of the summer hemisphere, and downwelling in the summer high latitudes below the stratopause and in the winter hemisphere. Monthly mean vertical residual velocity calculated from GEOS-4.0.2 analyses exhibits a similar structure, with some small cells of anomalies scattered around. In contrast, the results in GEOS-4.0.3 exhibit a very fragmented structure, with a string of alternating upwelling and downwelling cells extending from the stratosphere to the top levels of the data set.

Figure 5.18 shows the vertical residual velocity in January 2001 and August 2003. The fragmented structures in GEOS-4.0.3 arise mainly from similar structures in the zonal mean vertical velocity field, which is in turn a result of large gradient in the meridional wind. When wind fields plagued with such structures are used in offline transport models or in offline ozone assimilations, spurious transport result, leading to very noisy constituent fields.

Further investigations showed that changes in the observation error covariance of the decoupled wind below 150hPa are the main source of these structures while changes in the wind-mass relationship are the secondary source. This is not surprising since these are the two main mechanisms that account for the zeroth order changes in the wind analysis. Works done using an intermediate version of the assimilation system that has the same error covariance statistics with GEOS-4.0.3 showed that meridional wind fields in the stratosphere are replete with noise with 6-hrly period. When 6-hrly averaged diagnostic winds are used to calculate the residual circulation, the multiple-cell structures in GEOS- 4.0.3 vanish. The results become almost identical with GEOS-4.0.2 results calculated using diagnostic winds. This is shown in Figure 5.19. In fact, when 6-hrly averaged diagnostic winds are used in offline transport model or in ozone assimilation, the results are significantly better than those using 6-hrly instantaneous winds.
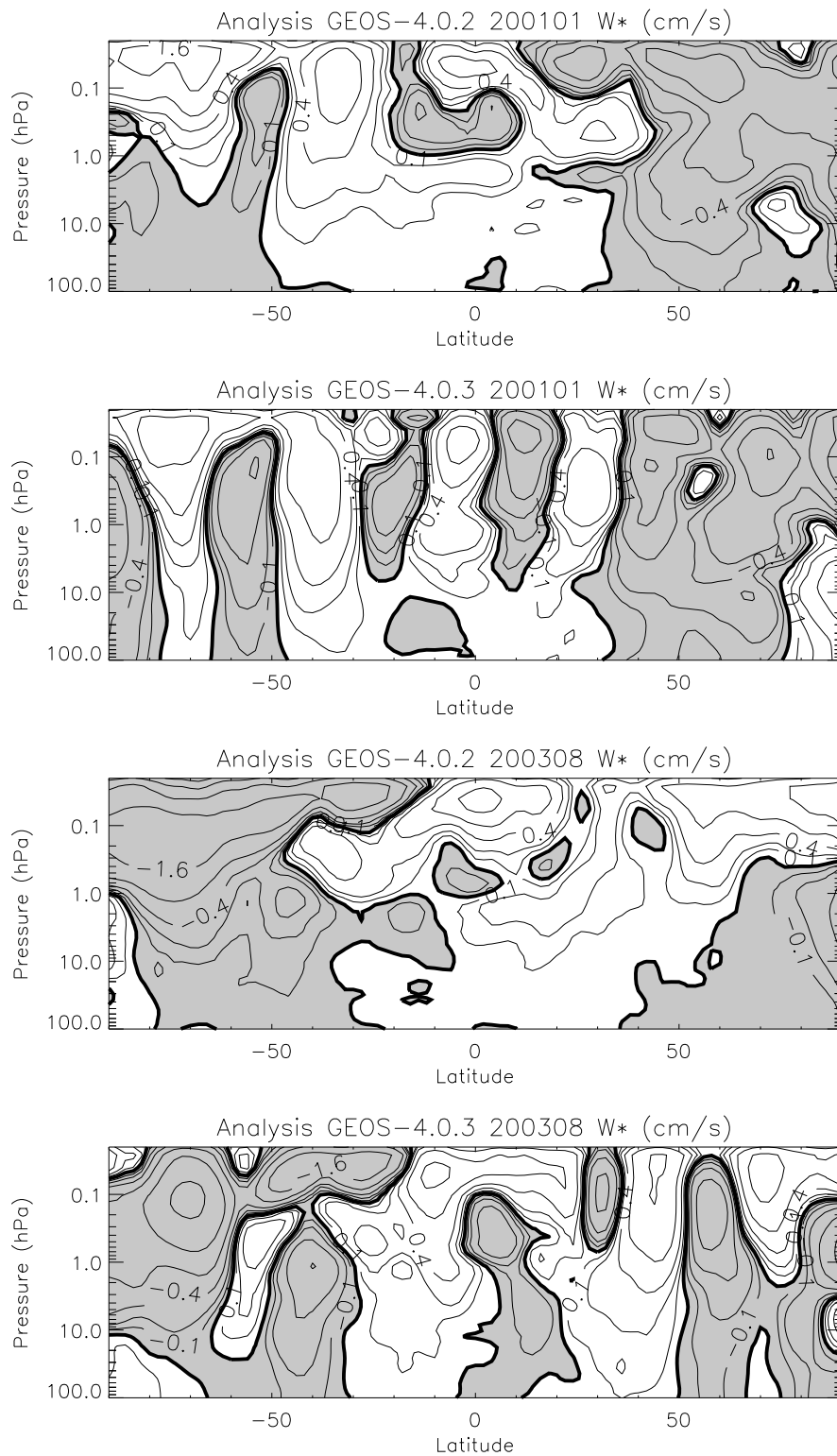
Figure 5.18: Vertical residual velocity in January 2001 and August 2003 calculated using 6-hourly instantaneous analyzed winds.
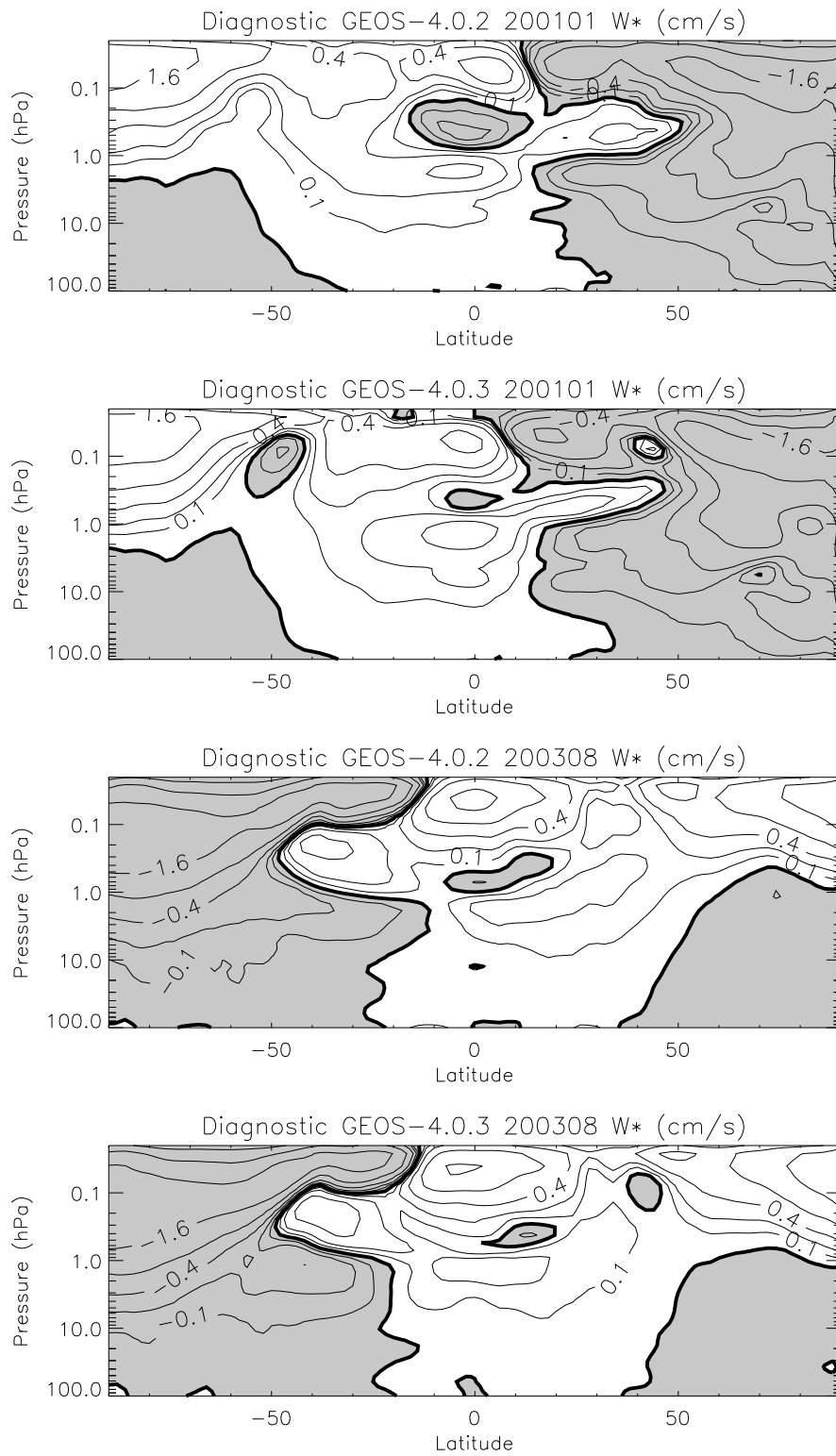
Figure 5.19: Vertical residual velocity in January 2001 and August 2003 calculated using 6-hourly averaged diagnostic winds.

5.3.6 Summary

The basic structures in the zonal mean temperature and zonal wind fields are similar between GEOS-4.0.2 and GEOS-4.0.3. Large differences can be found in the upper domain of the system, where no data was assimilated. GEOS-4.0.2 exhibits very large rates of isentropic transport and mixing. This is rectified in GEOS-4.0.3. The reduction in excessive isentropic transport is related to a decrease in unstable regions, which is a result of relatively small analysis increments of the wind fields in GEOS-4.0.3.

The instantaneous winds in GEOS-4.0.3 contain excessive noise that results in multiple-cell structures in the vertical residual velocity. Using these instantaneous winds in offline transport calculations lead to spurious structures in the constituent fields. The transport behavior was greatly improved with the use of 6-hour averages of the GEOS-4.0.3 winds, with these the noise was significantly reduced. Results from total column ozone assimilation show that realistic features can indeed be obtained using 6-hourly averaged GEOS-4.0.3 diagnostic winds.

5.4   Ozone Validation

The ozone assimilation system developed at GMAO, along with a parameterized ozone chemistry and transport model were used to evaluate the quality of GEOS-4 assimilated winds. The 6-hourly wind averages from GEOS-4.0.3 performed well. However, *instantaneous* 6-hourly forecast winds from GEOS-4.0.3 had undesirable features for the transport of ozone in the Stratosphere, and they are not recommended for use to drive chemistry and transport models (CTMs).

Assimilated ozone in GEOS-4.0.3 was evaluated using O-F statistics and comparisons with independent high quality observations. Improvements over GEOS-4.0.2 ozone product are seen mainly at pressure levels between 20 and 70 hPa globally, and in the total ozone columns in the Tropics. The key to these improvements is the use of 6-hourly wind averages to drive the transport in the GEOS-4.0.3 ozone assimilation system.

5.4.1   Background

The GMAO ozone assimilation system (Riishøjgaard *et al.*, 2000; Stajner *et al.*, 2001) includes a global three-dimensional parameterized chemistry and transport model (CTM). The transport uses a flux-form semi-Lagrangian advection scheme by Lin and Rood (1996). The chemistry scheme uses parameterized ozone production and loss rates (Fleming *et al.*2001), where production rates were adjusted so that the quotient of production and loss rates in the upper stratosphere agrees with an ozone climatology constructed by Langematz (2000). Total column ozone data from the Total Ozone Mapping Spectrometer (TOMS) (McPeters *et al.*, 1998) and Stratospheric ozone profiles from the NOAA 14 Solar Backscatter Ultraviolet/2 (SBUV/2) instrument (Bhartia *et al.*, 1996) are assimilated during the validation period in year 2000. The configuration that is run in near real-time since January 15, 2004 uses NOAA 16 SBUV/2 total ozone column and stratospheric ozone profiles. This system was used successfully for monitoring of satellite ozone data characteristics (Stajner *et al.*, 2004).

The ozone assimilation system provides a convenient in-house tool for evaluation of stratospheric winds produced by the GMAO. The main metric used in this evaluation is the size of the ozone observed-minus-forecast (O-F) residuals, *i.e.* the differences between incoming ozone observations and the short-term CTM forecast. Smaller ozone O-F residuals imply a better agreement between the model forecast and the incoming observations. In the lower stratosphere chemical processes are slow, and the transport processes are the dominant cause of the ozone variability. Most of the total ozone column is contained in the lower stratosphere. Thus, total ozone column O-F residual statistics is used as the primary metric for the evaluation of the wind quality in the lower Stratosphere.

5.4.2   Evaluation of Instantaneous 6-hourly Forecast Winds

Two CTM ozone simulations of several months duration were driven by instantaneous 6-hourly forecast winds taken from GEOS-4.0.2 and GEOS-4.0.3. The winds used in these runs were taken from the model-level output files in order to minimize vertical interpolation. The total column ozone fields are shown in Figure 5.20. In comparison with the TOMS data both
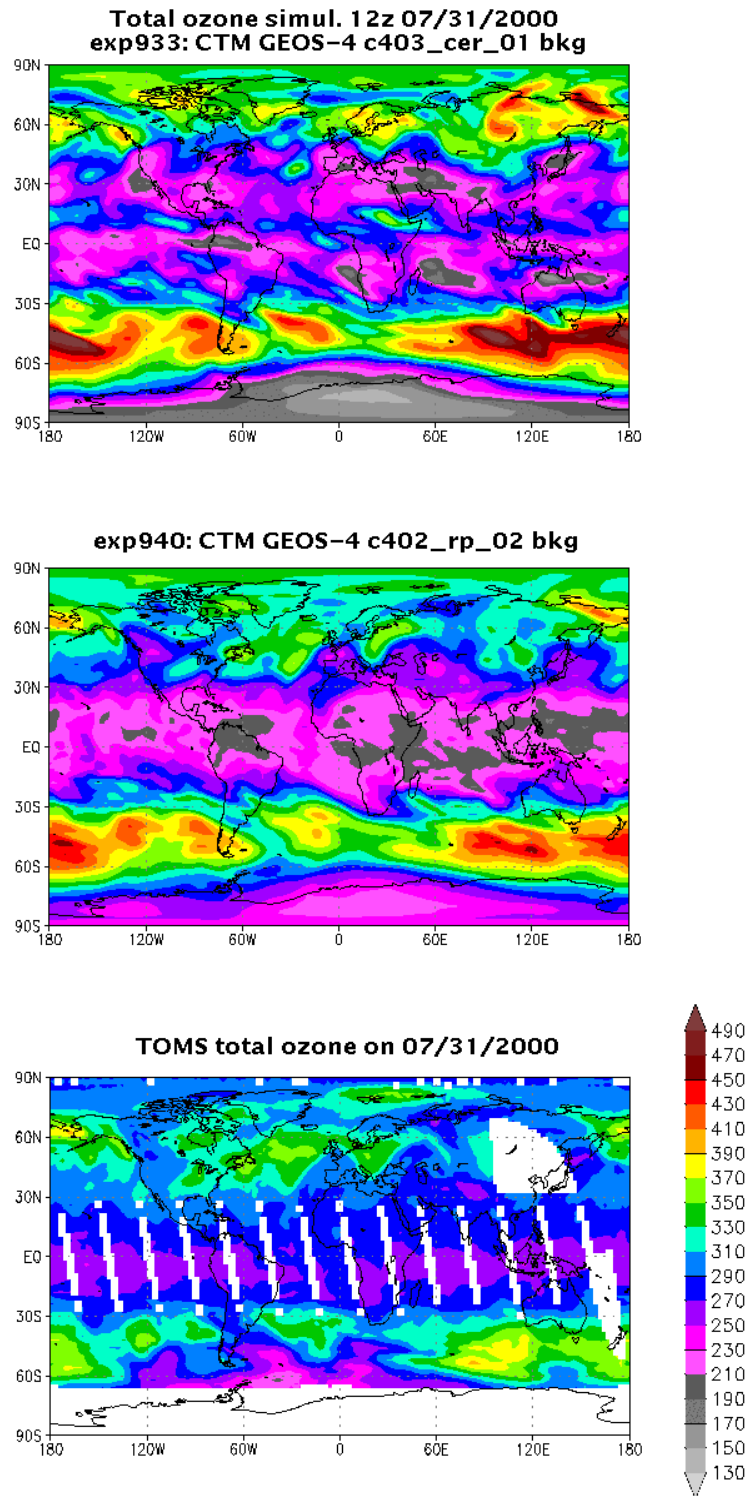
Figure 5.20: Total column ozone fields at 12z on July 31, 2000 are shown (in DU) for two CTM simulations that were driven by 6-hourly forecast winds from GEOS-4.0.3 (top), GEOS-4.0.2 (middle). Independent TOMS total ozone column data are shown in the bottom panel. Latitudinal biases are seen in both simulations, but they are larger for GEOS-4.0.3.
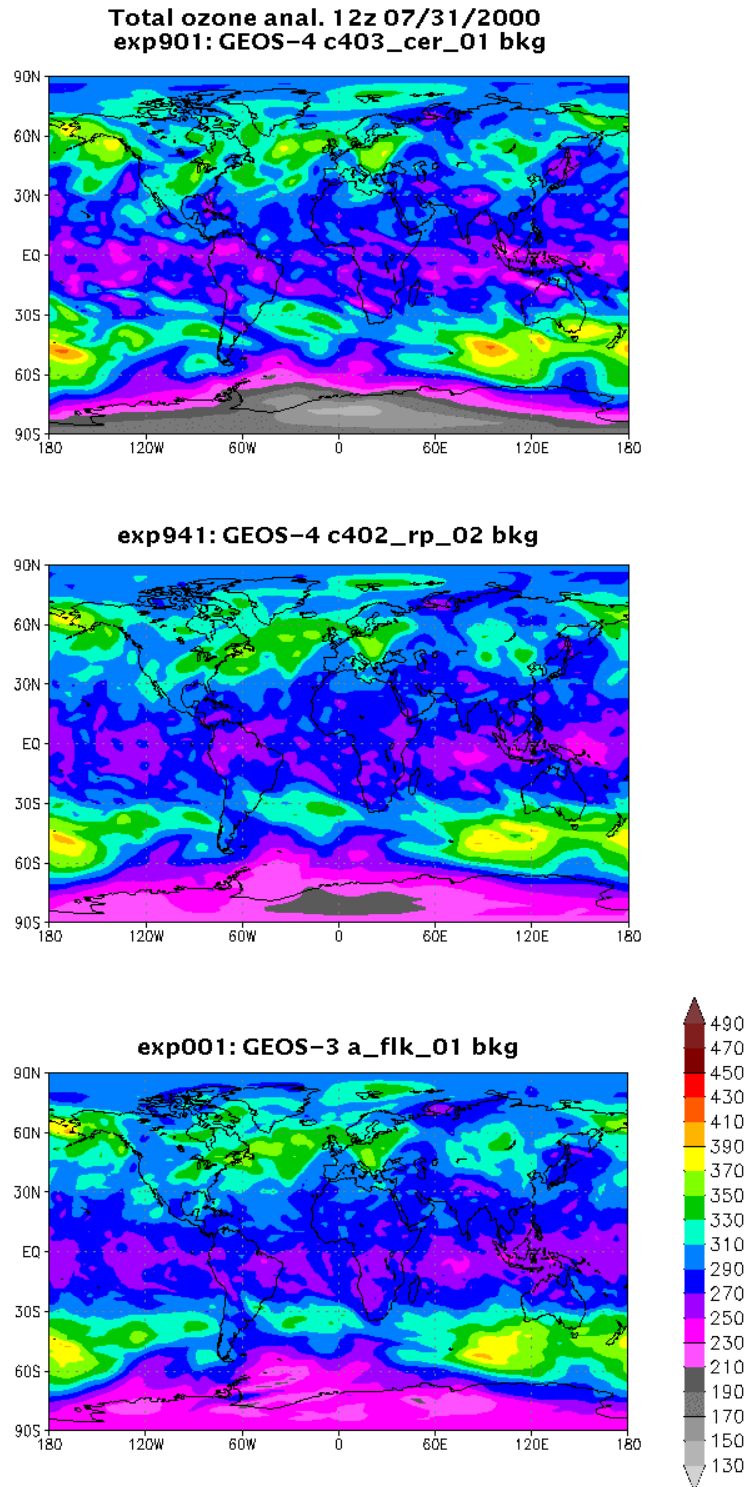
Figure 5.21: Total column ozone fields at 12z on July 31, 2000 are shown (in DU) for three ozone assimilation experiments that were driven by 6-hourly forecast winds from GEOS-4.0.3 (top), GEOS-4.0.2 (middle) and GEOS 3 (bottom). In all three figures there is excessive variability in the tropical total ozone column, and it is the largest for GEOS-4.0.3.
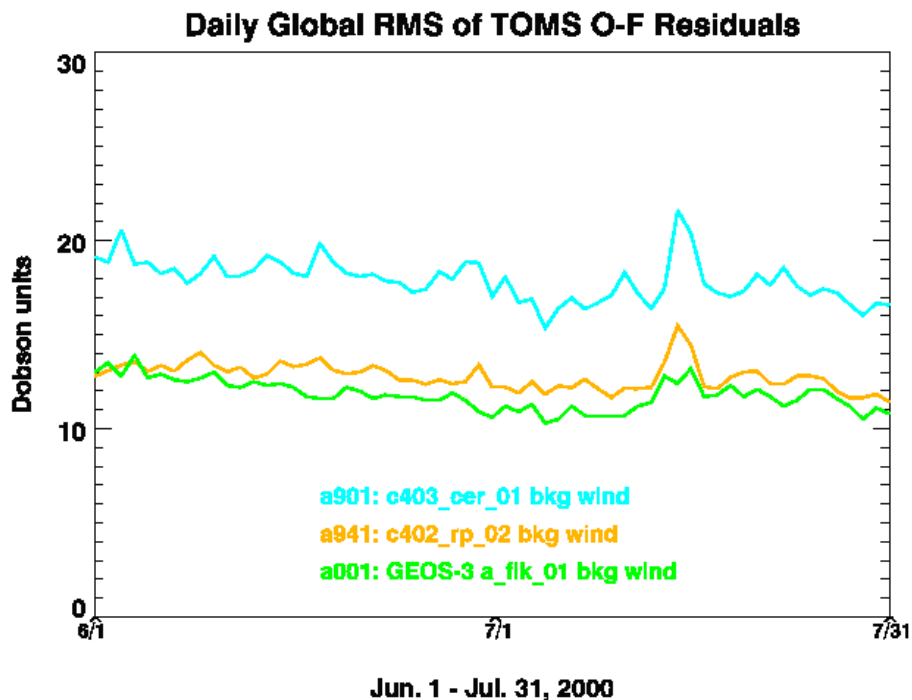
Daily Global RMS of TOMS O-F Residuals

Figure 5.22: Time series of daily global root-mean-square of the total column O-F residuals for TOMS data are shown for three ozone assimilation experiments driven by instantaneous 6-hourly forecast of the winds from GEOS-4.0.3 (cyan), GEOS-4.0.2 (orange), and GEOS-3 (green).

exhibit too low ozone in the Tropics and too high ozone in the middle latitudes, especially in the Southern (winter) Hemisphere. This slowly developing latitudinal bias in the total ozone is often seen in CTMs due to an excessive residual circulation that transports air from the Tropical Stratosphere upward and towards the winter midlatitudes. The disagreements between GEOS-4.0.3 and TOMS are larger. The latitudinal bias is stronger. There are two belts of low total ozone in GEOS-4.0.3: around the equator and near 30°N. Only one low-ozone belt is seen in the TOMS data, somewhat south of the Equator.

5.4.3   Evaluation of 6-hourly Averages of Winds

Ozone assimilation experiments driven by instantaneous 6-hourly forecast winds were performed using GEOS-4.0.3 and GEOS-4.0.2 winds and compared with those driven by GEOS-3 winds. Total column ozone fields from these experiments are shown in Figure 5.21. All three fields can be compared with TOMS total columns in Figure 5.20. Assimilated ozone fields are constrained by the TOMS and SBUV data, which prevent development of large latitudinal biases like those in CTM fields in Figure 5.20. Thus, the properties of the transport can be evaluated on shorter time scales, especially within 24 hours, which is the typical time between two ozone observations over the same location. A qualitative short-coming of 6-hourly forecast winds from GEOS-4.0.3 is seen from the excessive variability in the tropical total ozone at small spatial scales. Even though this problem is seen with GEOS-4.0.2 and GEOS-3 winds, it is manifested more strongly with GEOS-4.0.3 winds. A
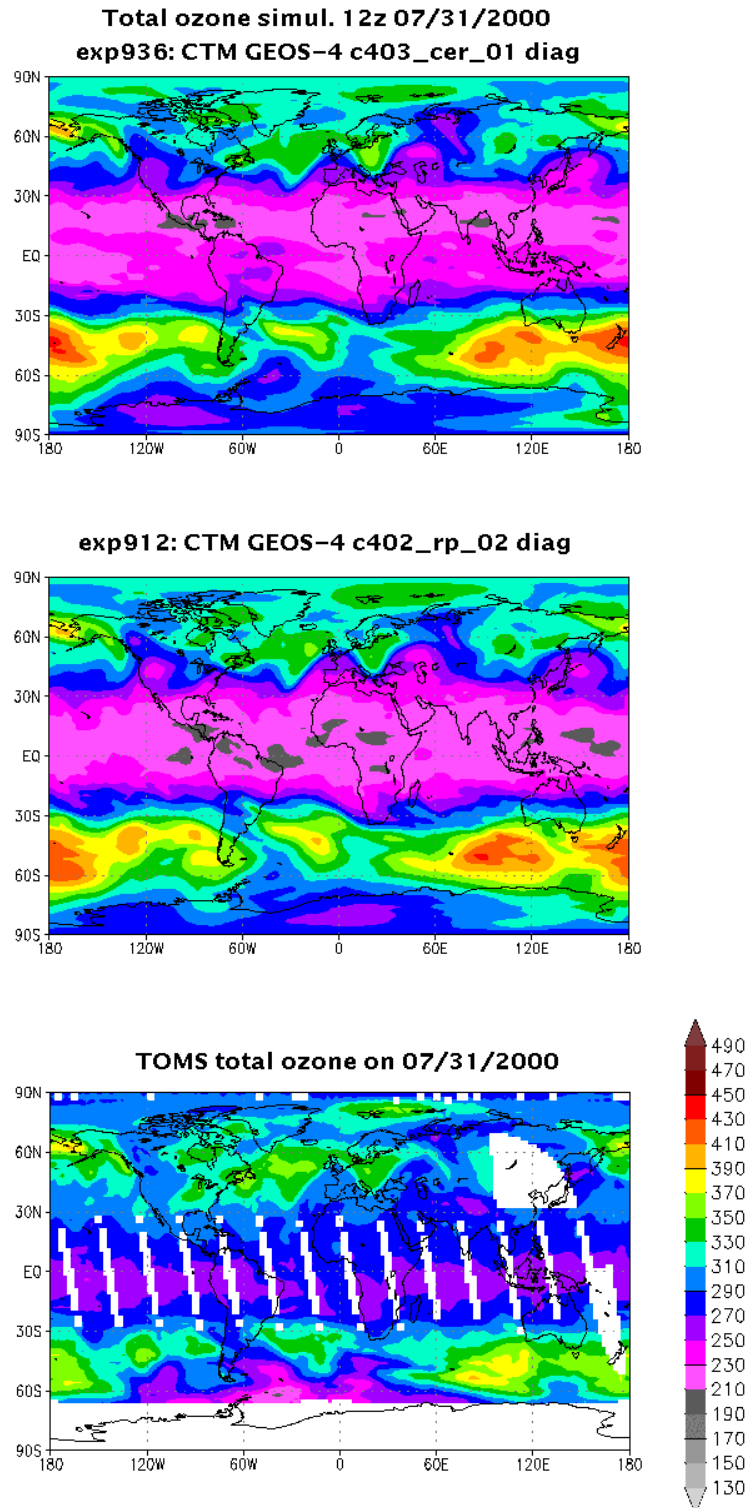
Figure 5.23: Total column ozone fields at 12z on July 31, 2000 are shown (in DU) for two CTM simulations that were driven by 6-hourly averages of the winds from GEOS-4.0.3 (top), GEOS-4.0.2 (middle). Independent TOMS total ozone column data are shown in the bottom panel.
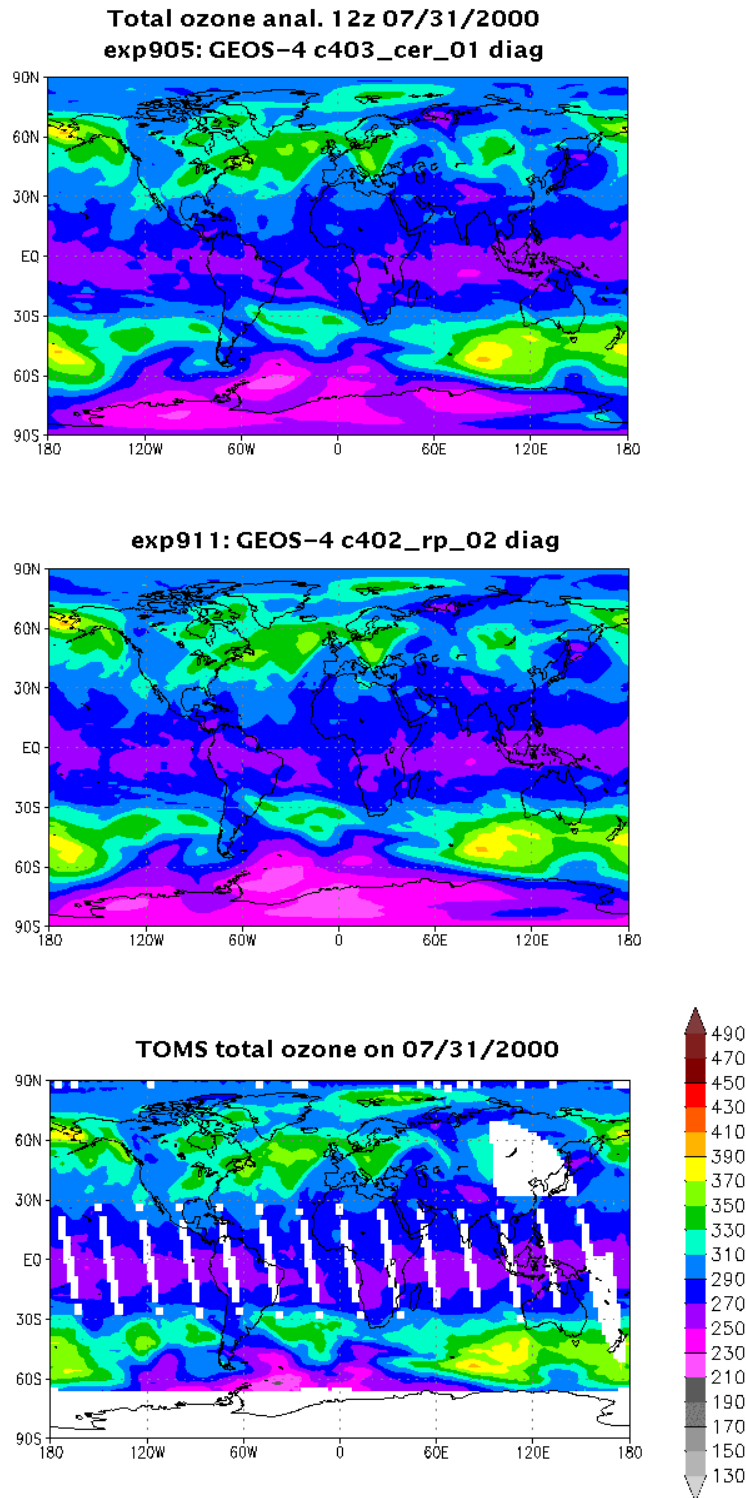
Figure 5.24: Total column ozone fields at 12z on July 31, 2000 are shown (in DU) for two ozone assimilation experiment s that were driven by 6-hourly averages of the winds from GEOS-4.0.3 (top), GEOS-4.0.2 (middle). Independent TOMS total ozone column data are shown in the bottom panel.
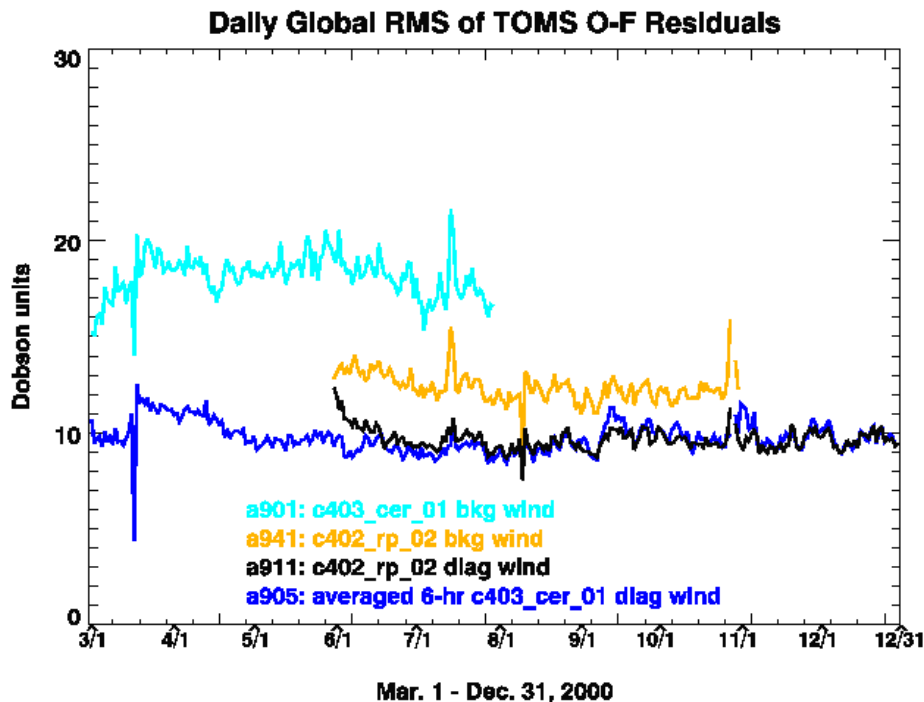
Figure 5.25: Time series of daily global root-mean-square of the total column O-F residuals for TOMS data are shown for three ozone assimilation experiments driven by 6-hourly averages of the winds from GEOS-4.0.3 (blue), GEOS-4.0.2 (black). For reference the same quantities are shown for experiments driven by instantaneous 6-hourly forecast winds GEOS-4.0.3 (cyan), GEOS-4.0.2 (orange).

quantitative measure of the quality of 6-hourly forecasts from three systems is seen in Figure 5.22, where time series of daily global RMS of TOMS total ozone column O-F residuals are shown for June and July 2000. These residuals average about 12 Dobson units (DU) for GEOS-3, about 13 DU for GEOS-4.0.2, and about 18 DU for GEOS-4.0.3. These results indicate that the instantaneous 6-hourly forecast winds from GEOS-4.0.3 are not suitable for driving CTMs or for ozone assimilation.

The above experiments were repeated using time averages of winds centered at the synoptic times (0, 6, 12, and 18Z) to drive the CTM and the ozone assimilation system. The averaging intervals were 6 hours for GEOS-4.0.3 winds and 12 hours for GEOS-4.0.2 winds. After two months of CTM simulations the total ozone fields develop latitudinal biases (Figure 5.23), but they are smaller than with instantaneous winds (Figure 5.20). Qualitatively, the zonal symmetry in the tropical ozone increases, which is also an improvement over the CTM fields in Figure 5.20. However, in the CTM driven by GEOS-4.0.3 winds the belt of lowest total ozone is positioned in the northern Tropics, rather than in the southern Tropics as in TOMS data.

Maps of total column ozone from assimilation experiments driven by time-averaged winds are shown in Figure 5.24. Tropical total ozone from these experiments is less variable and in better qualitative agreement with the TOMS total ozone than the fields in Figure 5.21. A quantitative comparison is shown in Figure 5.25. The daily global RMS of

TOMS O-F residuals is about 10 DU for both GEOS-4.0.3 and GEOS-4.0.2 time averaged winds, which is significantly lower than for the instantaneous 6-hourly forecast winds. An assimilation experiment was also performed, driven by GEOS-4.0.3 winds that were averaged over 12 hours. The longer averaging period resulted in an increased size of total ozone O-F residuals. Thus the use of 6-hourly averages of GEOS-4.0.3 winds for driving CTMs is recommended.

5.4.4 Evaluation of GEOS-4.0.3 Ozone Profiles

The ozone assimilation system in GEOS-4.0.3 (ozone007) includes a CTM driven by 6-hourly averages of winds. In the GEOS-4.0.2 ozone assimilation (ozone005) the transport was driven by instantaneous 6-hourly wind forecasts. Total ozone columns and stratospheric profiles from NOAA 16 SBUV/2 instrument are assimilated in both versions of the system. The GEOS-4.0.3 system became operational on January 15, 2004. This section summarizes the comparisons of parallel runs of GEOS-4.0.3 and GEOS-4.0.2 ozone assimilation for December 2003 and the first half of January 2004. The emphasis is on the quality of ozone profiles that is evaluated through comparison with high quality independent ozone observations.
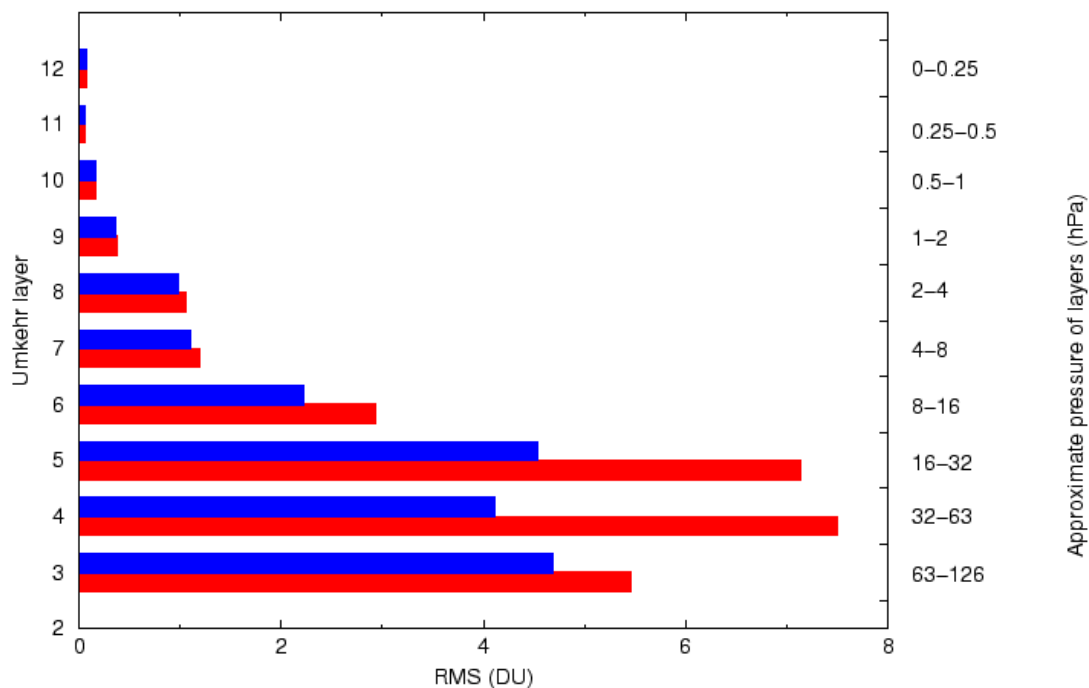

Figure 5.26: The RMS of O-F residuals for stratospheric SBUV layers (Umkehr layers) are shown for GEOS-4.0.2 (red) and GEOS-4.0.3 (blue) ozone assimilation systems. Approximate pressure ranges for the SBUV layers are shown on the right axis. The residuals are for 912 SBUV profiles on December 31, 2003, which is one month after the GEOS-4.0.3 ozone assimilation was initialized.

The RMS of O-F residuals for stratospheric SBUV layers (Umkehr layers) are compared for GEOS-4.0.2 and GEOS-4.0.3 in Figure 5.26. The residuals are from December 31, 2003, which is one month after the GEOS-4.0.3 ozone assimilation was initialized. The O-F residuals for GEOS-4.0.3 have a smaller RMS throughout the Stratosphere (Umkehr layers 3-9) and they are very close to those of GEOS-4.0.2 in the Mesosphere (Umkehr layers 10-12). The largest relative improvement in the O-F residuals that exceeds 30% is seen for layers 4 and 5, *i.e.* between 16 and 64 hPa. This is a region with sharp vertical gradients in ozone, and the quality of ozone fields is sensitive to details of vertical transport. Zonal means of O-F statistics indicate that the largest improvements are near 20°N and 20°S.
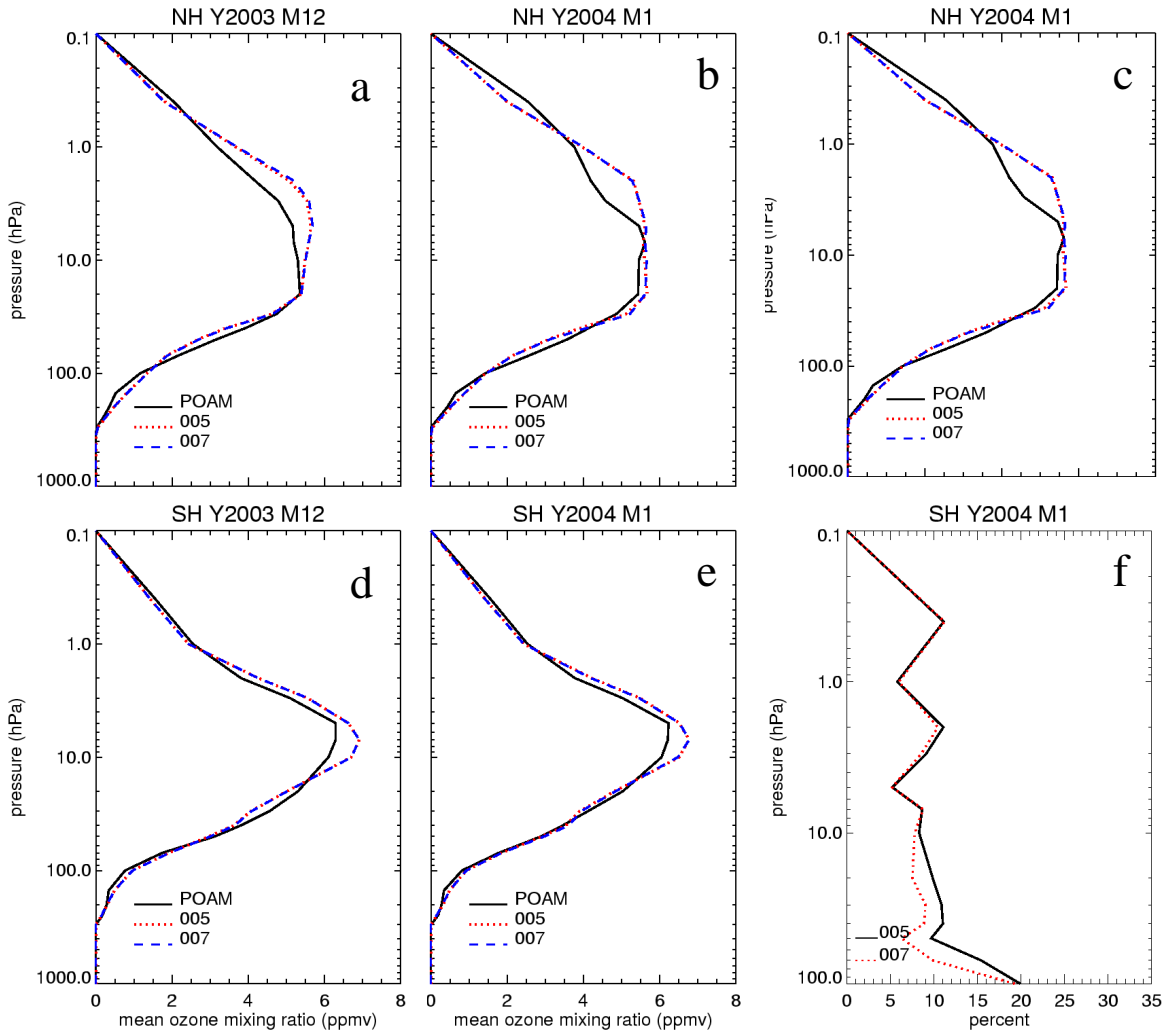

Figure 5.27: Mean POAM profiles (black) are compared with profiles of collocated GMAO ozone analyses from GEOS-4.0.3 (blue) and GEOS-4.0.2 (red) assimilation systems. Comparisons are shown separately for the Northern (a and b) and Southern (d and e) Hemisphere. The root-mean-square differences between POAM and GEOS-4.0.3 (red) and GEOS-4.0.2 (black) ozone analyses are shown for Northern Hemisphere (c) and Southern Hemisphere (f). POAM data from January 1-14, 2004 are used, except in a) and d) where POAM data for December 2003 are used.

The remaining figures show comparisons of GMAO ozone analyses against independent ozone profile data. High quality ozone profiles are available from the Polar Ozone and Aerosol Measurement III (POAM) occultation instrument (Lucke *et al.*1999). More than 600 POAM profiles are available during the validation period, however the coverage of POAM is limited to northern and s southern high latitudes (between about 60° and 65° in each hemisphere). Differences between analyses and POAM are shown in Figure 5.27, and they are generally small. Mean differences are the largest around 10 hPa in the Southern Hemisphere and around 2 hPa in the Northern Hemisphere. Differences between GEOS-4.0.2 and GEOS-4.0.3 ozone means are hardly visible. However, the RMS difference between GEOS-4.0.3 ozone and POAM is smaller than between GEOS-4.0.2 ozone and POAM at all pressure levels between 20 and 70 hPa.

Comparisons against ozone sondes launched from Neumayer, Antarctica, near 70°S and 8°W (G. Koenig-Langlo personal communication 2004) are shown in Figure 5.28. Both analyses agree well with sonde profiles. The largest differences in profile shapes of the analyses are seen in the pressure layer between 20 and 50 hPa. In this layer the laminar feature in GEOS-4.0.2 analysis is too strong, and the smoother shape of GEOS-4.0.3 analysis agrees better with the shape of sonde profiles.
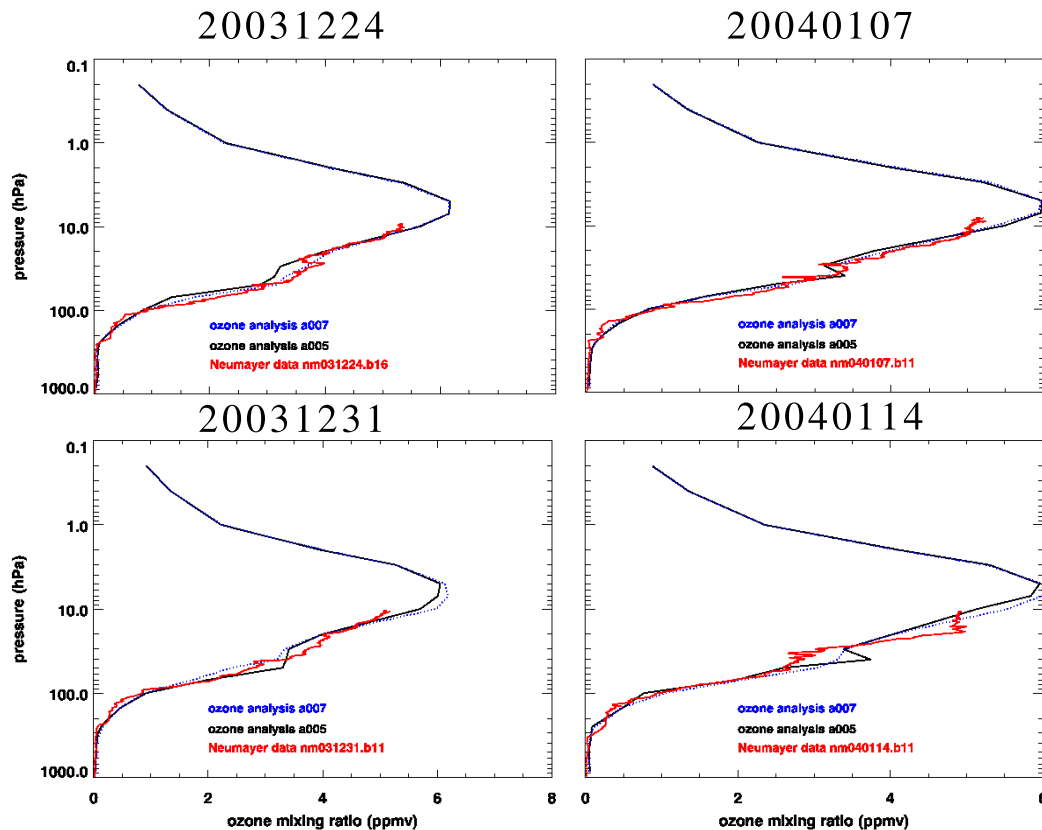

Figure 5.28: Ozone profiles from independent sondes (red solid line) that were launched from Neumayer, Antarctica, $(70°S, 8°W)$ and collocated GMAO ozone analyses from GEOS-4.0.3 (blue dashed line) and GEOS-4.0.2 (black solid line) systems are shown for December 24 and 31, 2003 and for January 7 and 14, 2004.

The limb sounding Michelson Interferometer for Passive Atmospheric Sounding (MIPAS) on board ESA s Environmental Satellite provides ozone profiles over a wide range of latitudes (Ridolfi et al., 2000). We used 2238 MIPAS ozone profiles from the first week of January 2004 to evaluate GEOS ozone analyses. About 600 of these profiles are in the Tropics, more than 350 in southern midlatitudes, and more than 400 in northern midlatitudes. A good agreement is seen between MIPAS and analyses means throughout the stratosphere in Figure 5.29. The means from two analyses are indistinguishable. However, in the RMS differences the GEOS-4.0.3 agrees better with MIPAS in the Stratosphere between 1 and 70 hPa. The largest improvement from GEOS-4.0.2 to GEOS-4.0.3 is seen near 20 hPa.

The above comparisons show very small changes in mean profiles between GEOS-4.0.2 and GEOS-4.0.3 ozone. The representation of ozone variability, which is quantified by RMS differences, improved in GEOS-4.0.3 in the stratosphere at pressure levels between about 20 and 70 hPa. Qualitative improvement to the total ozone column maps is the largest in the Tropics, where the fields are smoother and more zonally symmetric. This is consistent with a decrease in the total column O-F residuals from about 14 DU to about 10 DU. In summary, the ozone product in GEOS-4.0.3 is better than in GEOS-4.0.2. The key to this improvement is the use of time averaged winds, rather than instantaneous winds, to drive the ozone transport.
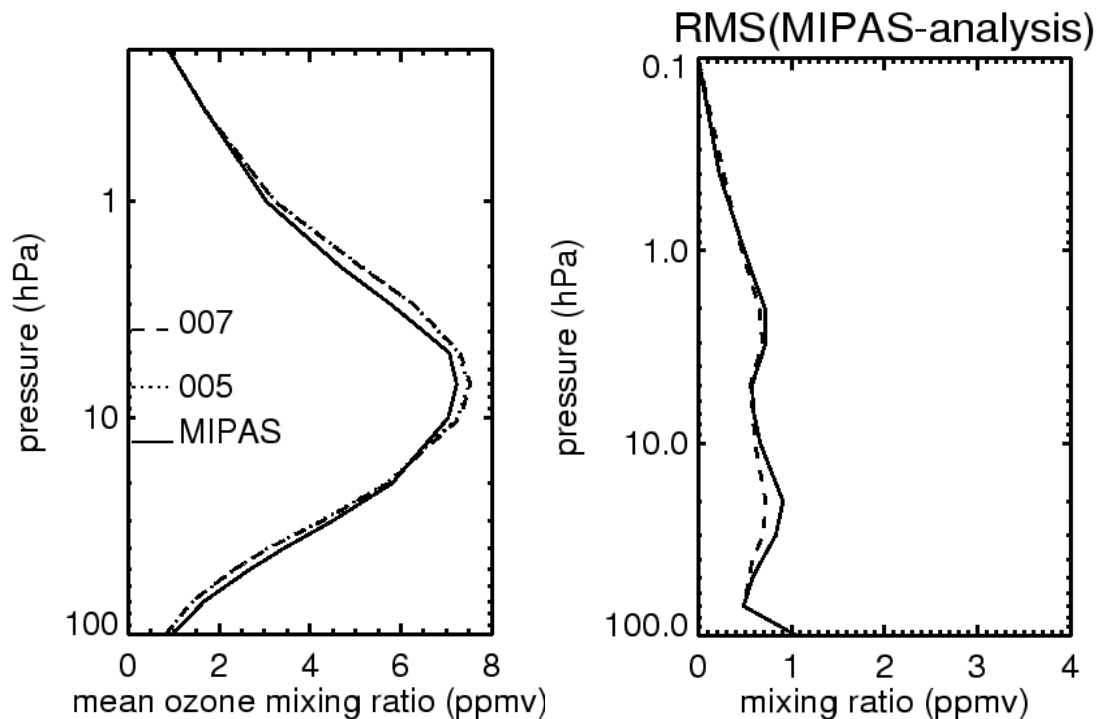

Figure 5.29: Mean profiles from MIPAS (solid) are compared with collocated assimilated ozone from GEOS- 4.0.2 (dotted) and GEOS- 4.0.3 (dashed) in the left panel. The RMS difference between MIPAS and collocated analyses are shown in the right panel for GEOS-4.0.2 (solid) and GEOS- 4.0.3 (dashed). Comparisons were done using over 2000 MIPAS observations for the period from January 1 to 7, 2004.

5.5   Monthly Mean Diagnostics

Examples of the longer time-scale behavior of the GEOS-4.0.3 system are shown here with diagnostics of monthly means of precipitation and surface stresses over oceans. This section complements the short-term system diagnostics of GEOS-4.0.3 shown in the next section on monitoring results (5.8).

5.5.1   Monthly Precipitation

The primary focus was on the January and July 2001 monthly mean precipitation fields (although some comparisons were carried out for all months of 2001). Intercomparisons were performed on precipitation products from:

- C403_cer_01 - the current system being validated (GEOS-4.0.3);

- C402_rp_02 - previous version of our system (GEOS-4.0.2);

- NCEP GDAS - the NCEP operational system;

- GPCP - an observational product used as verification.

These comparisons included maps of monthly means and their differences, and time series of daily values for selected area averages. The comparisons were summarized with bar charts (area means), and Taylor plots (points on the Taylor plots show the correlations and relative variances of any two time series; also discussed in section 3.1.3).

Both the NCEP GDAS and GEOS data were first regridded to match the 1-degree GPCP grid. Also, the 6-hourly GEOS and NCEP products were averaged to create daily means in order to compare with the daily GPCP product. The 1-degree daily GPCP product is described at:

http://precip.gsfc.nasa.gov/gpcp_daily_comb.html

Figure 5.30(a,b) shows the monthly mean differences of the GEOS-4.0.3 precipitation (in $mm\ day^{-1}$) compared to GPCP for January and July 2001. The precipitation is overestimated over the tropical oceans during all months of the year. The bias is largest during boreal summer (the tropical ocean average is a factor of 2 too large), especially over the western tropical Pacific (equator to 30°N) and the Caribbean. During the Boreal winter the bias is largest over the South Pacific Convergence Zone (SPCZ). On the other hand, the precipitation is underestimated throughout most of the extratropical oceans (poleward of 30°) especially in the North Pacific, and throughout the Southern Hemisphere extratropics. Area averages for these monthly statistics, and their differences, are given in Table 5.2. Note that the results in Figure 5.30(a,b) should be compared with their AMIP counterparts (Figures 3.1, 3.2, 3.3, and 3.4; the panels labeled "fvGCM" in each), with the caveat that the GPCP climatology in the AMIP comparisons spans more years than just the year 2001 used for the DAS precipitation comparisons. A close examination of the two (DAS, AMIP) sets of results does indicate that the DAS precipitation results tend to have a 50% to 100% greater disagreement with the corresponding GPCP verification, with the preponderance of the disagreement occurring in the Tropics.
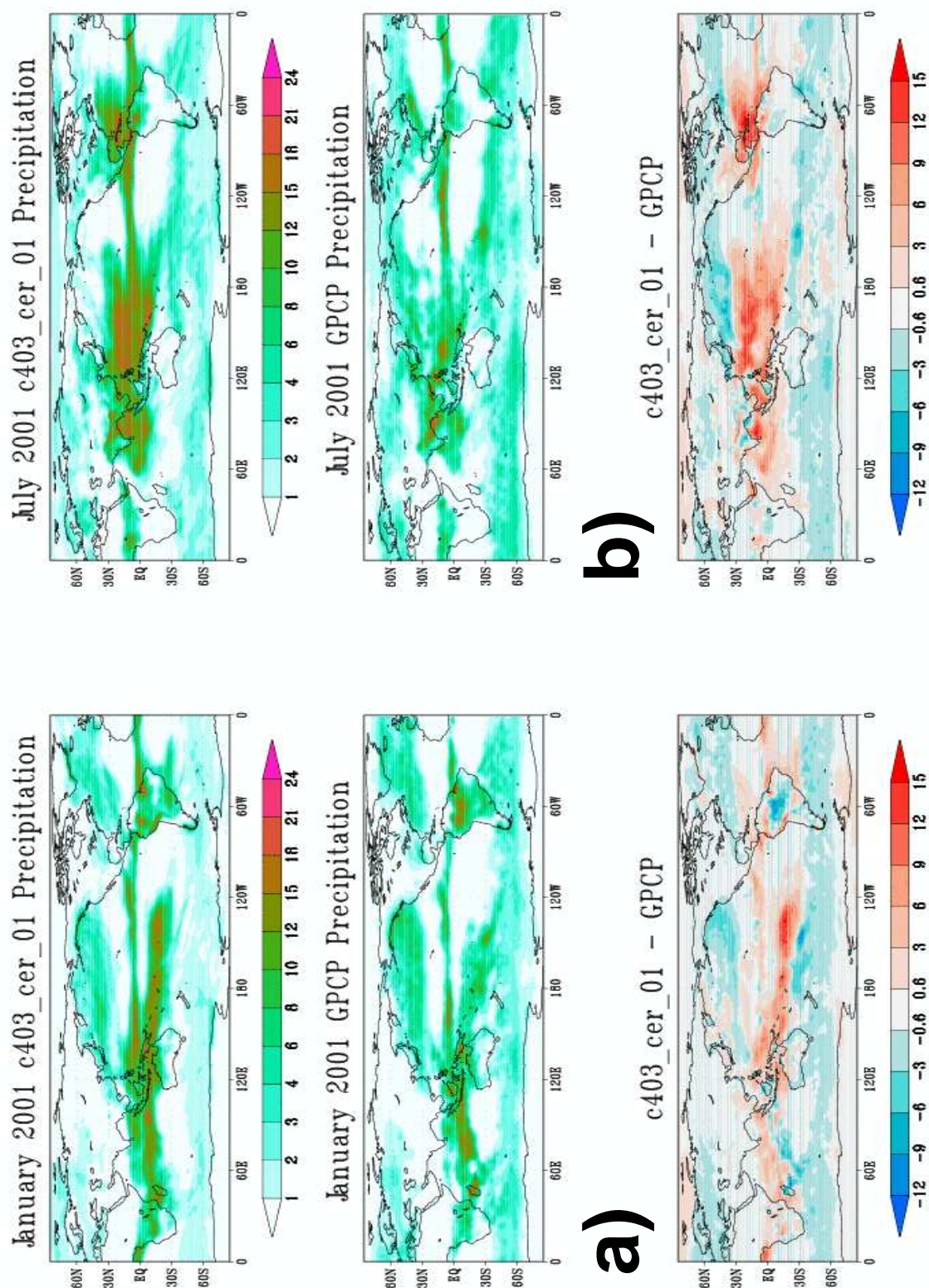
Figure 5.30: (a) January 2001 precipitation fields from c403 (top panel) and GPCP (middle panel). The difference field (c403- GPCP) is shown in the bottom panel. Units are $mm\ day^{-1}$. (b) Same as (a) but for July 2001.

January (July) Average Precipitation

System	Global		Tr. Ocean		Tr. Land		(30N-60N)		(30S-60S)	
C403	2.90	(3.50)	4.6	(5.7)	3.30	(3.30)	2.00	(2.10)	1.30	(2.20)
GPCP	2.60	(2.70)	2.8	(2.9)	3.10	(2.80)	2.70	(2.40)	2.60	(3.30)
C403-GPCP	0.32	(0.86)	1.8	(2.9)	0.25	(0.52)	-0.69	(-0.33)	-1.30	(-1.10)

Table 5.2: Precipitation averaged over the specified regions for January (July) of 2001. Units are $mm\ day^{-1}$.

Figure 5.31 shows the January and July 2001 precipitation results in the tropical band 30N - 30S for three DAS systems: GEOS-4.0.3, GEOS-4.0.2 and NCEP. The GEOS-4.0.3 bias is somewhat improved (reduced by 5-10% over tropical oceans) compared to the previous version of the system (GEOS-4.0.2). The bias is nevertheless still quite a large. For comparison, the precipitation from the NCEP operational system has only one half to one third of the precipitation bias compared to GPCP.

A sense of the variability of the DAS precipitation results is given in Figures 5.32, 5.33, and 5.34. These results should be compared with the AMIP results shown earlier (Figure 3.5, the blue "dots" depict fvGCM). Even for the global result (Figure 5.32), the July variability for GEOS-4.0.3 (green dot) is considerably less than its AMIP counterpart. As the region of interest is focused to the areas of greatest precipitation (first the Tropics, $20°S - 20°N$; then the Western Pacific, $15°S - 15°N$ and $120°E - 180°E$) the clustering so evident in the AMIP results largely disappears. The amplitude in the daily fluctuations of precipitation shows some improvement in GEOS-4.0.3 compared with those from GEOS-4.0.2. Correlations with the daily GPCP values tend to be low throughout the Tropics (generally less than 0.4), with somewhat larger values in the extratropics (in some places exceeding 0.8). These values (while low) are similar if not somewhat better than those based on a comparison between GPCP and NCEP GDAS values.

Figure 5.35 shows how the $30°S - 30°N$ average monthly mean precipitation varies by month during 2001 for GEOS-4.0.3, GEOS-4.0.2, NCEP and GPCP. In addition, the land and oceanic contributions to the averages are shown. The tropical ocean precipitation exhibits an unrealistic seasonal cycle with a substantial increase in precipitation during boreal summer that is not seen in the GPCP values. There is a uniform improvement in the bias and RMS statistics of the GEOS-4.0.3 precipitation over that from GEOS-4.0.2 in the monthly comparisons against GPCP for 2001.

In summary, a significant deficiency in GEOS-4.0.3 is its tendency to overestimate precipitation over the tropical oceans during all months of the year. The tropical ocean bias is largest during Boreal summer (area averaged precipitation is a factor of two too large), especially over the western tropical Pacific (equator to 30°N) and the Caribbean. In contrast, GEOS-4.0.3 underestimates precipitation over the extratropical oceans, particularly in the North Pacific, and in the Southern Hemisphere during January where the area-averaged values are underestimated by a factor of two.
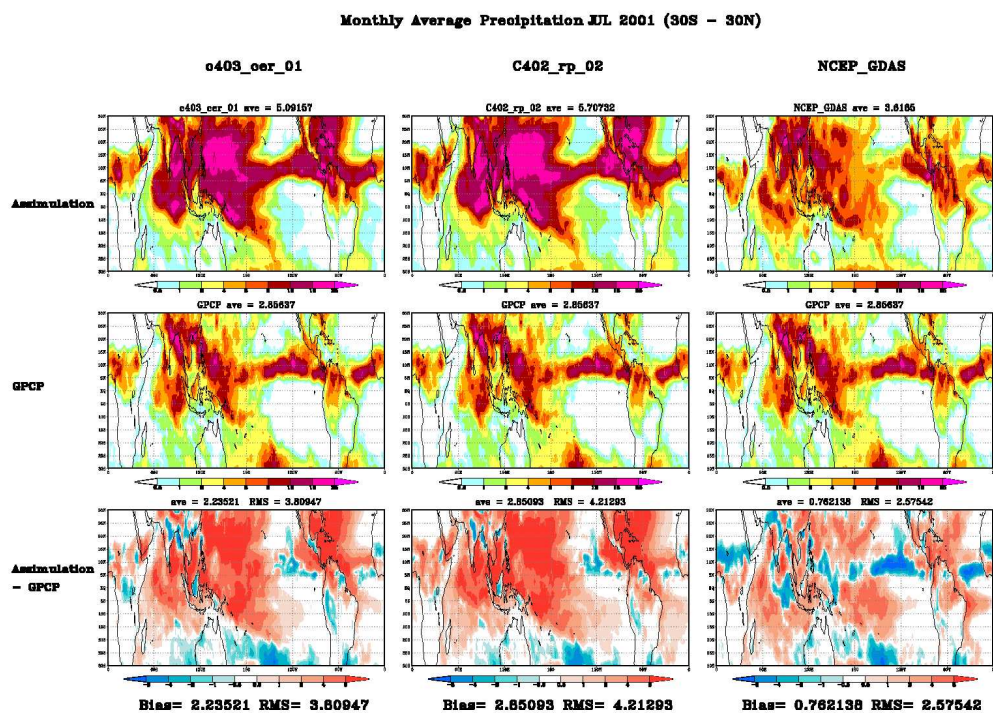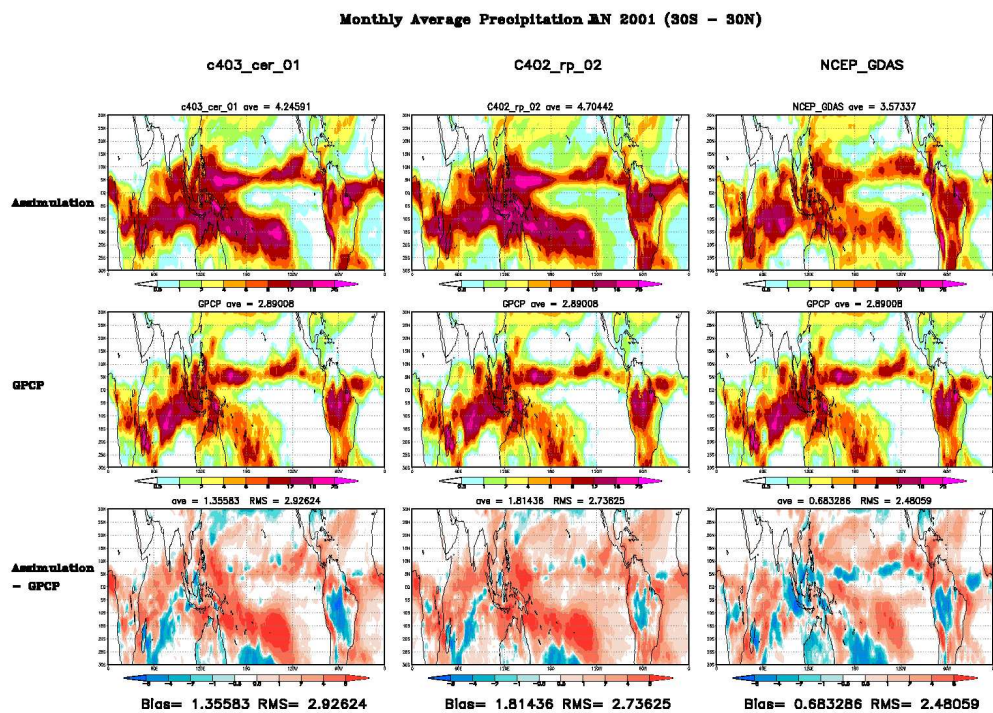
Monthly Average Precipitation JAN 2001 (30S − 30N)

c403_cer_01	C402_rp_02	NCEP_GDAS

Figure 5.31: Monthly average precipitation comparisons for tropical region $30°S − 30°N$, for January 2001 (top set) and July 2001 (bottom set). Middle panels in both sets are the GPCP verification data for that time. Units $mm\ day^{-1}$.

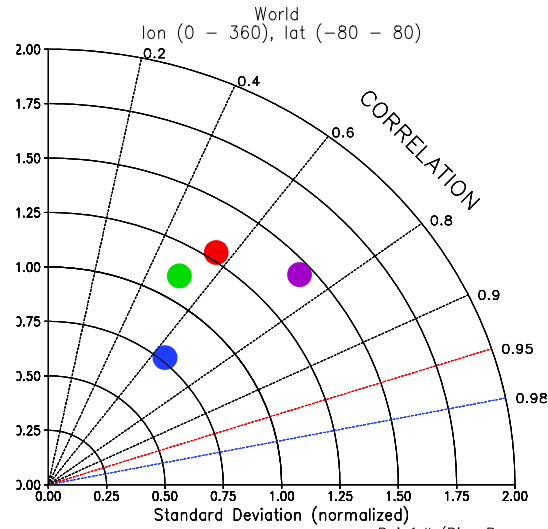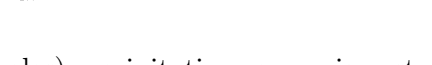Figure 5.32: Taylor plot showing global (excluding poles) precipitation comparison statistics against GPCP for GEOS-4.0.3 (green), GEOS-4.0.2 (red) and NCEP (blue). NCEP vs GEOS-4.0.3 (purple) added for reference. Also shown are daily time series of the averages with and without the bias. (a) January 2001. (b) July 2001. Units $mm\ day^{-1}$.

Taylor Plots
January 2001
Precipitation

c402_rp_02
c403_cer_01
NCEP_GDAS
(as compared to
GPCP data)

c403_cer_01
v. NCEP_GDAS

Tropics
lon (0 – 360), lat (–20 – 20)

a)

Ave.

5.71
5.21
4.34
3.43

Rainfall

Rainfall (Bias Removed)
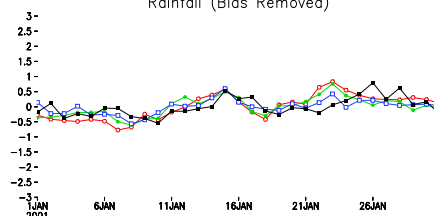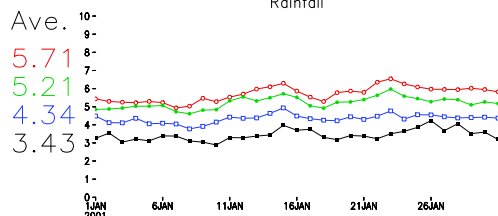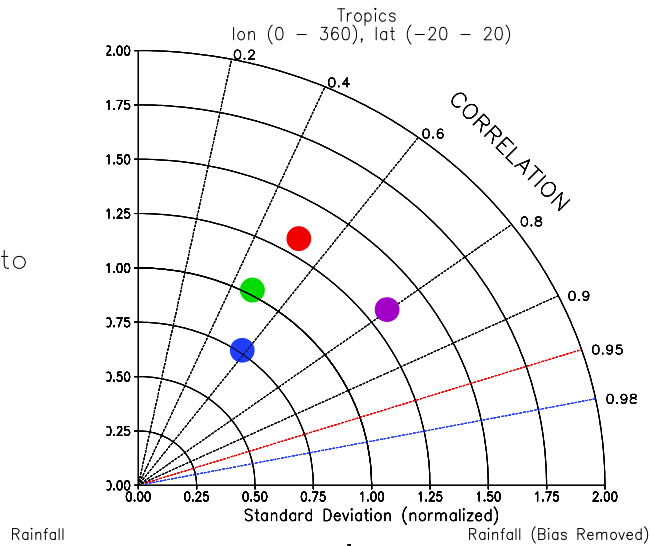
Taylor Plots
July 2001
Precipitation

c402_rp_02
c403_cer_01
NCEP_GDAS
(as compared to
GPCP data)

c403_cer_01
v. NCEP_GDAS

Tropics
lon (0 – 360), lat (–20 – 20)

b)

Ave.

6.45
5.79
4.11
3.20

Rainfall

Rainfall (Bias Removed)
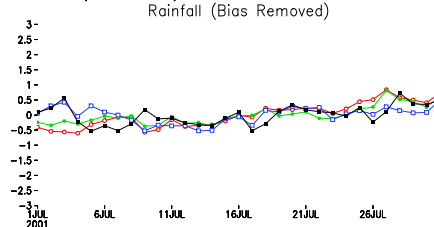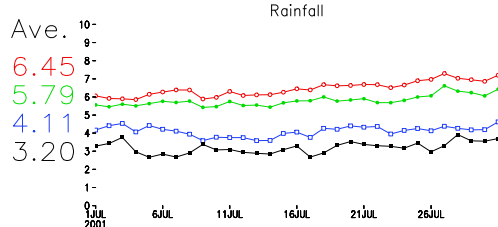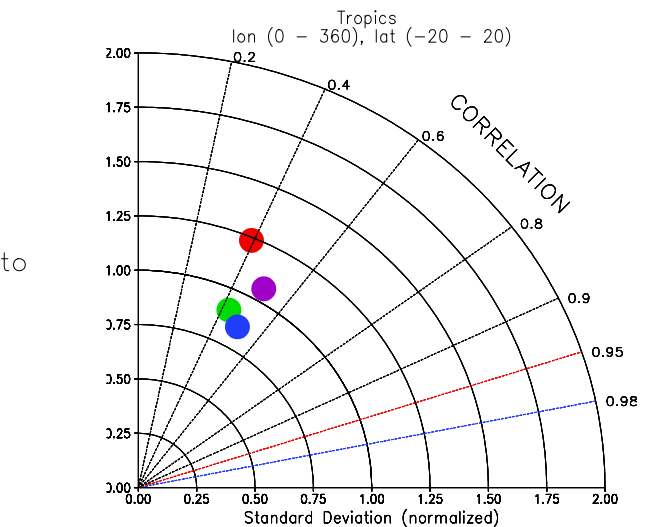
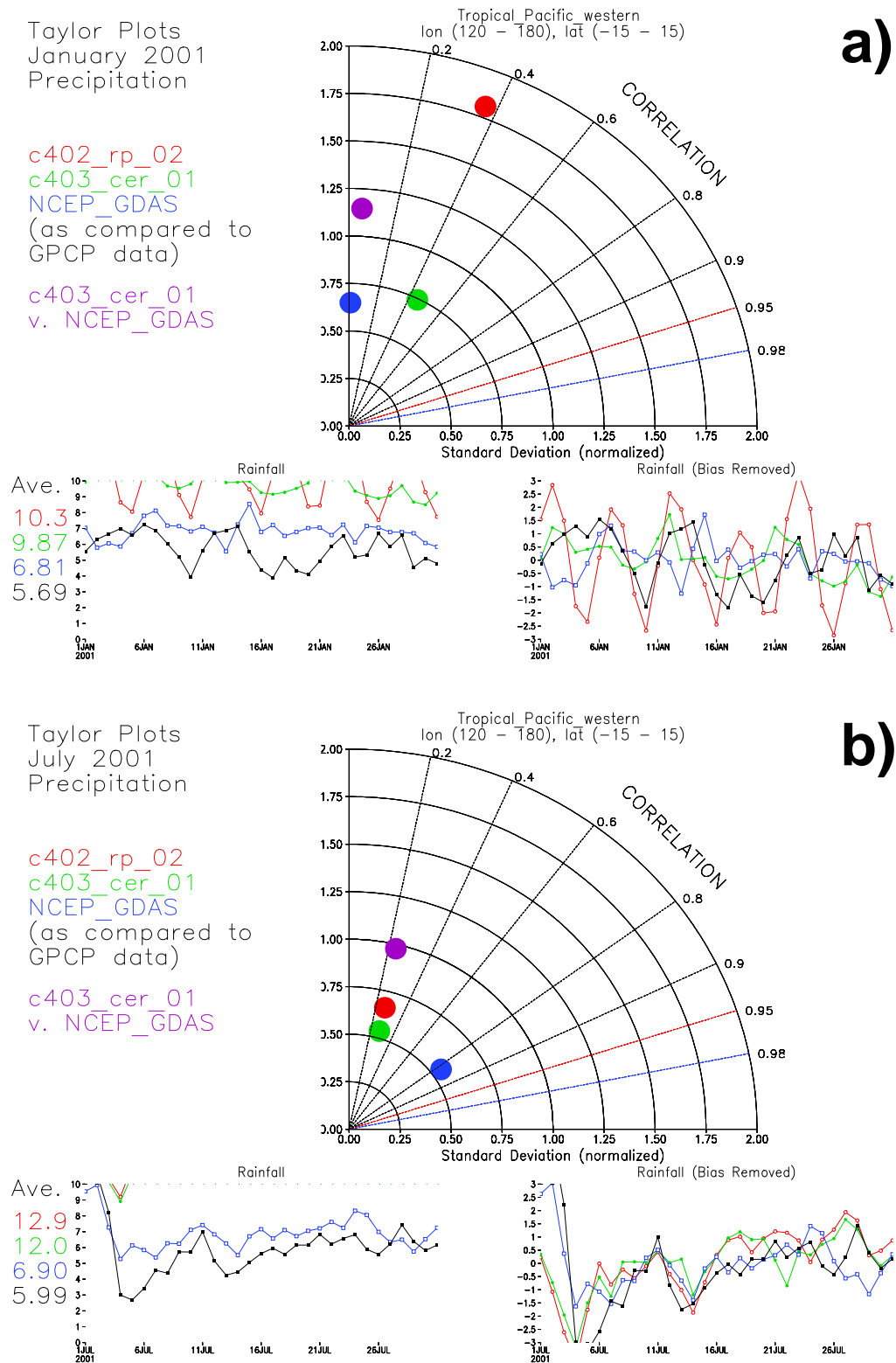Figure 5.33: Taylor plots as in Figure 5.32, only for the Tropics : $20°S - 20°N$.

Figure 5.34: Taylor plots as in Figure 5.32, only for the Tropical Western Pacific region: $15°S - 15°N$, $120°E - 180°E$.

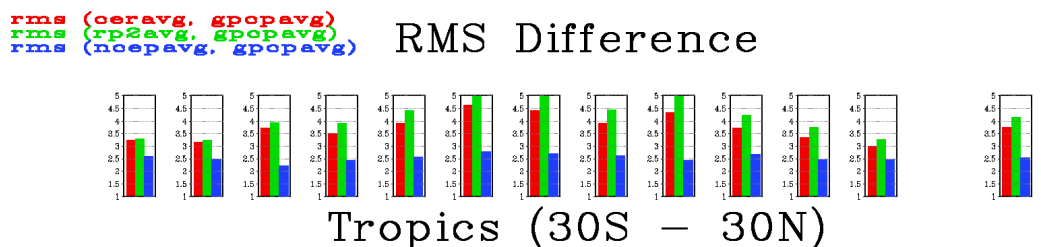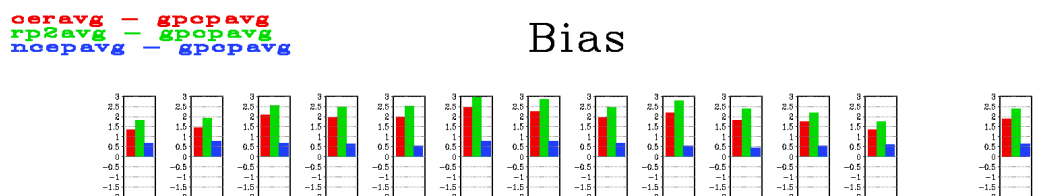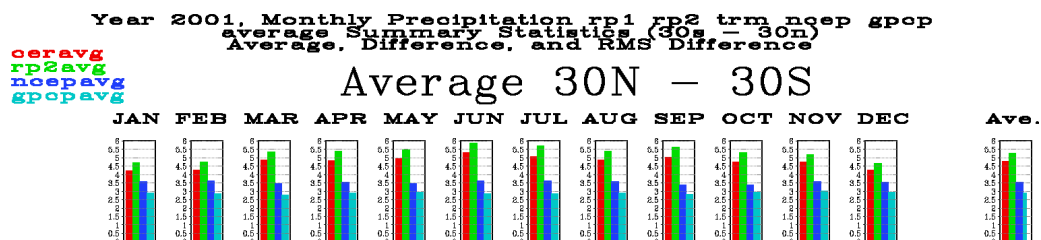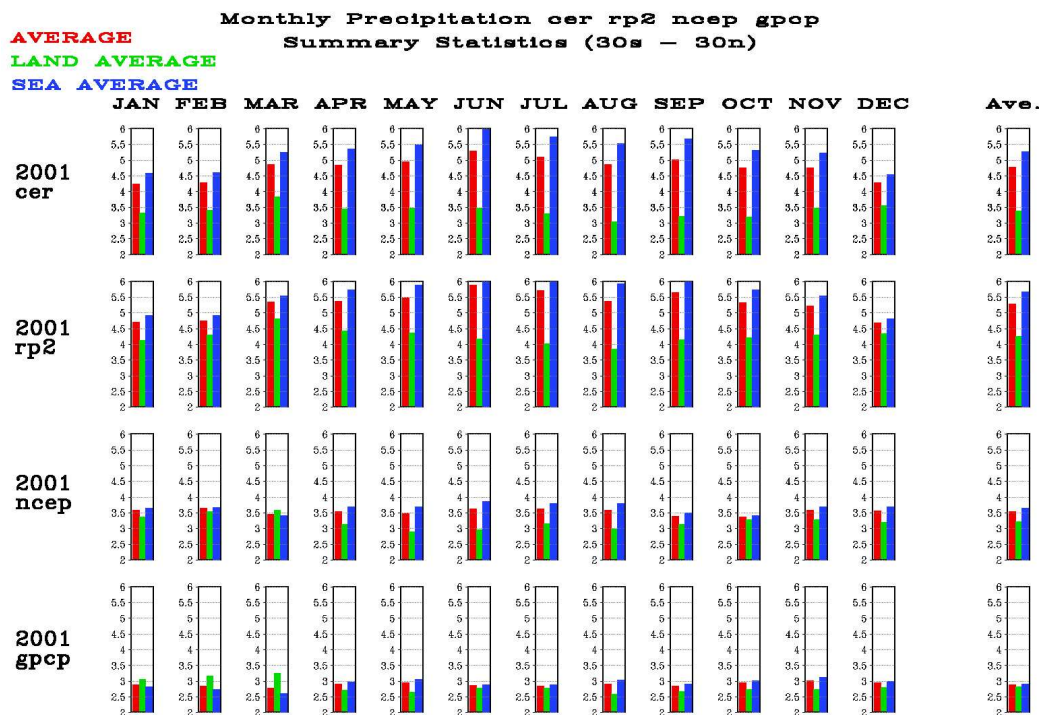Figure 5.35: Monthly Tropical precipitation averages for 2001, for GEOS-4.0.3 (cer), GEOS-4.0.3 (rp2), NCEP and GPCP verification. The land (green) and ocean (blue) contributions to the monthly averages (red) are also shown. Units $mm\ day^{-1}$.

5.5.2 Surface Wind Stress

Figure 5.36 compares the monthly mean (January and July) zonal and meridional components of the surface stresses in GEOS-4.0.3 with those from ERA-40 and values inferred from SSM/I data (using methods based on those described in Atlas et al. (1996)). In general, the GEOS values compare quite well with the stresses estimated from SSM/I. In fact, for both months and for both components of the stress, the biases (with respect to SSM/I) tend to be smaller than those from ERA-40. Notable exceptions are the larger regions of westerly bias for GEOS in the tropical Pacific and southern Indian Oceans. The comparison is quantified in several Taylor plots (Figures 5.37 and 5.38). These plots show that the monthly mean GEOS fields have consistently higher (compared with ERA-40) spatial correlations with the SSM/I fields and also tend to have spatial variances that are closer to SSM/I. The meridional component of the stress, in particular, is remarkably similar to the meridional stress derived from SSM/I data.
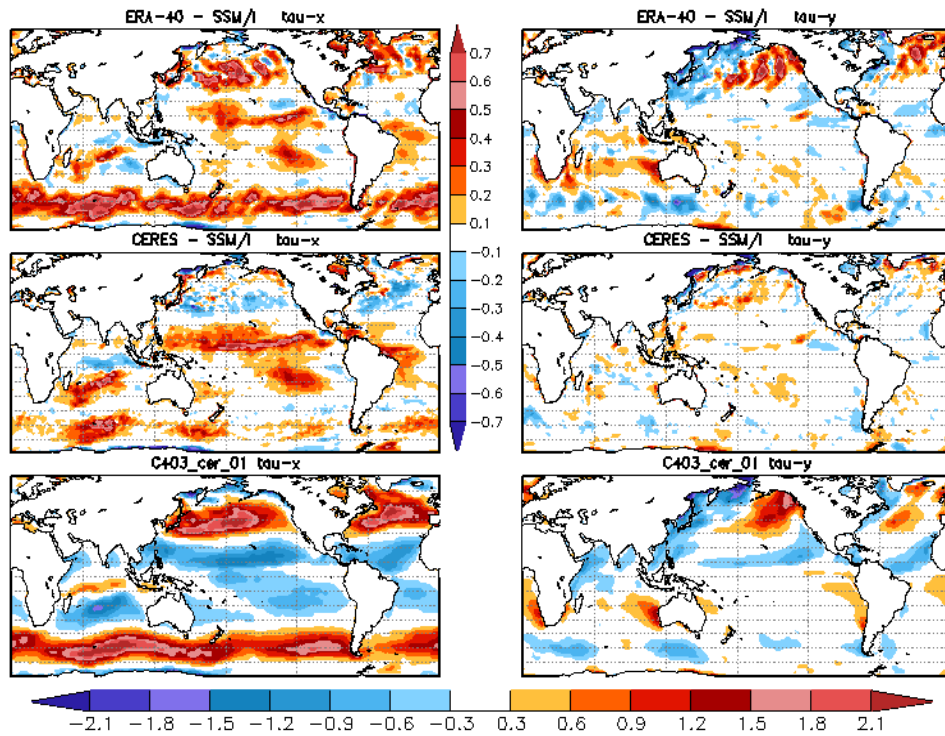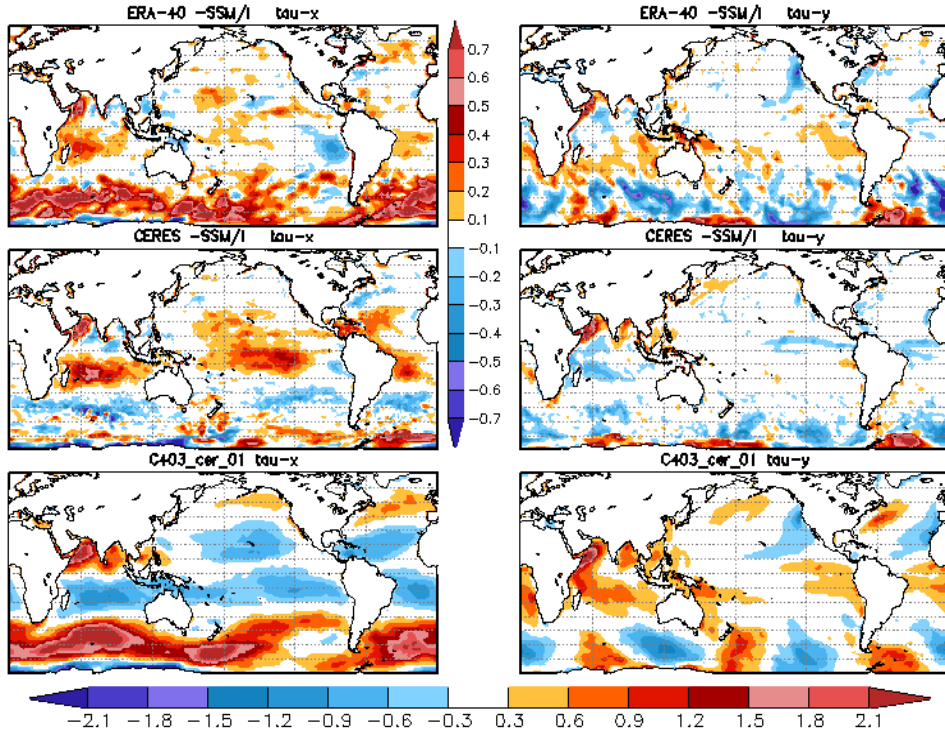
Figure 5.36: Monthly mean surface stresses, zonal component left and meridional component right column, for January 2001 (top set) and July 2001 (lower set). Compared are the stresses from the ERA-40 reanalysis, GEOS-4.0.3 ("CERES") and stresses derived from SSM/I data.
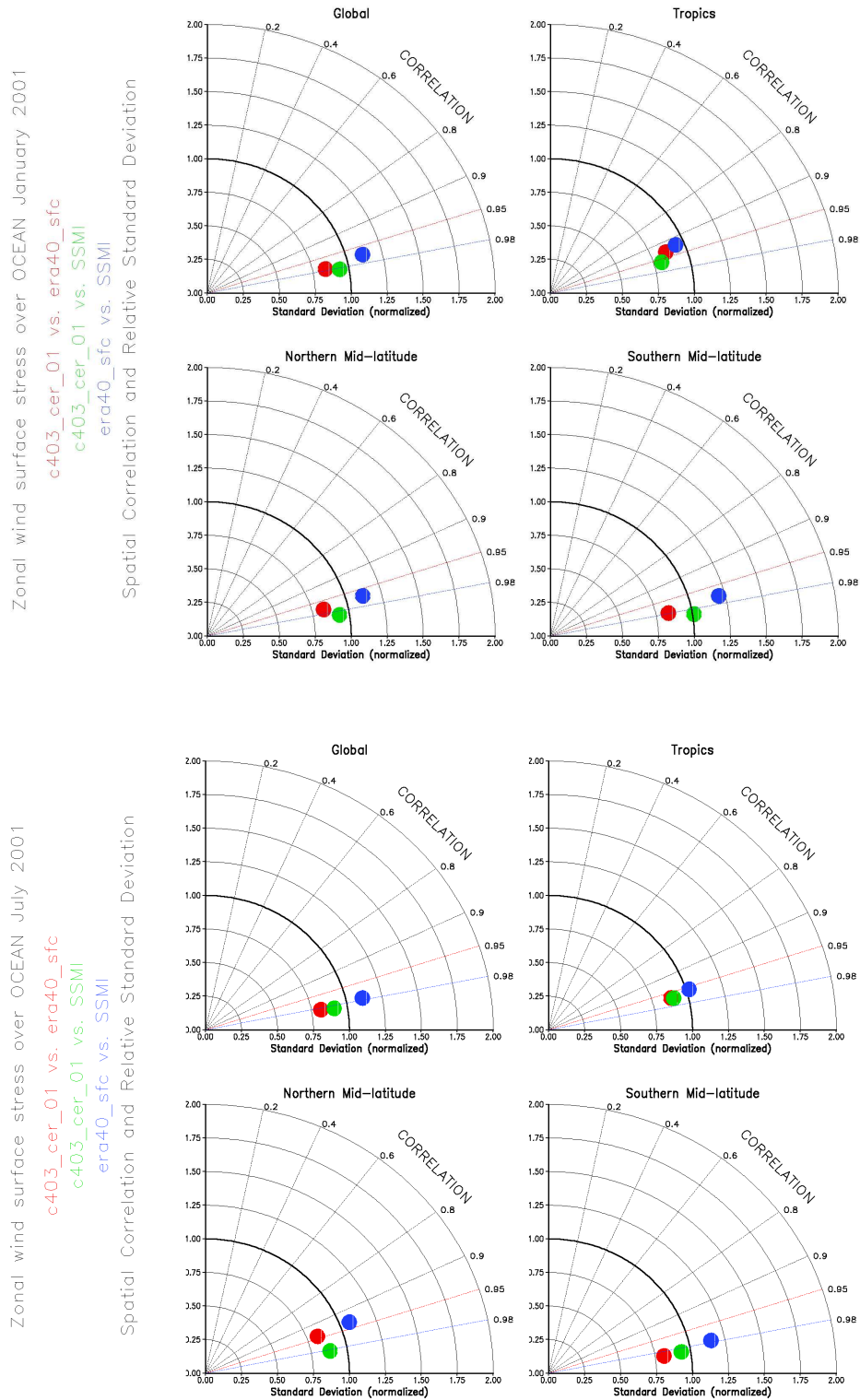
Figure 5.37: Taylor plots comparing zonal wind surface stresses over oceans for January 2001 (top set) and July 2001 (lower set) for four regions: Global, Tropics, Northern Mid-latitude and Southern Mid-latitude. Three comparisons on each plot: GEOS-4.0.3 vs ERA-40 (red); GEOS-4.0.3 vs SSM/I (green); ERA-40 vs SSM/I (blue).

Figure 5.38: Same as Figure 5.37, only for meridional stress component.

5.6 Precipitation Variability: MJO

This section examines the precipitation variability on the MJO/ISO time scale in the GEOS-4 system. Precipitation data were produced from the c403_cer_01 run of this system (intended for the CERES i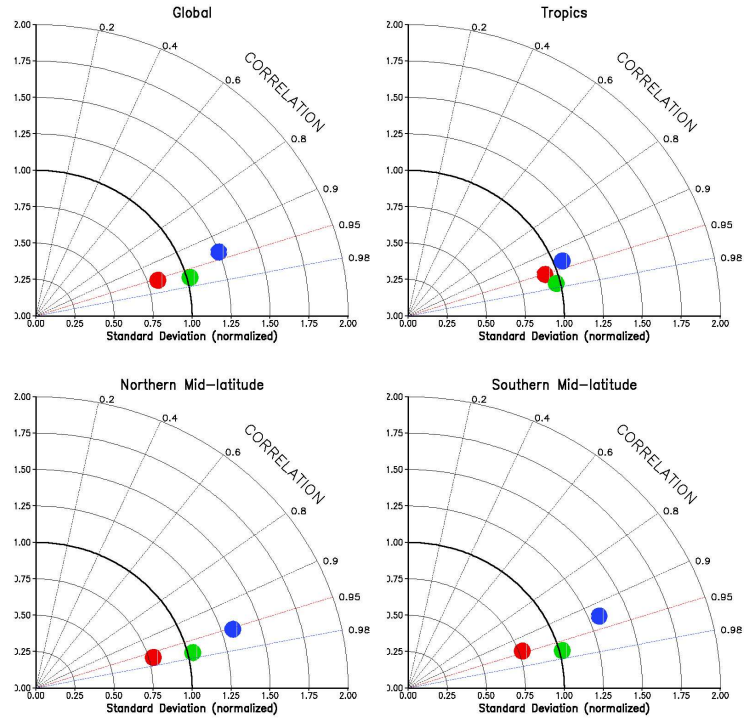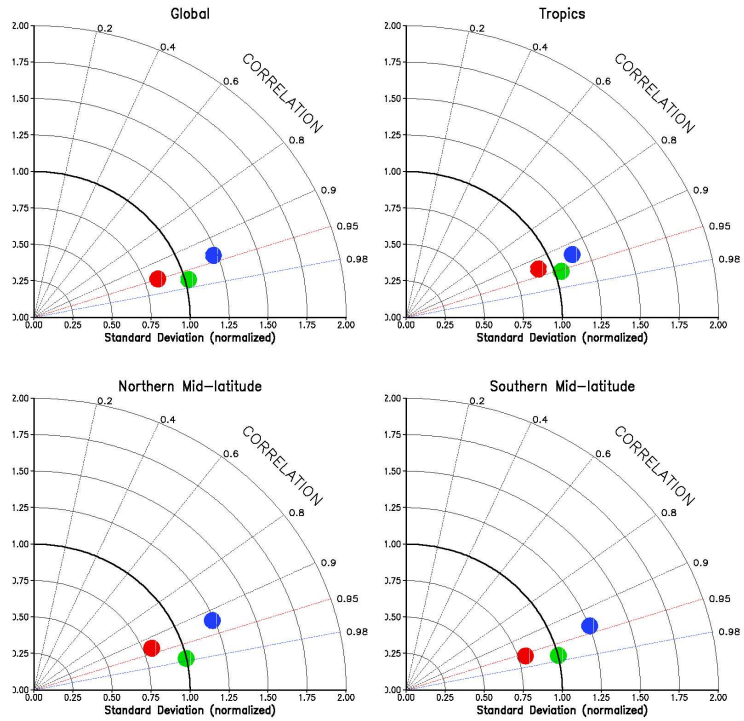nstrument team). Currently, very few GCM or assimilation systems are capable of producing reasonable precipitation variability on the MJO/ISO time scale, especially with the known MJO/ISO features during both hemispheric summer seasons. Previous results (*e.g.* Sections 5.1, 5.2) have shown that this system produces reasonable temperature and moisture profiles and surface skin temperature for the clear sky OLR computations. The issue here is how well the GEOS-4 system handles a specific type of longer time-scale organized atmospheric process.

5.6.1 Seasonal Mean

Figure 5.39 presents seasonal mean precipitation for summer (May through October) and winter (November through April) of 2000 and 2001. Four months of analysis data are compared with TRMM observational data. They are fv141_val_01 (an older version of GEOS4), C403_cer_01 (basically the current validation version of GEOS4, run in earlier time periods to support the CERES reprocessing), GDAS (NCEP reanalysis), and ERA-40 (ECMWF 40 years reanalysis).

Seasonal Precipitation Mean ($mm\ day^{-1}$)

System	Summer	Winter
TRMM	2.57	2.59
fv141_val_01	4.48	3.94
c403_cer_01	4.18	3.64
GDAS	3.63	3.59
ERA-40	2.29	2.32

Table 5.3: Seasonal mean preciptiation statistics, area averages (40S to 40N). See Figure 5.39.

The comparisons are between 40S to 40N. In order to compare the *patterns* among all of these runs in Figure 5.39, the two GEOS precipitation results have had a scale factor of 0.6 applied. Figure 5.39 shows that all the four analyses produce reasonable patterns, the two versions of the GEOS-4 overestimate precipitation over the western Pacific warm pool region. For clarity, the mean seasonal precipitations for each run (on the left hand of the figure) between 40S to 40N are summarized in Table 5.3. Among the four runs, ERA-40 shows a closer mean to observations than the other three, with the two versions of GEOS-4 overestimating precipitation from 70% to as much as 100%.
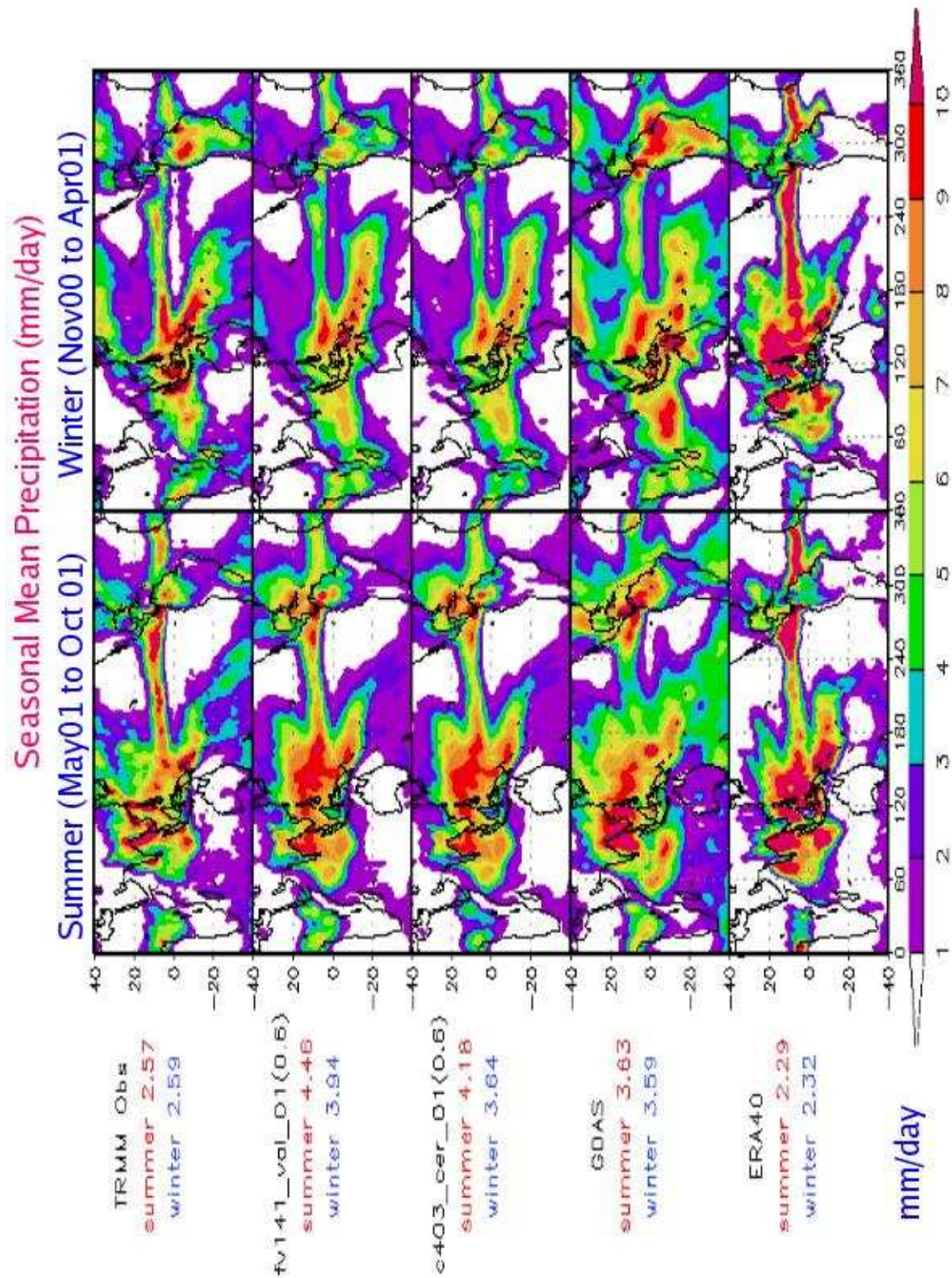
Figure 5.39: Seasonal mean precipitation for summer (May to Oct.) and winter (Nov to Apr.) Also shown are the area average (40S to 40N) seasonal means of precipitation.

The variability of precipitation on the MJO/ISO time scale for these runs is examined by comparing their standard deviations in Figure 5.40. This figure shows that all four analyses generally underestimate precipitation variability. As was done for the previous figure, the seasonal standard deviations are summarized in Table 5.4.

Seasonal Precipitation Std. Dev. ($mm\ day^{-1}$)

System	Summer	Winter
TRMM	1.85	1.93
fv141_val_01	1.44	1.48
c403_cer_01	1.39	1.42
GDAS	1.40	1.42
ERA-40	1.02	1.02

Table 5.4: Seasonal standard deviation preciptiation statistics, area averages (40S to 40N). See Figure 5.40.

Examining Figure 5.40, the areas of greatest disagreement between observations and the model-based precipitation varibility occur over the equatorial region (especially the central Pacific), and over the summer monsoon regions of both hemispheres.

A more detailed view of the precipitation processes on these time scales can be obtained by examining longitude-time (Figure 5.41) and latitude-time (Figure 5.42) cross sections. Figure 5.41 shows averages of the precipitation between 5S and 5N for the different runs along with the TRMM observations. Eastward propagating convection associated with the MJO/ISO activity, which starts in the Indian Ocean and extends to the west Pacific warm pool region, is clearly shown in the TRMM data. In comparison with TRMM, the two GEOS-4 runs perform somewhat better than GDAS, though not as well as ERA-40. Figure 5.42 presents latitude-time cross sections, averaged from 75E to 85E. This figure shows the northward propagation of precipitation associated with the tropical MJO/ISO activity. All systems examined here show a weak northward propagation during the summer season, which affects the monsoon variability over the Indian subcontinent.
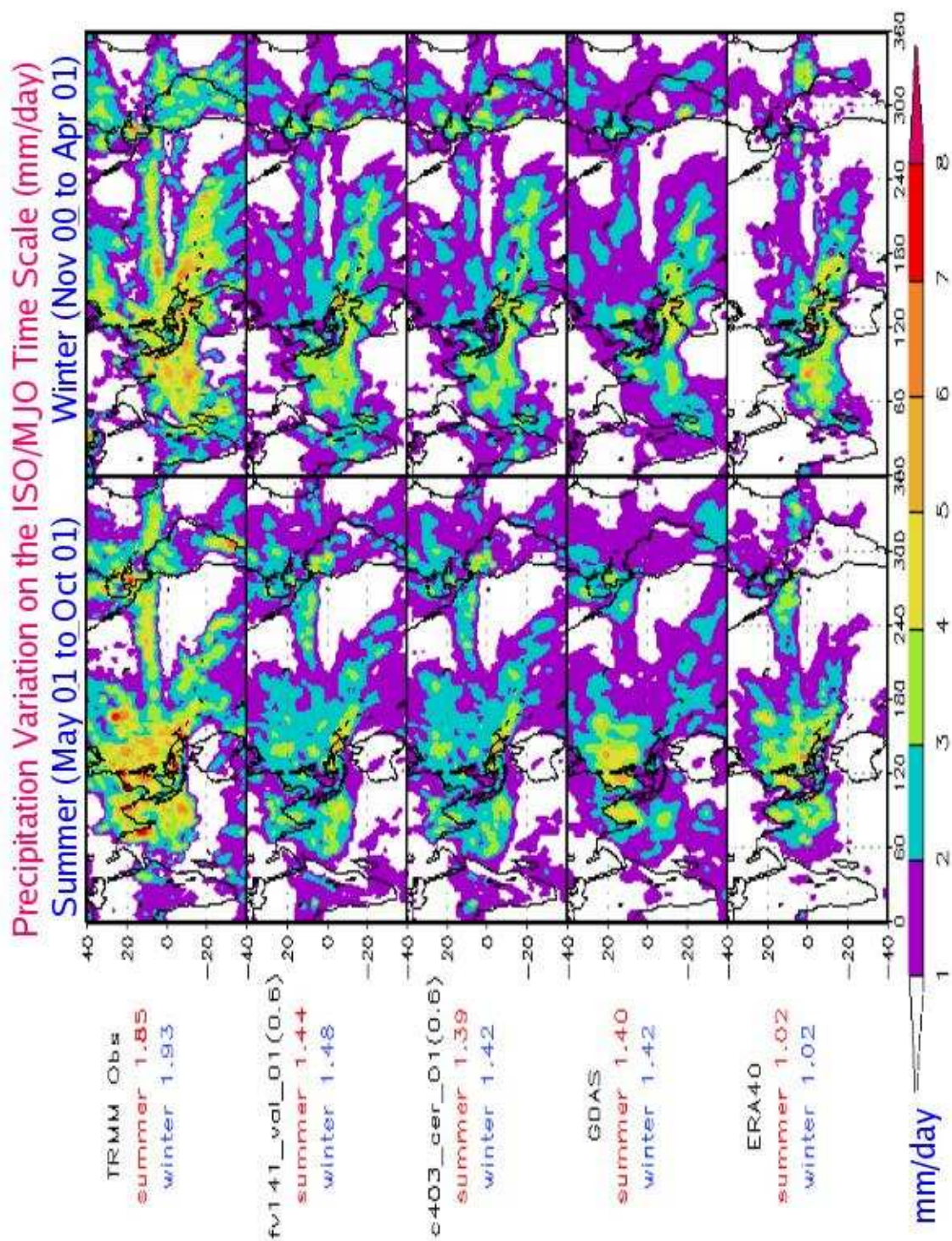
Figure 5.40: Seasonal standard deviation precipitation for summer (May to Oct.) and winter (Nov to Apr.). Also shown are the area average (40S to 40N) seasonal standard deviations of precipitation.
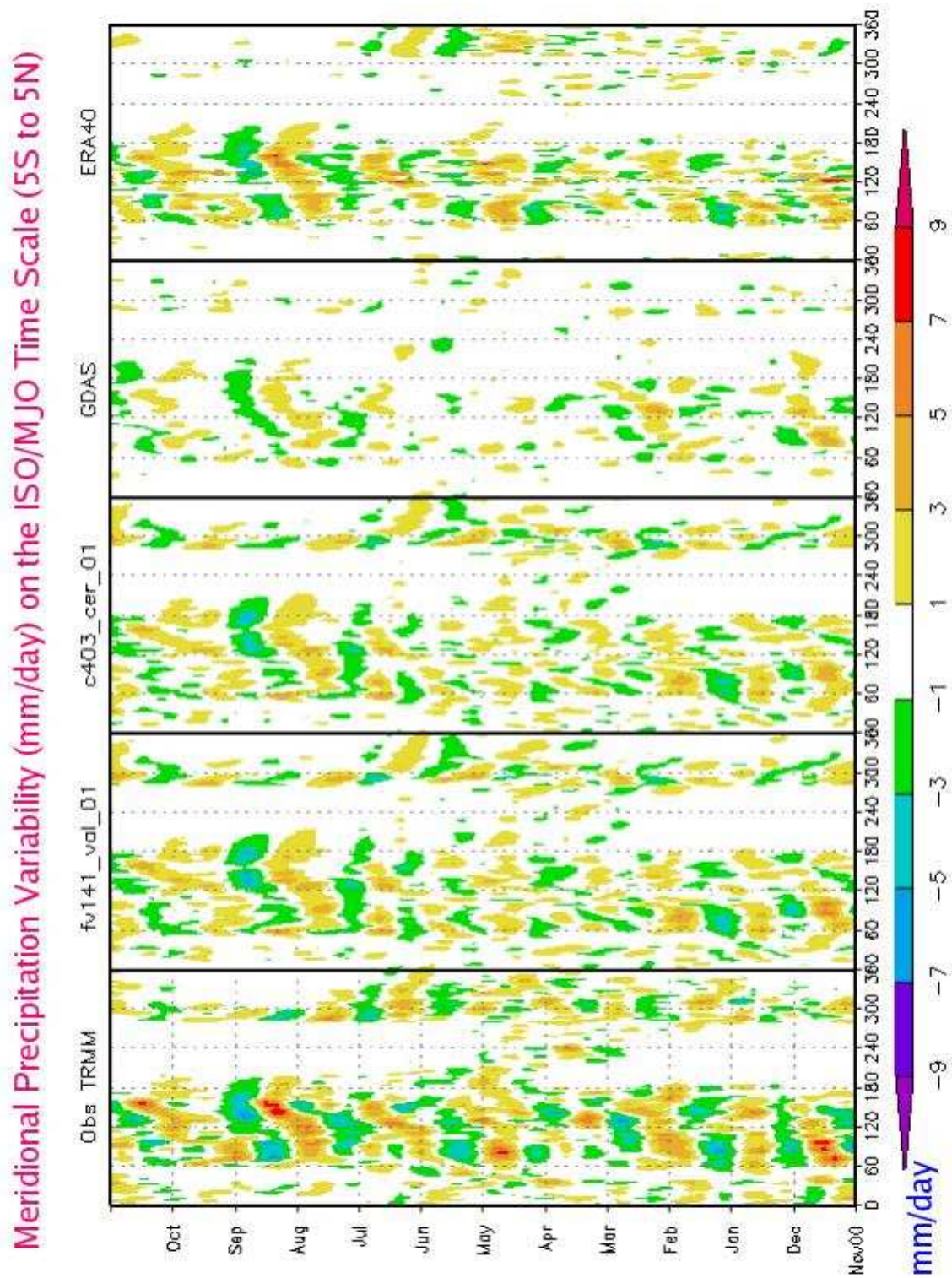
Figure 5.41: Longitude-time cross sections (averaged 5S to 5N) of precipitation standard deviation. TRMM observations are the left-most plot.
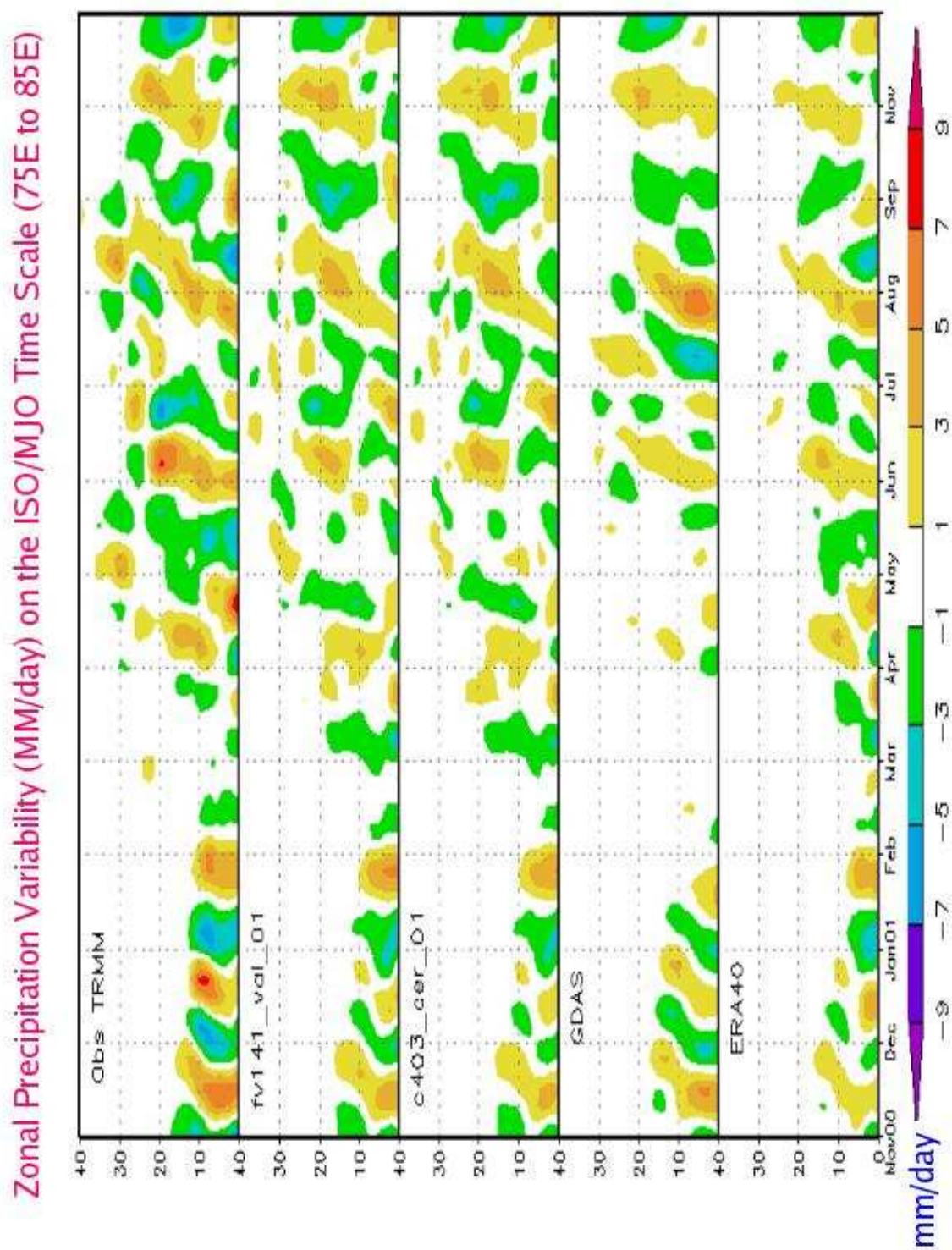
Figure 5.42: Latitude-time cross sections (averaged 75E to 85E) of precipitation standard deviation. TRMM observations are the left-most plot.

5.7   Data Impact

A series of data withholding experiments was conducted with GEOS-4.0.3 with the purpose
of determining the impact various observation types on the GEOS-4 assimilation system.
The initial experiments involved "data denial" from major observing systems (rawinsondes,
TOVS retrievals, satellite winds). Further experiments were also conducted which excluded
all wind data and all mass data; additionally, a pair of experiments were run which excluded
upper-level satellite winds and Quikscat winds respectively.

The experiment framework consisted of a two-week "spinup" period for the assimilations
followed by a two month evaluation period. During the evaluation period, 5-day forecasts
are run every other day for a total of 30 forecasts. The experiment periods used were
January-February 2003 and July-August 2003. The initial conditions for the assimilations
were taken from the CERES reanalysis assimilation run. The experiment setup is similar
to the CERES reanalysis except that the NOAA-17 radiance data is being used in these
experiments.

The following experiments were performed:

Data Impact Experiment Summary

Experiment	Description
r14_ctrl	control
r14_nraw	no rawinsondes
r14_nstw	no satellite winds (no CTW, no Quikscat)
r14_ntov	no DAOTOVS
r14_nups	no "uppersat" (= no sat wind, no DAOTOVS)
r14_wind	no height observations
r14_mass	no wind observations
r14_nctw	no cloud motion winds
r14_nqks	no Quikscat winds

Table 5.5: List of data withholding experiments and their identifying labels.

The results of these experiments were assessed using a variety of methods:

Assimilation assessment

- Assimilation anomaly correlation, RMS difference from control
- Bias and standard deviation of O-F (Observations minus Forecast)
- Quality control marks and QC rejection rates

Forecast skill assessment

- anomaly correlation
- RMS difference

A webpage with links to plots with outputs from these tests can be found at:

`http://gmao.gsfc.nasa.gov/intranet/personnel/msienkiewicz/r14_wexp/` .

The following discussion highlights some pertinent items from the results posted at that location.

The first four withholding experiments indicate that rawinsonde data is the primary source of information utilized by GEOS-4 in the Northern Hemisphere (NH). This was particularly true for the NH winter season, but applied to the NH summer season as well. This conclusion is drawn from the no-raob experiment having the largest impact in producing differences in the winter assimilation (vs the control, see Figure 5.43(top)), with lesser differences from the other experiments for the summer run (Figure 5.43(bottom)). The no-raob experiment showed the largest reduction in forecast skill of the four withholding experiments for both winter (Figure 5.44(top)) and summer (Figure 5.44(bottom)).

The "no-uppersat" (removing all satellite-derived data) had the largest impact in the Southern Hemisphere, during both experiment periods. (see Figures 5.45-5.46). Note that the removal of satellite winds (Quikscat and upper-level cloud cloud motion) had a larger impact than the withholding of satellite temperature retrieval data (compare the blue and green curves in Figures 5.45-5.46). Additional experiments were performed to determine the impact of removing Quikscat data and cloud-track wind data individually in the Southern Hemisphere. Figure 5.47 shows that withholding the Quikscat ocean surface wind data had a greater impact than withholding the upper-level cloud motion winds. This disparity may be a testament to the far greater and more persistent coverage of the Quikscat data in regions not receiving much coverage from the other components of the observing system.

A key aspect of the global observing system in 2003 was the presence of greatly improved satellite temperature sounding instruments, specifically ATOVS which has the Advanced Microwave Sounding Unit (AMSU). The ATOVS data had considerably less influence in the GEOS-4 assimilation system than is the case for the other NWP centers. That this is the case can be inferred by comparing the GEOS-4 impacts above with the position stated in the summary of the Third WMO Workshop on Impact of Observing systems on NWP (Alpbach, Austria March 2004, see

`http://www.wmo.int/web/www/GOS/Alpbach2004/Agenda-index.html`):

It is confirmed from all global data impact studies that satellite data, in particular ATOVS data, are the major source of information in NWP systems.

The consensus from other centers is that the impact of these data is on the order of 12-24 hours in forecast skill in the Northern Hemisphere extratropics, which is equivalent to or better than rawinsondes. It thus appears that the ATOVS data appear to be under-utilized in the GEOS-4 system.

Figure 5.43: (top) Analysis anomaly correlations, using NCEP analyses as verification, for the Northern Hemisphere, January-February 2003. Experiments here are the first 5 entries in Table 5.5. (bottom) As in (top), but for July-August 2003.

h500
Northern Hemisphere XTropics

h500
Northern Hemisphere XTropics

Figure 5.44: (top) Forecast Anomaly correlations, using their own analyses as verification, for the Northern Hemisphere, January-February 2003. Experiments here are the first 5 entries in Table 5.5. (bottom) As in (top), but for July-August 2003.
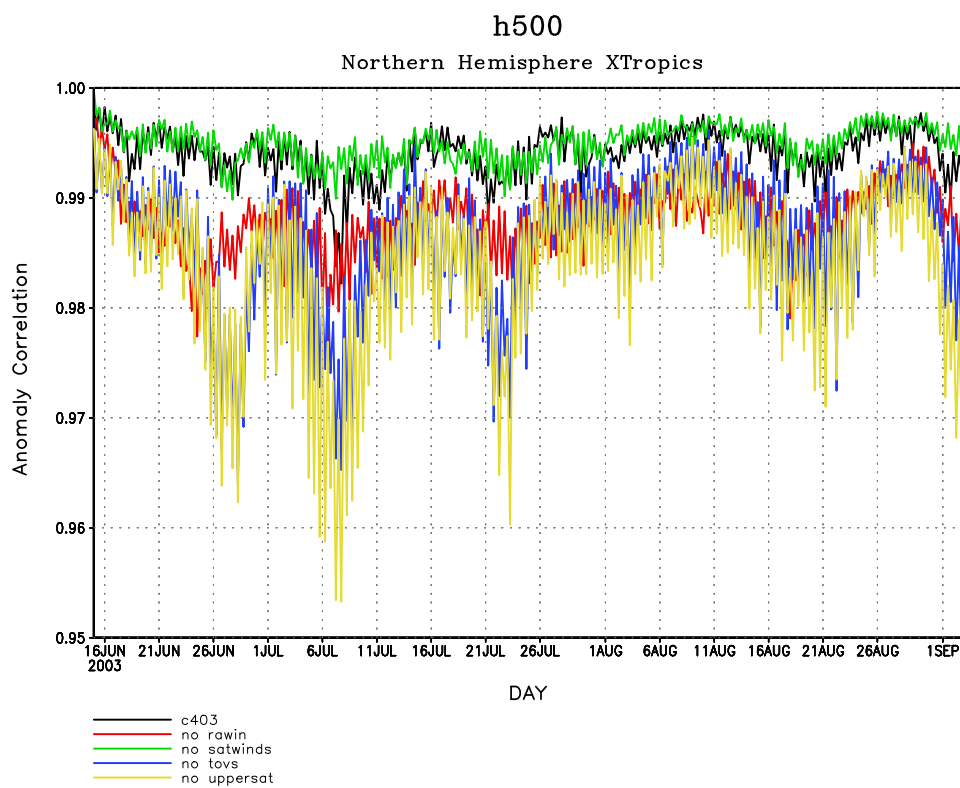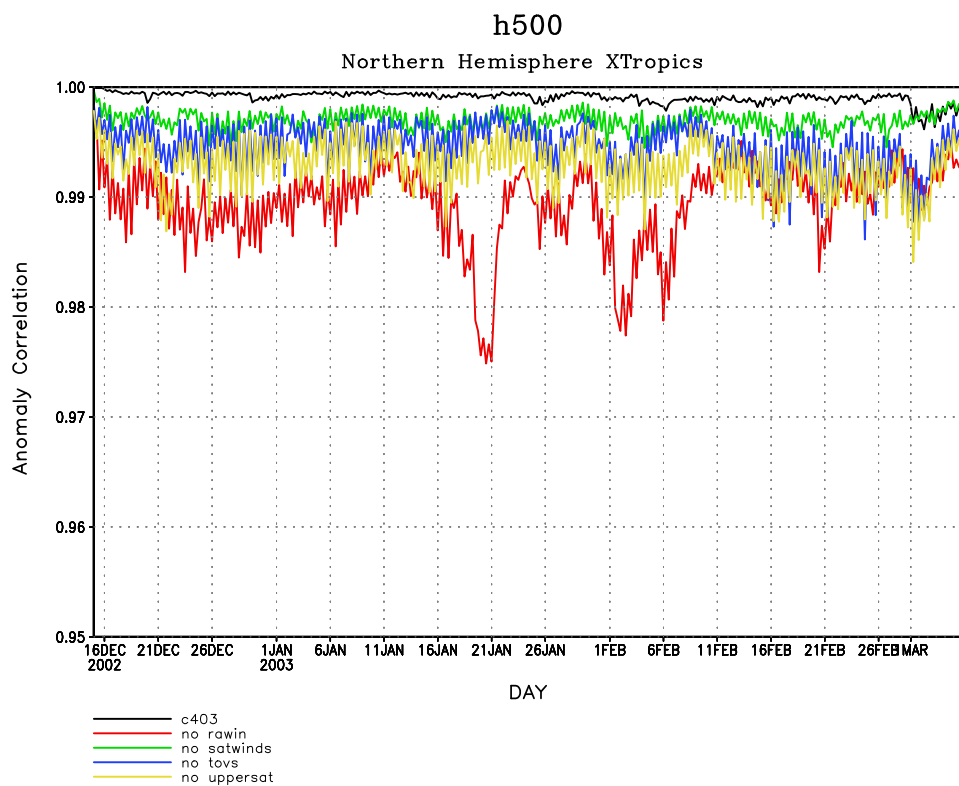
Figure 5.45: (top) Analysis anomaly correlations, using NCEP analyses as verification, for the Southern Hemisphere, January-February 2003. Experiments here are the first 5 entries in Table 5.5. (bottom) As in (top), but for July-August 2003.

h500

Southern Hemisphere XTropics

h500

Southern Hemisphere XTropics
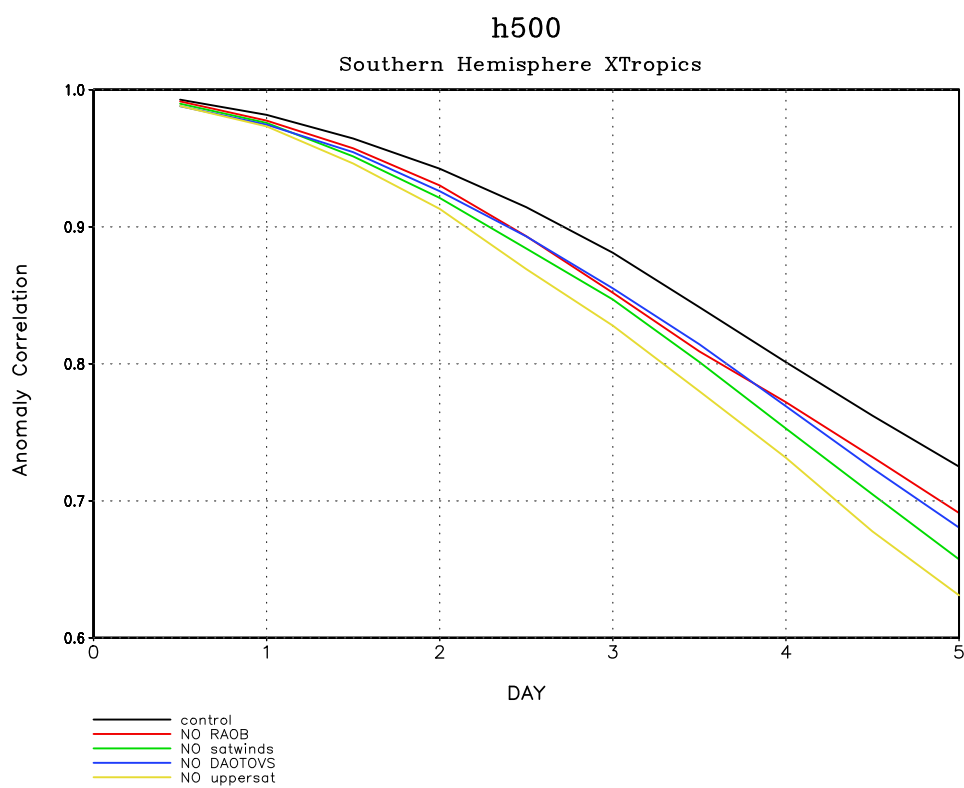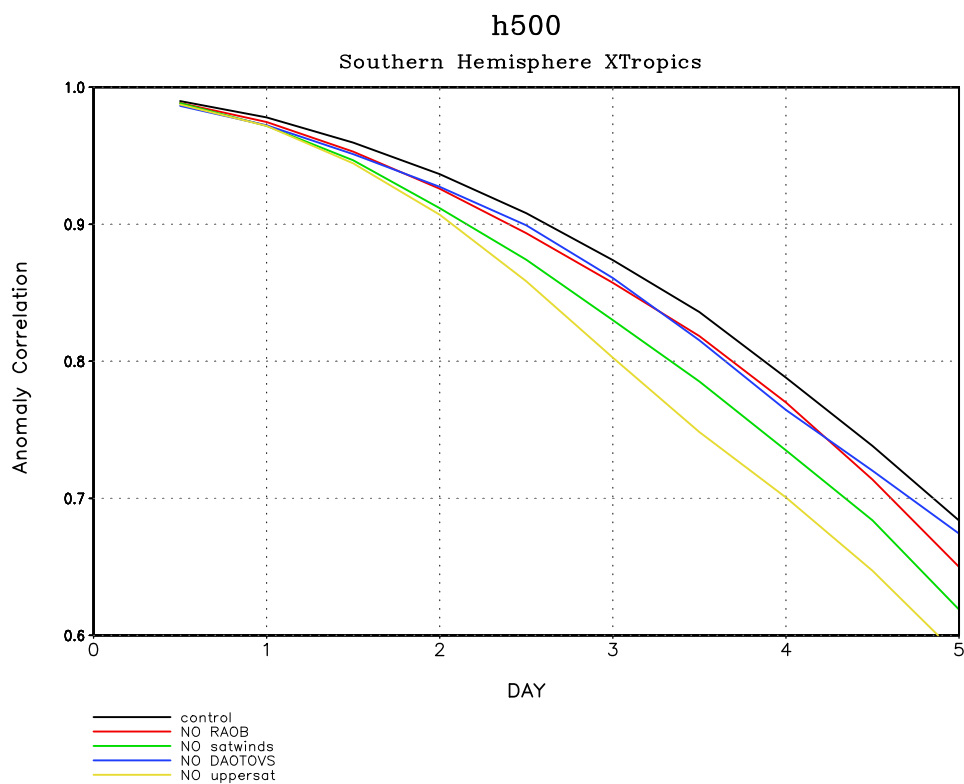
Figure 5.46: (top) Forecast Anomaly correlations, using their own analyses as verification, for the Southern Hemisphere, January-February 2003. Experiments here are the first 5 entries in Table 5.5. (bottom) As in (top), but for July-August 2003.
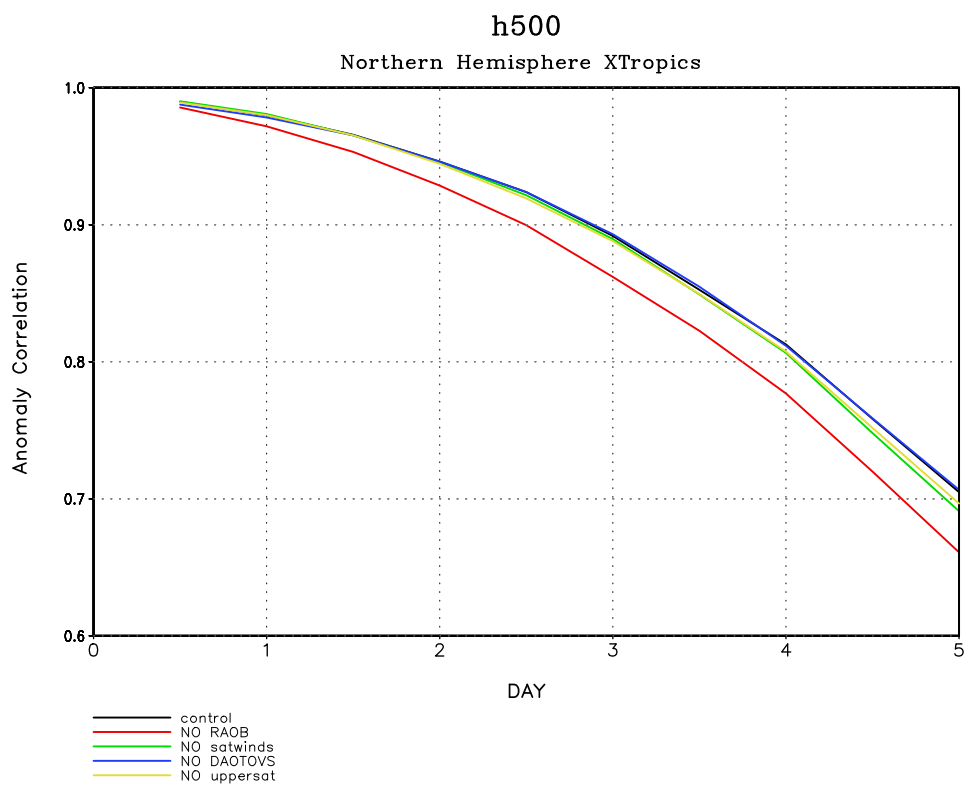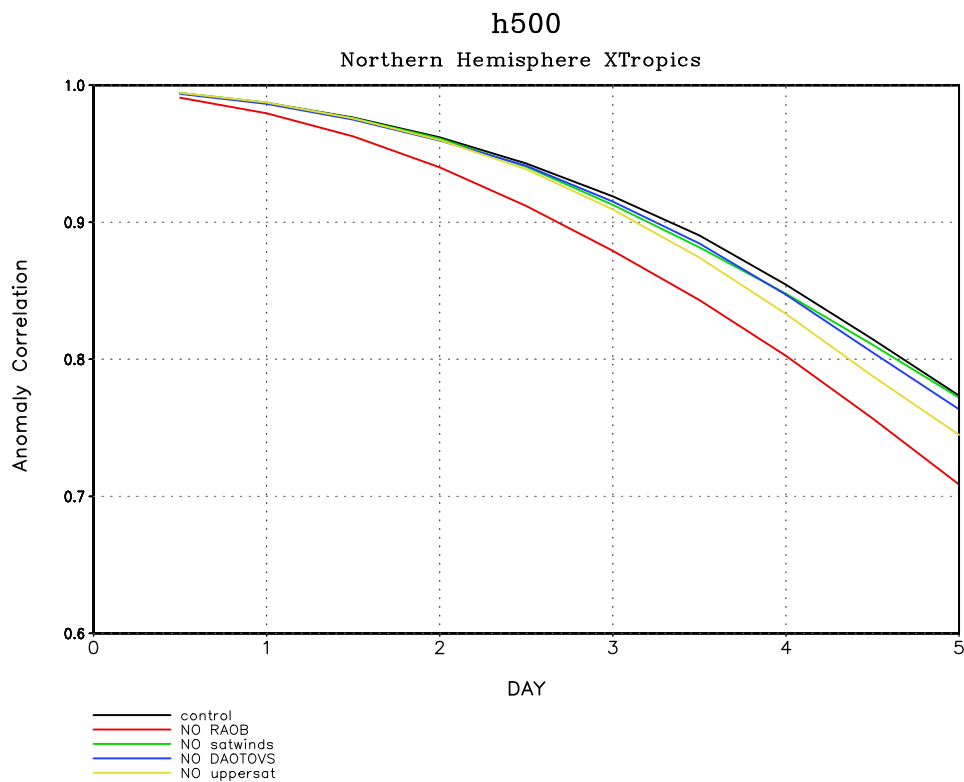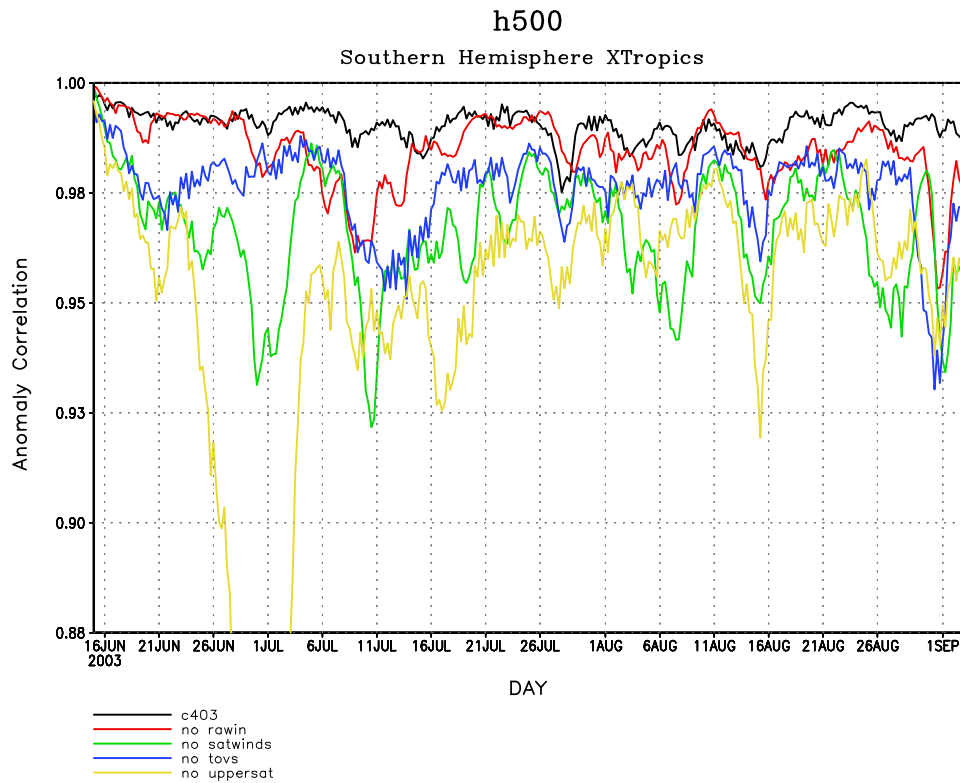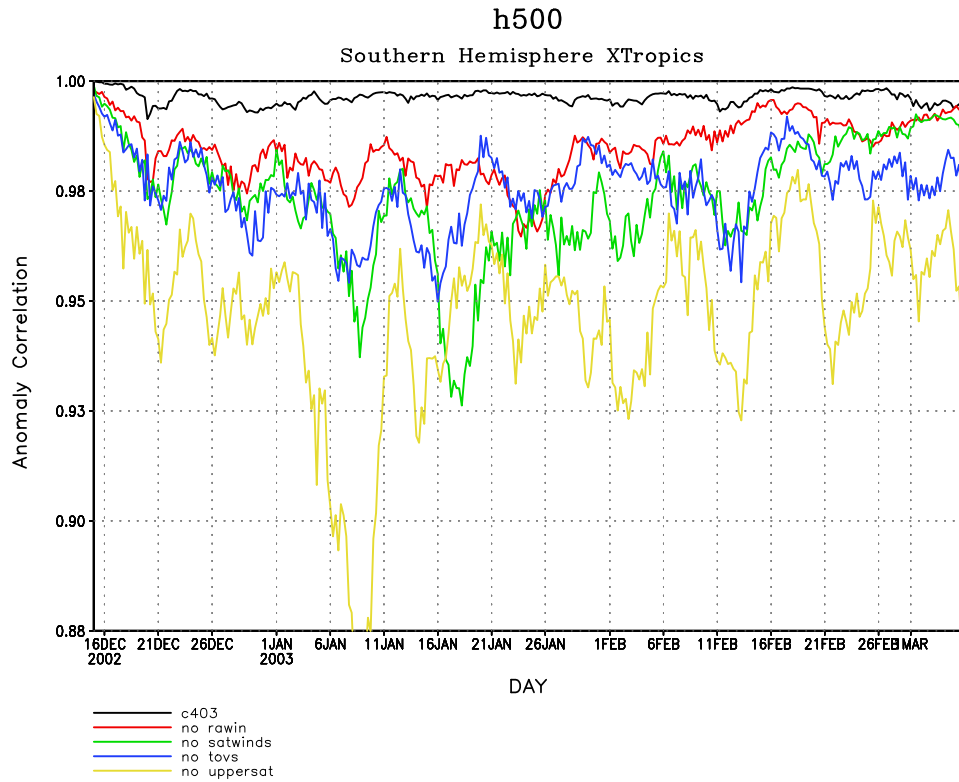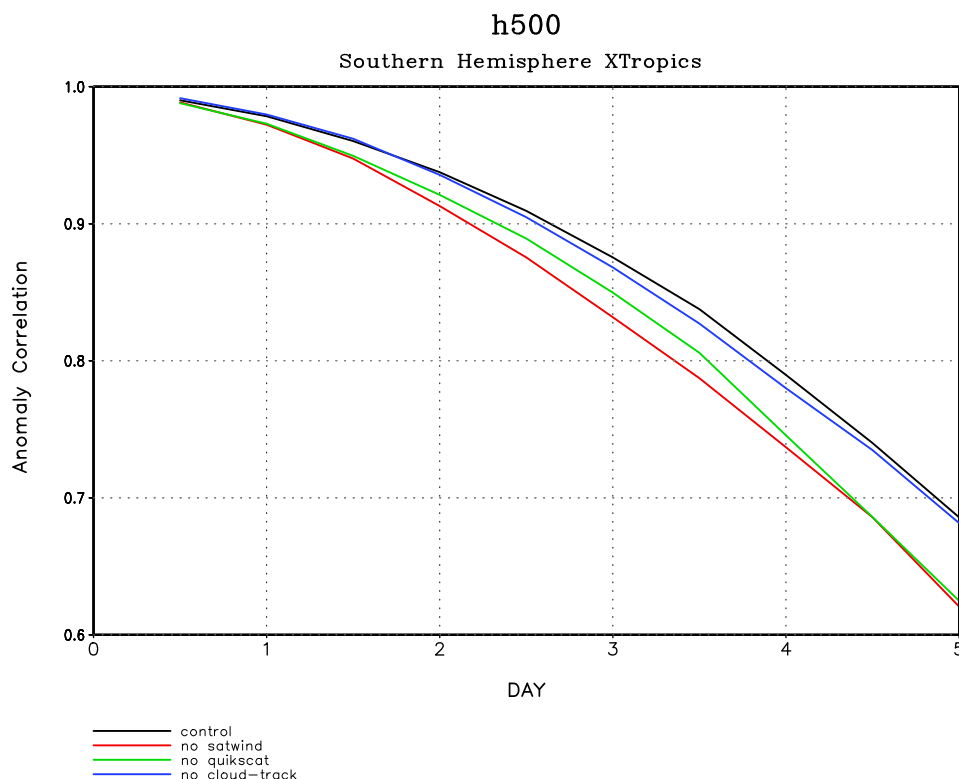
Figure 5.47: Forecast Anomaly correlations, using their own analyses as verification, for experiments examining the relative impacts of cloud motion winds and Quikscat surface winds, for the Southern Hemisphere, January-February 2003.

Profiles of (O-F) residuals for rawinsonde data for January and February 2003 were generated. The (O-F) values for the no-raob experiment (Figure 5.48) were calculated as a post-processing step using the same quality controlled rawinsondes as used in the control experiment. The no-raob experiment quite naturally had some large (O-F) bias especially in the Northern Hemisphere near 200 mb where we have previously seen some disagreement between rawinsondes and TOVS retrievals. The rawinsonde (O-F) bias for the no-TOVS and no-uppersat experiments were less than for the control experiment (the no-TOVS results are shown in Figure 5.49).
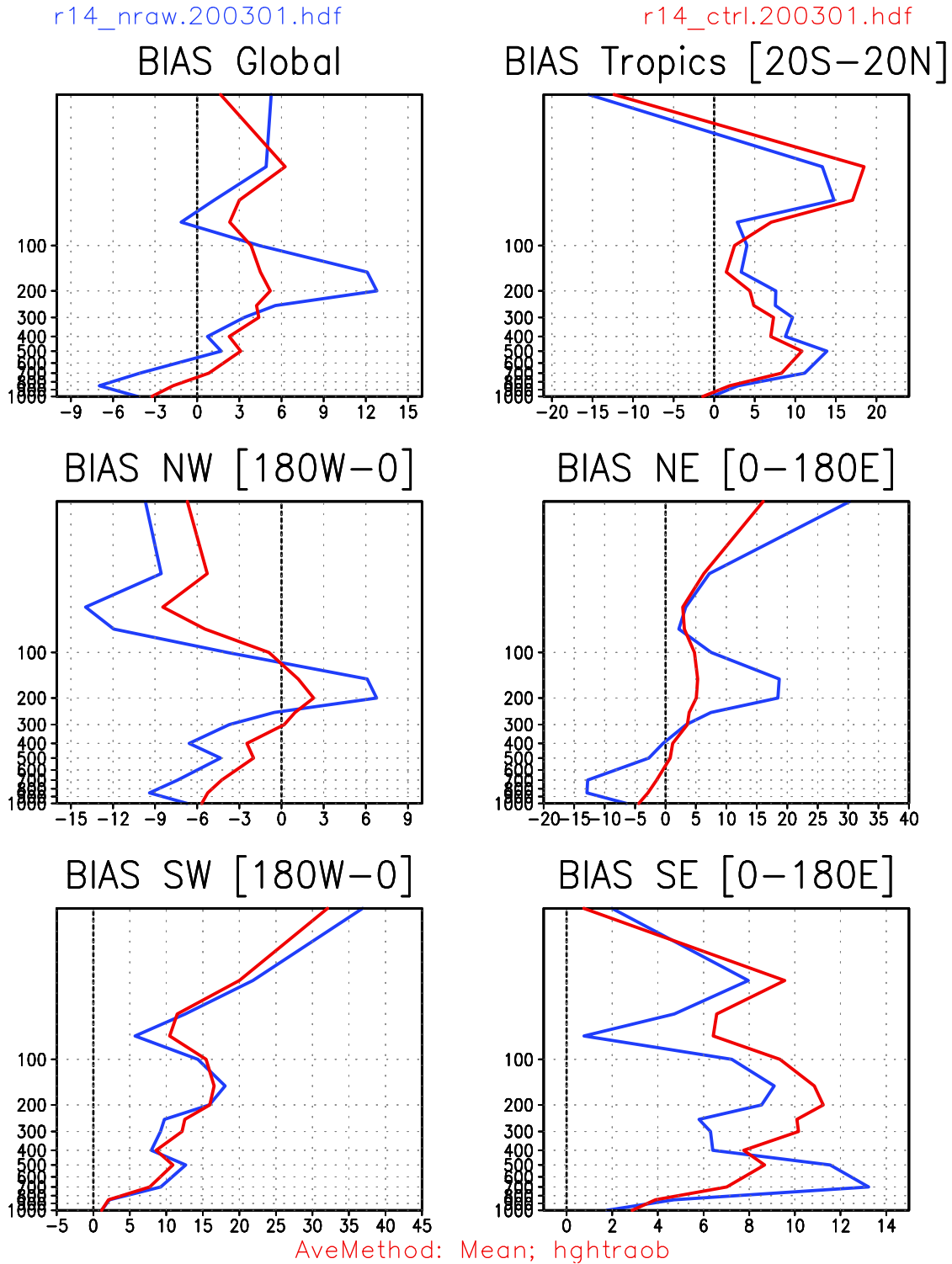
Figure 5.48: Profiles of areal mean O-F for the control (red) and no-rawinsonde experiments (blue), January-February 2003.
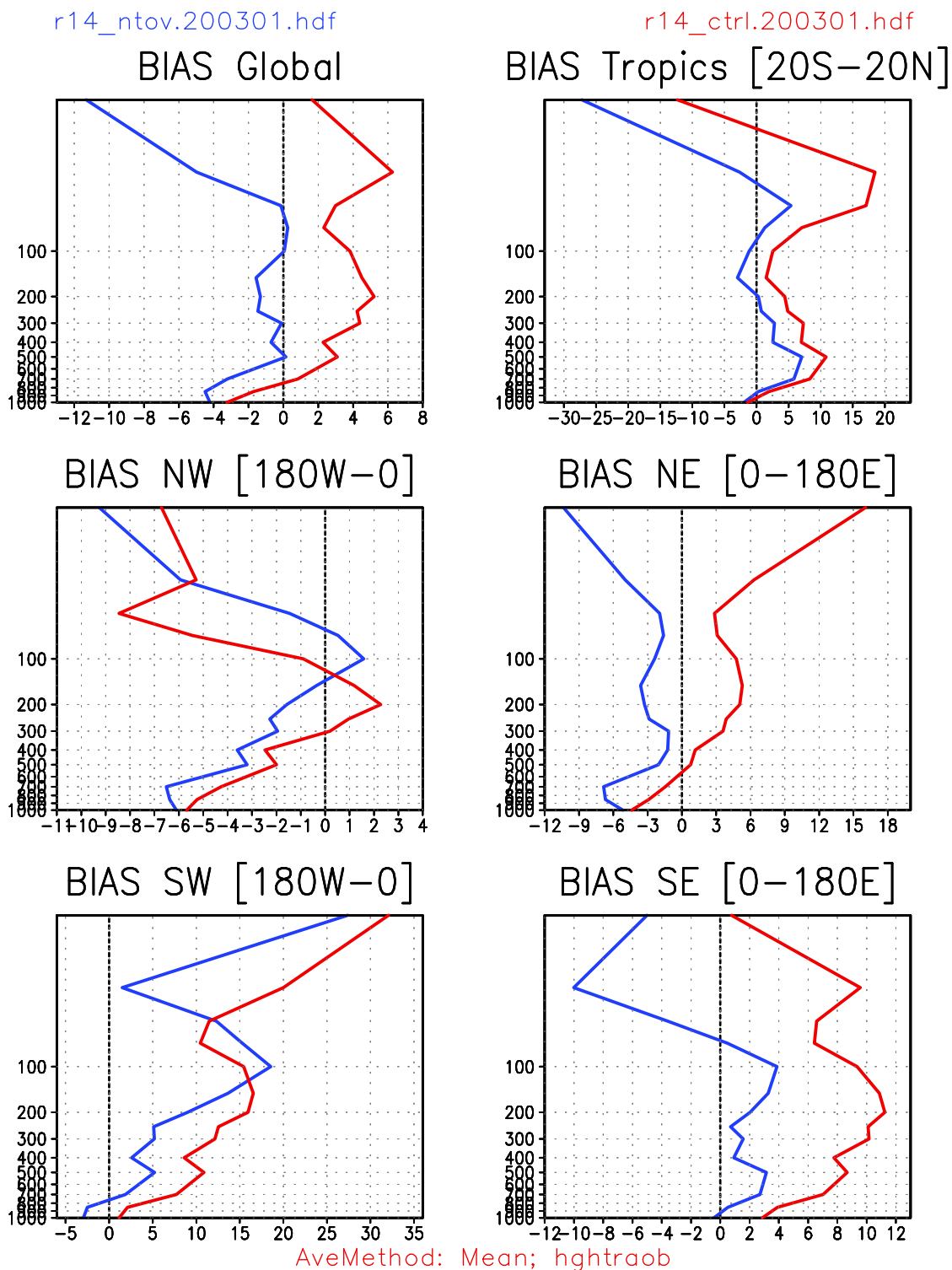
Figure 5.49: Profiles of areal mean O-F for the control (red) and no-TOVS experiments (blue), January-February 2003.

Complexities can arise in interpreting data withholding results, as can be seen from the no-wind versus no-mass experiments. Figure 5.50 shows that the no-mass assimilation (labeled "wind" in the figure) had a lower analysis anomaly correlation in the Northern Hemisphere than that from the no-wind experiment (labeled "mass" in the figure). The closeness of the control to the verifying analyses (from GEOS-4.0.1 in this case) is shown by the black curve in Figure 5.50. However, Figure 5.51 shows that the resulting forecasts from the above analyses had the opposite behavior; the no-mass experiment displayed greater forecast skill than did the no-wind experiment. Figure 5.52 shows that the no-wind assimilations consistently used more observations than did the no-mass assimilations (likely a result of the large number of TOVS height profiles in the no-wind assimilation). It should be noted that the forecast skill results discussed here were generated using their own analyses as verification. The results for the July-August 2003 no-mass and no-wind experiments behaved in a similar manner.

In summary, rawinsonde data in the GEOS-4 system have the largest impact on the Northern Hemisphere forecast skill, and the satellite winds (particularly Quikscat winds) have the largest impact on Southern Hemisphere forecast skill. Data withholding experiments with an earlier version of GEOS-4 (performed with data from 1998; results not presented here) indicated that the height data obtained from the interactive retrieval processing of TOVS radiances (see section 3.4) had only a modest impact on the GEOS-4 assimilation results. Although the impact of TOVS data on forecast skill is greater in GEOS-4.0.3 than in the prior versions of GEOS-4, the TOVS impact is still significantly less than that obtained by other centers. There is a concomitant over-sensitivity of the GEOS-4 system to rawinsonde data. Experiments with withholding mass and wind data show that a "better" analysis does not necessarily translate into better forecast skill.

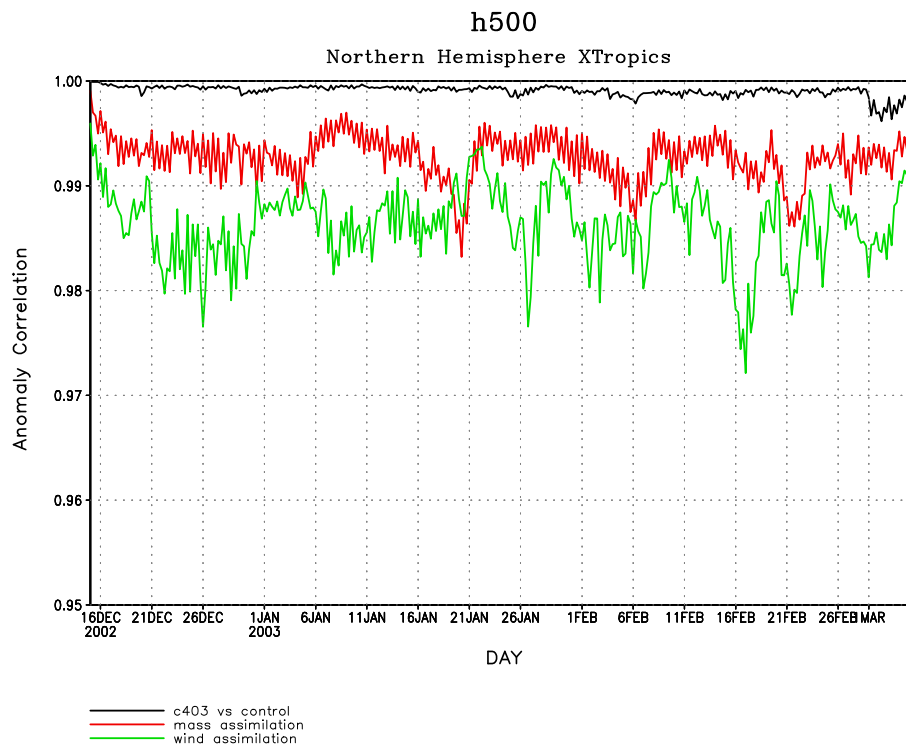Figure 5.50: Analysis anomaly correlation, GEOS-4.0.1 used as verifying analysis. No-wind assimilation (red), no-mass assimilation (green), control (black).
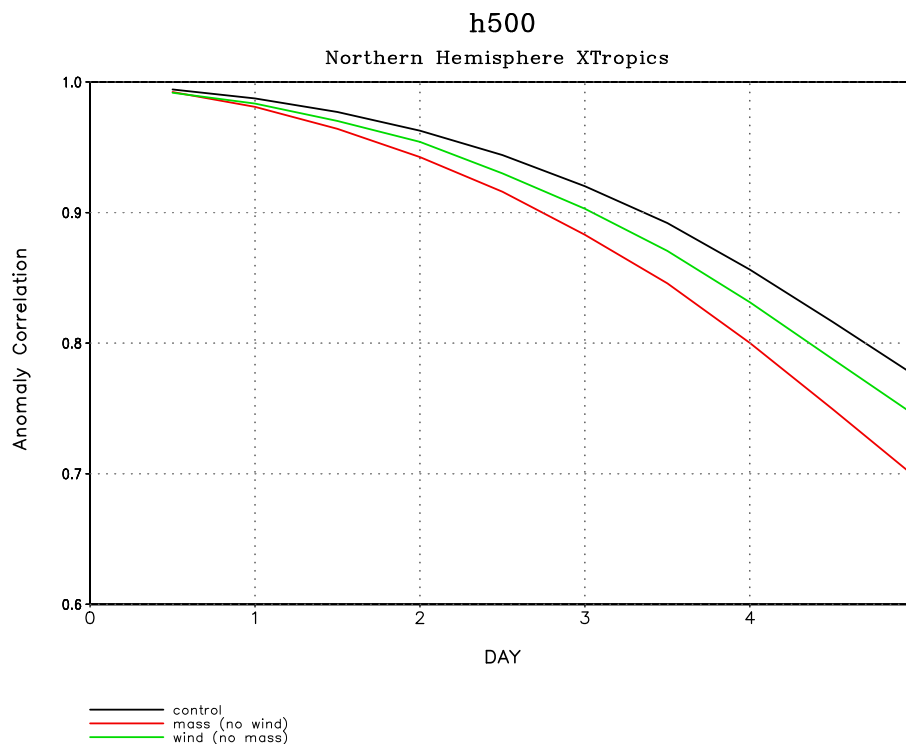

Figure 5.51: Anomaly correlation scores for January-February 2003, each experiment using its own analysis as verification.

Observation counts
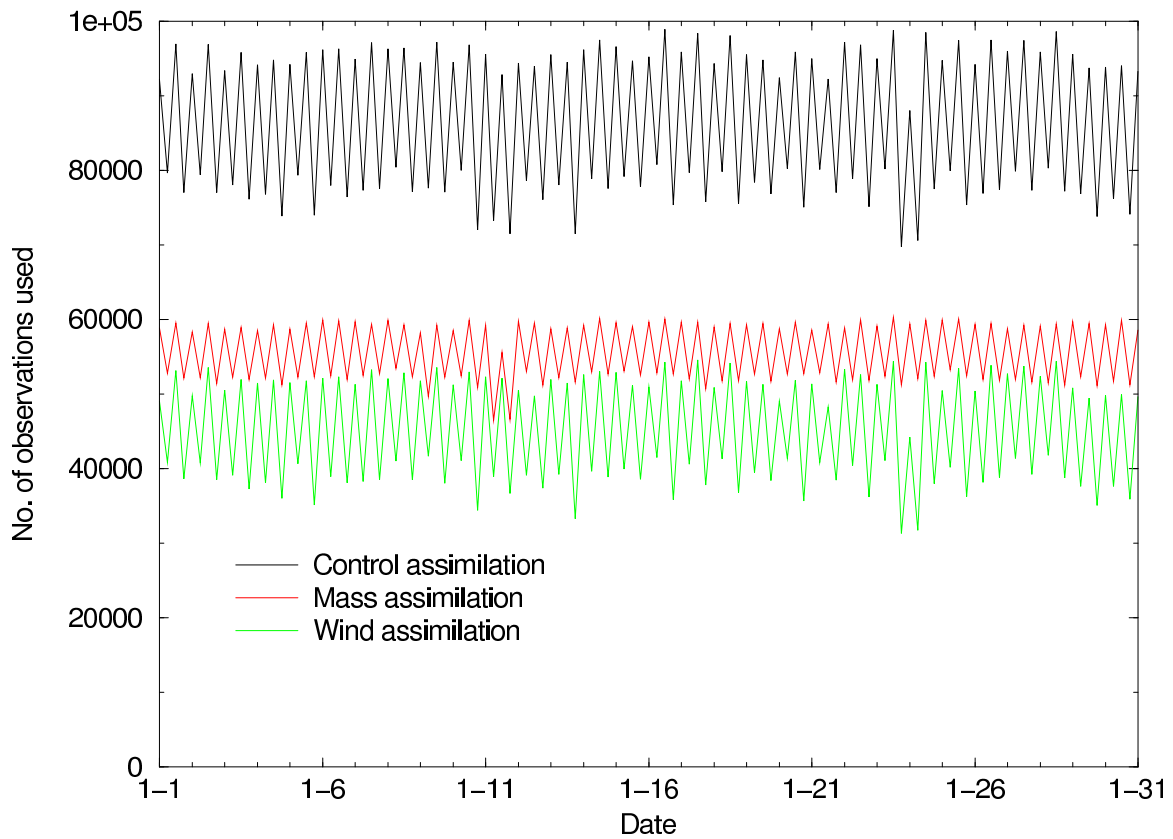
Figure 5.52: Observation counts during January 2003 for the control, no-mass and no-wind experiments.

5.8 Monitoring Results

One of the major components of the validation process is the assessment of the behavior of the candidate system while it is running in a "parallel" operational mode alongside of the previous operational version of the system. In this section, the behavior of the parallel system will be presented from the viewpoint of a number of broad monitoring categories: quality control statistics; observing system statistics (*e.g.* O-F and O-A time series); forecast skill scores; and individual case studies highlighting particular issues.

5.8.1 Quality Control

The overall behavior of the quality control process (described in section 3.3) is influenced by a number of factors, which can include both the errors in the observations as well as the assumptions about the model and observation error statistics. Figure 5.53 shows how the QC TOVS rejection statistics (for the month of September, 2003) changed from GEOS-4.0.2 to GEOS-4.0.3. The figure shows that the many changes made to obtain the GEOS-4.0.3 result in a markedly different TOVS QC rejection pattern. The older system had an unusual bimodal pattern, with significant rejections in the middle Troposphere, next to no rejections in the lower to mid Stratosphere, and a very steep rejection rate in the upper Stratosphere. The newer system flattens out this pattern, with the overall rejection rates tending to be lower, except for the lower to mid Stratosphere. Note that Figure 3.11 suggests that the "ideal" rejection rate should be roughly 4%.
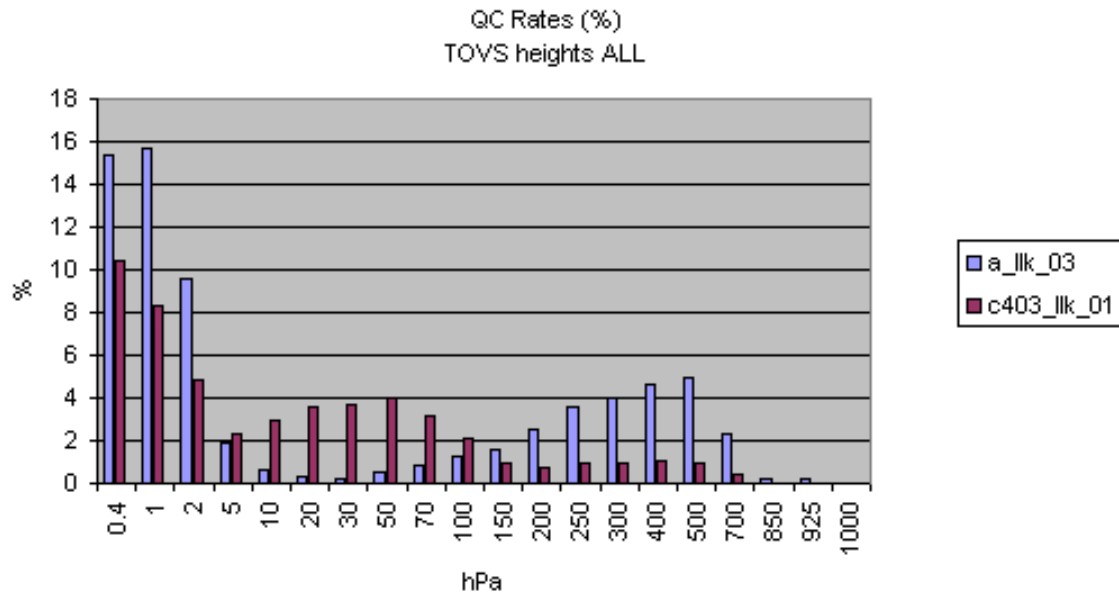
Figure 5.53: Quality control rejection rates for TOVS heights for two runs: GEOS-4.0.2 (blue) and GEOS-4.0.3 (red). Time period covered was September 2003.
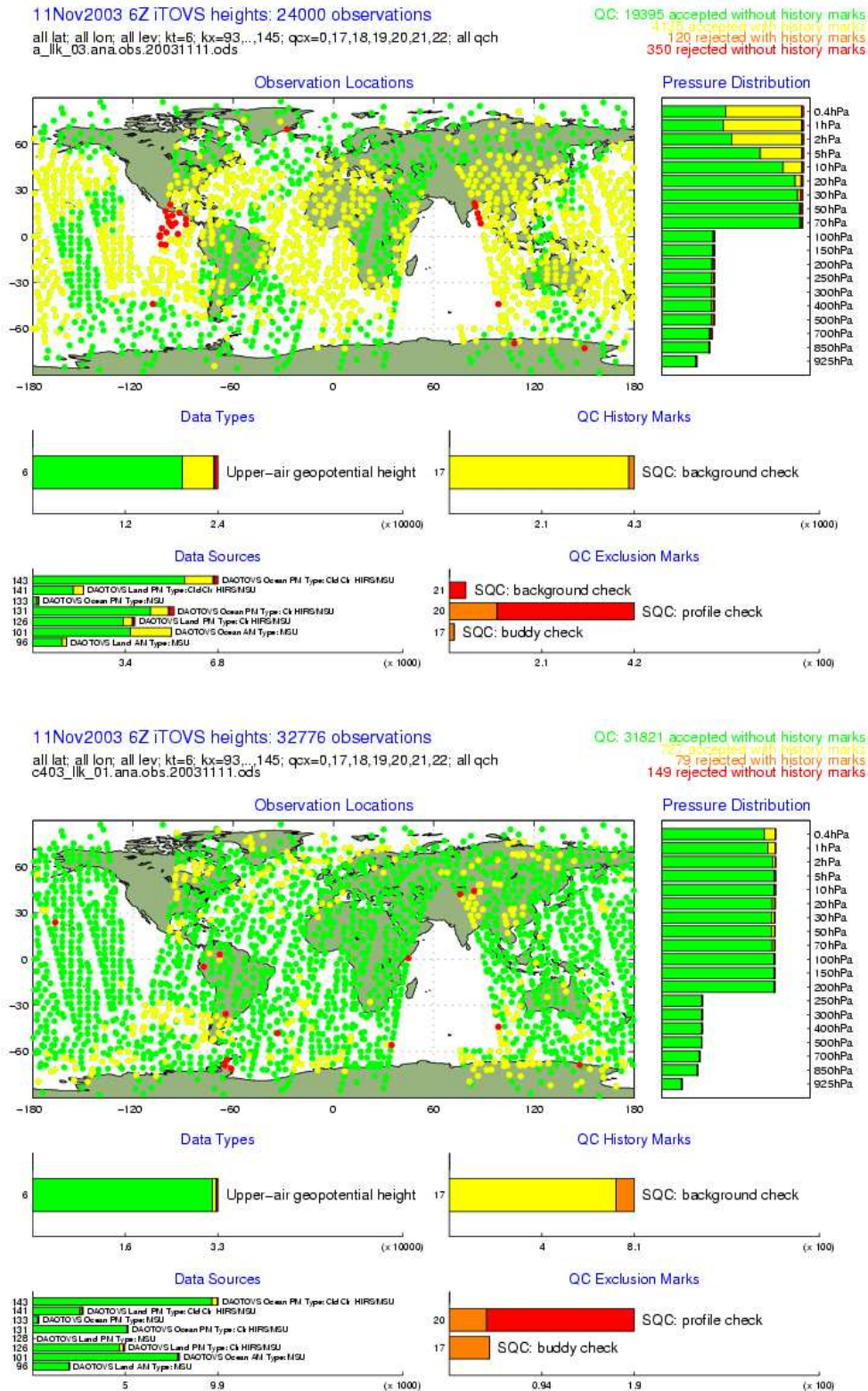
Figure 5.54: TOVS QC statistics for 11 November 2003 for GOES-4.0.2 (top) and GEOS-4.0.3 (bottom). Many fewer TOVS data are flagged in the newer system.
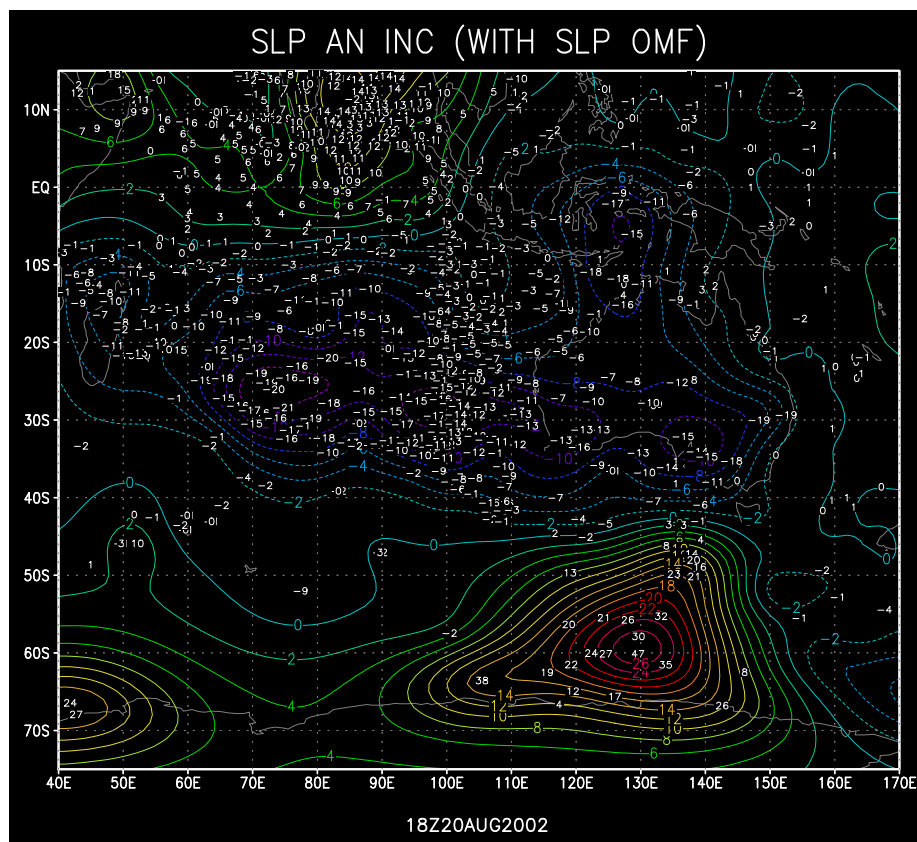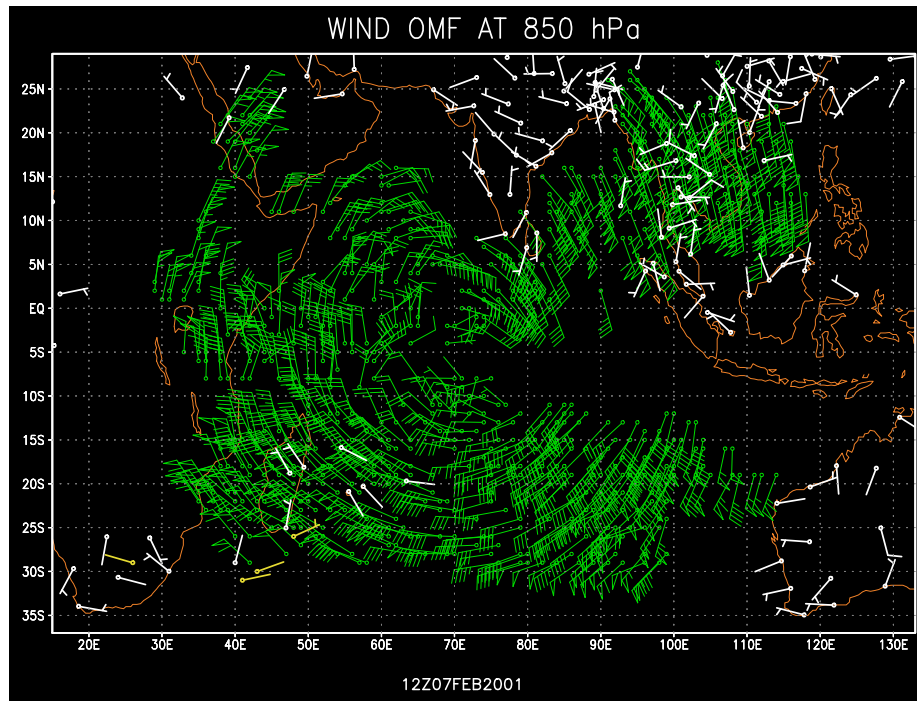
Figure 5.55: Two examples of ineffective background checking in older versions of GEOS. Top: inappropriate wind observations (green barbs, with each barb representing an O-F of $10\ m\ sec^{-1}$) in GEOS-4.0.2. Bottom: mislocated sea level pressure observations in GEOS-3 (white numerals, O-F units in hPa).
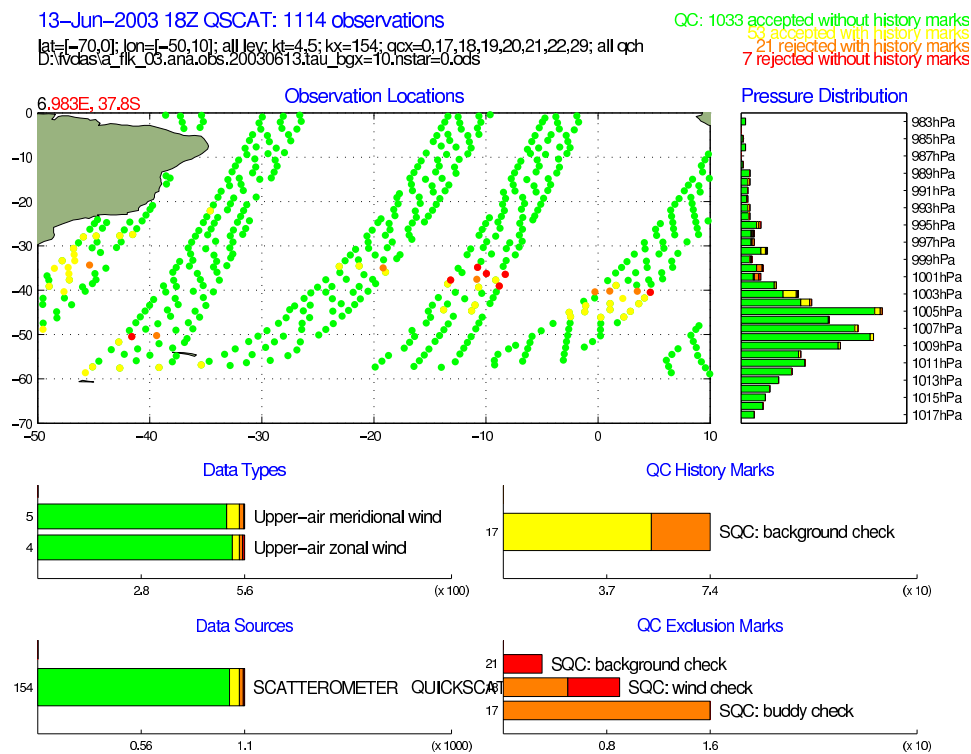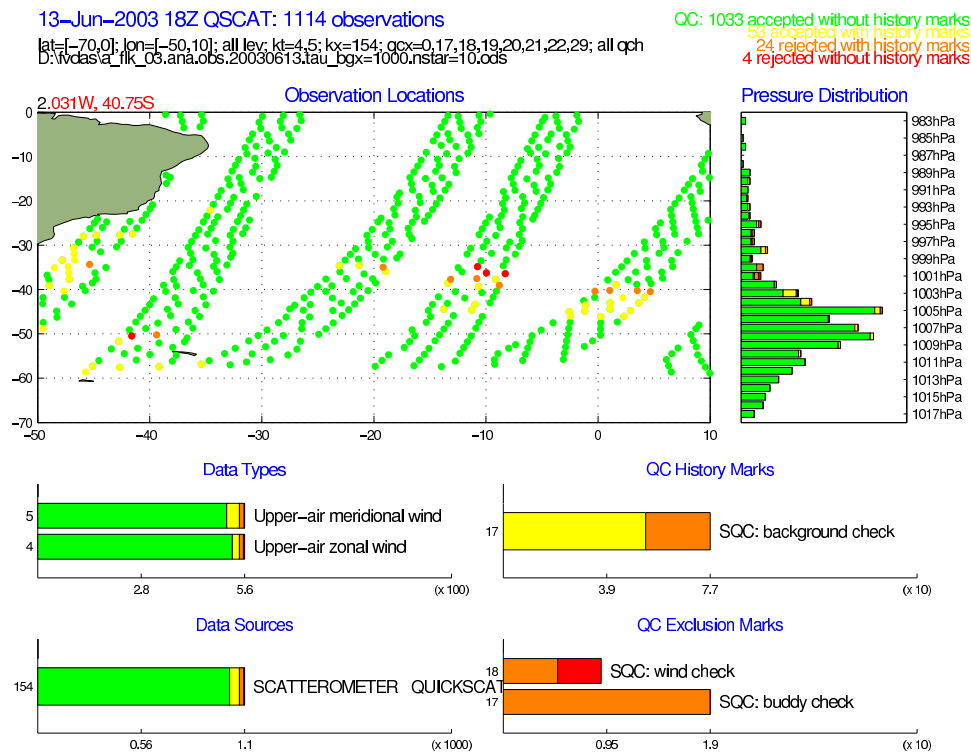
Figure 5.56: QuikScat QC statistics for 13 June 2003 for two runs which used two different values of τ_x (see section 3.3.2). Top panel used (old) $\tau_x = 1000$, bottom panel used (new) $\tau_x = 10$.

Another view of the difference in TOVS QC between GEOS-4.0.2 and GEOS-4.0.3 is shown in Figure 5.54. There is a large amount of information in each of the panels in this figure; the most striking aspect is the greatly reduced amount of data that were flagged/rejected in the newer system (compare the number of yellow or red dots between the top and bottom panels in Figure 5.54). The pressure distribution of the QC decisions (bar charts, top left in each panel) is also shows a significantly different behavior between the two systems, as there is something clearly strange occurring in the Stratosphere in GEOS-4.0.2, which will be shown in a different form in section 5.8.2. The difference in the level chosen as the cutoff for cloud-clearing in iRET (see section 3.4) between the two systems is marked by the change in where the abrupt "jump" in observation counts occurs in the pressure distribution charts (clearly showing the 200 hPa level chosen for GEOS-4.0.3).

A problem with the QC background check parameter (τ_x, see section 3.3.2) was identified in prior versions of GEOS. Figure 5.55 shows two extreme examples of poor QC behavior with $\tau_x = 1000$. In both cases, the failure of the background check to flag these *extremely* unrealistic data resulted in poor analyses; note the 50 $m\ sec^{-1}$ O-F winds at 850 hPa over Africa (top), and the 47 hPa sea level pressure O-F off the coast of Antarctica (bottom). Although the highly suspect data were flagged in each case, the buddy check was effectively swamped by the vast amount of suspect data and was therefore rendered ineffective.

Figure 5.56 shows an example of the impact on the QC decisions made for QuikScat winds by changing the background check parameter from 1000 to 10 (the value used for GEOS-4.0.3). In this case, 13 June 2003 over the South Atlantic, the change resulted in three additional QuikScat observations being rejected prior to the Buddy Check process. This case will be described in further detail in section 5.8.4.

5.8.2   Observing System Statistics

The most effective tools to date for monitoring the ongoing behavior of GEOS DAS systems have been time series of means or RMS for Observation minus Forecast ("OMF") or Observation minus Analysis ("OMA"), for specified regions and specific observation types. These diagnostics readily identify such observing system problems as data-dropout or instrument drift. In addition, some of the more subtle aspects of how a DAS is handling different aspects of the observing system can be inferred by examining how the OMF time series compares to the OMA time series.

Figure 5.57 shows a multi-year time series of OMF for GEOS-4.0.2 (red) and GEOS-4.0.3 (blue). There were two significant changes in the observing system over this time period: NOAA-15 HIRS (see section 3.2.3.4.1) was removed from iRET processing due to excessive noisiness starting 31 May 2000; NOAA-16 data began to be used in iRET processing starting 2 March 2001. GEOS-4.0.2 had an immediate Tropospheric response in March 2000, with the TOVS OMF global time series becoming much noisier (and larger). The Stratospheric OMF response in the older system was slower to appear, yet grew to very large amplitudes by November 2000. The GEOS-4.0.3 response to the loss of NOAA-15 was considerably milder, with smaller and less noisy values of TOVS OMF throughout. The response of both systems to the introduction of NOAA-16 data also had GEOS-4.0.2 having abrupt transitions in behavior, with a far more modest change in the behavior of OMF in GEOS-4.0.3. Note the divergent nature of the impact on 1 hPa OMF in the two systems,

Figure 5.57: Time series of global RMS TOVS O-F for height (units m). GEOS-4.0.3 (blue), GEOS-4.0.2 (red). Time period ranges from 16 January 2000 to 30 April 2003.
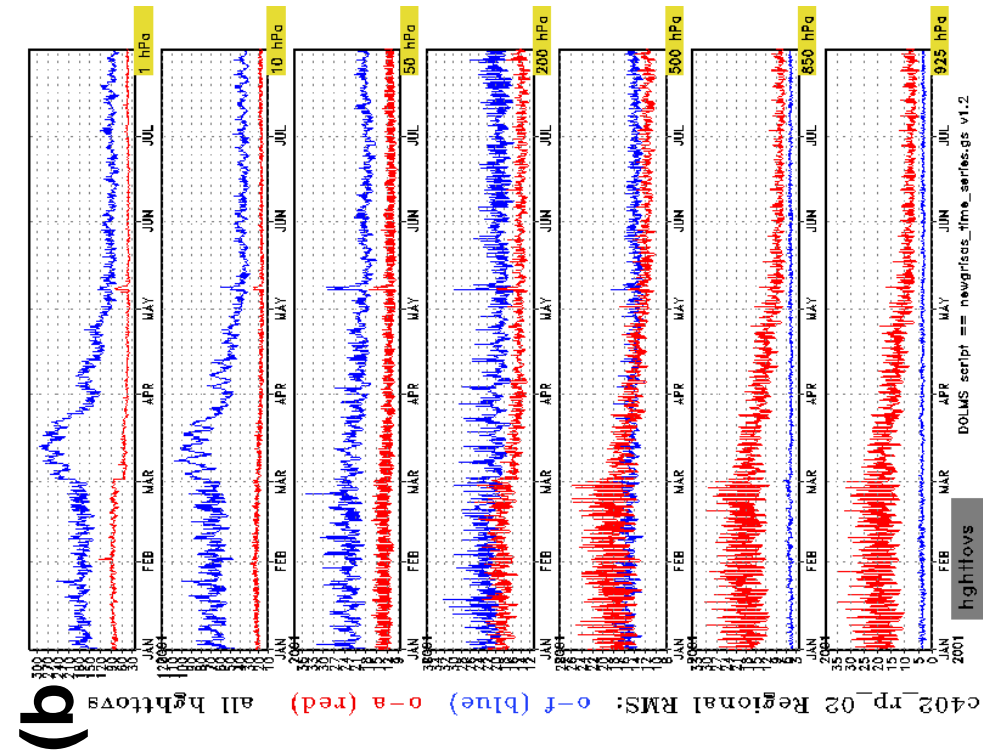
Figure 5.58: Time series of global RMS TOVS O-F (blue) and O-A (red) for height (units m); (a) GEOS-4.0.3 , (b) GEOS-4.0.2. Time period ranges from 1 January 2001 to 31 July 2001. Note the differing scales on the ordinates between the two sets of plots.
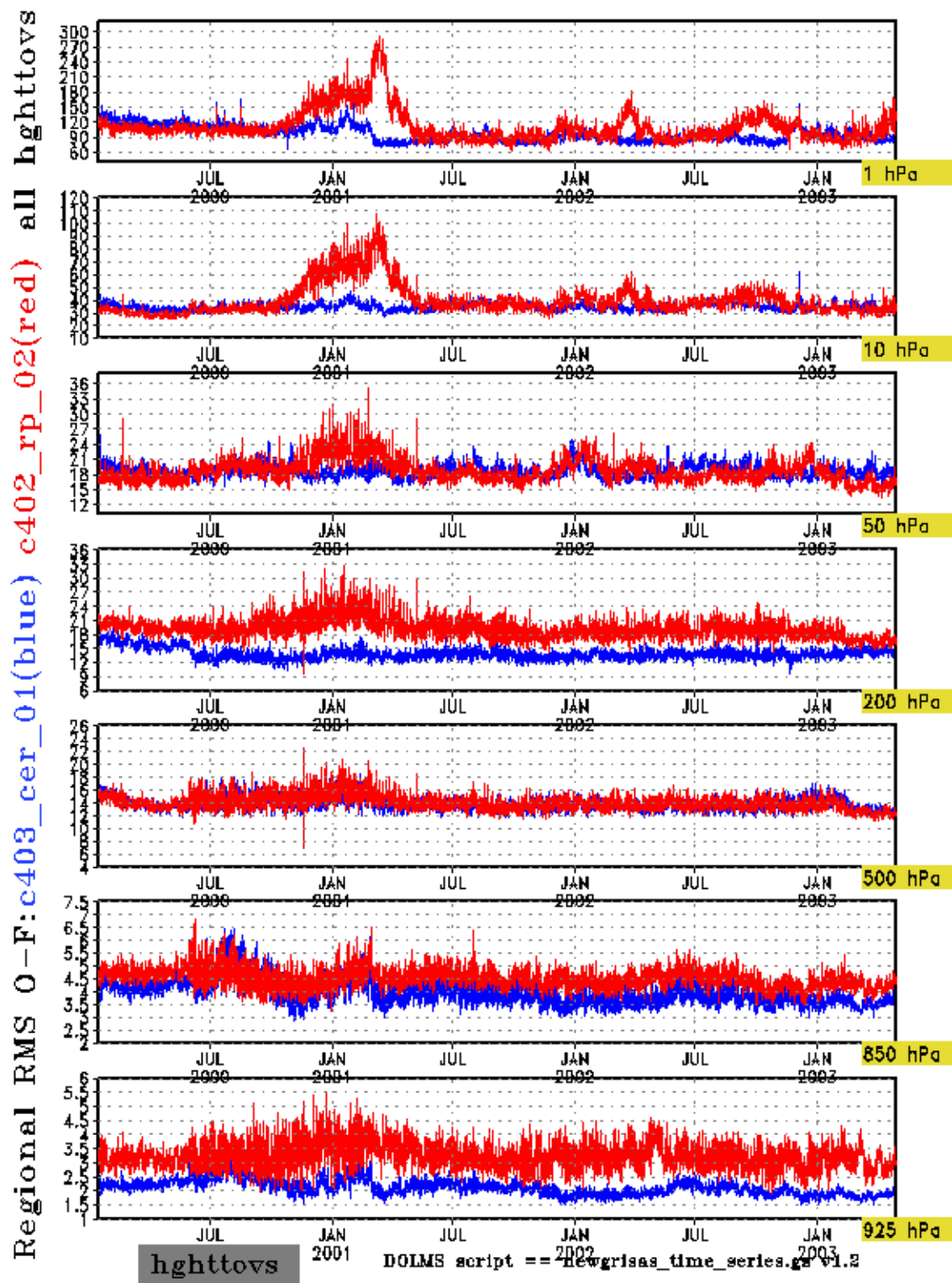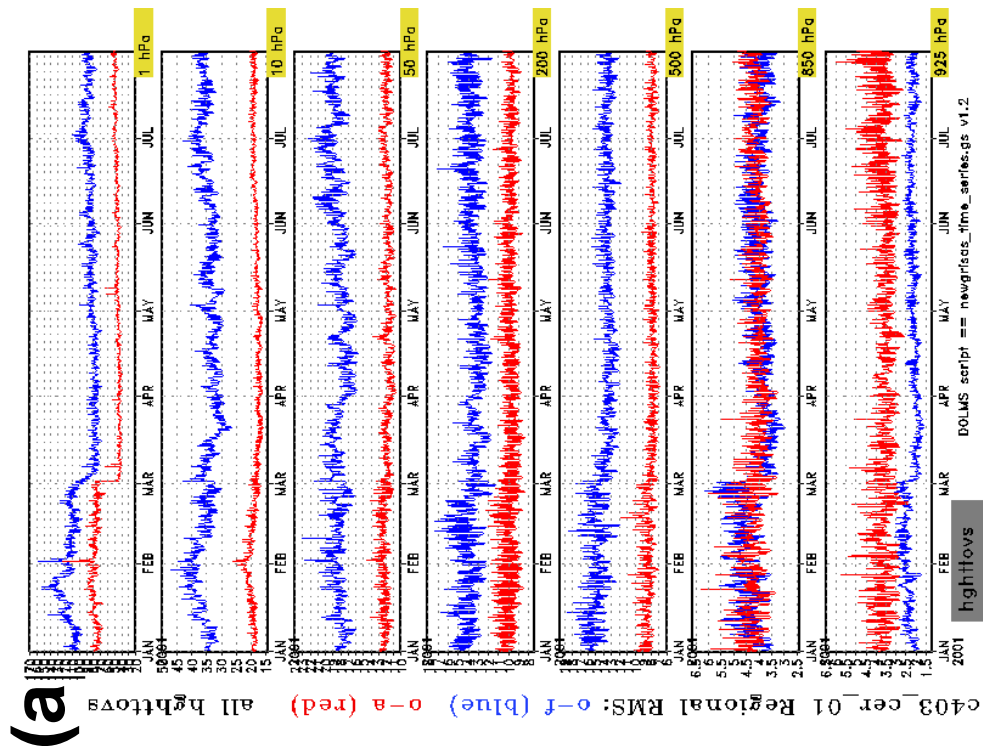
Figure 5.59: Time series of global RMS and global mean TOVS O-F for height (units m). GEOS-4.0.3 (blue), GEOS-4.0.2 (red). Time period ranges from 1 August 2003 to 24 November 2003.
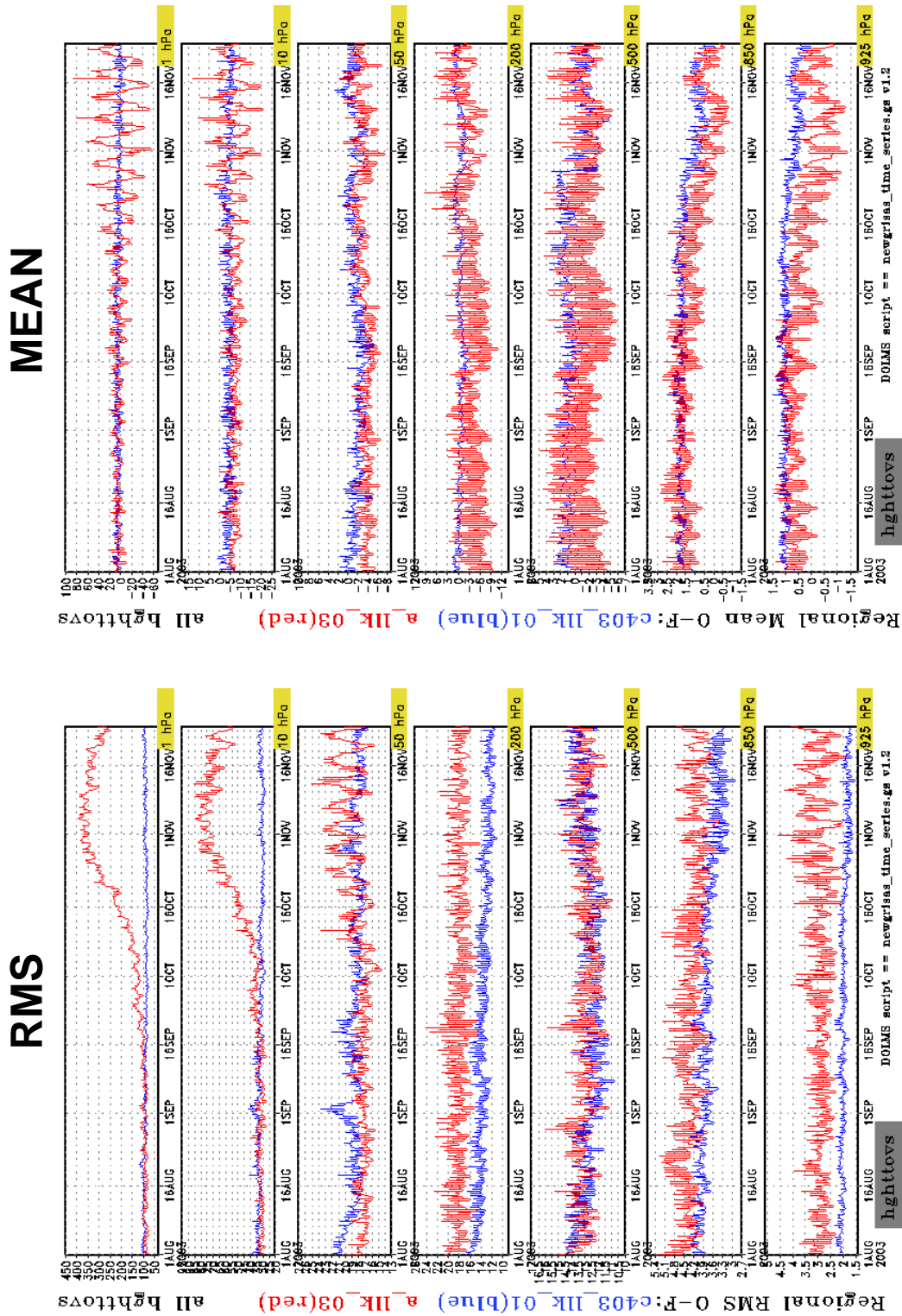
with the GEOS-4.0.2 OMF nearly doubling while the OMF from GEOS-4.0.3 is reduced by nearly half.

Figure 5.58 focuses on the NOAA-16 transition period, showing both OMF and OMA time series for GEOS-4.0.2 and GEOS-4.0.3. Of particular interest is the differences in OMA behavior between the two systems. In the Stratosphere, the OMA behavior is nearly the same for the two systems (note the differing ordinate scales in this figure), despite the very large differences in OMF. In the Troposphere, the TOVS OMA from GEOS-4.0.2 are significantly noisier and have greater magnitudes than those from GEOS-4.0.3 both before and after the NOAA-16 transition. In addition, the pre-transition OMA for GEOS-4.0.2 is larger than OMF for most of the Troposphere, to a much greater degree than is the case for GEOS-4.0.3. This suggests that even with a significantly reduced TOVS data coverage (roughly half, pre-transition), the contributions from other data types lead to analyses that better agree with the remaining TOVS data (*i.e.* smaller TOVS OMA) for GEOS-4.0.3. The post-transition reduction of OMA for GEOS-4.0.2 simply reflects the greater number of TOVS observations affecting the analysis. Finally, note that the transient effect of the observing system change lasts for nearly two months for GEOS-4.0.2, while it is nearly instantaneous for GEOS-4.0.3.

A more disturbing aspect of the behavior of GEOS-4.0.2 is shown in Figure 5.59, for a time period (August-November 2003) during which there was no significant change to the observing system. The RMS TOVS OMF for GEOS-4.0.2 grew nearly four-fold in the Stratosphere (while that from GEOS-4.0.3 remained level) over a two month period. The mean global TOVS OMF for GEOS-4.0.2 displayed a peculiar 3-4 day oscillation that grew in amplitude throughout the period. Although never fully diagnosed, this oscillation seemed to be a result of some feedback process involving the model, the analysis and the interactive retrieval system. It is not in evidence in GEOS-4.0.3.

In summary, previous versions of GEOS-4 (of which GEOS-4.0.2 is an example) were overly sensitive to perturbations in the observing system, and this sensitivity appears to have been reduced to reasonable levels in GEOS-4.0.3. In addition, the handling of TOVS data appears to be more consistent with other observations in GEOS-4.0.3 than in GEOS-4.0.2.

5.8.3 Forecast Skill

Forecast skill has long been (and remains, at operational centers) a crucial measure of performance for an assimilation system. Although the provision of forecast products is not the central mission of the GMAO, the forecast behavior of GEOS nevertheless provides a realistic quantitative context for judging the overall system performance. The tool of choice here is the *anomaly correlation*, which is the pattern correlation between an anomaly (*i.e.* difference from climatology) of a forecasted field against an anomaly of a verification analysis field. The principal fields examined by this approach are 500 hPa geopotential height and sea-level pressure; occasionally upper-air wind components are also tested.

For the results presented here, the anomaly correlations of 500 hPa heights and sea-level pressure were computed at $2° \times 2.5°$ degrees, using both the NCEP operational analysis and GEOS analyses as verification; forecast and verification fields were smoothed to the $2° \times 2.5°$ resolution. The climatology used for these calculations is a 10-year (1987-1998) average of a

$2° \times 2.5°$ gridded ECMWF product. The region covered in each hemisphere range from $20°$ to $80°$, so that the polar regions and the Tropics are excluded from the anomaly correlation calculation. Three time periods were examined: December 2000 through February 2001; June 2001 through August 2001; and 1 September 2003 through 19 November 2003. For the runs in 2001, 5-day forecasts were generated every third day, for a sample size of about 30 members. The 2003 runs generated a 5-day forecast every day, for a sample size of 70-80 (there were some drop-outs due to availability of verification data sets).

Figure 5.60 shows the 500 hPa anomaly correlation results from the 2003 period. In this figure, "SELF" indicates that each forecast used analyses from its own assimilation system as verification, while "NCEP" indicates the use of NCEP operational analyses for verification. There is a clear signal of a positive impact on forecast skill in going from GEOS-4.0.2 to GEOS-4.0.3. The signal is in both hemispheres, and it is robust with respect to choice of verification. The 2003 forecasting period corresponds to the period where the feedback problems evident in OMF and OMA (described in section 5.8.2) became very evident.

Very similar results (not shown) were obtained from the sea-level pressure anomaly correlation. Figure 5.61 shows the day by day variability in the Northern Hemisphere pattern correlation at 5 days, the average of which ends up being one point on a curve in Figure 5.60. Gaps in Figure 5.61 indicate missing verification data.

The results from the two time periods in 2001 are less definitive. In general, the 2001 anomaly correlations are lower than their counterparts in 2003. Figure 5.62 shows an example for sea-level pressure in the Northern Hemisphere. The GEOS-4.0.3 anomaly correlation (red curve in each figure) has nearly one day less skill for the 2001 cases (June-August) than for the 2003 cases (September-November). In addition, the impact of changing systems for the 2001 periods is greatly reduced. It appears that the observing system problems discussed in section 5.8.2 continued to affect the performance of both of the GEOS systems, even after the OMF signatures had quieted down during the Summer months of 2001.

5.8.4   Case Studies

A number of issues were examined via case studies during the parallel validation run of GEOS-4.0.3, examples of which include:

- a detailed examination of the QC process;

- an assessment of the improvement in low-level RH behavior over Antarctica;

- an examination of the precipitation behavior;

- a number of synoptic cases, mainly to assess the impact of the modification of the wind-mass balance covariance model.
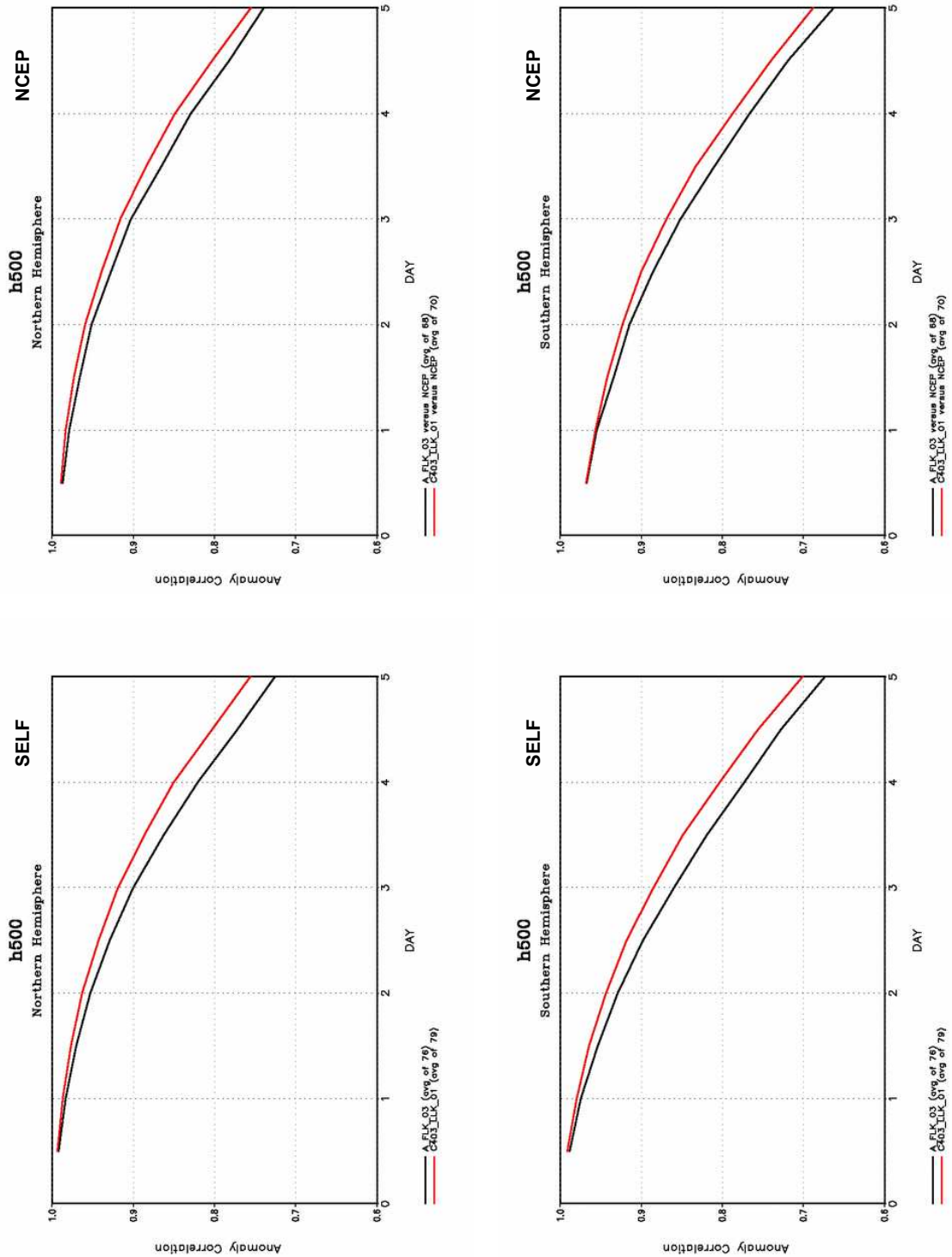
Figure 5.60: 500 hPa geopotential height anomaly correlation forecast skill. Left panels using GEOS (either 4.0.2 or 4.0.3) analyses as verification, right panels use NCEP analyses. Red curves are GEOS-4.0.3, black curves are GEOS-4.0.2. Cases span September-November 2003 (see figure 5.61).
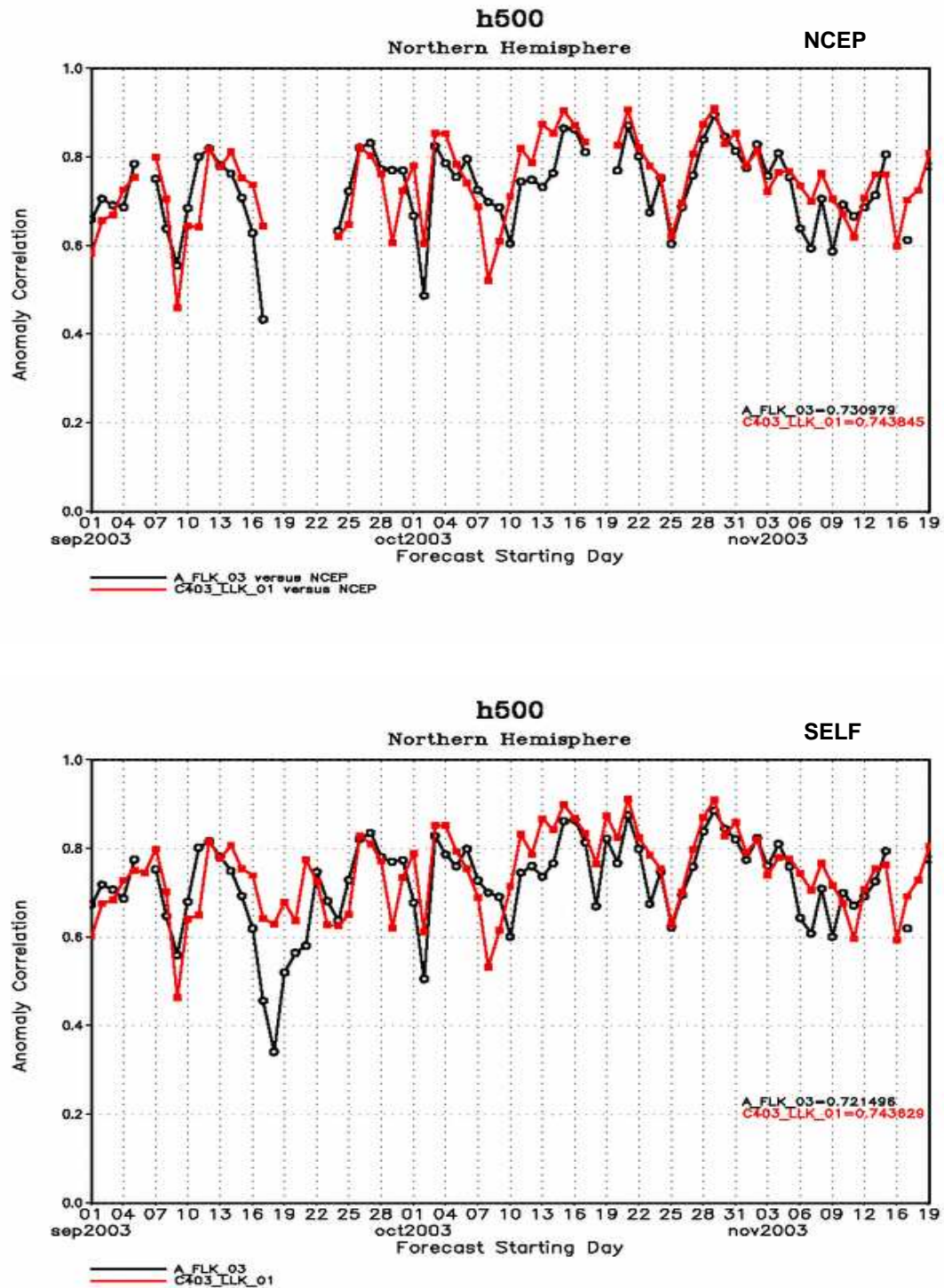
Figure 5.61: Time series of individual 5-day 500 hPa geopotential height forecast skills in the Northern Hemisphere. Top panel used NCEP analyses as verification, bottom panel used GEOS (either 4.0.2 or 4.0.3) analyses as verification. Red lines are GEOS-4.0.3, black are GEOS-4.0.2.
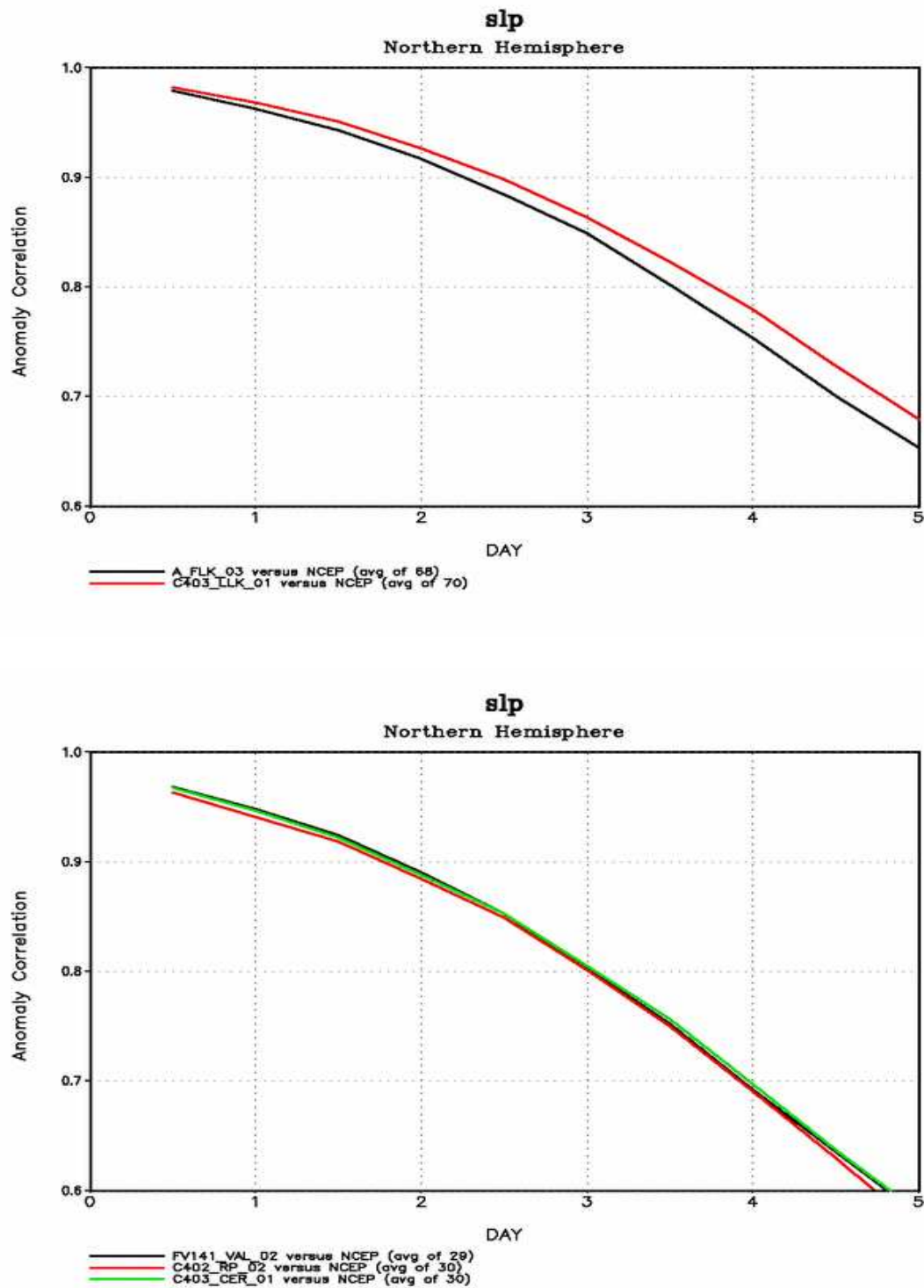
Figure 5.62: Sea level pressure anomaly correlation comparison. Upper panel has cases from September-November 2003, the red curve is GEOS-4.0.3 and the black curve for GEOS-4.0.2. Lower panel has cases from June-August 2001, the green curve is GEOS-4.0.3 and the red curve is GEOS-4.0.2.

5.8.4.1 QC example

The situation shown in Figure 5.56, 13 June 2003, merits further discussion. Figure 5.63 revisits this situation, showing the GEOS-4 analyzed winds at 1000 hPa, with the QC accepted wind observations (black) and QC rejected wind observations (heavy red) superimposed. The three observations affected by the QC change are outlined by heavy blue contours. The two observations near 12W and (especially) 8W definitely appear to be outliers, while the circled observation near 3E is in a region having a sharp discontinuity in wind direction.

Note that the analysis in GEOS-4 does not use surface data directly, but rather it uses boundary layer similarity approximations to infer values for the observations at 1000 or 925 hPa, depending on which level is above the bottom of the model. A sense of a potential problem with this procedure can be obtained from Figure 5.64, which compares the original QuikScat winds with 10 m winds taken from GEOS and NCEP.
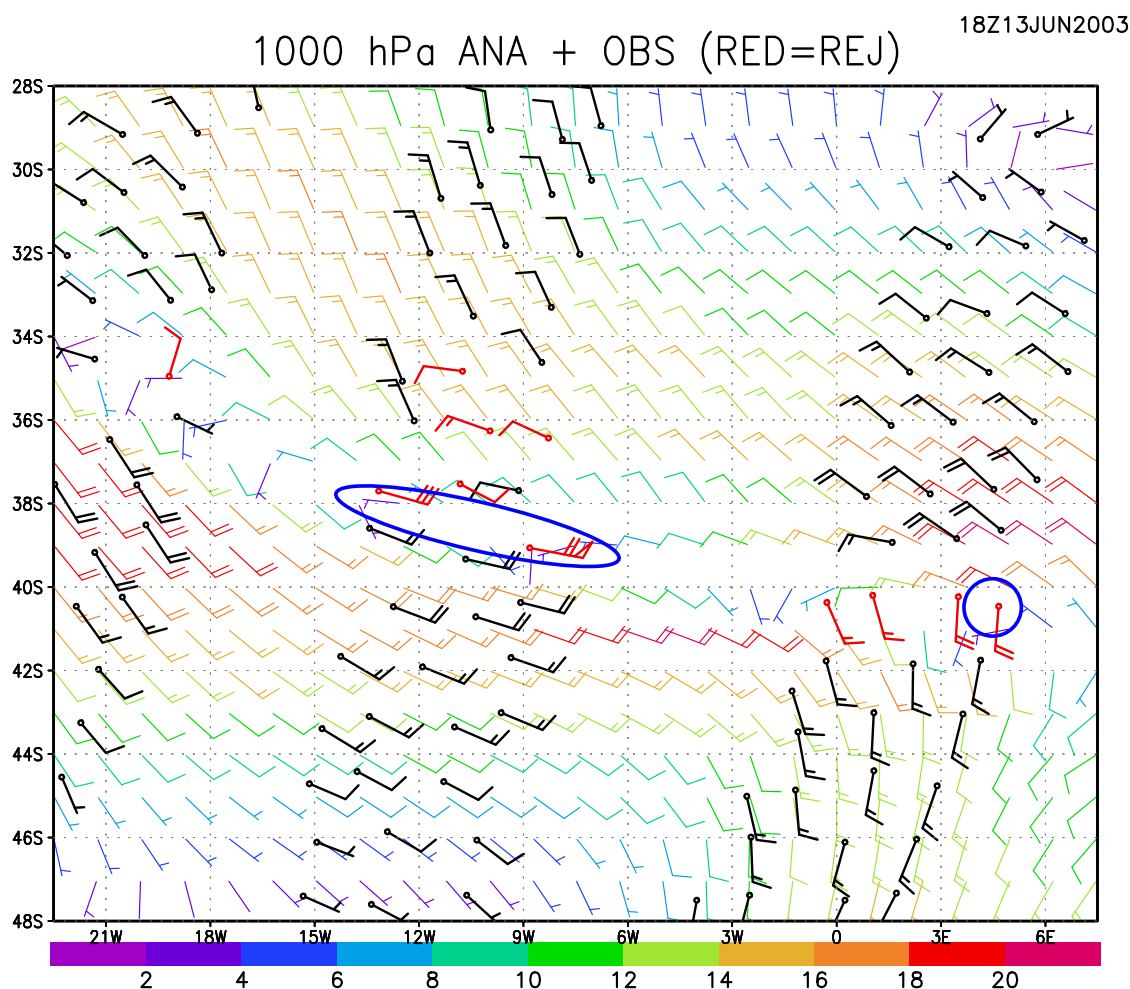
Figure 5.63: GEOS-4 1000 hPa analyzed wind field, with accepted wind observations (black) and rejected wind observations (red). Each barb is $10\,m\,s^{-1}$. Observations affected by the change in QC are outlined in heavy blue.
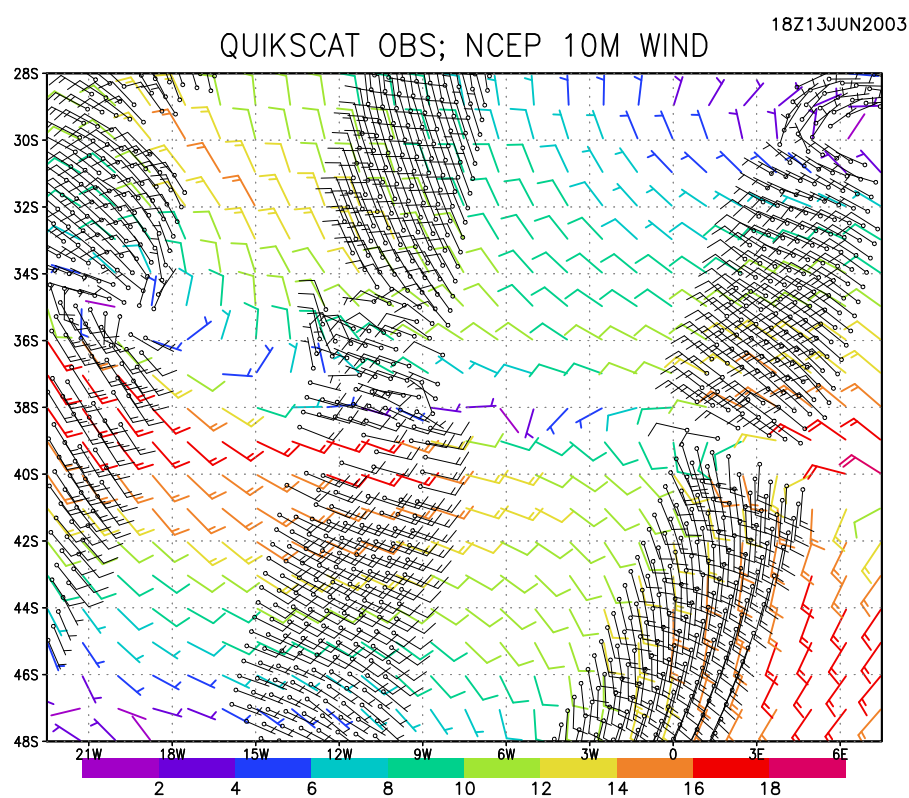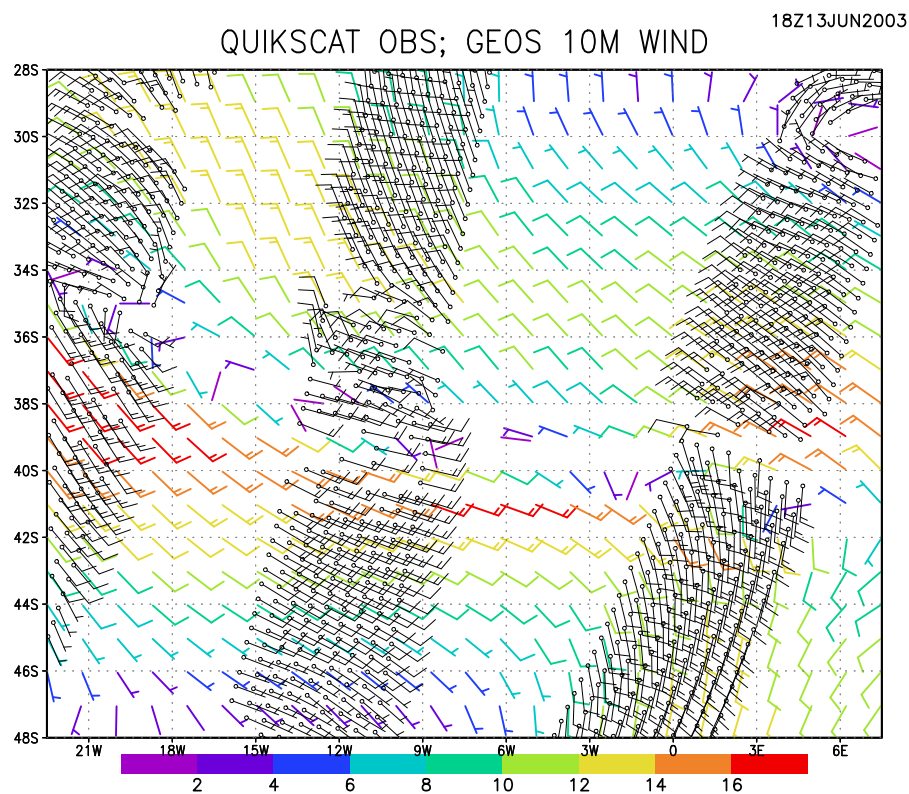
Figure 5.64: Comparison of 10 m winds from GEOS (top) and NCEP (bottom). QuikScat observations (black) superimposed on both. Each barb is $10 \, m \, s^{-1}$.

A close inspection of the QuikScat winds in Figure 5.64 reveals that the large values (especially the $70\,m\,s^{-1}$ 1000 hPa "observation" near 8W) are not present in the actual surface observations. In addition, the directional discontinuity has a much better agreement between the NCEP analysis and QuikScat, especially in the vicinity of 3E. Thus, the QC example shown in Figure 5.56 is actually pointing to more than just rejection of three observations; it leads to at least two broader issues affecting GEOS-4.0.3. The first is an apparent difficulty with the current QC process to handle situations involving strong discontinuities; this issue has appeared a number of times in the monitoring of the operational system. The second issue is the apparent "mangling" of perfectly acceptable observations by the inference process that puts them in a form acceptable for the current analysis process.

Figure 5.65 expands a bit on the last point, as it compares the original QuikScat observations with the inferred 1000 hPa observations used for the analysis. The left panel shows the high-density QuikScat observations, while the right panel shows the thinned (to roughly one degree resolution) 1000 hPa observations; also shown on the right panel is the background Tskin-T2m difference. The correspondence between badly inferred values and regions of high stability (*i.e.* areas of negative Tskin-T2m) is striking.
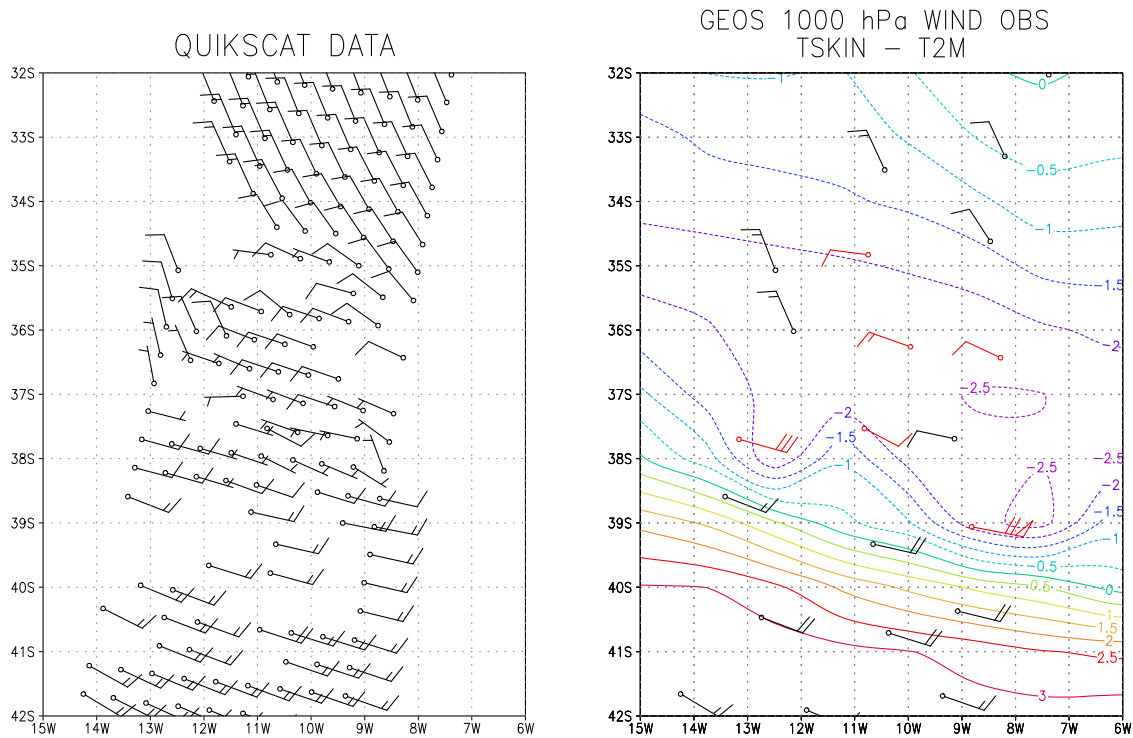
Figure 5.65: Comparison of the original QuikScat winds (left) with the inferred 1000 hPa observations (accepted black, rejected red) used in GEOS-4 (right). Superimposed on the 1000 hPa observations are contours of background Tskin - T2m. Each barb is $10\,m\,s^{-1}$, and the contour interval is 1 K.
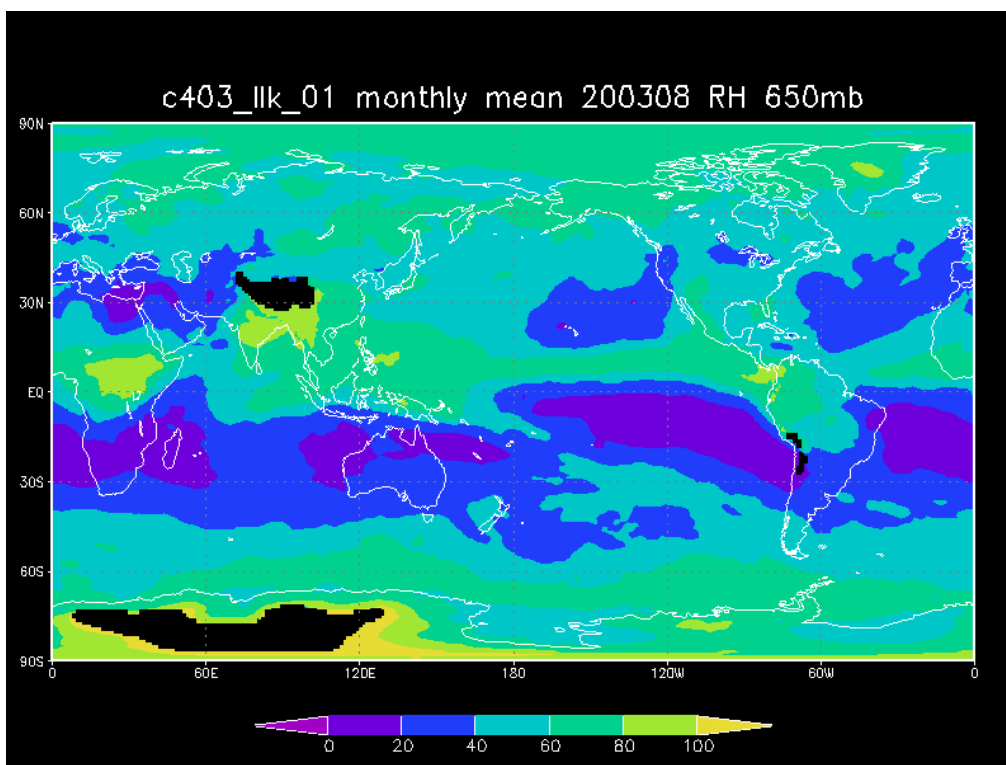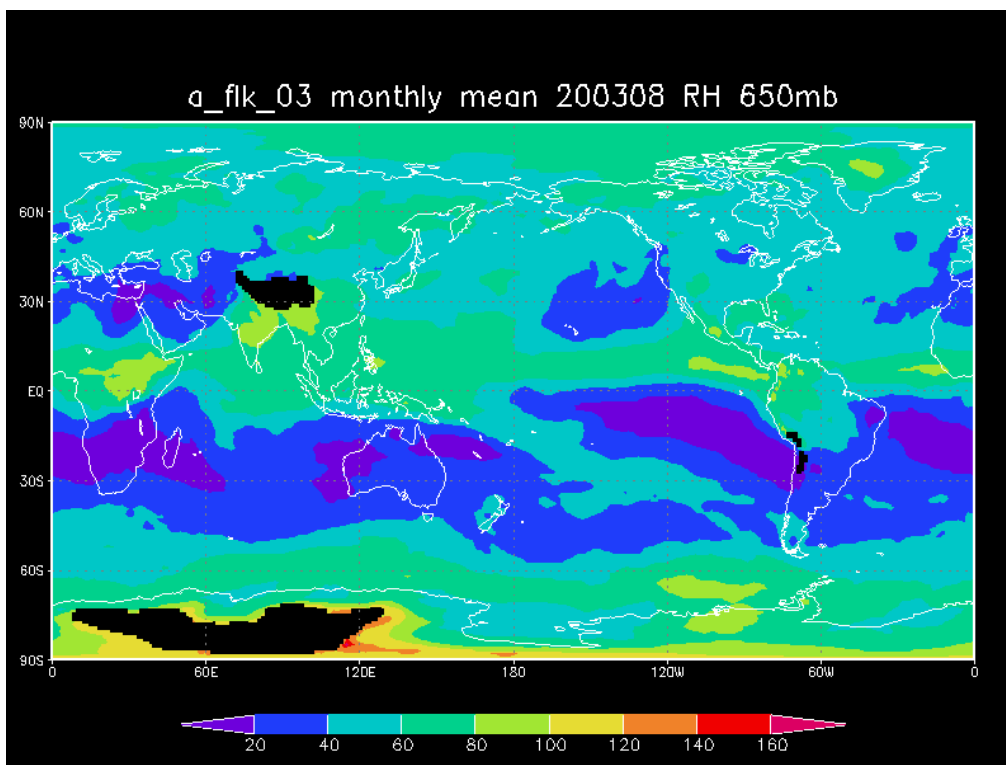
Figure 5.66: Impact of change to RH in GEOS-4.0.3 (bottom) compared to GEOS-4.0.2 (top). Note, this is a monthly mean, and individual cases had RH greater than 1000 in GEOS-4.0.2 near high topography over Antarctica.

5.8.4.2 RH Near Antarctic Topography

A problem with extremely unphysical values of RH near the ground in the Antarctic was noted in prior versions of GEOS-4. Figure 5.66 shows how GEOS-4.0.3 has improved considerably with respect to this problem as a result of a modification to the GCM radiation parameterization near the ground. This figure shows a monthly mean of global RH at 650 hPa, and even with a monthly average the prior system was producing RH greater than 100 % in the Antarctic region. For individual cases, the older system occasionally had RH's greater than 1000 %; GEOS-4.0.3 is vastly improved over the older system in those cases.

5.8.4.3 Precipitation Issues

Section 5.5 discussed the behavior of precipitation in GEOS-4 on monthly-mean time scales. The Monitoring activity had many opportunities to see the precipitation behavior of GEOS-4 on a case-by-case basis. Figure 5.67 shows an example of a positive impact on precipitation by using GEOS-4.0.3. The Caribbean area has often been an area of excessive precipitation in prior GEOS-4 versions, and this case shows GEOS-4.0.3 with significant decrease in precipitation.
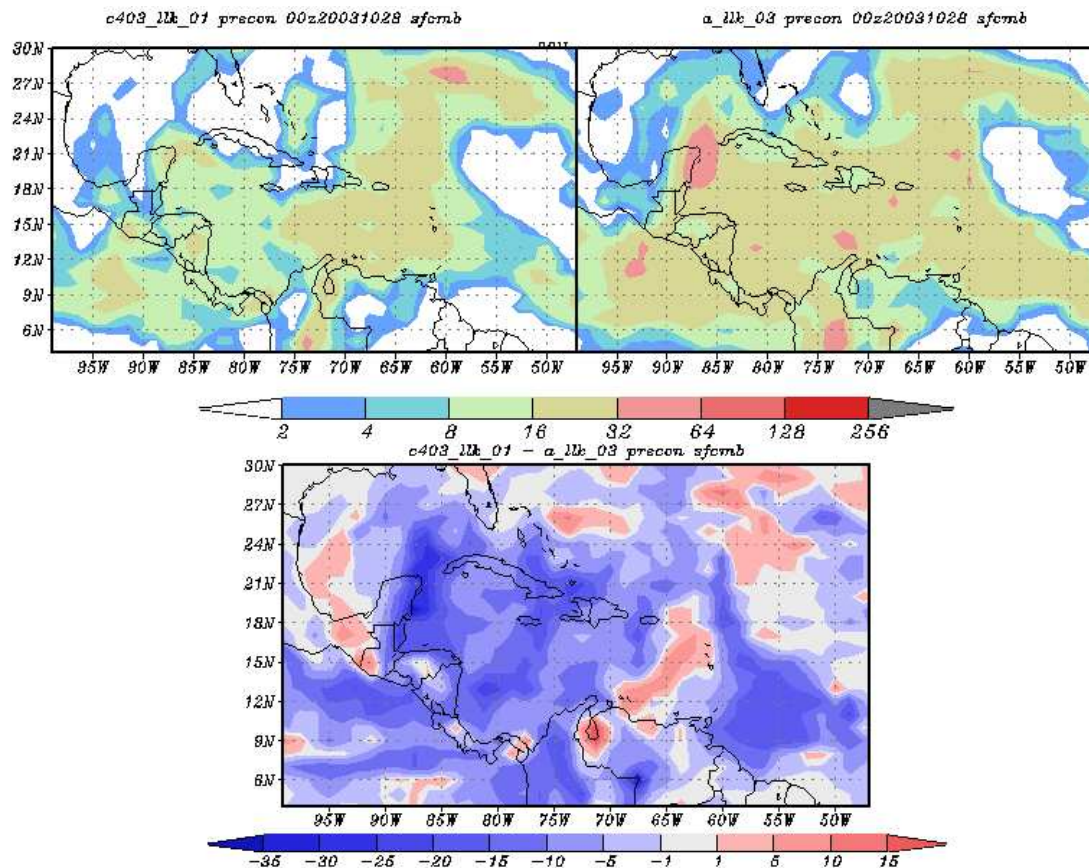
Figure 5.67: Comparison of 6 h average convective precipitation rate for a case at 00Z 28 October 2003; GEOS-4.0.3 (left), GEOS-4.0.2 (right), with the 403 - 402 difference (bottom). Units in $mm\,day^{-1}$.

By way of comparison, Figure 5.68 shows a CONUS IR view from the GOES-12 geo-stationary satellite for this time period. The nearly uniform distribution of convective precipitation in GEOS-4.0.2 is not confirmed by the satellite image, though the intense precipitation zone off the Yucatan coast does seem to verify. The "patchier" appearance of GEOS-4.0.3 appears to conform better to the satellite image, notably for the convection in southern Guatemala and the general minimum of convection over the central part of the area.
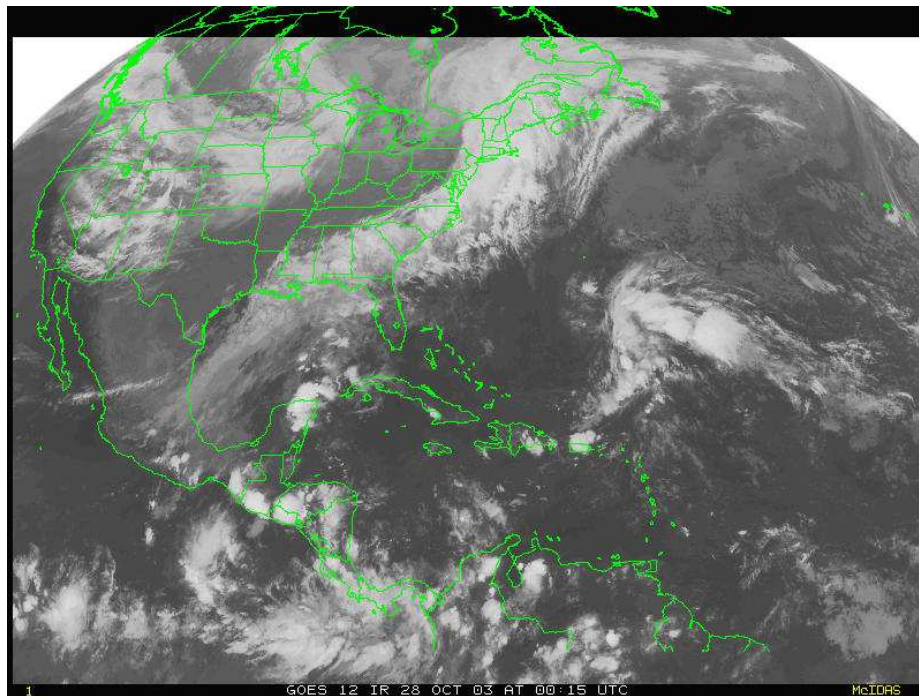
Figure 5.68: IR image from GOES-12 for 00Z 28 October 2003.

Figure 5.69 addresses a different issue: how does the excessive precipitation evident in the GEOS-4 assimilation system transition to the AMIP-like behavior of the GEOS-4 GCM (described in section 3.1.3)? In this figure, precipitation over the Indian Ocean region immediately following an analysis is shown in the leftmost and rightmost columns of panels (labelled "DAS"); the panels in between are day 1 through day 5 forecasts starting from the DAS states on the left. Each row is a separate 5-day forecast. Contours of sea level pressure are also displayed in all of the plots in the figure.

The most striking feature of this figure is the rapidity in how the GEOS-4 GCM transforms the large-scale and somewhat amorphous DAS precipitation patterns into more realistic smaller scale organized patterns that are more consistent with ITCZ structures in the Tropics. It is also instructive to see how similar the forecasted structures are (by following the plots diagonally, lower right to upper left) and how dissimilar they are to the nearest DAS plots (22Z being "close" enough to 00Z for these comparisons).
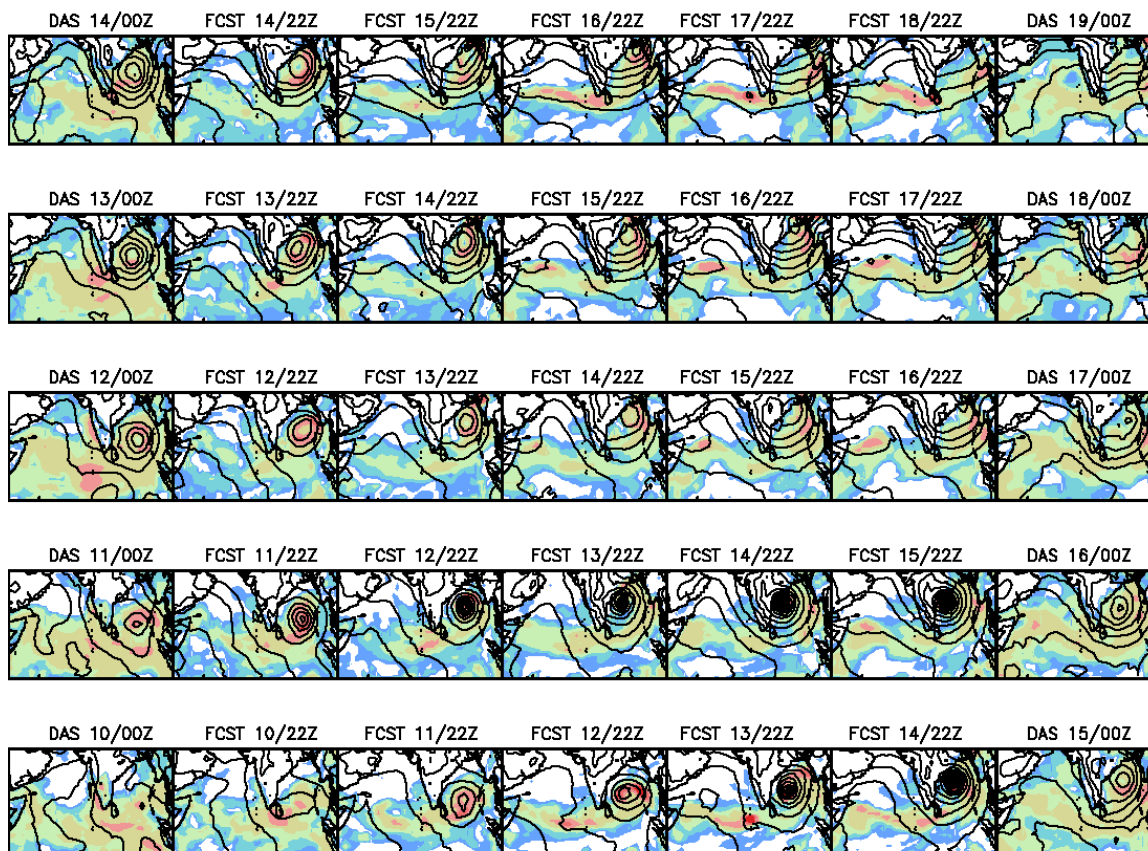
Figure 5.69: Progression of forecasted precipitation (shaded) and sea level (contours) from initial assimilation values (DAS). Shown here is series of five 5-day forecasts over the Indian Ocean region.

5.8.4.4 Synoptic Examples

Two examples of the impact of the changes in the covariance modeling are presented here. Figure 5.70(a) shows the change in a broad thermal trough at 700 hPa off the California coast at 06Z 10 November 2003. The GEOS-4.0.3 analysis has a much larger scale with much sharper temperature gradients. Figure 5.70(b) shows that the GEOS-4.0.3 analysis is in far better agreement with the corresponding NCEP analysis.

Figure 5.71 shows comparisons of the 500 hPa wind field over Northwest Africa: GEOS-4.0.2 vesus NCEP in the top three panels ("402"); GEOS-4.0.3 vesus NCEP in the bottom three panels ("403"). The GEOS-4.0.3 winds are in far better agreement with the NCEP analysis. This has been an area where the previous versions of GEOS were having ongoing problems due to problems with the wind-mass covariance modeling.
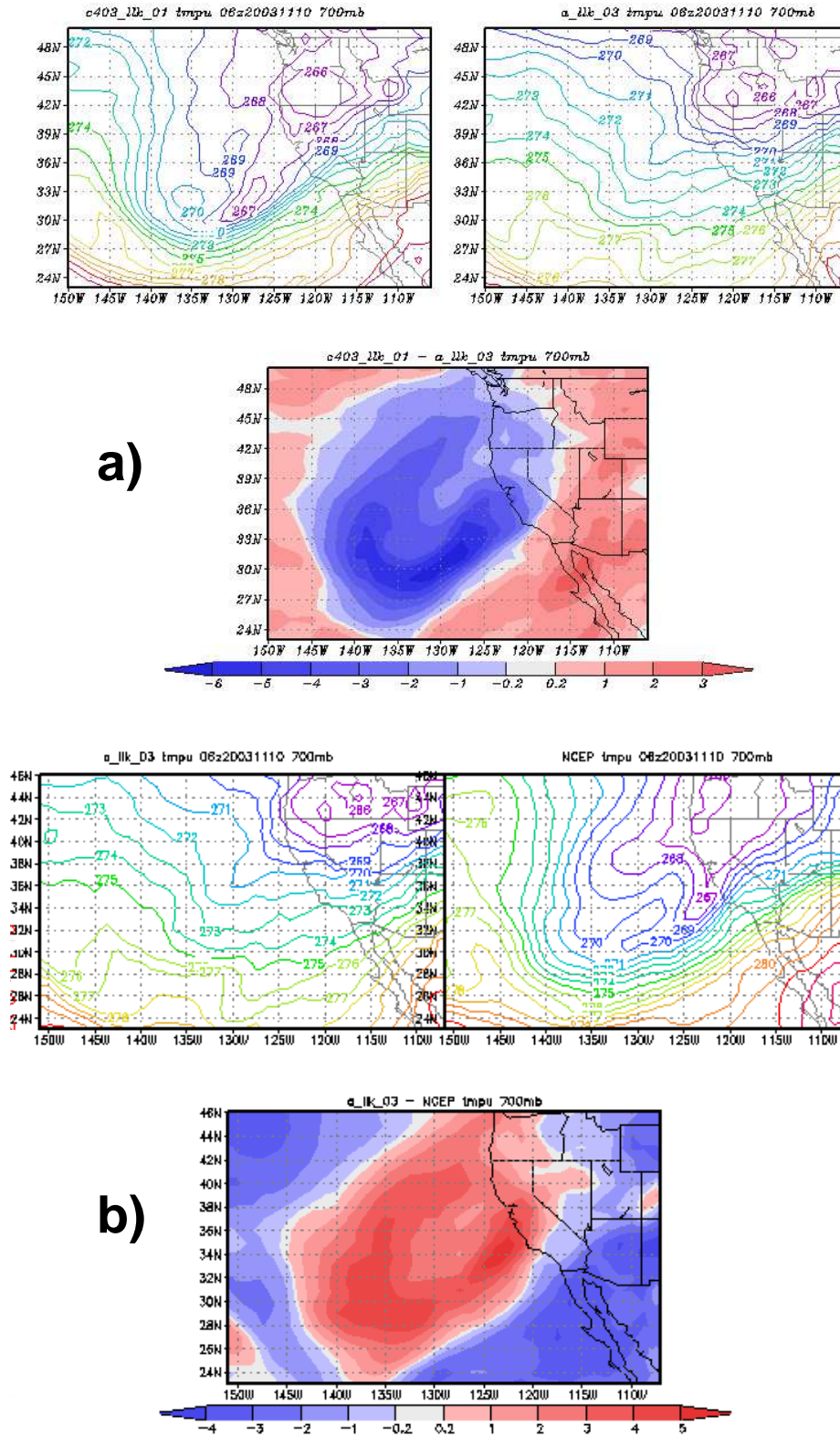
Figure 5.70: Comparisons of the 700 hPa temperature analysis at 06Z 10 November 2003. (a) GEOS-4.0.3 (left), GEOS-4.0.2 (right), and 403 - 402 difference (bottom). (b) GEOS-4.0.2 (left), NCEP analysis (right) and 402 - NCEP (bottom). units in K.
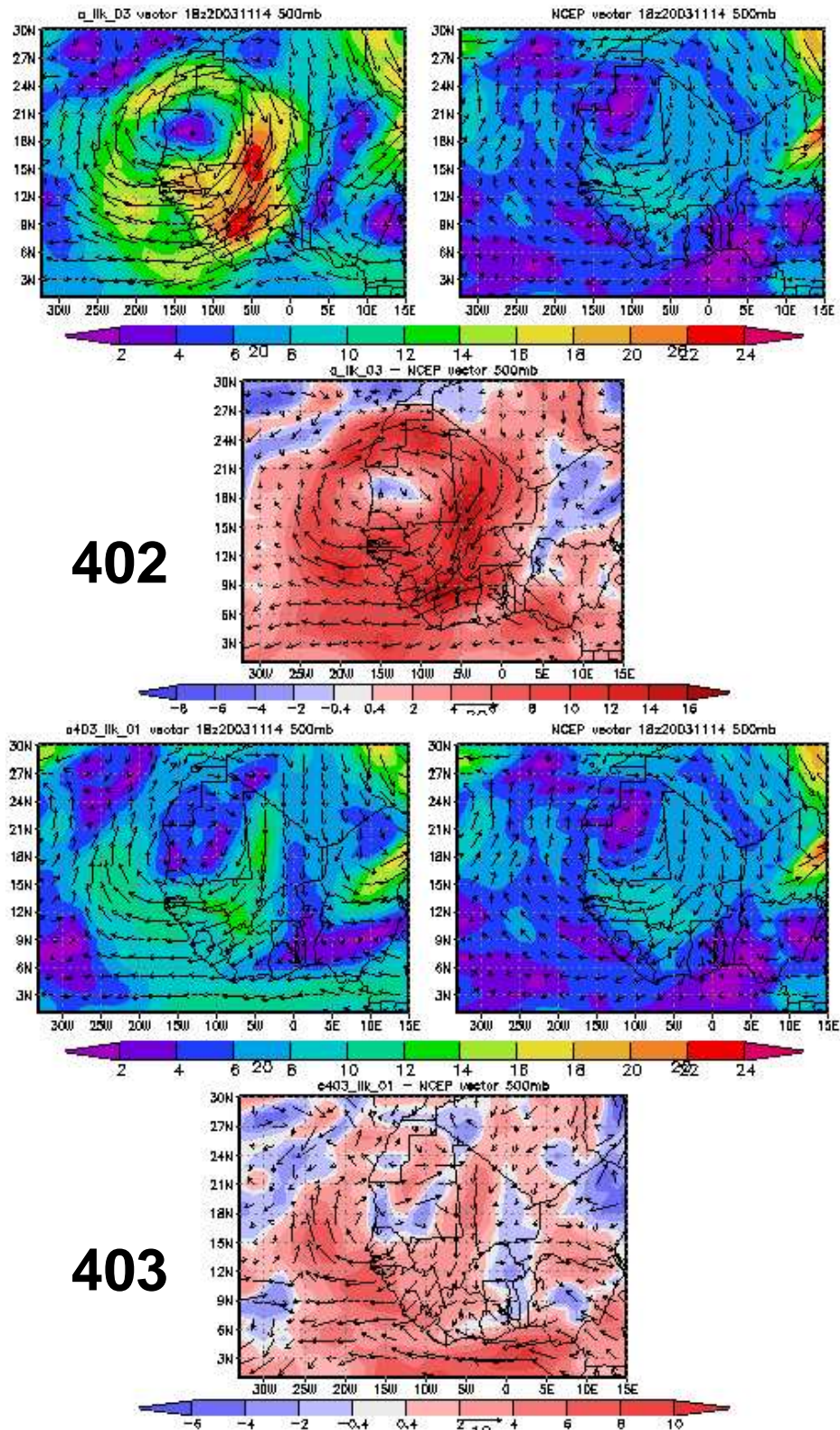
Figure 5.71: Example of change in mass-wind balance on wind analyses: "402" (top) is the 4.0.2 system using the old balance, "403" (bottom) is the 4.0.3 system using the revised balance. In each, the GEOS analysis is on the left, the NCEP comparison analysis on the right, with the difference plotted below.

Chapter 6

Summary

The validation themes discussed in section 4.2 were addressed by the results in section 5:

Customer requirements? GEOS-4.0.3 meets the requirements for CERES (section 5.1) and the chemical transport community (sections 5.3 and 5.4).

Intended changes successful?

- T_{skin} – sections 5.1 and 5.2
- mass-wind covariance modeling changes – sections 5.3, 5.4 and 5.8
- QC, moisture and CTW changes – section 5.8

Overall scientific behavior? The full range of scientific behavior of GEOS-4.0.3 was covered by the investigations in section 5, including land surface properties (5.1,5.2), Stratospheric structure and ozone transport (5.3,5.4), monthly mean statistics (5.5), Tropical dynamics (5.6), data impact (5.7), and synoptic behavior (5.8).

These validation results definitely indicate that GEOS-4.0.3 is a *significant* improvement over GEOS-4.0.2. The changes to the mass-wind covariance modeling (section 3.2.2.1.2) had profound positive effects throughout the entire assimilation atmosphere, affecting both Stratospheric and Tropospheric results. The other major set of changes, involving land surface modeling and T_{skin}, also resulted in significant improvements in GEOS-4.0.3 over GEOS-4.0.2. The other changes made for GEOS-4.0.3 (Quality Control tuning, RH fixes and CTW changes) were verified as improvements during the monitoring process.

There remain a number of problematic issues with GEOS-4.0.3. The most troubling is the tendency for GEOS-4 systems to produce excessive precipitation, both in monthly means (5.5), as well as in synoptic cases (5.8). This limits the value of GEOS-4 systems for use in general reanalysis projects. The instantaneous states in the Stratosphere of GEOS-4.0.3 are excessively noisy (5.3,5.4), although 6-hour averages of GEOS-4.0.3 Stratospheric winds do have utility for transport studies. Finally, while improved in GEOS-4.0.3, the forecast skill of the GEOS-4 systems remains generally substandard in comparison to the current forecasting capabilities at other centers. The data impact studies (5.7) performed for GEOS-4.0.3 tend to indicate that this system is not making full use of radiance data (compared to other centers), and this may be a significant factor in the poorer forecast skill results for GEOS-4.0.3.

Acronyms

1DVAR	One-dimensional (vertical column) Variational retrieval
AIRS	Advanced Infrared Sounder (on Aqua)
AMIP	Atmospheric Model Intercomparison Project
AMSU	Advanced Microwave Sounding Unit (on later TIROS)
AMV	Atmospheric Motion Vectors (also called CTW)
AQUA	EOS PM satellite
AURA	EOS CHEM satellite
ARM	Atmospheric Radiation Measurement program (DOE)
ATOVS	Advanced TOVS
CAPE	Convective Available Potential Energy
CCM3	Community Climate Model, version 3
CEOP	Coordinated Enhanced Observing Period
CERES	Clouds and the Earth's Radiant Energy System (TERRA,AQUA)
CERES-TRMM	CERES instrument on TRMM platform
CGDD	Climate and Global Dynamics Division (NCAR)
CLM, CLM2	Community Land Model
CONUS	Continental United States
CTM	Chemical Transport Model
CTW	Cloud Track Wind (now called AMV)
DAO	Data Assimilation Office (GSFC)
DAS	Data Assimilation System
DMSP	Defense Military Satellite Program
DU	Dobson Unit (Ozone amount in atmospheric column)
ECMWF	European Centre for Medium Range Weather Forecasting
EOS	Earth Observing System
ERS-1,2	Environmental Research Satellite (surface winds obtained using the AMI, Active Microwave Unit)
EUMETSAT	European Organisation for the Exploitation of Meteorological Satellites
FGGE	First GARP (Global Atmospheric Research Program) Global Experiment
fvDAS	finite-volume Data Assimilation System (GEOS-4)
fvGCM	finite-volume General Circulation Model
GCM	General Circulation Model (Atmospheric)
GDAS	Global Data Assimilation System (NCEP)
GEOS	Goddard Earth Observing System
GLATOVS	Goddard Laboratory for Atmospheres TOVS retrievals

GMAO	Global Modeling and Assimilation Office (GSFC)
GOES	Geosynchronous Operational Environmental Satellite
GPCP	Global Precipitation Climatology Project
GSFC	(NASA) Goddard Space Flight Center
GTOPO30	Global Digital Elevation Model (DEM), 30 arc second resolution
HALOE	Halogen Occultation Experiment
HIRS2,3	High-resolution Infrared Spectrometer
IAU	Incremental Analysis Updating (GEOS-3)
iRET	Interactive Retrieval system
ISCCP	International Satellite Cloud Climatology Project
ITCZ	Intertropical Convergence Zone
JMA	Japan Meteorological Agency
LAI	Leaf Area Index
MIPAS	Michelson Interferometer for Passive Atmospheric Sounding
MJO(/ISO)	Madden-Julien Oscillation (Intraseasonal Oscillation)
MLS	Microwave Limb Sounder
MODIS	Moderate Resolution Imaging Spectroradiometer
MPI	Message Passing Interface
MSU	Microwave Sounding Unit (part of TOVS)
NASA	National Aeronautics and Space Administration
NCAR	National Center for Atmospheric Research
NCEP	National Centers for Environmental Prediction
NESDIS	National Environmental Satellite, Data, and Information Service
NOAA	National Oceanic and Atmospheric Administration
NSIPP	NASA Seasonal-to-Interannual Prediction Project
NWP	Numerical Weather Prediction
OI	Optimum Interpolation
OISST	Optimum Interpolation applied to ocean Sea Surface Temperatures
OLR	Outgoing Longwave Radiation
OMA(O-A)	Observation Minus Analysis
OMF(O-F)	Observation Minus Background (or First Guess)
POAM	Polar Ozone and Aerosol Measurement
POES	Polar Operational Environment Satellite
PSAS	Physical-space Statistical Analysis System
QC	Quality Control
RH	Relative Humidity
RMS	Root Mean Square
SBUV/2	Solar Backscatter Ultraviolet Spectral Radiometer-2
SQC	Statistical Quality Control
SSM/I	Special Sensor Microwave/Imager (on DMSP satellites)
SSU	Stratospheric Sounding Unit (superseded by AMSU)
T2M	Atmospheric Temperature at 2 meters above the ground
TERRA	EOS AM Satellite

TIROS-N	Television and Infrared Observatory Spacecraft
TOMS	Total Ozone Mapping Spectrometer
TOVS	TIROS Operational Vertical Sounder
TPW	Total Precipitable Water
TRMM	Tropical Rainfall Measurement Mission
UARS	Upper Atmosphere Research Satellite
WACCM	Whole-Atmosphere Community Climate Model
WMO	World Meteorological Organization

References

Atlas, R., R.N. Hoffman, S.C. Bloom, J.C. Jusem, and J. Ardizzone: 1996, A Multiyear Global Surface Wind Velocity Dataset Using SSM/I Wind Observations. *Bull. Amer. Meteor. Soc.*, **77**, 869–882.

Beven, K.J. and M.J. Kirkby: 1979, A physically-based, variable contributing area model of basin hydrology. *Hydro. Sci. Bull.*, **24**, 43–69.

Bonan, G.B.: 1996, The NCAR land surface model (LSM version 1.0) coupled to the NCAR Community Climate Model. Technical Report *NCAR Tech. Note NCAR/TN-429+STR*, NCAR.

— 1998, The land surface climatology of the NCAR Land Surface Model coupled to the NCAR Community Climate Model. *J. Climate*, **11**, 1307–1326.

Bonan, G.B., K.W. Oleson, M. Vertenstein, S. Levis, X.B. Zeng, Y.J. Dai, R.E. Dickinson, and Z.L. Yang: 2002, The land surface climatology of the Community Land Model coupled to the NCAR Community Climate Model. *J. Climate*, **15**, 3123–3149.

Briegleb, B.P.: 1992, Delta_Eddington approximation for solar radiation in the NCAR Community Climate Model. *J. Geophys. Res.*, **97**, 7603–7612.

Chou, M.D., K.T. Lee, and M.J. Suarez: 1999, The NCAR land surface model (LSM version 1.0) coupled to the NCAR Community Climate Model. *NASA Tech. Memo.*, **15 (104606)**, 40 pp.

Chou, M.D., M.J. Suarez, X.Z. Liang, and M.H. Yan: 2003, A thermal infrared radiation parameterization for atmospheric studies. *NASA Tech. Memo.*, **19 (104606)**, 55 pp.

Dai, Y.J., X.B. Zeng, R.E. Dickinson, I. Baker, G.B. Bonan, M.G. Bosilovich, A.S. Denning, P.A. Dirmeyer, P.R. Houser, G.Y. Niu, K.W. Oleson, C.A. Schlosser, and Z.L. Yang: 2003, The Common Land Model. *Bull. Amer. Meteor. Soc.*, **84**, 1013–1023.

Dee, D.P., L. Rukhovets, R. Todling, A.M. da Silva, and J. Larson: 2001, An adaptive buddy check for observational quality control. *Quart. J. Roy. Meteor. Soc.*, **127**, 2451–2471.

Dee, D.P. and A.M. da Silva: 1999, Maximum-Likelihood Estimation of Forecast and Observation Error Covariance Parameters Part I: Methodology. *Mon. Wea. Rev.*, **127**, 1822–1834.

— 2003, The choice of variable for atmospheric moisture analysis. *Mon. Wea. Rev.*, **131**, 155–171.

Dee, D.P. and R. Todling: 2000, Data Assimilation in the Presence of Forecast Bias: The GEOS Moisture Analysis. *Mon. Wea. Rev.*, **128**, 3268–3282.

Dickinson, R.E., G.L. Wang, X.B. Zeng, and Q.R. Zeng: 2003, How does the partitioning of evapotranspiration and runoff between different processes affect the variability and predictability of soil moisture and precipitation? *Adv. Atmos. Sci.*, **20**, 475–478.

Gaspari, G. and S.E. Cohn: 1999, Construction of correlation functions in two and three dimensions. *Quart. J. Roy. Meteor. Soc.*, **125**, 723–7.

Guo, J., J.W. Larson, G. Gaspari, A. da Silva, and P.M. Lyster: 1998, Documentation of the Physical-space Statistical Analysis System (PSAS) Part II: The factored-operator error covariance model formulation. *DAO Office Note*, **1998-04**.

Guo, J. and A. da Silva: 1997, Computational aspects of Goddard's Physical-space Statistical Analysis System (PSAS). *Numerical simulations in the environmental and earth sciences*, Garcia et al., ed., Cambridge University Press, iSBN 052158047.

Hack, J.J.: 1994, Parameterization of moist convection in the National Center for Atmospheric Research Community Climate Model (CCM2). *J. Geophys. Res.*, **99**, 5551–5568.

— 1998, Sensitivity of the simulated climate to a diagnostic for formulation for cloud liquid water. *J. Climate*, **11**, 1497–1515.

Helfand, H.M. and J.C. Labraga: 1988, Design of a nonsingular level 2.5 second-order closure model for the prediction of atmospheric turbulence. *J. Atmos. Sci.*, **45**, 113–132.

Holtslag, A.A.M. and B.A. Boville: 1993, Local versus nonlocal boundary-layer diffusion in a global climate model. *J. Climate*, **6**, 1825–1842.

Hong, S.Y. and H.L. Pan: 1998, Convective trigger function for a mass-flux cumulus parameterization scheme. *Mon. Wea. Rev.*, **126**, 2599–2620.

Hou, A.Y., D.V. Ledvina, A.M. da Silva, S.Q. Zhang, J. Joiner, R.M. Atlas, G.J. Huffman, and C.D. Kummerow: 2000a, Assimilation of SSM/I-Derived Surface Rainfall and Total Precipitable Water for Improving the GEOS Analysis for Climate Studies. *Mon. Wea. Rev.*, **128**, 509–537.

Hou, A.Y., S.Q. Zhang, A.M. da Silva, and W.S. Olson: 2000b, Improving assimilated global datasets using TMI rainfall and columnar moisture observations. *J. Climate*, **13**, 4180–4195.

Hou, A.Y., S.Q. Zhang, A.M. da Silva, W.S. Olson, C.D. Kummerow, and J. Simpson: 2001, Improving global analysis and short-range forecast using rainfall and moisture observations derived from TRMM and SSM/I passive microwave sensors. *Bull. Amer. Meteoro. Soc.*, **82**, 659–679.

Joiner, J. and L. Rokke: 2000, Variational cloud-clearing with TOVS data. *Quart. J. Roy. Meteor. Soc.*, **126**, 725–748.

Kiehl, J.T., J.J. Hack, G.B. Bonan, B.A. Boville, B.P. Briegleb, D.L. Williamson, and P.J. Rasch: 1985, Description of the NCAR Community Climate Model (CCM3). Technical Report *NCAR/TN-420+STR*, NCAR, Boulder, CO.

Kiehl, J.T., J.J. Hack, G.B. Bonan, B.A. Boville, D.L. Williamson, and P.J. Rasch: 1998, The National Center for Atmospheric Research Community Climate Model: CCM3. *J. Climate*, **11**, 1131–1150.

Krasnopolsky, V.M., W.H. Gemmill, and L.M. Breaker: 2000, A neural network multi-parameter algorithm for SSM/I ocean retrievals: Comparisons and validations. *Remote Sens. Environ.*, **73**, 133–142.

Larson, J.W., J. Guo, G. Gaspari, A. da Silva, and P.M. Lyster: 1998, Documentation of the Physical-space Statistical Analysis System (PSAS) Part III: The software implementation of PSAS. *DAO Office Note*, **1998-05**.

Lin, S.J.: 1997, A finite-volume integration method for computing pressure gradient force in general vertical coordinates. *Quart. J. Roy. Meteor. Soc.*, **123**, 1749–1762.

Lin, S.J. and R.B. Rood: 1996, Multidimensional flux-form semi-Lagrangian transport schemes. *Mon. Wea. Rev.*, **124**, 2046–2070.

— 1997, An explicit flux-form semi-Lagrangian shallow-water model on the sphere. *Quart. J. Roy. Meteor. Soc.*, **123**, 2477–2498.

— 1998, A flux-form semi-Lagrangian general circulation model with a Lagrangian control-volume vertical coordinate. *The Rossby-100 symposium*, Stockholm, Sweden.

McFarlane, N.A.: 1987, The effect of orographically excited wave drag on the general circulation of the lower stratosphere and troposphere. *J. Atmos. Sci.*, **44**, 1775–1800.

Pfaendtner, J., S. Bloom, D. Lamich, S. Seablom, M. Sienkiewicz, J. Stobie, and A. da Silva: 1995, Documentation of the Goddard Earth Observing System (GEOS) Data Assimilation System - Version 1. *NASA Tech. Memo.*, **4 (104606)**, 44 pp.

Ramanathan, V. and P. Downey: 1986, A nonisothermal emissivity and absorptivity formulation for water vapor. *J. Geophys. Res.*, **91**, 8649–8666.

Randel, W.J., F. Wu, J.M. Russell III, A. Roche, and J. Waters: 1998, Seasonal cycles and QBO variations in stratospheric CH4 and H2O observed in UARS HALOE data. *J. Atmos. Sci.*, **55**, 163–185.

Reynolds, R.W., N.A. Rayner, T.M. Smith, D.C. Stokes, and W.Q. Wang: 2002, An improved in situ and satellite SST analysis for climate. *J. Climate*, **15**, 1609–1625.

Schubert, S.D., R.B. Rood, and J.W. Pfaendtner: 1993, An assimilated data set for earth science applications. *Bull. Amer. Meteor. Soc.*, **74**, 2331–2342.

Sienkiewicz, M.: 1996, The GLA TOVS Rapid Algorithm Forward Radiance Modules and Jacobian Version 1.0. *DAO Office Note*, **1996-08**.

da Silva, A. and J. Guo: 1996, Documentation of the Physical-space Statistical Analysis System (PSAS) Part I: The Conjugate Gradient Solver Version PSAS-1.00. *DAO Office Note*, **1996-02**.

Slingo, J.M.: 1987, The development and verification of a cloud prediction scheme for the ECMWF model. *Quart. J. Roy. Meteor. Soc.*, **113**, 899–927.

Sud, Y.C. and G.K. Walker: 1999, Microphysics of Clouds with the Relaxed Arakawa-Schubert Scheme (McRAS). Part I: Design and evaluation with GATE Phase III data. *J. Atmos. Sci.*, **56**, 3196–3220.

Sundqvist, H.: 1988, Parameterization of condensation and associated clouds in models for weather prediction and general circulation simulation. *Physically-based Modeling and Simulation of Climate and Climate Change, Vol 1*, M.E. Schlesinger, ed., Kluwer Academic, 433–461.

Susskind, J., J. Rosenfield, and D. Reuter: 1997, An accurate radiative transfer model for use in the direct physical inversion of HIRS and MSU temperature sounding data. *J. Geophys. Res.*, **88**, 8850–8568.

Wentz, F.J.: 1997, A well-calibrated ocean algorithm for SSM/I. *J. Geophys. Res.*, **102 C4**, 8703–8718.

Zeng, X., M. Shaikh, Y. Dai, R.E. Dickinson, and R. Myneni: 2002, Coupling of the Common Land Model to the NCAR Community Climate Model. *J. Climate*, **15**, 1832–1854.

Zhang, G.J. and N.A. McFarlane: 1995, Sensitivity of climate simulations to the parameterization of cumulus convection in the Canadian Climate Centre general circulation model. *Atmos-Ocean*, **33**, 407–446.